Special Instrumentation for Two-Phase Flow

Politecnico di Torino
Dipartimento Energia

Dottorato di Ricerca in Energetica - Ingegneria Nucleare
XXVI Ciclo (2010-2013)

TESI DI DOTTORATO

Special Instrumentation for Two-Phase Flow

RELATORI

Prof. Mario De Salve

Prof. Bruno Panella

CANDIDATO

Grazia Monni

CONTENTS

NOMENCLATURE

A	area (m^2)
$a(i,j)$	WMS geometrical weight matrix
C	Capacitance (F)
C_D	Drag coefficient
C_d	VFM discharge coefficient
D	diameter (m)
d_b	bubble diameter (m)
D_{wire}	WMS wires diameter (m)
E_∞	equilibrium entrainment
f	frequency (Hz), friction factor
F_a	VFM thermal expansion correction factor
G	mass flux (kg/m^2s)
h^*	interface position
J	superficial velocity (m/s)
K	instrument calibration coefficient
L	length (m)
$M(t)$	chordal void fraction time evolution index
p	pressure (bar)
p	WMS wires pitch (m)
Q	volumetric flow rate (m^3/s)
S	Slip Ratio, Signal
t	time (s)
T	temperature (°C)
T_T	total observation time (s)
U	velocity (m/s)
V	Volts (V), Volume (m^3),
$V(i,j,k)$	WMS output matrix
V^*	WMS normalized signal
W	mass flow rate (kg/s)
x	flow quality
Y	VFM compressibility coefficient
z	vertical coordinate (m)

Subscripts

1	VFM inlet section subscript
2	VFM constricted area subscript
acq	acquisition
b	bubble
c	core
D	drag disk (DD)
d	droplets, discharge
est	estimated

ex	excitation
exp	experimental
f	film (liquid)
g	gas
h	liquid level height (m)
i	i-th vertical WMS index
int	internal
irr	irreversible
j	j-th horizontal WMS index
k	WMS time index
l	liquid
max	maximum
min	minimum
p	pipe
s	slug
t	target (DD)
T	Turbine
tot	total
TP	Two-Phase

Special characters

α	void fraction
β	D_2/D_1 VFM diameter ratio, volumetric flow rate ratio, blade TFM pitch angle
ε	electrical permittivity (F/m)
μ	dynamic viscosity (Pa·s)
ρ	density (kg/m^3)
σ	surface tension (N/m), standard deviation
τ	moving average time, characteristic time (s)
δ	film thickness (mm)
θ	swirl angle (TFM), divergent/convergent angle (VFM), angle between electrodes (ECP)
ω	TFM rotational speed (rad/s)
Δp	differential pressure (bar)
Δpirr	VFM irreversible pressure losses (bar)
ΔpV= p1 - p2	VFM inlet (1) - throat (2) section pressure drops
χ2	Lockart-Martinelli parameter (eq. 4.21)
χ2mod	modified Lockart-Martinelli parameter
ϕ_k^2	Two-phase flow multiplier (eq. 4.20)

Adimensional numbers

$Eu = \frac{\Delta p}{\rho U^2}$ Euler number

$Fr = \frac{U}{\sqrt{gD}}$ Froude number

$M = \frac{U}{U_{sound}}$ Mach number

$\mathrm{Re} = \frac{\rho U D}{\mu}$ Reynolds number

$St = \frac{f \cdot D}{J}$ Strouhal number

$We = \frac{\rho U^2 D}{\sigma}$ Weber number

Abbreviations

ADS	Automatic Depressurization System
ANSI	American National Standards Institute
API	American Petroleum Institute
ASME	American Society of Mechanical Engineers
DAQ	Data AcQuisition
DBA	Design Basis Accident
DD	Drag Disk
DEG	break line
DTT	Drag Disk - Turbine Transducer
DVI	Direct Vessel Injection
DW	Dry Well
EBTs	Emergency Boration Tanks (),
ECP	Electrical Capacitance Probe
EHRS	Emergency Heat Removal System
f.s.v	full scale value
FFT	Fast Fourier Transform
ITF	Integral Test Facility
LGMS	Long Term Gravity Make-up System
LOCA	Loss of Coolant Accident
LOFT	Loss-of-Fluid Test Facility
NPP	Nuclear Power Plant
ORNL	Oak Ridge National Laboratory
PCC	Passive Containment Cooling
PDF	Probability Density Function
PSD	Power Spectral Density
PSS	Pressure Suppression Systems
PWR	Pressurized Water Reactor
QCV	Quick Closing Valve
QT	Quench Tank
r.v	read value
RC	Reactor Cavity
RMS	Root Mean Square
SBLOCAs	Small Break LOCA
SMR	Small Modular Reactor
SP	Spool Piece
SPES3	Simulator for PWR Safety Experiments
SPLIT	break line
TFM	Turbine Flow Meter
TTFMS	Two Turbine Flow Meter System
VFM	Venturi Flow Meter
WMS	Wire Mesh Sensor

LIST OF FIGURES

Chapter 2

Chapter 3

Chapter 4

Chapter 5

Chapter 6

Chapter 7

Chapter 8

Chapter 9

LIST OF TABLES

1. INTRODUCTION

The design of engineering systems, involving two-phase flow, such as nuclear water reactors, requires the ability to model and predict the detailed behavior of those flows and the phenomena that they manifest, with a required degree of accuracy. There are three ways in which such models are explored: experimentally, through laboratory-sized models equipped with appropriate instrumentation, theoretically, using mathematical equations and models for the flow, and computationally, using numerical model, implemented in complex codes, to address the complexity of the flow.

More than 50 years have been spent on developing various solutions for measuring two-phase flow with the aim to obtain local or integral information, build very sensitive (but usually also fragile) instruments, try to improve the precision of the existing sensors, and develop techniques that are simple to use and to interpret.

In spite of these efforts, there is no and perhaps never will be an optimum instrumentation. Measuring two-phase flow will always require experienced researchers using special solutions for each required purpose.

Successful application of a measuring system in a two-phase test setup does not automatically guarantee its applicability in every flow or loop conditions. In addition, two-phase measuring techniques in many cases do not measure directly the two-phase properties (such as velocities of the single phases, density of the mixture, etc.) so that an interpretative model must be used and verified and the comparison of calculated and measured data is needed.

The design of nuclear reactors requires to carry out integral and separate effect tests on simulation facilities, as well as to perform safety systems verification and safety code validation. The analysis of thermal-hydraulic processes that might occur in a nuclear water reactor containment building under severe accident conditions is very complex. This complexity arises from the large number of dependent variables which must be considered for the analysis. The variety of physical phenomena occurring during the evolution of a transient introduce additional levels of complexity to this analysis.

The thermal hydraulics research facilities must produce flow and thermal data for studies on the thermal processes that are sufficiently detailed to provide the industry and academic

researchers with insights into the flow and thermal processes which occur within the nuclear engineering systems.
The "separate effect tests" focus on single parameters. In many of these cases two-phase flow phenomena can be simulated in tests under well-defined boundary conditions. In these separate effect experiments many kinds of two-phase measurement devices have been used with good success, because the instrumentation could be optimized to only a few parameters. Two-phase flow instrumentation is also necessary for the interpretation of "integral effect tests", for example simulating the thermo-hydraulics of a PWR in a scaled-down test facility. Under these conditions, instrumentation consists of mechanical parts installed in the flow path and they can influence the system behavior itself. So an optimum balance between the amount of measuring information needed and the flow disturbance must be found.
Concerning the computational analysis, different predictive simulations can be performed using different approaches: RELAP and TRAC are usually used in 1-D simulations, while CFD software, such as CFX, STAR-CCM+ or RELAP 3-D are used to perform detailed analysis of the thermal-hydraulics in limited regions or single components, due to the high computational costs. In every case the simulation's results are compared with the available experimental data.
Reliable two-phase instrumentation is therefore essential for the connection between analysis and experiment especially in the nuclear safety research where accident scenarios have to be simulated in experimental facilities and predicted by complex computer code systems.

In the past a significant amount of effort has been addressed to the development of intrusive and nonintrusive measurement techniques of two-phase flows, with special application to the determination of mass flow rates. Many extensive experiments are being performed to investigate in detail loss of coolant accidents (LOCA). During these experiments the coolant is released as a two-phase mixture through a simulated break of a coolant pipe, and the measurement of the mass flow rate of the two phases was required to analyze the accident evolution and consequences. In this context, most flow meters have been designed to measure the single-phase flow of a Newtonian fluid, and then used to measure quantities in more complex fluids. The key to fundamental understanding of two-phase flow is still the careful development of specialized instrumentation, in particular for special and complex geometrical applications.
Moreover new experimental campaigns are now required for the licensing of the new, advanced reactors, so that the development of new instruments or instruments models for the measurement of the fundamental parameters of the flow, under many possible two-phase conditions, is required.
Within the framework of an Italian R&D program on Nuclear Fission, supported by the Ministry of Economic Development, the SPES3 experimental facility [1.1], able to simulate the innovative small and medium size PWR nuclear reactors, is being built and will be operated at SIET Company laboratories. In such facility some design and beyond design basis accidents, like LOCAs, with and without the emergency heat removal systems, will be simulated. In most accident simulations, a two-phase flow mixture will occur in the lines, during the transient evolution, due to the simulated strong depressurization of the system.
An accurate accident analysis requires the measurement of the mixture mass flow rate and for this reason, instruments and methodologies to evaluate different two-phase flow parameters need to be developed. Typically a set of instruments (Spool Piece - SP) must be

installed in order to evaluate the mass flow rate of the phases in a large range of flow patterns, pressures and temperatures. An ideal SP is a control volume constituted by different measurement instruments, fed with a two-phase flow. In single-phase flow, each instrument is able to measure a well defined flow parameter, while the instrument signal interpretation, in two-phase flow, is not easy due to the different flow patterns and the to the large number of parameters that influence the flow, so that a model of the SP, depending on the geometry and on the SP orientation, is required. Moreover the selection of the instruments strongly depends on the experimental conditions: pressure, temperature and phases velocities.

The need of mass flow rate measuremtent is not limited to nuclear safety applications.
Practical applications of a gas-liquid flow, of a single substance or two different components, are commonly encountered also in the power generation (steam generators), space (where two-phase flow is present in the power and thermal management systems, fluid and propellant management systems, and environmental control and life support systems), petroleum (oil, extraction, gas extraction, flow of oil and gas or water and gas in long pipelines), chemical (fluidised beds, pumping of slurries, pumping of flashing liquids, raining bed driers, etc..), refrigeration (moisty air flow), geothermal industries (flow in wellbore of the weels), but also paper manufacturing, food manufacturing and medical applications.
The two phases may be of different components and/or there could be a phase change due to evaporation and condensation of a single fluid; but in every case, from given operating conditions, the correct prediction of both mass flow rates and void fraction (or liquid hold-up, if refered to the liquid fraction) is fundamental for a proper design of the all equipment: for gathering, pumping, transporting and storing.

The thesis work consists in the development of special instrumentation and in the development of models, based on the analysis of experimental data, that are able to interpret the measurement signals for many possible two-phase conditions.
The two different measurement fields, internal flow structure investigation and instrument modeling for phases mass flow rate reconstruction purposes, have been analyzed.

In the first field the instrumentation must be able to characterize momentum, mass, energy balance with a resolution sufficient to investigate local phenomena and characteristic structure (interface evolution, void profiles, liquid film level, characteristic frequencies, etc..).
The investigation of an horizontal two-phase flow has been performed by means of a Wire Mesh Sensor, as described in chapter 5. Local, chordal, cross-section void fraction values are derived from the sensor data in a wide range of phases superficial velocities, and a new signal methodology, able to characterize the flow in terms of phases distribution (flow patterns) and time evolution, has been developed. Moreover the methodology allows the extraction of important flow information, such as the local and time average void fraction, the interface evolution, and characteristic frequencies.
The evolution of the void fraction profiles has been related to the superficial velocity of the two-phases (J_g and J_l) and the flow evolution in time and space has been analyzed and discussed, showing that such methodology is useful to identify and characterize in detail the two-phase flow.

Concerning the second measurement field, in chapter 4 and more in details in [1.4] the analysis of the instruments used for two-phase flow measurement applications has been described. This bibliographic research allowed the definition of the candidate instruments suitable to be installed in a nuclear safety experimental facility, and their measurement characteristics.
The selection of the candidate instruments has been made defining some fundamental criteria that should be satisfied: range of measurement, dynamic response, installation requirements, materials/electrical compatibility with pressure and temperature conditions, flow velocity compatibility.

The selected meters are:
- Turbine [1.5]
- Drag disk [1.5]
- Venturi [1.6]
- Impedance Probes:
    - Concave sensors
    - Wire mesh sensor [1.7]
    - Electrical Capacitance Probe (ECP) [1.8]→ designed by SIET

Also considering limits and drawbacks of these instruments, these are the only analyzed devices that could operate in the whole range of conditions expected in the break lines:
- Void fractions (from 0 to 1),
- Pressure (up to155 bar),
- Temperature (span: 200°C and in some lines 400°C)
- Velocity (gas velocity up to 200 m/s)

The instruments described in chapter 4 have been experimentally studied in different pipe configurations, and different models have been developed for each one. Different instrument combinations have been tested, and the performance of each one has been analyzed in terms of estimation of the mass flow rate of the two phases.

The performed research allows the identification of the advantage and drawbacks of the different instrument combinations, and the identification of the phases mass flow rate measurement accuracy achievable for each SP configuration.

In chapter 6 has been analyzed the SP consisting of a turbine flow meter (volumetric device) and a drag disk (momentum measurement device), under annular and stratified annular air-water two-phase flow. The analysis showed that, in the tested operating range, the knowledge of the flow pattern, and then of the void fraction, is indispensable to evaluate the two-phase flow parameters, so that the SP has been integrated with a void fraction measurement device (impedance concave sensor).
The experimental data have been used to construct an operating map of the SP, able to evaluate the mass flow rates of the phases in the mixture, with the relative errors, and to predict the flow pattern.

Compared with the first experimental campaign the new data cover a wide range of flow superficial velocities, corresponding to different flow patterns from bubbly to annular flow.
The measurement of the void fraction allows the use of the Aya's model in all the experimented range, obtaining the mass flow rate of the phases with an accuracy of 15% in the 75% of the cases.

In chapter 7 the analysis of the signals and the developed model of the SP, consisting of a VFM and WMS is reported. The developed methodology allows the estimation of the mass flow rate of the phases in air-water horizontal flows with a good accuracy in a large range of the flow conditions (J_g = 0.14 - 32 m/s and J_l = 0.019 - 2.62 m/s), with observed flow patterns ranging from stratified flow to intermittent flow (slug and plug) and annular flow.
The VFM response has been modeled by defining the two-phase flow discharge coefficient, $C_{d\text{-}TP}$, and its Re dependency. A modified Lockart-Martinelli correlation for x-α, able to represent the WMS experimental data, has been developed and included in the SP model.
By means of the developed signal analysis the mass flow rate has been estimated with an error lower than 10% in the 73.3% of the cases. Moreover the estimation error has been found considerably lower for the flow characterized by high values of quality and void fraction. In this range, with reference to facility SPES3 test conditions, the error in the mass flow rate estimation is always lower than 10% and 20% for water and air respectively.

In chapter 8, the analysis and the characterization of the impedance sensor (Electrical Capacitance Sensor – ECP, developed by the SIET company), consisting of 10 measurement electrodes (9 external and 1 internal), in vertical annular and annular-mist flow, is described.
The response of the sensor has been characterized in terms of single-phase flow sensitivity and signal variation dependence. Geometry and fluid-dynamic influences on the signal have been investigated experimentally and numerically, by means of a FEM software. Although the sensitivity in single-phase flow is low, two-phase flow void fraction variations lower than 1% have been detected. The central electrode signal has been related to the average cross-section void fraction, difficult to measure with external electrodes, due to the presence of the wall liquid film, that acts as a screen. The variation of the signal measured in the external electrodes has been related to the average liquid film thickness that has been evaluated by means of the Ishii model. The tests have shown the potentiality of this technology for the measurement of two-phase flow parameters at very high void fraction conditions (higher than 95%).

In the last chapter the modeling of a VFM, specifically designed for two-phase flow investigation purpose, is described. The instrument has been analyzed in vertical upward annular two-phase flow. The dependency of the pressure drops, evaluated between the VFM inlet and throat and between the inlet and outlet sections (irreversible pressure loss), on the characteristic flow parameters (flow velocities, quality and void fraction) have been analyzed and discussed.
The analysis highlights that, from the measurement of the VFM irreversible pressure losses, important information can be derived concerning the effect of the liquid dispersed phase on the total pressure drops. A correlation for the VFM pressure drops and a correlation for the irreversible pressure losses have been developed. For both correlations, the prediction error is lower than 5%.

Two different approaches for the mass flow rate measurement of the phases have been analyzed.
In the first one, the model of the discharge coefficient of the VFM coupled with the void fraction measurement, performed by means of the Quick Closing Valves (QCVs) technique, permitted to estimated the mass flow rate of the phases with an accuracy of 2% for air and 30% for water.
The second approach has been developed in order to estimate the mass flow rate of the two phases, avoiding the direct measurement of the void fraction. This approach can be used, in very limited range of flow parameters and only if the flow pattern is not changing. In that conditions, the developed correlations describing the relation between velocities and VFM pressure drops and irreversible pressure losses have been used to estimate the mass flow rate of the phases.
The developed model allows the evaluation of the flow quality of the mixture with an error of 1% and the estimation of the mass flow rate of air and water with an error of 2% and 10% respectively, showing that in particular conditions a single instruments can be used to estimate the mass flow rate also in two-phase flow.

2. SPES-3 FACILITY AND FLOW PARAMETERS RANGE

A considerable amount of resources has been devoted at the international level during the past three decades for establishing and conducting experimental programs in scaled-down integral test facilities (ITFs). These were aimed at solving open issues for current nuclear power plant (NPP), demonstrating the technical feasibility of innovative designs, and generating reference databases to support codes development and assessment.

The experimental data from such facilities are applicable to full-scale nuclear plant conditions; if the test facilities and the initial and boundary conditions of experiments are properly scaled, for example, the scaling will not affect the evolution of physical processes important for the postulated accident scenario. This evaluation determines whether the data may be used in nuclear plant safety analyses of a postulated accident.

Tens of ITFs have been built and operated so far all over the world. Few of them, related to existing water reactor technology, are currently in operation or under refurbishment, while some others, constructed or under design, are focused on innovative water reactor concepts [2.1].

Despite the past trend to construct large size reactors, justified by the economy of scale, starting from the mid-1980 a new set of requirements has motivated the development of Small Modular Reactor (SMR) in some countries aimed for the markets that cannot accommodate NPP with high power reactors. At present, there are advanced SMRs already available for deployment and reactors under development.

With reference to the pressurized water reactors, the integral design PWR differ from conventional PWR, as they have no external pressurizers and steam generators. The steam space under the reactor vessel dome acts as a pressurizer, while the steam generators are located inside the reactor vessel. This in-vessel location configuration eliminates or minimizes by design the consequences of Loss of coolant accidents (LOCA).

The gross electric output varies between 15 and 350 MW. SMR can be divided in two design families:

- Integral design PWR;
- Compact modular PWR

The advanced SMR projects, belonging to the first group, are IRIS (USA), B&W mPower (USA), NuScale (USA), CAREM-25 (Argentina), SMART (Republic of Korea) and NHR-200 (China). The compact modular SMRs are: KLT-40S, ABV, and VBER-300.
An Integral Testing Facility (ITF) has been designed and erected or its construction is in progress for some of the SMR under development [2.1].
The SPES-3 facility is an integral simulator of the IRIS reactor [2.3], suitable to test the plant response to postulated design basis accidents and to provide experimental data for code validation and IRIS plant safety analyses [2.4]. The integrated IRIS reactor layout is shown in Fig.2.1, and the schematic of the safety systems is detailed in Fig.2.2.

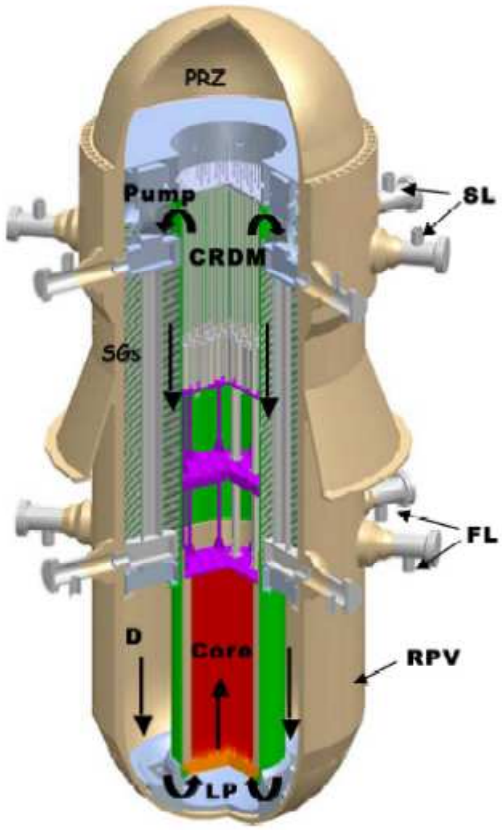

Fig.2.1: IRIS integral layout

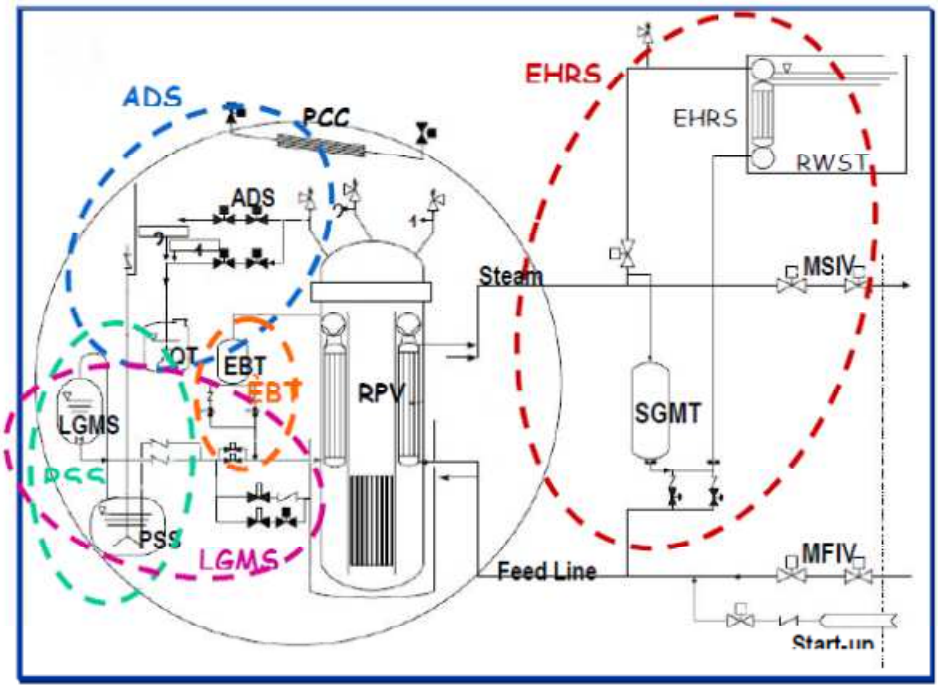

Fig.2.2: IRIS safety systems

The SPES-3 facility is shown in Fig.2.3. The comparison between the IRIS reactor characteristics and the scaled-down facility characteristics are described in Tab.2.1.

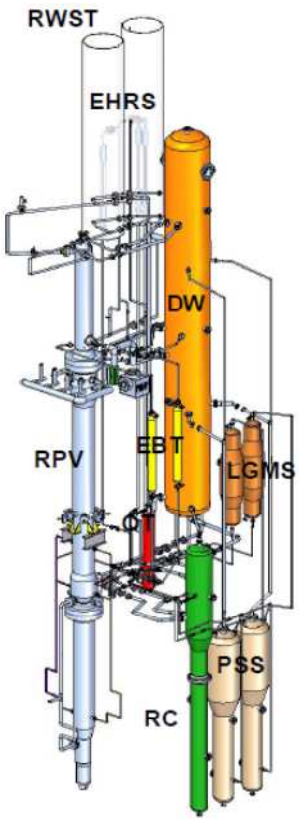

Fig.2.3: SPES-3 facility view

System/Component	IRIS	SPES-3
Primary side integral RPV	yes	Yes apart the pump
Pumps Number	8	1
Core power (MW)	1000	6.5
EBT Number	2	2
Steam generators	8	3
Secondary loops Number	4	3
SG tubes Number	700	14, 14, 18
SG height (m)	9.2	8.2
SG tube average lenght (m)	32	32
Containment system	Yes	Yes
EHRS Number	4	3
RWST Number	2	2
Dry Well Number	1	1
PSS Number	2	2
LGMS Number	2	2
Quench Tank Number	1	1
ADS trains Number	3	2

Tab.2.1: Comparison between IRIS and SPES-3 characteristics

In the SPES-3, the IRIS integral configuration is maintained for all components of the primary system, except for the pumps, which are placed outside of SPES-3 reactor pressure vessel. The IRIS containment compartments are simulated in SPES-3 by separate tanks, properly connected, representing the Dry- Well, two Pressure Suppression Systems (PSS), two Long Term Gravity Make-up System (LGMS), the Reactor Cavity (RC) and the Quench Tank (QT) for Automatic Depressurization System. Shape and dimensions are fixed in order to reproduce the trend of IRIS compartment volumes versus height. The Passive Containment Cooling (PCC) and a portion of the Direct Vessel Injection (DVI) lines are included in the containment as well. The safety systems include the Emergency Boration Tanks (EBTs), the Emergency Heat Removal System (EHRS) and the Automatic Depressurization System (ADS). Three EHRS loops represent the four IRIS systems. The design pressure of the primary and secondary systems, up to the main isolation valves is 172.5 bar, with its corresponding saturation temperature of 353.5 °C. The primary and secondary side operating pressure is 155 bar and 58 bar, respectively. The containment design pressure is 15 bar with its corresponding saturation temperature of 198.2 °C, while its operating pressure is 1.013 bar.
All primary, secondary and containment systems are simulated in SPES3 with 1:100 volume and power scaling, 1:1 elevation scaling, while the fluid is at IRIS pressure and temperature nominal conditions [2.3]. The pipe diameters range between 1/2” and 8”.

Even if the SPES-3 facility reproduces the IRIS thermal-hydraulics, the capability of the facility to simulate the transients behavior of a generic advanced SMR has been tested and verified in [2.2].

A reference test matrix, shown in Tab.2.2, establishes the simulation of a series of SBLOCAs and secondary breaks, whose data will be fundamental for the NRC certification process of the SMRs.
The data obtained for the SPES-3 facility simulation of Design Basis Accident transients [2.5], by means of the RELAP5 thermal-hydraulic code [2.6], have provided the reference

conditions to define the main thermal-hydraulic parameter ranges and the set of instruments suitable to measure them and to derive the required quantities. Document [2.7] describes the lines involved in the two-phase mass flow measurements and the range of the main thermal-hydraulic variables.
For each base case the most important locations for the measurement of the two-phase mass flow rate have been chosen. For each location a monitoring volume has been defined for the extraction of the variables necessary to the setting of the instrumental range.
The monitoring volumes in the break lines are located downstream of the orifice that simulates the break, while the monitoring volumes in the ordinary lines have been defined in order to minimize the possible pipe works influence on the flow profile itself. In RELAP code the mass flow rate value is coupled to a particular structure called junction. Each line has been associated to a junction number in order to get the value of the mass flow rate in the line itself.
The tests that will be performed are:

- Low elevation SBLOCA (small break LOCA): this accident is caused by the rupture of a DVI line. Both the double-ended guillotine and the split break tests will be simulated.
- High elevation SBLOCA (small break LOCA): the high elevation break is located in the EBT connection to the RV. One of the two EBT tanks in SPES3 is equipped with two break lines (double- ended guillotine break line and split break line).
- ADS break: the ADS break is located on one of the two ADS lines in SPES3. This line is equipped with two break lines that connect the ADS to the Drywell.
- Feed water line break: one of the three feed lines in SPES3 is equipped with two break lines (double-ended guillotine line and split break line) that are connected to the Cavity.
- Steam line break: one of the three feed line in SPES3 is equipped with two break lines (double-ended guillotine line and split break line) that are connected to the Drywell.

In all the cases the double ended guillotine break (DEG) has been simulated. The five base cases that will be analyzed are summarized in Tab.2.2.

RELAP base case Number	Case name	Description
SPES 89	DVI break	Double ended guillotine break of the Direct Vessel Injection Line B
SPES 90	EBT break	Double ended guillotine break of the top connection between the Emergency Boration Tank and the Reactor Vessel B
SPES 91	ADS break	Double ended guillotine break of the Automatic Depressurization System B, on the Single Train line
SPES 92	SL break	Double ended guillotine break of the Steam line B
SPES 93	FL break	Double ended guillotine break of the Feed line B

Tab.2.2: Base cases for the SPES3 break transients

In the SPES3 facility the break is reproduced involving two lines: the DEG break line and the SPLIT break line. In order to define the required instrumentation range, the main variables to be taken into consideration are:

- The void fraction and the flow quality
- The mass flow
- The gas and liquid velocity
- The pressure
- The gas and liquid temperature

3. TWO-PHASE FLOW DEFINITION AND MAIN IMPORTANT PARAMETERS

Multiphase flow is a complex phenomenon which is difficult to understand, predict and model. Common single-phase classifications according to the structure of flow (laminar, transitional and turbulent) or other characteristics such as velocity profile and boundary layer, are not sufficient to describe the nature of such flows.
In two-phase flows, due to the existence of multiple, deformable and moving interfaces, there are in principle an infinite number of ways in which the interfaces can be distributed within the flow. These distributions can be classified into a number of interfacial distributions and the types of interfacial distributions are the flow patterns (or flow regimes).
For most two-phase flow problems, the local instant formulation based on the single-phase flow formulation with explicit moving interfaces encounters mathematical and numerical difficulties, and therefore it is not a realistic or practical approach. This leads to the need of a macroscopic formulation based on proper averaging which gives a two-phase flow continuum formulation by effectively eliminating the interfacial discontinuities.

3.1 Two-phase flow models and classification

The methods used to analyze a two-phase flow are extensions of those already developed for single-phase flows: the basic equations governing the conservation of mass, momentum, and energy, coupled with various simplifying assumptions. Three main types of assumption are usually made [3.1]:

- *The homogeneous flow model*. It is, the simplest approach to the problem, the two-phase flow is assumed to be a single-phase flow having pseudo-properties obtained by suitably weighting the properties of the individual phases, and considering the phases flowing with the same velocity.

- *The separated flow model*. In this approach the two phases of the flow are considered to be segregated, or separated by the interfaces. Two sets of basic equations are written, one for each phase. Alternatively, the equations can be combined. In either case information must be given about the area of the channel occupied by each phase (or alternatively, about the velocities of each phase) and about the frictional interactions with the channel wall. In the former case additional information concerning the frictional interaction between the phases is also required. This information is inserted into the basic equations, either from separate empirical relationships in which the void fraction and the wall shear stress are related to the primary variables, or on the basis of simplified models of the flow.
- *The flow pattern models*. In this more sophisticated approach the two phases are considered to be arranged in one of three or four definite prescribed phases distribution geometries. These geometries are based on the various configurations or flow patterns found when a gas and a liquid flow together in a channel. The basic equations are solved within the framework of each of these idealized representations. In order to apply these models it is necessary to know when each should be used and to be able to predict the transition from one pattern to another.

The flow pattern has a great influence on the flow characteristics and the heat and mass transfer characteristics; moreover, it also affects the measurement about the flow parameters and the operating characteristics of two-phase flow system. As a result, the study of the flow pattern of the two-phase flow has an important practical value and academic significance; it has been therefore an important topic of this research field.
In general, the concept of two-phase flow pattern is defined based on a macroscopic volume or length scale which is often comparable to the system length scale [3.2].
This implies that the concept of two-phase flow regimes and regime dependent model requires an introduction of a large length scale and associated limitations. Therefore, regime-dependent models may lead to an analysis that cannot mechanistically address the physics and phenomena occurring below the reference length scale.
This highlight the difficulties encountered in developing generalized method for analyzing such flow. The two-phase flow physics are fundamentally multi-scale in nature. At least four different scales can be important in multiphase flow. These are: system scale, macroscopic scale required for continuum assumption, meso-scale related to local structures, and microscopic scale related to fine structures and molecular transport.
In the meso-scale we can define the phenomena related to the turbulence effects for momentum and energy as well as for interfacial exchanges for mass, momentum and energy transfer. Since the interfacial transfer rates can be considered as the product of the interfacial flux and the available interfacial area, the modeling of the interfacial area concentration is essential [3.3].
The parameters that govern the occurrence of a given flow pattern are numerous, the most important are flow rates and fluid properties of each phase, pipe geometry, pipe inclination, and flow direction (upward, downward, co-current, counter-current). The most common cases involve horizontal flow and vertical up-flow where both phases are flowing upwards [3.4].

The major flow regimes found in vertical gas-liquid up-flow in a pipe of circular cross-section are illustrated in Fig.3.1 displayed from left to right in order of increasing gas flow rate at a given constant liquid flow rate.

- *Bubbly flow*: at low gas flow rates this is the predominant flow regime, where the gas flows as a myriad of bubbles in a continuous liquid phase.
- Slug flow: as the gas flow rate increases, collisions between bubbles are more frequent and they coalesce, eventually forming large bullet shaped bubbles, often called Taylor bubbles. The liquid slugs between the Taylor bubbles often contain a dispersion of smaller bubbles.
- *Churn flow*: with further increase in gas flow rate, the Taylor bubbles in slug flow break down into an unstable pattern in which there is a churning or oscillatory motion of liquid in the tube. The gas now exists predominately as large irregularly shaped bubbles with smaller bubbles entrained in the liquid phase.
- *Annular flow*: when the gas flow rate is sufficiently large to support a liquid film at the surface of the pipe, the gas flows continuously through the center of the pipe. The liquid flows along the pipe wall as an annular film and can also be carried along the central gas core as small liquid droplets.
- *Wispy annular flow*: as the liquid flow rate is increased the droplet concentration in the gas core of annular flow increases and, ultimately, droplet coalescence occurs leading to large lumps or streaks as wispy liquid occurring in the gas core. This regime is characteristics of high mass velocity flows.

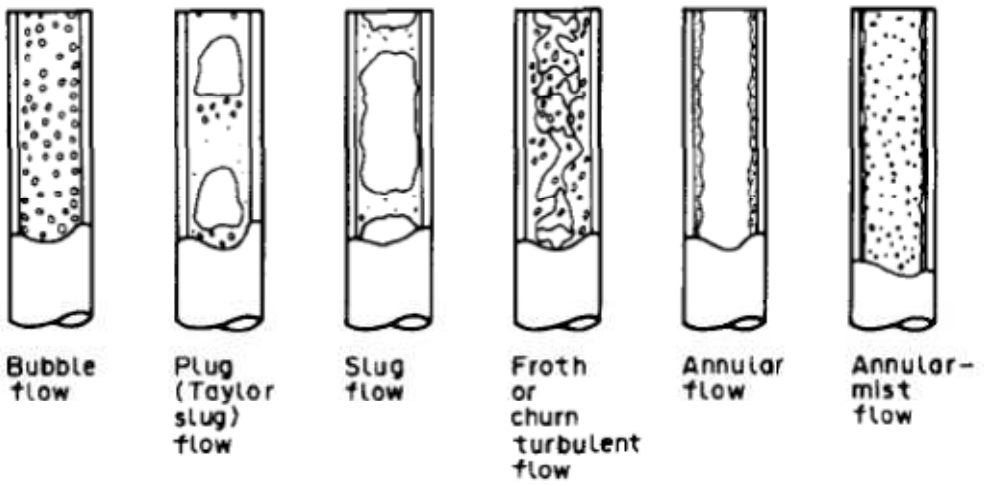

Fig.3.1: Schematics of vertical flow regimes

The flow regimes in horizontal pipes are similar to the vertical flow regimes above, except the effect of gravity now tends to cause the gas phase to flow predominantly along the top of the pipe. The flow regimes are summarized in Fig.3.2, from top to bottom in order of increasing gas flow rate.

- *Stratified flow*: In this flow pattern the liquid flows in the lower part of the pipe the gas above with smooth interface. In real situations, the gas-liquid interface is rarely smooth, and ripples appear on the liquid surface.
- *Wavy flow*: it occurs as the ripples increase in amplitude generating waves due to the increase in gas flow rate

- *Plug flow*: when the gas flow rate is increased, bubbles coalesce forming bullet shaped bubbles as also observed in vertical flow, but here they travel along the top of the pipe.
- *Slug flow*: when the amplitude of the waves travelling along the liquid surface become sufficiently large that they touch the top of the pipe. The gas flows as bigger bubbles and in the liquid slugs many smaller bubbles may be entrained.
- *Annular flow*: occurs when the gas flow rate is large enough to support a liquid film around the pipe walls. Liquid is also transported as droplets distributed throughout the continuous gas stream flowing along the center of the pipe. The liquid film is thicker along the bottom of the pipe because of the effect of gravity.

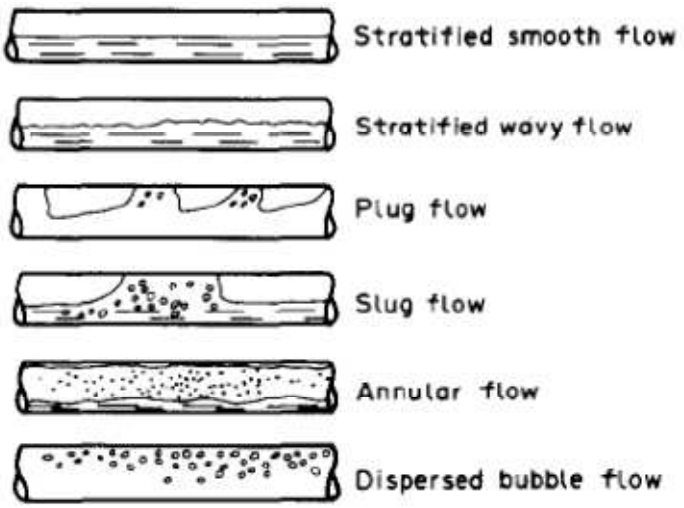

Fig.3.2: Schematics of horizontal flow regimes

The central task is to predict which flow pattern will exist under any set of operating conditions (like flow rates of each phase, their physical properties, orientation of the tube as well as the manner in which the phases are introduced in the system) as well as to predict the value of characteristic fluid and flow parameters (bubble or droplet size) at which the transition from one flow-pattern to another will take place.
The usual way of presenting results of observations of flow patterns is to plot them on a graph whose axes represent the flow rates of the two phases; an alternative is to plot total mass flux on one axis and the mass fraction of the flow which is vapor or gas on the other axis. When all the observations have been recorded, lines are drawn on the graph to represent the boundaries between the various regimes of flow. The resultant diagram is called a “flow regime map”.

3.2 Two-phase flow parameters

The modeling of a two-phase flow, and then the selection of the instruments for two-phase flow measurements requires the definition of the characteristic parameters of the flow.
Frequently used properties are defined in the following.
The total mass flow rate is defined as

$$\dot{W}_{tot} = W_l + W_g \tag{3.1}$$

and the volumetric flow rate is given by

$$Q_{tot} = Q_l + Q_g = \frac{W_l}{\rho_l} + \frac{W_g}{\rho_g} \tag{3.2}$$

The mass flux or mass velocity, G:

$$G_{tot} = G_l + G_g = \frac{W_l}{A} + \frac{W_g}{A} \tag{3.3}$$

and the volumetric flux, or superficial velocity:

$$J_{tot} = J_l + J_g = \frac{G_l}{\rho_l} + \frac{G_g}{\rho_g} \tag{3.4}$$

The mass fraction of the phase, usually referred to the gaseous phase, and called also flow quality, is defined as:

$$x = \frac{W_g}{W_l + W_g} \tag{3.5}$$

The volumetric quality, in a similar way is defined as:

$$\beta = \frac{Q_g}{Q_l + Q_g} \tag{3.6}$$

The phase fraction for gas-liquid flows is commonly known as the void fraction α for the gas phase and the liquid hold-up for the liquid phase. Both quantities are interchangeable with help of the continuity equation which requires the sum of gaseous and liquid phase fraction to equal unity. Void fraction is a dimensionless quantity indicating the fraction of a geometric or temporal domain occupied by the gaseous phase. It is one of the most import parameters used to characterize multiphase flows. In two-phase flow analysis, the void fraction and the relate interfacial area concentration represent the two fundamental geometrical parameters and, therefore, they are closely related to two-phase flow regimes.
It is the key physical value for determining numerous other important parameters, such as mixture density and viscosity, for obtaining the relative averaged velocity of the phases, and is of fundamental importance in models for predicting flow pattern transitions, heat transfer and pressure drop.
The void fraction is needed in order to calculate the hydrostatic and accelerational pressure drop of the flow, because it determines important flow parameters such as average fluid

density and average flow velocity at a particular location in the pipe. Accurately determining the average density and effective flow velocity of two-phase flows is difficult because it depends upon the slip ratio, S. These parameters are also needed for flow-induced vibration analyses for predicting fluid forces and the fluid elastic instability threshold of a tube array subjected to two-phase flows.
Various geometric definition are used for specifying the void fraction: local, chordal, cross-sectional and volumetric. Moreover instantaneous or time averaged values of those quantities can be defined.
The local void fraction refers to that at a point (or very small volume): if *P(r,t)* represent the local instantaneous presence/absence of vapor (or gas) at some point *r* at the time *t*, the local time-averaged void fraction is defined as:

$$\alpha_{local}(r) = \frac{1}{t}\int_t P(r,t)dt \tag{3.7}$$

where
P(r,t) = 1 for gas phase
P(r,t) = 0 for liquid phase
The local void fraction defined in this way, represents the residence time of the phase in a specific location of the control volume.
For a sufficiently long measurement time t_{tot}, eq. 3.7 can be approximated by

$$\alpha_{local}(r) = \frac{\sum t_g}{t_{tot}} \tag{3.8}$$

Where t_g is the total time the dispersed phase was present at measurement point *r*.
The chordal void fraction is defined as:

$$\alpha_{chordal}(t) = \frac{L_g}{L_g + L_l} = \frac{L_g}{L_{tot}} \tag{3.9}$$

Where L_g is the length of the line through the vapour/gas phase and L_l is the length of the line through the liquid phase.
The cross-sectional void fraction is defined as:

$$\alpha_{cross-sectional}(t) = \frac{A_g}{A_g + A_l} = \frac{A_g}{A_{tot}} \tag{3.10}$$

where A_g is the area occupied by the vapour/gas phase and A_l is the area occupied by the liquid phase.
The volumetric void fraction is:

$$\alpha_{volume}(t) = \frac{V_g}{V_g + V_l} = \frac{V_g}{V_{tot}} \tag{3.11}$$

where A_g is the volume occupied by the vapour/gas phase and V_g is the volume occupied by the liquid phase.
The relation between flow quality and void fraction can be written as:

$$x = \frac{W_g}{W_l + W_g} = \frac{U_g A_g \rho_g}{U_l A_l \rho_l + U_g A_g \rho_g} = \frac{\alpha \cdot U_g \rho_g}{(1-\alpha) \cdot U_l \rho_l + \alpha \cdot U_g \rho_g} = \frac{\alpha}{\frac{(1-\alpha)}{\alpha} \cdot \frac{\rho_l}{\rho_g} \cdot \frac{1}{S} + 1} \quad (3.12)$$

where U_l and U_g are the real velocities of the two phases.
The parameter *S*, called slip ratio, represents the ratio between the actual velocity of the gaseous phase and the actual velocity of the liquid phase and, as the other parameters, can be local and instantaneous or averaged in space and/or time. The Slip Ratio is higher than 1 for most flows. When S > 1, the void fraction is lower than the homogeneous void fraction (which is the maximum value).
A large number of correlations (Tab.3.1), empirical or semi/empirical [3.5] have been proposed for evaluation of the void fraction. Many of them are expressed in terms of the slip ratio, S.
The problem is related to the identification of the important variables that affects the velocity ratio and to form dimensionless groups that are appropriate to the development of the model. It is clear that the buoyancy of the gas phase was the driving force behind the velocity ratio, without which it would be close to unity. The density difference, $\Delta\rho$, and the average two-phase density, ρ, are considered to be key parameters. The viscosity of the liquid phase, μ_l, is selected since it affects the ability of the gas bubbles to rise through the liquid. Surface tension, σ, iss selected since it affects bubble size and shape. Experiences showed that the gas phase velocity increased as the bubble size increased, owing to the increased buoyancy of a larger gas bubble. The tube diameter, *D*, and the length *L*, are thought to play a role in velocity ratio, since they influence the frictional pressure drop through the pipe.

The fundamental parameters influencing the slip ratio are reported in the following equations

$$S = \frac{U_g}{U_l} = f\left(\Delta\rho, \rho, \mu, U, \sigma, g, D, L, \vartheta, p, \Delta p, etc..\right) \quad (3.13)$$

$$S = f\left[\left(\frac{gL}{U^2}\right)^a, \left(\frac{\rho U^2 L}{\sigma}\right)^b, \left(\frac{U \cdot L}{\rho\mu}\right)^c, \left(\frac{\Delta p}{\rho U^2}\right)^a, \left(\frac{\Delta\rho}{\rho}\right)^e, \left(\frac{p}{L}\right)^f, \left(\frac{D}{L}\right)^g\right] \quad (3.14)$$

The first four dimensionless groups are the Froude *Fr*, Weber *We*, Reynolds *Re*, and Euler *Eu*, numbers.

Author	Correlation
Homogeneus:	$\alpha = \left[1+\left(\frac{1-x}{x}\right)\cdot\left(\frac{\rho_g}{\rho_l}\right)\right]^{-1}$
Thom (1964):	$\alpha = \left[1+\left(\frac{1-x}{x}\right)^{0.89}\cdot\left(\frac{\rho_g}{\rho_l}\right)^{0.18}\right]^{-1}$
Zivi (1964):	$\alpha = \left[1+\left(\frac{1-x}{x}\right)\cdot\left(\frac{\rho_g}{\rho_l}\right)^{0.67}\right]^{-1}$
Lockhart-Martinelli (1949):	$\alpha = \left[1+0.28\cdot\left(\frac{1-x}{x}\right)^{0.64}\cdot\left(\frac{\rho_g}{\rho_l}\right)^{0.36}\cdot\left(\frac{\mu_l}{\mu_g}\right)^{0.07}\right]^{-1}$
Baroczy (1966):	$\alpha = \left[1+\left(\frac{1-x}{x}\right)^{0.74}\cdot\left(\frac{\rho_g}{\rho_l}\right)^{0.65}\cdot\left(\frac{\mu_l}{\mu_g}\right)^{0.13}\right]^{-1}$
Armand (1966):	$\alpha = 0.833\alpha_h$ α_h is the homogeneous void fraction
Chisholm (1983):	$\alpha = \frac{1}{\alpha_h + (1-\alpha_h)^{0.5}}\alpha_h$
Wallis (1969):	$\alpha = \left[1+X_{tt}^{0.8}\right]^{-0.38}$ with $X_{tt} = \left[\left(\frac{1-x}{x}\right)^{0.9}\cdot\left(\frac{\rho_g}{\rho_l}\right)^{0.5}\cdot\left(\frac{\mu_l}{\mu_g}\right)^{0.1}\right]$

Tab.3.1: Literature void fraction correlations

The other parameter used the define the relative motion between the phases is the *drift velocity* [3.2], [3.6] and [3.7], defined as the velocity of one of the two components in a frame of reference moving at a velocity equal to the total superficial velocity J_{tot}, and is therefore given by:

$$U_{gj} = U_g - J_{tot} \tag{3.15}$$

$$U_{lj} = U_l - J_{tot} \tag{3.16}$$

The drift fluxes of the phases J_{gj} and J_{lj} are defined as follows:

$$J_{gj} = \alpha \cdot U_{gj} = \alpha \cdot (U_g - J_{tot}) \tag{3.17}$$

$$J_{lj} = (1-\alpha) \cdot U_{lj} = (1-\alpha) \cdot (U_l - J_{tot}) \tag{3.18}$$

It follows that:

$$J_{lj} + J_{gj} = 0 \tag{3.19}$$

Other properties such as the mixture density, the mixture viscosity or thermal conductivity cannot be reliably obtained from such simple weighted means.
As reported by Friedel [3.8], the definition of mass density

$$\rho = \frac{MASS}{VOLUME} \tag{3.20}$$

at a given pressure and temperature is an invariable property for a single-phase fluid; in two-phase pipe flow, the volume and the transport concentrations can change, also in steady state flow, due to the slip between the phases. A two-phase density can be derived by using the volume concentration or the mean void fraction; this density is known as gravitational density and represents the density of the mixture in a control volume at a given time:

$$\rho = \frac{M_{tot}}{V_{tot}} = \frac{M_g + M_l}{V_{tot}} = \frac{\rho_g V_g + \rho_l V_l}{V_{tot}} = \frac{\alpha \cdot \rho_g V_{tot} + (1-\alpha) \cdot \rho_l V_{tot}}{V_{tot}} = \alpha \cdot \rho_g + (1-\alpha) \cdot \rho_l \tag{3.21}$$

and can be experimentally obtained by the measurement of the liquid mass detected between two quick-closing valves in a defined control volume. According to the definition, the gravitational density is representative only of a static material balance in a pipe flow with a constant flow cross-section.
A second definition can be derived considering the mass flow quality, *x*:

$$\rho = \frac{M_{tot}}{V_{tot}} = \frac{M_{tot}}{V_g + V_l} = \frac{M_{tot}}{\frac{x \cdot M_{tot}}{\rho_g} + \frac{(1-x) \cdot M_{tot}}{\rho_l}} = \left[x / \rho_g + (1-x) \cdot \rho_l \right]^{-1} \tag{3.22}$$

usually called *homogeneous density*, even if based on the hypothesis of the conservation of the volume, and not under the assumption that S=1.
If an heterogeneous flow is assumed, and a relation for the slip is introduced, different definition of the density can be derived depending on the different model used.
Friedel [3.8] summarized the most important two-phase densities as reported in the following table, where the basis model used for each density definition are highlighted.

Basics	**Mixture density**
Gravity	$\alpha \cdot \rho_g + (1-\alpha) \cdot \rho_l$
Momentum balance	$\left[x^2 / (\alpha \cdot \rho_g) + (1-x)^2 / ((1-\alpha) \cdot \rho_l) \right]^{-1}$
Kinetic energy balance	$\left[x^3 / (\alpha \cdot \rho_g)^2 + (1-x)^3 / ((1-\alpha) \cdot \rho_l)^2 \right]^{-1}$
Homogeneous mixture	$\alpha \cdot \rho_g + (1-\alpha) \cdot \rho_l = \left[x / \rho_g + (1-x) / \rho_l \right]^{-1}$
Superficial velocity	$\left[x^2 / \rho_g + (1-x)^2 / \rho_l \right]^{-1}$
Linear weighing	$\left[x \cdot \rho_g + (1-x) \cdot \rho_l \right]$
Density addition	$\left[x / \sqrt{\rho_g} + (1-x) / \sqrt{\rho_l} \right]^{-2}$
Volume flux weighing	$\left[x / \rho_g + (1-x) / \rho_l \right]^{-1} \approx \rho_g$

Tab.3.2: Mixture density definitions

4. TWO-PHASE FLOW MEASUREMENT

The objective of the two-phase flow measurement is the determination of the flow rates of the phases flowing in a pipe, for example water and gas or water and steam; but also the characterization of the fundamental parameters of the flow, such as the phases distribution, the interfacial area, etc...
For the purpose of the mass flow rate measurement, there is no a single instrument, which will measure these parameter directly and it is necessary to couple several devices, each one sensitive at the different properties of the flow (momentum, velocity, density, void fraction, etc..), in a Spool Piece (SP). The analysis of the combined readings can then be used as input for the SP model that is used to evaluate the mass flow rate of the phases.

4.1 Instrument classification

In the previously paragraph the parameters that characterized the two-phase flow has been defined.
For measurement purpose an instrument classification can be made considering which parameter can be measured and through which physical principle the instrument operates.
The following main categories can be applied:

- In-line measurement
- Separation phases measurement
  - Full two-phase gas/liquid separation
  - Partial separation
  - Separation in sample line

In-line meters performe directly in the multiphase flow line, hence, no separation and/or sampling of the fluids are required.
The volume flow rate of each phase is represented by the area fraction multiplied by the velocity of each phase. This means that a minimum of six parameters has to be measured or estimated (T, p, v, W, x, α or ρ) with suitable models. The flow meters can be classified based on the parameter measured or based on the measurement physical principles, as reported in Tab.4.1.

Measurement physical principle
Mechanical
Hydraulic
Acoustic
Electrical
Gamma and X-ray
Neutrons
Microwave attenuation
Infrared spectroscopy

Tab.4.1: Instrument classification based on physical principle

The different physical working principle are used to measure different parameters [4.1], as reported schematically in Tab.4.2.

Excellent reviews have been written on the state of the art of two-phase flow instrumentation. See, for example, Baker [4.1], Miller [4.2], Bertani et al. [4.3] and Hewitt [4.4].

Measurement of void fraction (α):	**Measurement of density (ρ)**
Gamma-ray (γ) absorption	Gamma-ray (γ) absorption
Neutron (n) interrogation	Neutron (n) interrogation
Optical sensors	Weighing of tube
Quick-closing valves	Hot film anemometer
Capacitance / Conductance probes	Capacitance / Conductance probes
	Ultrasonic flow meter
Measurement of velocity (U)	**Measurements of mass flow (ρU)**
Pulsed-neutron activation	True mass flow meter
Electromagnetic flow meter	Vibrating tube
Turbine flow meter	Differential pressure flow meters
Gamma-ray cross correlation	Measurements of momentum flux (ρv^2)
Neutron cross correlation	Venturi meter
Acoustic cross correlation	Drag Disk
Capacitance/conductivity sensors cross correlation	
Laser Doppler velocimeter	

Tab.4.2: Instrument classification based on the measured flow parameters

4.2 General meter selection factors for two-phase flow measurements

There are a number of specific issues to keep in mind when choosing a flow-metering instrument. Different flow meters are designed for optimum performance in different fluids and under different operating conditions. That is why it is important to understand the limitations of each measurement device. Measuring the flow of liquid and gases (two-phase flow) demands superior instrument performance. Performance parameters include accuracy (uncertainty or flow meter's ability to measure the *correct* or *true* flow), repeatability, resolution, rangeability, and dynamic response.

Economic considerations include flow meter hardware cost (sensor, transmitter or conditioner, tubing, wiring), installation requirements (flanges, straight pipe lengths, taps), pressure drop, reliability, maintainability, and frequency of calibration.

The choice of a meter to measure flow quantities in two-phase flow [4.4] depends on the purpose for which the measurement is made, whether an average or a local quantity is needed and on the accuracy required. In order to evaluate the accuracy of the measure, the entire acquisition system must be considered: the information coming from the fluid, is transferred through the sensor, is converted form analogical to digital electric signal and it sent to the pc through the DAQ. At each step some distortion and noise are introduced, and the amplitude of that distortion must be minimized. The selection of the flow meter, and the related accuracy also depends on the nature of the flow field and the two phases involved.

The relative magnitudes of the instrumental length scales (pipe diameter for Venturi flow meters, drag plates area for drag disk, probe tip radius or probe plate area for impedance sensors, piezoelectric crystal diameter, wave length of the sensing radiation (whether electromagnetic or acoustic), etc.., compared with the length scale of the flow objects (drop or bubble diameters, film thickness, interface area, etc...), restrict the nature of the information provided by any device and hence affect how information are deduced and analyzed.

The devices employed can be either nonintrusive (external to the flow field or, at most, part of the pipe/fluid interface) or intrusive (thus distorting the flow geometry at the place of measurement).

Nonintrusive devices can use tomographic techniques to sense local characteristics of the motion. Some intrusive devices provide global measurements, and some (local optical, electrical, or pressure probes) provide local information.

In the last few years many efforts were made by scientists all over the world to understand the physics of the chain ‘pipe configuration-disturbed flow profile-change in flow meter behaviour and to find out effective methods and techniques to minimize these installation effects.

The relation between disturbed flow profile and change of flow meter behavior alone already presents a huge field of problems. Installation effects basically depend on the technical principle and construction of the flow meter itself. The resulting problems are therefore unique for every type of flow meter.

The response of a meter in two-phase flow tends to be high sensitive to the flow pattern and to the upstream configuration and flow history. The best practice is to calibrate the instruments with known phase flow rates and with an exact simulation of the upstream pipe flow. The flow pattern is likely to be also time dependent in transient tests. The response of a flow meter may be different in transient situation and it’s better to find a way to correct for

this. Though the ideal is to use in situ calibration, the more usual method is to interpret the measurement from an instrument in terms of a theory whose validity is tested by conducting separate experiments. Very often these experiments are conducted for very different flow conditions and fluids: instruments used for steam/water flows are frequently calibrated using air/water flows.

The basis of a proper meter selection is then a clear understanding of the specific application requirements.

Flow meters with few or no moving parts require less attention than more complex instruments. Meters incorporating multiple moving parts can malfunction due to dirt, grit and grime present in the process fluid. Meters with impulse lines can also plug or corrode, and units with flow dividers and pipe bends can suffer from abrasive media wear and blockages. Moving parts are a potential source of problems, not only for the obvious reasons of wear, lubrication and sensitivity to coating, but also because they require clearance spaces which sometimes introduce “slippage” into the flow being measured.

In the reactor studies context this measurement is complicated by the fact that during the transient, the fluid becomes a non homogeneous mixture of liquid water and steam at, or very near, saturation.

In addition, materials from which the transducer is made must be carefully chosen for their ability to survive the destructive effects of the water conditions (temperature, pressure, viscosity and chemistry) and plant conditions (ambient temperature and humidity).

A final point to consider is that large parameters excursions should be monitored and their possible effects on the flow meter system must be evaluated. Items such as voltage spikes, spurious noise, pressure spikes (water hammer), and temperature spikes should be addressed as to their possible negative effects and as to the need to design methods to mitigate such effects.

In experimental programs involving loss-of-coolant studies, [4.6]-[4.20] and [4.44]-[4.45], because of the severe environments present during the blow-down, relatively few instrument can be used; these include turbine meters, drag flow meters, gamma densitometers, Venturi flow meters/pitot tubes and impedance sensors (pressure and temperature measurements are also required for reduction of data from the other instruments) located in a relatively short piping segment called Spool Piece (SP).

The design of the SP is important because intrusive meters may seriously alter the flow regime. On the other hand, location of all the instruments in close proximity is desirable because of the often unsteady and inhomogeneous nature of two-phase flow.

The fundamental criteria defined for the first selection were: range of measurement, dynamic response, installation requirements, materials/electrical compatibility with pressure and temperature conditions, flow velocity compatibility.

Also considering limits and drawbacks, the only analyzed devices that could operate in the whole range of conditions expected in the break lines (high pressure and temperature, high and fast variation of the flow parameters and very high steam velocity) are:

- Drag Disk,
- Turbine Flow Meter,
- Venturi Flow Meter,
- Impedance Probes.

The selected instruments have been experimentally/theoretically analyzed and different possible SP combinations have been evaluated.

4.3 Turbine Flow Meter

The turbine-meter is essentially a turbine rotor which rotates as the fluid passes through its blades. The turbine output, registering a pulse for each passing blade, can be used to calculate the fluid velocity and the volumetric flux; is actually the most important volumetric meter.
According to the installed direction of a rotor shaft, two types of turbine flow meter are available: axial type turbine flow meter and tangential type turbine flow meter. The axial type turbine is the reference turbine flow meter.
As it can be noticed in Fig.4.1, the rotor spins as the liquid passes through the blades and the rotational speed is a direct function of the volumetric flow rate:

$$S_T = K_T \cdot Q \tag{4.1}$$

$$U = Q_{tot} \cdot A_p \tag{4.2}$$

where U is the mean flow velocity [m/s] sensed by the instrument and K_T is the calibration coefficient that takes into account all the uncertainties.

The axial turbine flow meter, when properly installed and calibrated, is a reliable device capable of providing high accuracies (of about 0.2%) for both liquid and gas volumetric flow measurement, in single-phase flow conditions.

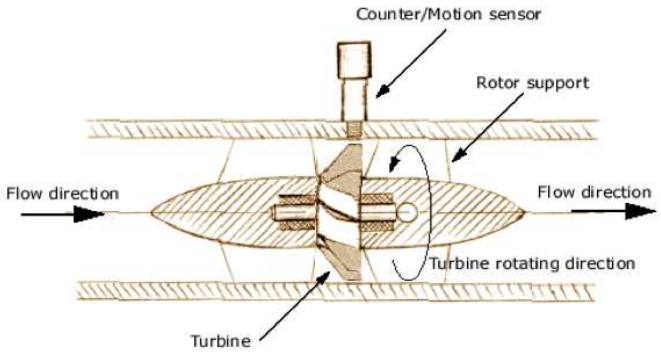

Fig.4.1: Axial turbine flow meter

Typical measurement repeatability is ±0.1% of reading for liquids and ±0.25% for gases with up to ±0.02% for high accuracy meters.
Turbine flow meters have a working dynamic range of at least 10:1 over which the linearity is specified. The maximum flow rate is determined by design factors related to size versus maximum pressure drop and maximum rotor speed. The minimum of the range is determined by the linearity specification itself. Due to small, unavoidable, manufacturing variances, linearity error curves are unique to individual meters and are normally provided by the manufacturer. Higher accuracy specifications usually correspond to a 10:1 flow range down from Q_{max}, while extended operating ranges usually correspond to reduced accuracies. The hump in the depicted curve is a characteristic feature caused by flow velocity profile changes

as Re approaches the laminar region. Sensitivity and repeatability performance degrades at low Re.
Both one-directional and bidirectional designs are currently available, and a calibration for each flow direction is necessary.
Calibration of the flow-meter together with straighteners is recommended to eliminate the effect of upstream flow effect. ANSI/API suggested an upstream length of 20D and a downstream length of 5D. Baker [4.1] shows an example of suggested upstream spacing from manufacturer, for elbow and bends effects on installation.
Temperature differences between calibration and operation cause dimensional changes, viscosity changes, density changes and velocity pattern shift and then affect the turbine meter signal.
There are numerous, often proprietary, designs incorporating variations in rotors, bearings, pickups and other components in format and materials which are tailored to different applications.
The most common types of rotation sensor are magnetic, modulated carrier and mechanical, while optical, capacitive and electrical resistance are also used.
Mechanical pickups, which sometimes incorporate a magnetic coupling, are traditional in some applications, can have high resolution and one advantage that they require no electrical power. However the pickup drag tends to be high. The magnetic and modulated carrier types utilize at least a coil in a pickup assembly which screws into the meter housing near the rotor.
Multiple magnetic pickups are also used in some designs to provide increased measurement resolution.
Usually the momentum exchange approach is used to describe the fluid driving torque in terms of momentum exchange in the axial turbine flow meter.
In a hypothetical situation, where there are no forces acting to slow down the rotor, it will rotate at a speed which exactly maintains the fluid flow velocity vector at the blade surfaces.
In Fig.4.2, the difference between the ideal (subscript *i*) and actual tangential velocity vectors is the rotor slip velocity and is caused by the net effect of the rotor retarding torques.

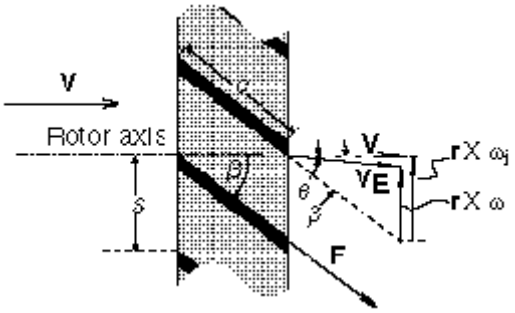

Fig.4.2: Vector diagram for a flat-bladed axial turbine rotor

In the picture: V incident fluid velocity vector; V_E exit fluid velocity vector; θ exit flow swirl angle due to rotor retarding torques; β blade pitch angle, same as angle of attack for parallel flow; ω rotor angular velocity vector; r rotor radius vector; F flow induced drag force acting on each blade surface; c blade chord; s blade spacing along the hub; c/s rotor solidity factor.
Assuming that the rotor blades are flat and that the velocity is everywhere uniform and parallel to the rotor axis, then referring to Fig.4.2:

$$\omega_i = U \cdot \tan\beta \tag{4.3}$$

When one introduces the total volumetric flow rate this becomes:

$$\frac{\omega_i}{Q_{tot}} = \frac{\tan\beta}{r_{RMS} A} \tag{4.4}$$

Where ω_i is the *ideal* rotational speed, A is the area of the annular flow cross section and r_{RMS} is the root-mean-square of the inner and outer blade radii.
Hence, according to the second equation, in the ideal situation the meter response is perfectly linear and determined only by geometry.
In practice, there are instead a number of rotor retarding torques of varying relative magnitudes. Under steady flow the rotor assumes a speed which satisfies the following equilibrium:

Fluid driving torque = rotor blade surfaces fluid drag torque + rotor hub and tip clearance fluid drag torque + rotation sensor drag torque + bearing friction retarding torque

Referring again to Fig.4.2, the difference between the actual rotor speed, $r \cdot \omega$, and the ideal rotor speed, $r \cdot \omega_i$, is the rotor slip velocity due to the combined effect of all rotor retarding torques as described in the equilibrium equation above, and as a result of which the fluid velocity vector is deflected through an exit or swirl angle, θ.

In most flow meter designs, especially for liquids, the latter three of the four retarding torques described in the equilibrium equation are small under normal operating conditions compared with the torque due to induced drag across the blade surfaces.
The effects of the rotor retarding torques, and a number of important meter design and aerodynamic factors, such as rotor solidity and flow velocity profile, are considered in the value of the K_T factor.

For steady flows the meter factor K_T of a specific meter depends on dimensionless parameters such as:
• the Reynolds number Re
• the Mach number M
• the ratio of mechanical friction torque, to the driving fluid torque

The manufacturer uses steady flow calibrations at different pressures to distinguish between Reynolds number effects and the influence of mechanical friction. In general the Mach number dependency is a small correction due to a Mach number effect in the temperature measurements at high flow rates.

In unsteady condition the response of the meter will also depend on:
• the Strouhal number St
• the amplitude of the perturbations
• the ratio of fluid density, ρ, and rotor material density, ρ_m

Ideally, the volume flow is proportional to the rotation speed. However, slight deviations are observed as a function of the Reynolds number. Inlet velocity profile, the pressure drag of the wake and other friction forces, if not considered in the analysis, can introduce systematic errors on the measurements, and for a more accurate model it is necessary to include realistic tip clearance effects.
Another important source of systematic errors are time dependent perturbations in the flow. Above a critical frequency, determined by the inertia of the rotor, the turbine meter will not be able to follow the variations in volume flow in time. The structural damage due to two-phase flow is another important parameter to take in account; cavitation is recognized as a destructive phenomenon in turbine flow meters. The intermittent impact of liquid in a liquid/gas flow may damage the internals of the meter and it is possible that erosion and abrasion may occur [4.1].

4.3.1 Two-phase flow measurement capability and modeling

In two-phase flow applications, the evaluation of the force components acting on the blades is clearly even more complicated that in single-phase flow. The basic model used in analyze the flow meter response assumes a homogenous flow that can be analyzed using the same approach of the single-phase flow.
The total two-phase flow mass flow rate can be evaluated as:

$$W_{tot} = K_T \rho_{TP} \omega \tag{4.5}$$

where the two-phase mixture density ρ_{TP} can be expressed in different ways as reported in the paragraph 3.2.
Rouhani [4.10] has shown that the appropriate density for the turbine meter is the momentum density; so that the calculation of the two-phase mixture density ρ_{TP} requires, the side measurement of the void fraction α. Acceptable results can be obtained with existing empirical correlations for the void fraction α deduced for channel flow (which normally requires the knowledge of the local pressure and the local mixture quality, whose accessibility is to be evaluated).
The proportionality constant K_T can be extrapolated from single-phase flow literature (provided the meter is single-phase standard design) and tailored on the basis of preliminary in-situ testing.

The measurement of two-phase flow by a turbine meter usually incorporates an evaluation model which relates the metered velocity to the actual velocities of the gas and liquid phases. The turbines are more sensitive to the gas phase velocity at high void fractions and to the liquid velocity at low void fractions; at intermediate void fractions some theories have been studied, but none of them is widely accepted.

Some models, developed to interpret the response of a turbine flow meter and related to the true mass flow rate, are lists below:

Volumetric model [4.12]:
This model is based on the assumption that the measured velocity is equal to the volumetric flow rate divided the cross sectional area, and gives:

$$\overline{U} = \alpha U_g + (1-\alpha) U_l \tag{4.6}$$

Aya's model [4.6]:
The model has been derived for a SP made up of a densitometer, a drag disk and a turbine, under the assumption that the force that the gas flow exerts upon the turbine blades is equal to the force that the blades are exerting on the liquid flow.
A momentum balance on the turbine blade segment gives:

$$\alpha\rho_g \cdot \left(U_g - \overline{U}\right)^2 \cdot \sin^2(\beta) = \frac{K_{Tl}}{K_{Tg}} (1-\alpha)\rho_l \cdot \left(\overline{U} - U_l\right)^2 \cdot \sin^2(\beta) \tag{4.7}$$

where K_{Tg} and K_{Tl} are the single-phase calibration coefficients.

Rouhani's model [4.10]:
Also this model is based on a momentum balance calculation, as the previous one, but the authors used different ways of expressing the momentum terms. The average flow velocity is then expressed as:

$$\overline{U} = xU_g + (1-x)U_l \tag{4.8}$$

According to [4.24], some experiments at the Oak Ridge National Laboratory (ORNL) showed that the first model is working better for down flow with slip ratio<1, while Aya and Rouhani model predict the turbine velocity more accurately for horizontal flow or for down flow with slip ratio>1.

The turbine meter has been largely used in experiments to model nuclear plants operating in accidents conditions; in unsteady flow a valid model to analyze the output turbine signal is the Kamath and Lahey model [4.16].
Kamath and Lahey [4.16]-[4.17] have developed analytical models for the dynamic response of free-field turbine-meters and drag-disks. These models have been combined with various density and velocity profile models to synthesize a predictive technique for global mass flux and void fraction.
Comparison of this model with the data taken at Wyle Labs has indicated that a DTT rake is capable of predicting global mass flux trends.
Parametric studies indicate that for a typical blow-down transient, dynamic effects such as rotor inertia can be important for the turbine-meter. In contrast, for the drag-disk, a frequency response analysis showed that the quasi-steady solution is valid below a forcing frequency of about 10 Hz, which is faster than the time scale normally encountered during blow-downs.

4.3.2 Two-phase flow applications

Starting from the fifties of the last centuries, several authors analyzed and developed models for turbine two-phase flow measurement, especially in nuclear safety studies [4.6]-[4.20]. The maximum applied pressure used in two-phase experiments with turbine meter is 240-400 bar for threaded design, the maximum temperature is 310ºC [4.1].

Hewitt [4.4] stated that the interpretation of the performance of a turbine flow meter in two-phase flow is difficult for flow regimes other than those close to homogeneous. For example, the response in annular flow, for a certain mass flux and void fraction, is likely to be different from that for homogenized flow with the same characteristics (mass flow rate and void fraction). A good knowledge of the expected flow regimes is therefore necessary to calculate the mass flux with the lower uncertainty.

Hardy [4.8] demonstrated that the turbine flow-meter response is sensitive to the variation in the flow pattern (see Fig.4.3). The dotted lines in the figure delimit the regions of the graph characterized by different flow patterns.

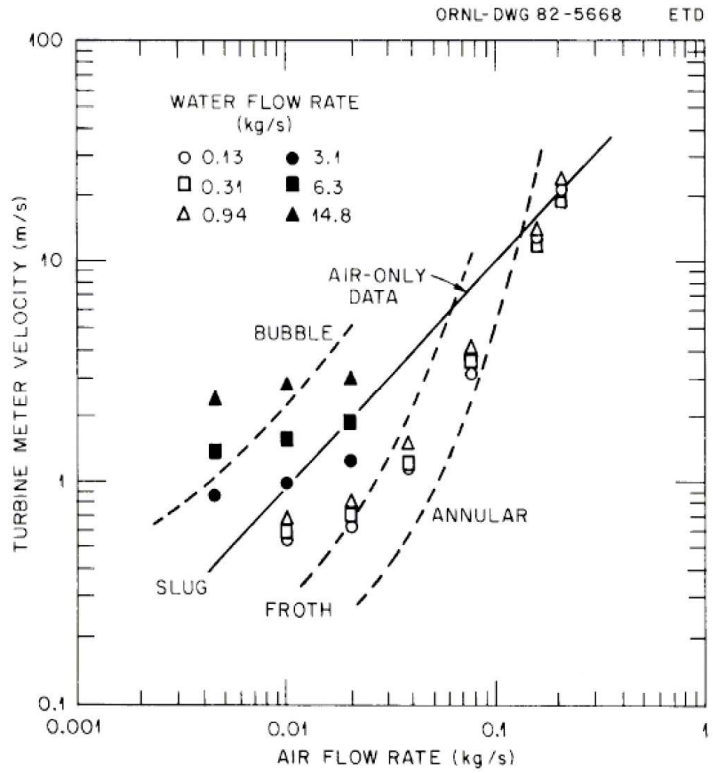

Fig.4.3: Turbine meter velocities as a function of the air flow rate in two-phase vertical up-flow [4.8]

The turbine response is dominated by the water velocity: the introduction of the gas phase tends to slow down the flow-meter. For increasing values of the air flow rate, the turbine velocity approaches the air only line (empty symbols) and finally, in the case of annular-mist flow regime, the turbine response is dominated by the air flow. At low air flows and high

water rates the liquid phase is continuous and the turbine response is dictated by the water flow (black symbols).
Later on Hardy and Hylton [4.45] confirmed that the response of a turbine flow-meter is likely to be more sensitive to the gas phase at high-void condition, while at low-void flows they tend to react more to the liquid phase. In intermediate void fraction condition, like. slug flow regime, their behavior is not well understood.

To attend sufficient accuracy in two-phase flow, it is clear that the turbine flow meter must be used with an auxiliary sensor. This may either be a void fraction sensor or a pressure drop device such as a Venturi Flow Meter (VFM) or Drag Disk (DD), of which the pressure drop approach appears to be technically more promising. A differential pressure producing flow meter such as a VFM in series with a turbine is known to be a technically appropriate and straightforward method for measuring the volumetric and mass flow rates.

Two techniques currently studied do not require an auxiliary in-line sensor. The first uses the turbine meter itself as the drag body and combines the output of the turbine with that of a small differential pressure sensor connected across the inlet and outlet regions. This technique requires a homogenizer ahead of the turbine and measurement accuracies of ±3% for the volumetric flow rates of both phases have recently been reported for air/water mixtures up to a void fraction of 80% [4.21]. The second technique is based entirely on analysis of the turbine output signal and has provided significant correlations of the signal fluctuations with void fraction. Accuracies of water volumetric flow rate measurement of ± 2% have been reported when using air/water mixtures with void fractions of up to 25% [4.22].
A new method for measuring the volumetric flow rate of the two phases, air and water, flowing upwardly in a vertical tube is developed by [4.23]. The Two Turbine Flow Meter System (TTFMS), is composed of two turbine flow meters, a valve, two thermocouples, and two pressure transducers. For a given two-phase flow, the rate of rotation of the turbine flow meter is found to depend only upon the volumetric flow rates of gas and liquid at the point of measurement.

4.4 Drag Disk

The Drag Disk (DD) is a very simple device capable of measuring the force exerted by the fluid flow on a portion of the pipe cross section. The disk can have different geometry and dimension; when the target is a disk less than 10% of the pipe cross-section is also know as a target flow meter.
The flow range of the strain gage target flow meter is determined by the target size. By changing targets the flow range can be altered. Unidirectional/Bidirectional meters for a wide range of flow conditions (up to 207 bar and 150 °C) and mass flow rates have been constructed with typical accuracy of ± 0.5% of full scale and an excellent time response ranging from 0.002 to 0.1 s.
Largely used in the past, it is not popular today, the only type actually produced is the body-target-type meter, that detects the force exerted by the flow using a strain gauge circuitry [4.25].

The dynamic force of fluid flow, or velocity of the approaching stream, is sensed as a drag force on a target (disk) suspended in the flow stream. This force is transmitted via a lever rod and flexure tube to an externally bonded, four active arms strain gage bridge. This strain gage bridge circuit translates the mechanical stress due to the sensor (target) drag into a directly proportional electrical output. Translation is linear and the drag force itself is proportional to the flow rate squared.

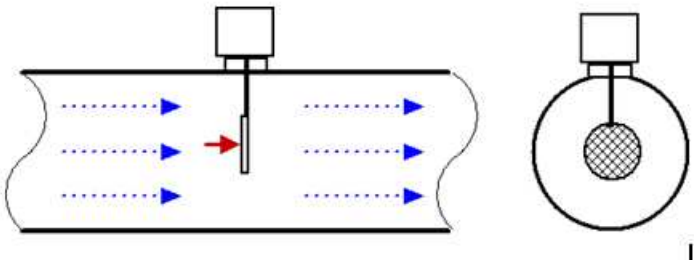

Fig.4.4: Drag disk scheme

The physics working principle of the DD is that a body immersed in a flowing fluid is subjected to a drag force given by:

$$F_D = \frac{1}{2} C_D A_t \cdot \left(\rho U^2\right) \tag{4.9}$$

where C_D is the drag coefficient and A_t is the cross section area of the target.

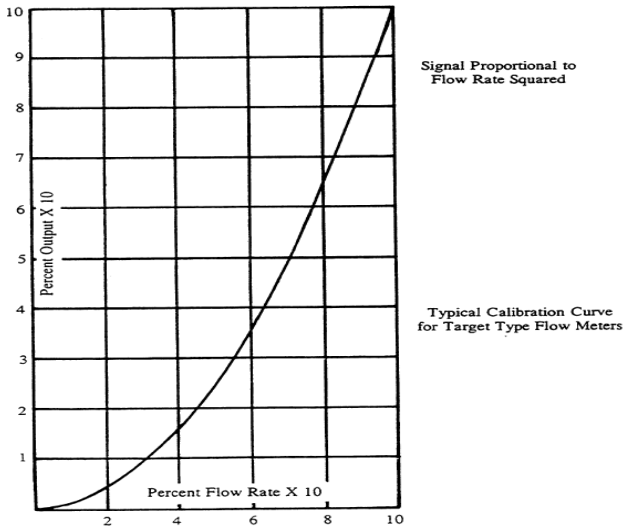

Fig.4.5: Typical Calibration Curve for Target flow Meters

The force sensed by the meter is proportional to the square of the velocity for turbulent flows, while in the laminar regime (low velocity flow, high viscosity flow or both) the results are not so predictable because the sensor output may be affected by viscosity. Laminar flow exists below Re = 400 and a transition range exists between 400 and about 2000. The drag coefficient of the target, C_D, may vary in an unpredictable manner when Re is in the transition or laminar regions.

The drag coefficient is almost constant in a wide range of Re; Hunter and Green [4.1] suggested the following curve to fit the C_D values:

$$C_D = C_0 + C_1\left(\frac{A_t}{A_p}\right) + C_2\left(\frac{A_t}{A_p}\right)^2 + C_3\left(\frac{A_t}{A_p}\right)^3 + C_4\left(\frac{A_t}{A_p}\right)^4 \qquad (4.10)$$

They didn't introduce any term depending on the Re number.
Anderson [4.11] was found that a full-flow drag plate of the type, shown in Fig. 4, yielded a constant drag coefficient over a large Reynolds number range ($10^4 – 10^7$).

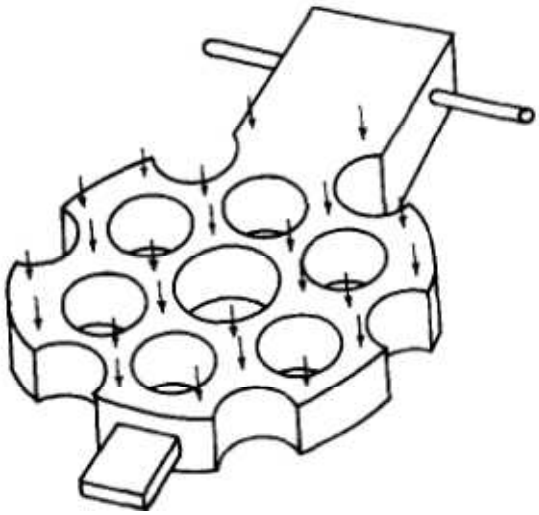

Fig.4.6: Full-flow drag disk

Averill and Goodrich [4.12] using a circular disc plate, found a coefficient C_D as in Fig.4.7.

The two important parameters considered for calibration are: the target diameter and the force factor.
The effect of the drag is to produce a force on the target support rod, resulting in an electrical output signal from the strain gage transducer in the flow meter. The relationship between the force applied on the rod and the signal is called the force factor and is a measure of the system sensitivity.
On bidirectional targets, both the upstream and downstream edges should be measured.

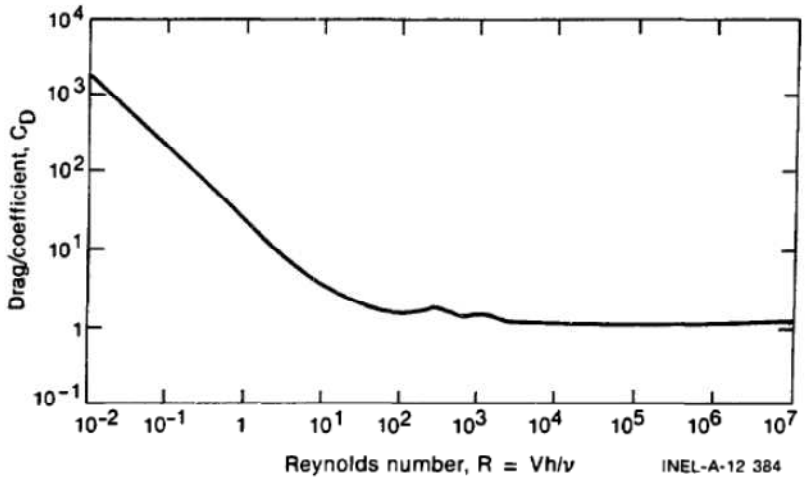

Fig.4.7: Drag coefficient of circular and square plates (in normal flow) as a function of Re [4.12]

4.4.1 Two-phase flow measurement capability and modeling

For two-phase applications, a drag disk cannot easily be used because of the variation in momentum flux in the cross section due to void migration to the centre of a tube. Even with full-flow drag devices, it is difficult to determine the correct value of the momentum flux to be applied. The only known parameters are the cross-sectional void fraction obtained from measurements and the individual-phase mass flows.
Anderson [4.11] developed a simple model with cross-sectional averaged properties. Using a two-velocity separated flow model, he assumed that the forces on the drag body were equal to the sum of the individual forces due to both phases.
After some algebraic manipulation, the drag force was shown to be equal to

$$F_D = \frac{1}{2} C_D A_t \cdot \left[\alpha \cdot \left(\rho U^2\right)_g + (1-\alpha)\left(\rho U^2\right)_l\right] \tag{4.11}$$

This model is the same used by Aya to analyze the behavior of a turbine meter and a drag meter in a SP.
Drag coefficient C_D in two-phase flow, can be correlated with the mass flux G:

$$C_{D-TP} = C_{D-SP}\left(1 + a \cdot (\alpha G) + b(\alpha G)^2\right) \tag{4.12}$$

Where a and b are experimental coefficient, that are dependent on the void fraction and flow pattern.

In transient analysis the Kamath and Lahey model [4.16] can be used, but due to the fast time response of the flow meter, the quasi-steady approach is valid below about 10 Hz. Above this frequency transient effects must be taken into account. Fortunately, for many cases of practical significance, a 10 Hz frequency response is adequate, and thus the equations above can normally be employed to calculate the transient mass flux.

4.4.2 Temperature effect

Averill and Goodrich [4.12] during the Loss-of-Fluid Test at the LOFT facility at the Idaho National Engineering Laboratory, have measured the mass flow rates with the drag-disc turbine transducer (DTT).
The drag disc, used in the LOFT facility, is temperature sensitive; therefore, the authors proposed the following correction:

$$\rho U^2 = \left(Z_0 + Z_1 T\right)\frac{S_0 + S_1 T}{D_1} + \left(S_0 + S_1 T\right)V\left(t\right) \tag{4.13}$$

Where:

Z_0 is the zero offset from the zero offset temperature equation

Z_1 is the change in the zero offset with temperature

S_0 is the zero offset from the slop calibration temperature equation

S_1 is the change in slope calibration with temperature

D_1 is the full flow calibration at ambient temperature.

Hardy and Smith [4.26], showed that the influence of the temperature induced changes on the resistance of the wires that connected the sensor to the control room could have influenced negatively the signal reading.
The average thermal output was ±0.02 N/ºC. This correspond to an uncertainty for thermal effects of ±0.1% f.s.

4.4.3 Two-phase flow applications

Because it is a momentum-sensing device, the drag meter has been used in conjunction with volume-sensing flow meters, or with densitometer to allow density and mass flow to be deduced in a large number of nuclear loss-of-coolant experiments.

Hardy [4.8] tested a SP where the drag has been coupled with a string probe. The instrumentations have been devised and calibrated for two-phase mass flux measurement under simulated pressurized-water reactor reflood conditions. The drag disk used in that experiment was bidirectional and forced calibrated in both direction. This spool gave mass flux estimation between + 40% and -30%, using the simplest model: homogeneous model. In two-phase flow, two distinct correlations were required to fit the data obtained. The reason of this can be a flow pattern transition: from droplet mist to froth flow. But other possible reasons were flow disturbances and slip ratio change.
The two correlations has been defined for mist and froth flow; the major criterion that delineates between the curves has been found in the void fraction value, as shown in Fig.4.8.

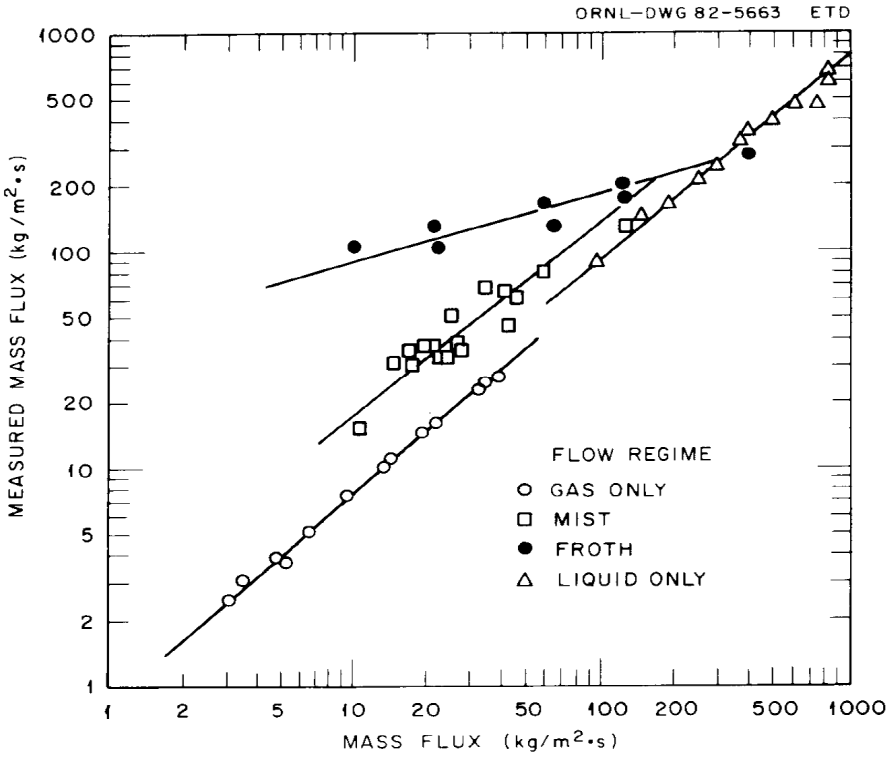

Fig.4.8: Drag disk and string probe data vs. measured mass flux for single and two-phase flow [4.8]

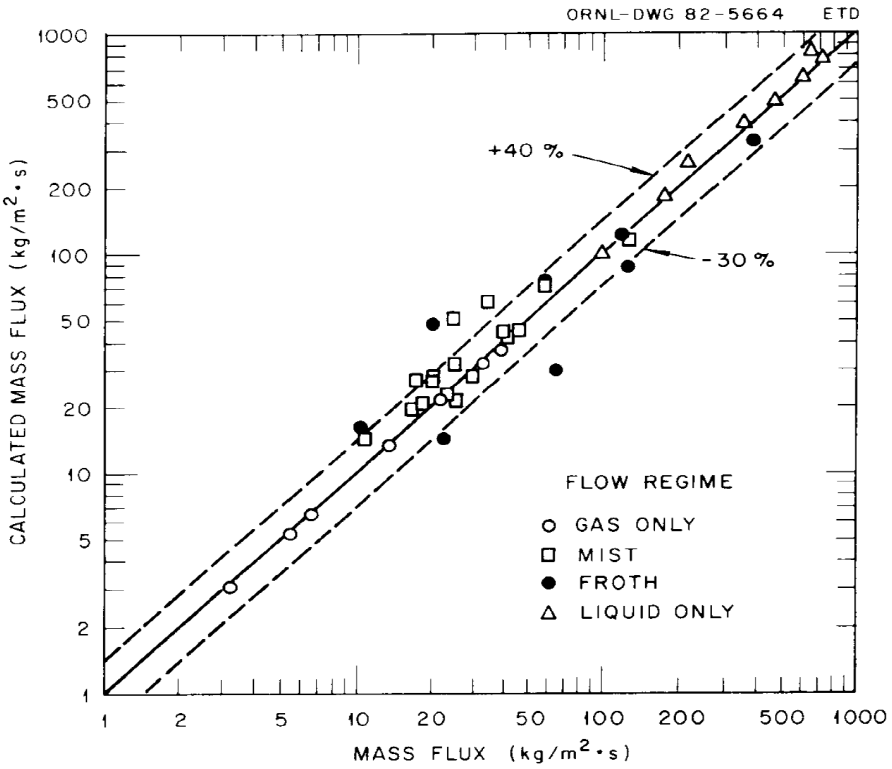

Fig.4.9: **Comparison of calculated with actual mass flux for single and two-phase flow [4.8]**

Sheppard et al. [4.19] demonstrated that, in two-phase flow, if the drag meter is installed in a spool piece, with a turbine meter, accurate calculated measurements were attained only when the drag disk is positioned upstream of the turbine and a flow disperser is installed.
A possible explanation is that the rotational motion of the turbine meter separates the phases and induces an annular flow rather than a dispersed flow. This factor highlight the strong sensitivity of the instruments to the flow configuration and to the phases distribution.

Hardy and Smith [4.26] in order to calculate the two-phase mass flow rate, combined the momentum measured with the drag plate with the velocity detected by a turbine flow-meter:

$$W_{tot} = \left(\frac{\left(\rho U^2\right)_D}{U_T} \right) A_p \tag{4.14}$$

The results are showed in Fig.4.10. The data provide a good estimate of the mass flow rate; almost all the data fell in an error band ± 20%.

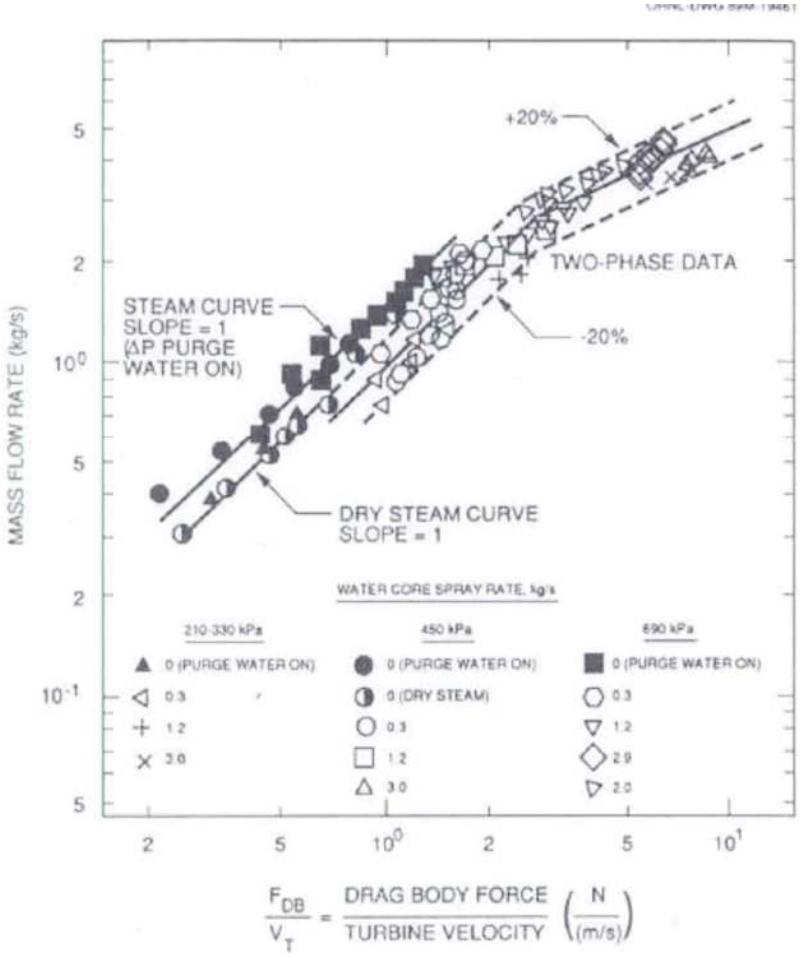

Fig.4.10: Comparison of mass flow rate from measured inputs with a mass flow model combining drag body and turbine meter measurement [4.26]

4.5 Differential Pressure Meters

The calculation of fluid flow rate by reading the pressure loss across a pipe restriction is perhaps the most commonly used flow measurement technique in industrial applications. The pressure drops generated by a wide variety of geometrical restrictions have been well characterized over the years, and these primary flow elements are used in a wide variety of configurations, each with specific application strengths and weaknesses. Different geometries are used for different measurements, including the orifice plate, flow nozzle, and Venturi Flow Meter (VFM). In this section general performance and characteristics for VFM are reported.

The classical Herschel Venturi (Fig.4.11) has a very long flow element characterized by a tapered inlet and a diverging outlet. The entrance is a converging cone with a 15^o to 20^o angle. It converges down to the throat, which is the point of minimum cross-sectional area, maximum velocity, and minimum pressure in the meter. The exit portion of the meter is a diverging cone with an angle of 5^o to 7^o which completes the transition back to full pipe diameter. Inlet pressure is measured at the entrance, and static pressure in the throat section. The pressure taps feed into a common annular chamber, providing an average pressure reading over the entire circumference of the element.

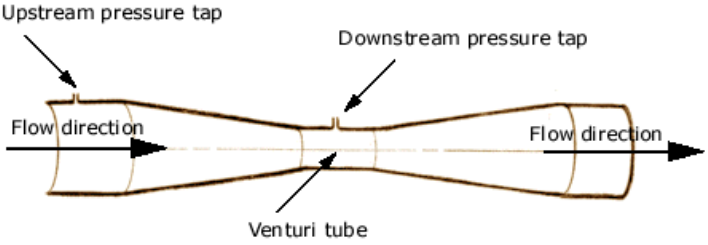

Fig.4.11: Classical Venturi Flow Meter

In the short form Venturi, the entrance angle is increased and the annular chambers are replaced by pipe taps (Fig.4.12-A). The short-form Venturi maintains many of the advantages of the classical Venturi, but at a reduced initial cost, shorter length and reduced weight. Pressure taps are located 1/4 to 1/2 pipe diameter upstream of the inlet cone, and in the middle of the throat section. Piezometer rings can be used with large Venturi tubes to compensate for velocity profile distortions.

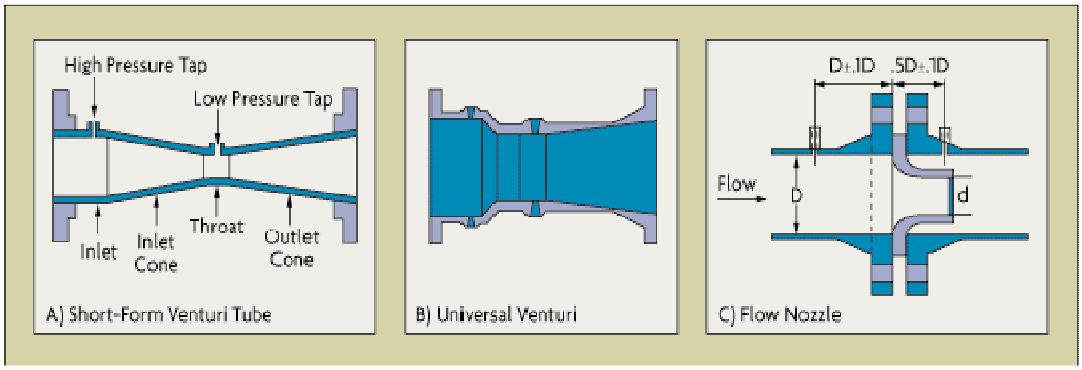

Fig.4.12: Venturi flow meter types

The changes in cross section area cause changes in velocity and pressure of the flow. Because of the smooth gradual transition down to the throat diameter and back to the full pipe diameter, the friction loss in a VFM is quite small. This leads to the value of a VFM discharge coefficient, C_d, being nearly one. Typical discharge coefficient values for a VFM range from 0.95 to 0.995 in liquid flow.
Venturi tubes are available in sizes up to 72", and can pass 25 to 50% more flow than an orifice with the same pressure drop. Furthermore, the total unrecovered head loss rarely exceeds 10% of measured pressure drop (Fig.4.13).

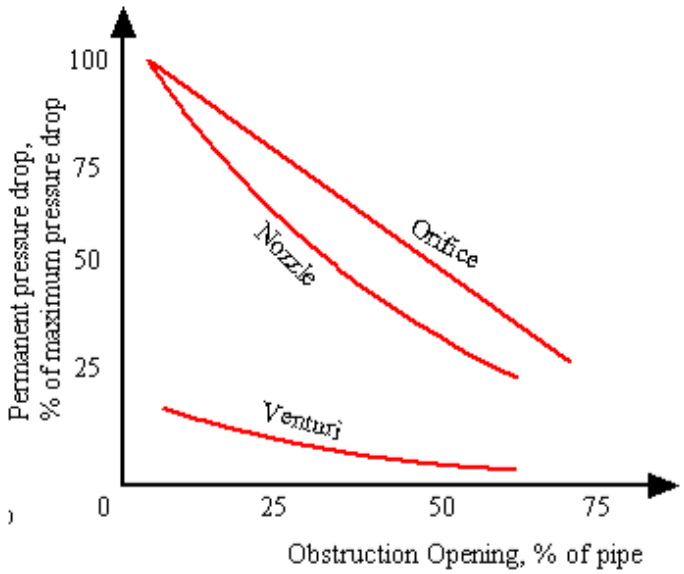

Fig.4.13: Permanent pressure drop in differential flow meter [4.43]

VFMs are insensitive to velocity profile effects and therefore require less straight pipe run than an orifice. Their smoothed geometry makes the device immune to corrosion and erosion so that it is characterized by very low installation and operating and maintenance costs.

Differential meters are typically one-directional. Bi-directional capability can be obtained either with a modified design or with in-situ testing of a one-directional meter in reverse flow conditions.

4.5.1 Theory of differential flow meter in single-phase flow

Starting from the Bernoulli's equation that established the relationship between static and kinetic energy in a flowing stream, the general Differential Flow Meter equation can be written as:

$$Q = C_d A_2 \left(\frac{2\Delta p}{\rho(1-\beta)^4} \right)^{0.5} \tag{4.15}$$

where C_d is discharge coefficient for the particular meter, and $\Delta p = p_1 - p_2$ is the pressure difference between the undisturbed upstream pressure in the pipe (1) and the pressure in the pipe at the constricted area, A_2; while β is the diameter ratio D_2/D_1.

If also compressibility and thermal expansion effects are considered the equation becomes [4.39]:

$$Q = C_d A_2 \left(\frac{2\Delta p}{\rho(1-\beta^4)} \right)^{0.5} \cdot F_a \cdot Y \tag{4.16}$$

F_a thermal expansion correction factor
Y compressibility coefficient
The numerical values of F_a for orifice plates given in ISO5167 [4.27] are based on data determined experimentally. For nozzles and Venturi tubes they are based on the thermodynamic general energy equation, and is calculated with different formulas depending on the device geometry. For liquids (uncompressible fluids), is always F_a=1. For steam and gases (compressible fluids) F_a >1.

The discharge coefficient C_d is influenced by the Reynolds number and by β, the ratio between the throat diameter of the flow meter and the inside diameter of the pipe.
Additional parameters or correction factors can be used in the derivation of C_d, depending on the type of flow element used. These parameters can be computed from equations or read from graphs and tables available from the ISO, the American National Standards Institute (ANSI), the American Petroleum Institute (API), the American Society of Mechanical Engineers (ASME).
The discharge coefficients are determined by laboratory tests that reproduce the geometry of the installation. Published values generally represent the average value for that geometry over a minimum of 30 calibration runs. The uncertainties of these published values vary from 0.5% to 3%. By using such published discharge coefficients, it is possible to obtain reasonably accurate flow measurements without in-place calibration. In-place calibration is required if testing laboratories are not available or if better accuracy, than that provided by the uncertainty range noted above, is desired. The relationship between flow and pressure drop varies with the velocity profile, which can be laminar or turbulent as a function of the Reynolds number (Re).
At low Reynolds numbers (generally under Re = 2000), the flow is laminar and the velocity profile is parabolic. At high Reynolds numbers (well over Re = 3000), the flow becomes fully turbulent, and the resulting mixing action produces a uniform axial velocity across the pipe.
The transition between laminar and turbulent flows can cover a wide range of Reynolds numbers; the relationship with the discharge coefficient is a function of the differential flow meter.

Jitschin [4.37] performed some experiments using a classical VFM and a thin orifice in gas flow. He found that the discharge coefficient C_d approaches the value 1 at large Reynolds numbers (in agreement with DIN 1952 and EN ISO 5167-1), which gives the result

C_d=0.990±0.005 (depending on wall roughness) at $Re>2\times10^5$. The discharge coefficient becomes significantly lower than 1 with decreasing Reynolds numbers. The reason for this behavior is, for the author, an increasing importance of friction at the walls.

Bernoulli's equation states that the pressure drop across the constriction is proportional to the square of the flow rate. Using this relationship, 10% of full scale flow produces only 1% of the full scale differential pressure. At 10% of full scale flow, the differential pressure flow meter accuracy is dependent upon the transmitter, being accurate over a 100:1 range of differential pressure. Because of the nonlinear relationship between flow and differential pressure, the accuracy of flow measurement in the lower portion of the flow range can be degraded. Accuracy can also be degraded when Reynolds number is low.
For this reason, differential flow meters have historically been limited used within a limited range 3:1 or 4:1 [4.40].
Flow meter rangeability can be increased without effect on accuracy by installing two or more transmitters in parallel onto the same element, one for 1-10%, the other for 10-100% of full scale (f.s.) produced Δp.
In some applications (as gas flow rate measure or in presence of pressure and temperature variations) the flow meter should be designed carefully because changes in operating pressure and operating temperature can dramatically affect the flow measurement. In other words, the fluid density can vary significantly during operation. As a result, the differential pressure produced by the flow meter can also vary significantly during operation. Failure to compensate for these effects can cause flow measurement errors of 20% or more in many applications [4.40]. Moreover, errors due to incorrect installation of the meter can be relevant (up to 10%). Causes of such errors can be insufficient straight pipe runs and pressure tap and lead line design errors.

The Δp generated by the VFM fluctuates due to not only the mechanical vibrations of the pipe line but also to the irregular disturbances of the micro-structures inside the fluid.
As the fluctuation of the Δp signal does not contribute to the measurement of the flow rate, it is commonly filtered out by specially designed pressure taps or by the Δp transmitter. For example, the capacitance-based Δp transmitter is generally insensitive to vibrations above 10 Hz. This aspect has to be considered when the flow meter is used in two-phase flow applications; in these conditions the fluctuation due to the flow interaction and structure must be identified and separated from noise fluctuations.

4.5.2 Differential flow meters in two-phase flow

In the last decades, many investigations focused on air-water or steam-water two-phase flow measurement using orifices and VFM.
Compared with other kinds of differential pressure devices, the VFM has little influence on flow regimes [4.36], the smallest pressure loss, the shortest straight pipe upstream and downstream and it is less likely to cause blockage to the liquid phase [4.38].
The presence of the two-phase mixture causes an increase in the measured differential pressure because of the interaction between the gas and the liquid phase, so that the single-phase formulation over predicts the effective flow rate.

This over-reading is usually ‘corrected’ using available correlations derived from experimental data to determine the actual gas mass flow rate.

To use differential meter with two-phase flow, there are three approaches [4.1]:
- adjusting the value of density to reflect the presence of a second component.
- adjusting the discharge coefficient to introduce the presence of the second component
- relating two-phase pressure drops to those which would have occurred if the whole flow was passing either as a gas or as a liquid.

The general equation of the VFM in a two-phase flow can be written as:

$$W_{tot} = K \cdot \sqrt{2\Delta p_{TP} \rho_{TP}} \tag{4.17}$$

where

$$K = \frac{C_{d-TP} \cdot F_a \cdot Y}{\sqrt{1-\beta^4}} A_2 \tag{4.18}$$

Considering the value of Y and F_a equal to one, the two parameters, that have to be defined, are the two-phase discharge coefficient and the two-phase density.
The correction of the density can be made considering the different mixture density definitions, defined in the paragraph 3.2, leading to the:
- Homogeneous flow correlation
- Separated flow correlation
- James’ Correlation [4.34]

The James’ correlation is a modification of the homogenous correlation, in which the two-phase flow density in expressed as:

$$\rho_{TP} = \left(\frac{x^n}{\rho_g} + \frac{(1-x)^n}{\rho_l} \right)^{-1} \tag{4.19}$$

where n =1.5.

The proportionality constant K can be extrapolated from single-phase flow literature (provided the meter is single-phase standard design) and tailored on the basis of preliminary in-situ testing (coupling with the second approach).

The third approach, the most used, is based on the work of Lockhart and Martinelli [4.28] that investigated the relation between the pressure drop in single-phase flow and in two-phase flow through the so called two-phase flow multiplier:

$$\frac{\left(-\frac{dp}{dz}\right)_{TP}}{\left(-\frac{dp}{dz}\right)_{k}} = \phi_k^2 \tag{4.20}$$

where

$$\left(\frac{dp}{dz}\right)_{k}$$

represents the pressure gradients for single-phase gas and liquid flow as fractions of the total two-phase mass flow rate, respectively [4.41] and are related to the Lockart-Martinelli parameter as:

$$\chi^2 = \frac{\left(\frac{dp}{dz}\right)_{l}}{\left(\frac{dp}{dz}\right)_{g}} \tag{4.21}$$

Assuming that the two phases are flowing under turbulent regime and using the Blasius correlation for the single-phase friction factor coefficients calculation:

$$f = 0.0079/Re^{1/4} \tag{4.22}$$

the parameter χ^2 can be written as:

$$\chi^2 = \left(\frac{1-x}{x}\right)^{0.875} \cdot \left(\frac{\rho_g}{\rho_l}\right)^{0.5} \cdot \left(\frac{\mu_l}{\mu_g}\right)^{0.125} \tag{4.23}$$

For a two-phase mixture flowing in orifice and Venturi devices, according to Collier and Thome [4.1], the parameter is usually written in the following form:

$$\chi^2_{\text{mod}} = \left(\frac{1-x}{x}\right) \cdot \left(\frac{\rho_g}{\rho_l}\right)^{0.5} \tag{4.24}$$

Using this approach the total mass flow rate in the VFM can be written as:

$$W_{tot} = K_{TP} \cdot \sqrt{2\Delta p_{TP}\rho_{TP}} = K_k \sqrt{2\Delta p_k \phi_k^2 \rho_k} = W_k \cdot \phi_k \tag{4.25}$$

Many researchers studied the relationship between the mass flow rate of gas-liquid flow and the differential pressure across the flow meter [4.29],[4.30],[4.31],[4.35].

The correlations currently available for the two-phase flow signal correction have been derived from a limited set of data and may only be suitable to cover restricted ranges of the flow meter parameters, for example, a specific diameter ratio and are closely dependent on experiment conditions such as pressure, temperature, medium, devices, etc.
The use of correlations outside the conditions used to define them can result in large errors in the calculation of the gas mass flow rate.

Most of the available correlations for two-phase flow are valid only for low (x<0.1) or very high (x>0.95) steam quality.

Murdock's Correlation [4.29]**:**
Murdock derived a correlation to predict the behavior of an orifice plate in two-phase horizontal flow.
The correlation is expressed as:

$$W_{tot-M} = W_g \cdot (1+1.26\chi_{\mathrm{mod}}) \tag{4.26}$$

The constant (1.26) is an empirical value.
The correlation is dependent only on χ, while the influence of the flow pattern is not considered. Although initially derived for orifice flow meter, Miller [4.2] suggests the Murdock equation can be used in a Venturi meter, using the constant value 5 instead of 1.26.

Lin's Correlation [4.35]**:**
It was originally developed for orifice meter. It considers the influence of the pressure and of the liquid mass content on the meter response:

$$W_{tot-L} = W_g \cdot (1+\theta\chi_{\mathrm{mod}}) \tag{4.27}$$

where ϑ is correlated with the density ratio:

$$\begin{aligned}\vartheta = {} & 1.48625 - 9.26541\left(\frac{\rho_g}{\rho_l}\right) + 44.6954\left(\frac{\rho_g}{\rho_l}\right)^2 - 60.6150\left(\frac{\rho_g}{\rho_l}\right)^3 \\ & -5.12966\left(\frac{\rho_g}{\rho_l}\right)^4 - 26.5743\left(\frac{\rho_g}{\rho_l}\right)^5\end{aligned} \tag{4.28}$$

Chisholm's Correlation [4.30]**:**
Chisholm (1969) developed a two-phase flow correlation, considering the slip between the fluids. It was assumed to be an incompressible two-phase flow, with negligible upstream momentum, no phase change, irrelevant drag forces in the wall when compared to the interfacial forces between the phases, and a constant void fraction across the differential pressure device. Chisholm's correlation is defined by:

$$W_{tot-C} = W_g \cdot (1+C\chi_{\mathrm{mod}} + \chi^2_{\mathrm{mod}}) \tag{4.29}$$

where

$$C = \frac{1}{S}\left(\frac{\rho_l}{\rho_g}\right)^{0.5} + S\left(\frac{\rho_g}{\rho_l}\right)^{0.5} \tag{4.30}$$

and S is the *slip ratio* is assumed equal to:

$$S = \left(\frac{\rho_l}{\rho_g}\right)^{1/4} \tag{4.31}$$

He concluded that the meter response to two-phase flow in horizontal pipe does not only depend on the modified Lockart-Martinelli parameter (χ_{mod}), but also on the gas-liquid density ratio (and then on the pressure).

De Leeuw's Correlation [4.31]**:**
The most used correlation for Venturi tubes, in wet gas applications, is that reported by de Leeuw in 1997.
He used data collected from a 4-inch, 0.4 diameter-ratio Venturi tube and fitted the data using a modification of the Chisholm model. The correlation is valid only for gas with a small amount of liquid (the Lockhart-Martinelli parameter has to be less than 0.3):

$$W_{tot-D} = W_g \cdot (1 + C\chi_{\text{mod}} + \chi_{\text{mod}}^2) \tag{4.32}$$

$$C = \left(\frac{\rho_l}{\rho_g}\right)^n + \left(\frac{\rho_g}{\rho_l}\right)^n \tag{4.33}$$

$$\begin{cases} n = 0.606 \cdot \left(1 - e^{-0.746Fr}\right) & \text{Fr}_g \geq 1.5 \\ n = 0.41 & 0.5 \leq \text{Fr}_g < 1.5 \end{cases} \tag{4.34}$$

where Fr_g is the Froude number evaluated using the gas properties.

The difference between the de Leeuw formulation and the Chisholm formulation is the values of the *n* exponent. De Leeuw showed that *n* was a function of the gas Froude number, a parameter that was not considered in the previous Chisholm correlation.
De Leeuw stated that the value of *n* is dependent on the flow regime.
For stratified flow (for *Fr* <1.5) *n* is constant and equal to 0.41. As the flow pattern changes from stratified to annular mist and towards mist flow, the over reading for a set value of the quality will increase. He practically assumed that below *Fr* =1.5 the gas dynamic forces were too weak to produce flow patterns other than stratified flow. He claimed that for that meter geometry, for a known value of the liquid flow rate and within the test matrix parameters of the used data set, this correlation is capable of predicting the gas mass flow rate with ±2% uncertainty.

The knowledge of the β ratio influence on the Venturi meter response limits the application of the de Leeuw correlation to those cases in which the actual β ratio is very close to the value of the original experiment. If the correlation is applied to higher values of β ($\beta >$ 0.401), there will be a systematic over correction of the actual over reading.

For all the correlations, the knowledge of the flow rate of one of the phases or of the quality is necessary, since the calculation of the Lockart-Martinelli parameter is based on the single-phase pressure drop evaluation. Thus the coupling of a venturi and a quality detecting device is, in principle, needed for the calculation of the total mass flow rate.

Zhang's Correlation [4.42]**:**
To take into account the two-phase flow occurrence, Zhang et al. (2005) suggested the introduction of the K_L parameter to summarize the necessary corrections for correlating the two-phase mass flow rate to the two-phase pressure drop:

$$W_{tot} = \frac{C_{d-TP} \cdot F_a \cdot Y}{\sqrt{1-\beta^4}} A_2 \cdot \sqrt{2\Delta p_{TP} \rho_l} \cdot K_L \tag{4.35}$$

$$K_L = \left[c\left(\frac{\alpha}{1-\alpha}\right)^n \left(\frac{\rho_l}{\rho_g}\right)^m + 1 \right]^{-1/2} \tag{4.36}$$

$$X = c'\left(\frac{\alpha}{1-\alpha}\right)\left(\frac{\rho_g}{\rho_l}\right)^H \tag{4.37}$$

where *c, n, m, c'* , and *H* are constants which are dependent on the flow regimes and on the test conditions. For bubbly and slug flow, they are equal to 0.50, 0.95, 0.02, 0.51, and 0.65, respectively.
The two-phase discharge coefficient $C_{d\text{-}TP}$, can be evaluated based on pre tests calibration.
The correlation is based on experiments with low quality (x < 2%) oil–air flow through a venturi.

Oliveira et al. [4.39] tested this formula in a SP using venturi and orifice plate coupled with a void fraction sensor. Fig.4.14 shows, in a logarithmic graph, the comparison between the experimental quality values and those predicted through the x-S-alpha correlation, assuming the non-slip condition (S = 1), and Zhang correlation. The quality predicted assuming the non-slip condition (S = 1) was underestimated for most values. The performance was good for bubbly and slug regimes, but when the transition to churn and annular occurred, and mean void fractions over 0.7 and quality over 1% were reached, the predicted quality values deviated from the reference line. The results obtained using the Zhang correlation overestimated the experimental values. The correlation, created with an oil–air flow data set, did not obtain satisfactory results, and RMS deviation values over 200% were reached.

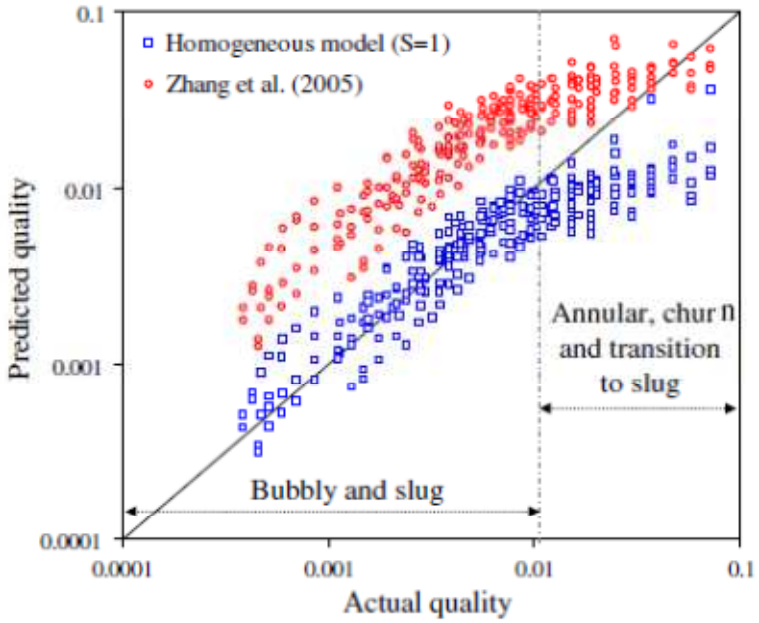

Fig.4.14: Comparison between experimental and predicted quality using homogeneous and Zhang model [4.39]

The authors make a comparison also with other correlations. As with the homogeneous model, Chisholm's correlation achieved better results with the venturi. A deviation of 6.8% was obtained for this meter in the vertical direction. It should be noted that Chisholm's correlation had the best performance of all the tested correlations.

4.5.3 Transient operation capability (time response)

Orifice plates and VFM are typically designed for steady state applications. Fast transient response requires special care in the design and may require the correction of the signal on the basis of the modeling of the meter, which is doable but not straightforward.
If the flow is not steady, the measurement error will increase because of different reasons [4.1]:

- square root error
- resonance
- limitations in the pressure measurement device.

The first one is connected to the capability of a fast response of the pressure meter, the second to the possibility of a correspondence between the pulsating frequency and the resonance frequency of some components. The response is highly influenced by the length of transmission pipe lines and the used medium (gas or liquid). The only research found in literature about dynamic response is proposed by Xu et al. [4.32].

4.6 Impedance Probes

In two-phase flow research, the impedance (conductance or capacitance) technique has been applied for almost four decades in void fraction measurements, especially in laboratory experiments.
The fast response of the impedance meter makes it possible to obtain information about virtually instantaneous void fractions and their distributions across a pipe section. The impedance void-meter is a low-cost device. The economic feature makes it a more attractive approach than other techniques. In addition, the void-meter can be constructed easily in a non-intrusive structure. A variety of probe geometries has been applied, including those in which the ground and emitter are placed in opposite test section walls, and those which are completely immersed in the two-phase flow.
The impedance method is based on the fact that the liquid and gas phases have different electrical conductivities and relative permittivities; the proper definition of the electronic circuit (excitation frequency, excitation signal, etc..) allows the possibility to make the device more sensitive to the conductance or to the capacitance of the flow.

4.6.1 Theory: effective electrical properties of a two-phase mixture

This type of instruments operates on the principle that the electrical impedance of a mixture is usually different from the impedance of each component.
A correlation between the void fraction and the mixture impedance is possible if the two constituents have dissimilar electrical properties.
Gases are generally poor conductor with a low dielectric constant, while liquids if not good conductors will at least assume a higher value of the dielectric constant due to a larger concentration of dipoles.
The measurements of the impedance take place in a volume defined by the lines of an electric field associated with the electrodes system.

There are, however, several disadvantages of the impedance technique, which are sometimes difficult to resolve. For example, the capacitance measurement is sensitive to the void fraction distribution or flow regimes. This drawback can be compensated by first identifying the flow pattern. The measurement is also sensitive to the changes in electrical properties of the two phases due to temperature. The noise due to the electromagnetic field around the sensor and connecting wires can significantly affect the signal and needs to be minimized through proper design of the sensor shield. As mentioned by Olsen [4.46], the polarization effect due to the ions in the liquid introduces an additional impedance localized in the vicinity of the liquid-electrode interface. This parasitic impedance can be removed by a proper choice of the electric frequency. If insulated electrodes are used, a proper model on the cell impedance should include the capacitive effect of the insulator.

The relation between the admittance of the mixture and the void fraction is not univocal and for a single admittance value there could be different void fraction values, based on different flow patterns.

The analytical treatment has been first done by Maxwell [4.47]. His solution is obtained by considering a dilute suspension of spheres having a conductivity ε_i in a continuous medium of conductivity ε_o. Maxwell found the following equation:

$$\frac{\varepsilon_{TP}}{\varepsilon_o} = 1 - \frac{3\alpha}{\left(\frac{2\varepsilon_o + \varepsilon_i}{\varepsilon_o - \varepsilon_i}\right) + \alpha} \tag{4.38}$$

For the case of air bubbles in water the equation reduces to

$$\frac{\varepsilon_{TP}}{\varepsilon_l} = 1 - \frac{3\alpha}{2 + \alpha} \tag{4.39}$$

because $\varepsilon_l >> \varepsilon_g$.

Van Beek (1967) gave a more general form of this equation:

$$\frac{\varepsilon_{TP}}{\varepsilon_l} = \left[1 + \frac{n\alpha\left(\varepsilon_g - \varepsilon_l\right)}{\varepsilon_g + \left(n-1\right)\varepsilon_l}\right] \tag{4.40}$$

Where n is a function of particle shape: 3 for spheres correspond to Maxwell's equation. For oblate spheroids is ~ 1 and for prolate spheroids is >3.
Bernier [4.48] proposed a model that consider the *true* void fraction, α_T as a function of the relative capacitance (α_C) and a *dispersion factor* (*m*)

$$\alpha_T = f\left(\alpha_C, m\right) \tag{4.41}$$

with

$$\alpha_C = \frac{C_l - C_{TP}}{C_l - C_g} \tag{4.42}$$

where *C* is the capacitance of the fluid and m is the dispersion factor (determined by the shape and distribution of the dispersed phase which, at high void fraction, is usually liquid). By definition :

$$\frac{C_l}{C_g} = \varepsilon_l \tag{4.43}$$

$$\frac{C_{TP}}{C_g} = \varepsilon_{TP} \tag{4.44}$$

And $\varepsilon_g = 1$ is the dielectric constant for the gas phase.

Rewriting the equation:

$$\alpha_C = \frac{\varepsilon_l - \varepsilon_{TP}}{\varepsilon_l - \varepsilon_g} \tag{4.45}$$

The relationship between relative capacitance and void fraction is described by:

$$1 - \alpha_T = 1 - \alpha_C = \frac{\varepsilon_l - m \cdot \varepsilon_g}{\varepsilon_l \cdot (1 - \alpha_C) + \varepsilon_g \cdot (m + \alpha_C)} \tag{4.46}$$

Note that *m = 2* corresponds to Maxwell's theoretical equation.

Jaworek [4.59] proposed different models that can be applied to the situation of two-phase flow.

These models calculate the equivalent permittivity of the mixture:

- plate voids placed perpendicularly to the electrodes, which can be reduced to two capacitances connected in parallel. The effective relative permittivity can be calculated as:

$$\varepsilon_{TP} = \varepsilon_g \alpha + \varepsilon_l (1 - \alpha) \tag{4.47}$$

where ε_g is the relative permittivity of the gaseous phase, ε_l the relative permittivity of the liquid phase.

- plate voids placed parallel to the electrodes, which can be reduced to two capacitance connected in series:

$$\varepsilon_{TP} = \frac{1}{\frac{\alpha}{\varepsilon_g} + \frac{(1-\alpha)}{\varepsilon_l}} \tag{4.48}$$

- a continuous medium (water) with cylindrical voids placed parallel to the electrodes, which could be a model for annular flow:

$$\varepsilon_{TP} = \frac{(2\alpha - 1)(\varepsilon_g - \varepsilon_l) + \sqrt{(2\alpha - 1)^2 (\varepsilon_g - \varepsilon_l)^2 + 4\varepsilon_g \varepsilon_l}}{2} \tag{4.49}$$

- a continuous medium with spherical voids, that could be a model for bubble flow:

$$\varepsilon_{TP} = \frac{2(\alpha\varepsilon_g + (1-\alpha)\varepsilon_l) - (\alpha\varepsilon_l - (1-\alpha)\varepsilon_g) + \sqrt{2(\alpha\varepsilon_g + (1-\alpha)\varepsilon_l) - (\alpha\varepsilon_l - (1-\alpha)\varepsilon_g)^2 + 8\varepsilon_g\varepsilon_l}}{4} \tag{4.50}$$

Fig.4.15 represents the effective relative permittivity of the precedent models as a function of the void fraction.

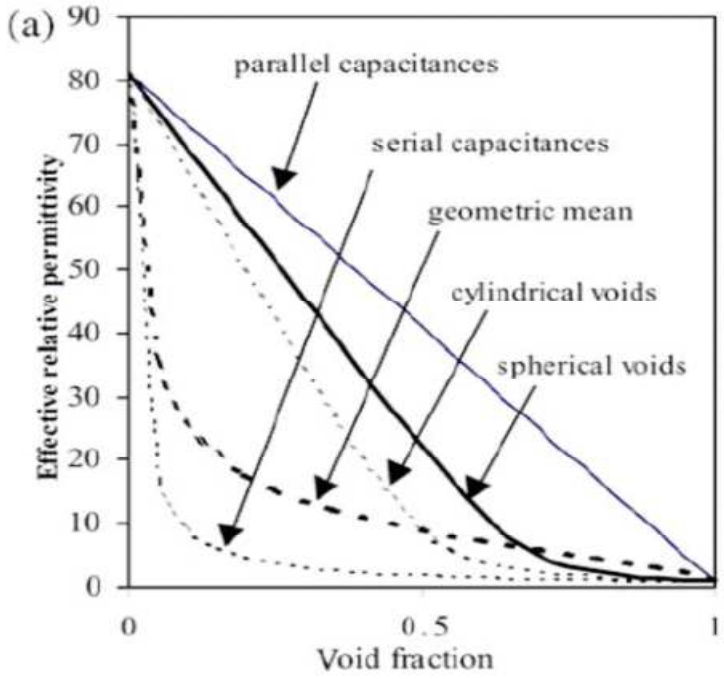

Fig.4.15: Effective relative permittivity as a function of the void fraction

The formula that relates the dielectric constant (or relative permittivity) ε and the capacitance C for a parallel plate capacitor with a surface area *A* and the distance between the plates equal to *d* is:

$$C \approx \varepsilon A/d \tag{4.51}$$

provided that $A \propto d^2$.

4.6.2 Sensor design criteria

The measurements of void fraction with impedance sensor are quasi-local: the sensor determines the percentage of both phases not strictly in a selected cross section of the pipe but in a certain volume, based on the electrodes height (except that for wire sensor that are installed inside the pipe and perpendicular to the flow). The exact boundary of this volume cannot be precisely drawn due to fringe effects.
To minimize the non-local effects, the height of the electrodes along the pipe should be as short as possible, but the effect of the fringe field cannot be eliminated. Short electrodes have, however, small capacitance and low sensitivity, and in this case a compromise is needed. The sensor was shielded to minimize the distortion effects due to outer objects and electromagnetic fields. The shield dimensions should be as large as possible in order to minimize stray capacitance.

Because of the electric properties of the fluid, the impedance consists of capacitive and of resistive components. The simplest model consist of a capacitance and of resistance in parallel.
The measurements of capacitance of a capacitor filled with a conducting liquid, like water, are difficult because equivalent resistance of the liquid, which is usually low, is connected in parallel with capacitive component of the admittance, provided the water component is the continuous phase in the mixture. For low frequencies, this resistance is like a 'short-circuit' to the capacitance. To cut-off the effect of the resistance, the sensor admittance has to be measured in high frequency range.
It's better to operate at high frequencies to obtain a capacitance dominance effect, because the liquid conductivity can change by orders of magnitude with the temperature and the ion concentration, whereas the dielectric constant varies less.
Stott et al. [4.49] tested external and internal capacitance of a sensor but only for low frequency of 1.6 kHz. Abouelwafa and Kendall [4.50] used a radio-frequency bridge operating at the frequency of 1 MHz, however, it was still too low to overcome the liquid conductance component of the sensor capacitance. Huang et al. [4.51] excited the capacitance sensor with frequency of up to 5 MHz. The frequency of 80 MHz for excitation of a capacitance sensor used in laboratory tests of void fraction measurement was proposed by Jaworek [4.59]. The method of oscillation frequency deviation was used by the author for determination of the capacitance variation of a water/steam mixture using two electrodes mounted outside a pipe operating at RF frequencies.

Concerning the electrodes geometry, many different configurations were studied by a number of authors.
The different geometries can be classified in four general type; within each type there are only minor differences related to the specific environment of the probe or the number of the electrodes:

- Coaxial
- Parallel flat plates
- Wire grid
- Wall flush mounted circular arc

Selecting the optimum shape is a non simple task. It was realized that the relationship between void fraction and impedance depends on flow regime. The difference in the electrode geometry results in different electric fields within the measurement volume and hence in the sensitivity and response of the sensors.

The coaxial system permits to have a quasi-uniform electric field; however this type is very sensitive to void distribution and flow pattern.
One of the most interesting device, to overtake the problem of non homogeneous configuration of the flow pattern, was studied by Merilo et al. [4.52]. Six electrodes are mounted flush with the tube wall and respective pairs of these are energized by oscillators such that the electric field vector rotates. The results obtained tacking the average of the three values is a better approximation of the mean cross-sectional void fraction, but cannot be used to characterize the internal distribution of the phases.

Elkow and Rezkallah (1996) compared the performance of concave and helical type sensors and determined that the problems associated with helical type sensors, including the nonlinear response, poor sensitivity and poor shielding, can be eliminated by using the concave type sensors. The accuracy of the concave parallel sensors can be improved by having both electrodes of equal length to decrease the non-uniformity of the electric field between the two electrodes and eliminate the non-linear response. Based on several tests, they also recommended that the distance between the electrodes and the shield should be large relative to the separation distance between the two electrodes in order to improve the immunity to stray capacitance.

Ahmed [4.53] presented, a systematic method for the design of capacitance sensors for void fraction measurement and flow pattern identification.
Two different configurations of the sensors were considered: concave and ring type (Fig.4.16). For the ring types sensor each electrode covers the entire circumference, except for a small gap to facilitate the installation of the sensor around the tubes, and are separated in the axial direction of the tube, while in the concave sensor, two brass strips are mounted on the tube circumference opposite to each other.

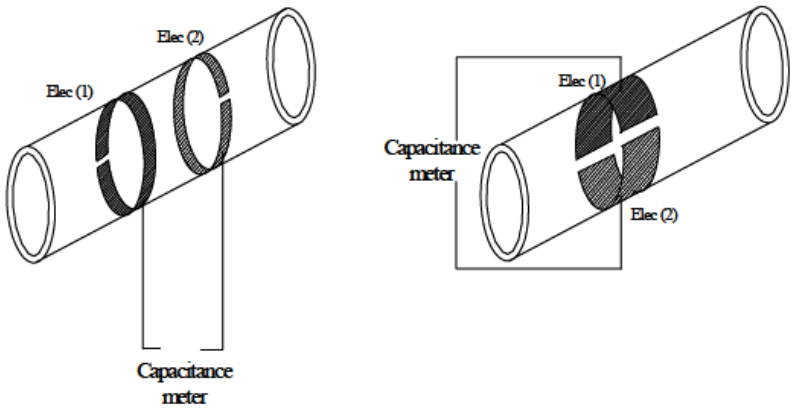

Fig.4.16: Scheme of ring and concave type sensor

Ahmed [4.53] shows that the relationship between the capacitance and the void fraction is dependent on the dielectric values of the two phases, but also on the cross-sectional area of the sensors, and the separation distance between the two electrodes.

4.6.3 Transient response

The definition of the time constant of the capacitance sensor here is referred to the time interval required for the sensor-meter to change 70% from one state or condition to another. Ahmed [4.53] found that, from ring and concave type, the time constant is approximately 40 μs, corresponding to a dynamic response of 25 kHz.

$$\frac{Y_t - Y_{initial}}{Y_{\max} - Y_{initial}} = 1 - e^{T/\tau} \tag{4.52}$$

The time constant for both types of capacitance sensors was obtained experimentally by applying a unit step signal and recording the sensor response.

4.6.4 Effect of fluid flow temperature on the meters response

In gas–liquid flows through test loops, the fluid temperature increases, causing a change in the dielectric properties, mainly of the liquid component, which interferes with the response of the impedance void fraction meters. This phenomenon causes, depending on the sensor geometry, deviations of about 4% in the meter response for each 10 °C variation of temperature in the air–water flow [4.44].
Therefore, if the capacitive device is calibrated at a given temperature and the flow temperature changes during operation in the field, an error is introduced in the two-phase void fraction measurement.
The capacitance *C* depends on the effective dielectric permittivity of the media among the electrodes, ε_m (quantity and local distribution of each component: gas, liquid, pipe material among the electrodes),which, in turn, depends on the system geometrical configuration and on the system conditions, such as its temperature. If the output voltage *V* is a function only of the capacitance *C* and for a given flow configuration, the effective permittivity becomes a function only of the flow temperature; the capacitance *C* and the output transducer voltage *V* are also functions only of the flow temperature *T*:

$$\frac{dV}{dT} = \frac{dV\left(\varepsilon_m(T)\right)}{dT} \tag{4.53}$$

Yang et al. [4.57] observed that the response of the capacitance transducer circuit, *V = V(C)*, was basically linear, with a coefficient of correlation of about 0.9999. A linear dependence was also found for the relation between the capacitance and the dielectric permittivity [4.58], so $dV/d\varepsilon_m$ can be assumed constant, then integrating:

$$V_0 = V - \alpha\left[\varepsilon_m(T) - \varepsilon_m(T_0)\right] \tag{4.54}$$

where

$$\frac{dV}{d\varepsilon_m} = \alpha \tag{4.55}$$

The effective dielectric permittivity, $\varepsilon_m(T)$, is related basically to the volumetric concentration of each component, liquid and gas, and the pipe material has a minimal influence if the electrodes are mounted flush with the internal pipe wall.
In this case the authors assumed:

$$\varepsilon_m(T) = \varepsilon_g(T)\alpha(T_0) + \varepsilon_l(T)\left[1-\alpha(T_0)\right] \quad (4.56)$$

$$\varepsilon_m(T) \cong \varepsilon_l(T)\left[1-\alpha(T_0)\right] \quad (4.57)$$

because the little variation of the gas permittivity and because $\varepsilon_l \sim 80\ \varepsilon_g$.

Substituting:

$$V_o = V - a[1 - \alpha(T_o)][\ \varepsilon_L(T) - \varepsilon_L(T_o)] \quad (4.58)$$

This equation can be solved iteratively for V_o knowing the calibration curve $\alpha(T_o) = f(V_o)$, and the value of a, obtained experimentally.

The relative dielectric permittivity of water as a function of temperature is calculated from empirical equations:

$$\varepsilon_L(T) = A \exp(BT) \quad (4.59)$$

where

$A = 87.8149$

$B = -0.004558951$

which is valid from 0 to 100 °C, with differences smaller than 0.1% for pure water test data.

Concerning the impedance probes, it is clear that, one of the most important drawbacks of these sensors is the strong sensitivity to the flow pattern.

The need of knowledge of the flow pattern can be obtained increasing the resolution in time and space of the void fraction flow meter.

The most ambitious goal is a resolution that allows us to identify individual gas bubbles and to determine their parameters (shape, volume, diameter etc.). For this purpose, the spatial resolution must be in the range of the dimensions of the lowest bubble fraction to be detected and the measuring volume must be well defined.

Another important dilemma encountered in multiphase flow measurements is that probes or instruments should be placed outside the flow domain so as not to disturb the flow itself; however, phase distributions cannot easily be measured from the boundary, as described above.

To solve these problems, in the last year tomographic image reconstruction using the impedance probes have been developed. In this way impedance probes are able to measure phases distributions inside the measured volume.

Two different technology have been developed:

- Multi-electrodes sensor (capacitance and conductance)
- Wire Mesh sensor (capacitance and conductance)

Using these instruments it is possible to know the phases distribution inside the channel so that, the mean cross sectional void fraction information can be supported by additional information able to characterize in details the flow.

4.6.5 Wire Mesh Sensor

One of the first studies on the void fraction measurement by using the WMS has been proposed by Hardy et al. [4.45]: the string (wire) probe consisted of two parallel sets of 12 electrodes, able to detect the impedance variation of the mixture between any two pair of wires. The first tomographic WMS, with approximately 100 frames per second, has been described by Reinecke et al. [4.61]. It is based on the measurement of the instantaneous conductivity of the two-phase mixture between all pairs of adjacent parallel wires of three electrode grids. The obtained three projections are subsequently used for a numerical reconstruction of the two dimensional gas fraction distribution. Prasser et al. [4.62] developed a new WMS able to measure directly the conductivity between pairs of crossing wires to avoid tomographic reconstruction algorithms and to increase the space and time resolution. The first generation of signal acquisition units worked at a framing rate of 1200 Hz while the second generation has reached a time resolution of 10 000 frames per second. The sensor has been used, in different geometries and configurations, to study the mean cross-section void fraction and to measure the bubble size and to analyze the break up and coalescence phenomena in two-phase flow applications [4.63]. Da Silva et al. [4.64] developed a WMS system based on permittivity (capacitance) measurements which has been applied to investigate multiphase flows involving non-conducting fluids, extending the application of the WMS to new application fields. Recent progresses have been made in designing and constructing such sensors for an application in a hot steam–water mixture [4.66].
The sensor is essentially a mesh of wire or bar electrodes, one plane of electrodes being the current emitter electrodes and another plane arranged orthogonal to the emitter plane being the current receiver electrodes. Between the emitter and receiver electrodes there is a gap of a few millimeters distance where conductivity is measured in the crossing points of the electrodes.

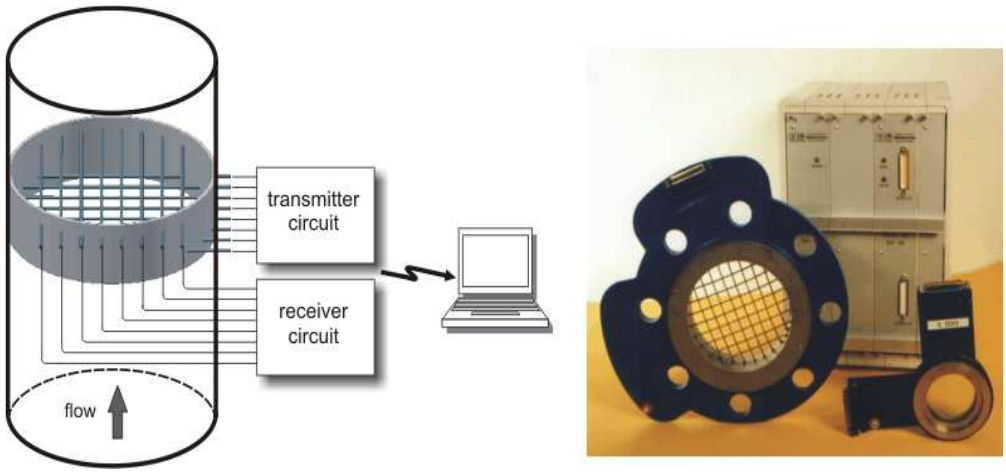

Fig.4.17: Principle of wire-mesh sensor having 2 x 8 electrodes (left). Wire-mesh sensor for the investigation of pipe flows and associated electronics (right) [4.65]

The transmitter electrodes are sequentially activated while all receiver electrodes are parallel sampled, in such a way, that an electrical property (conductivity or permittivity) of the fluid in each crossing point is evaluated. Based on those measurements the sensor is thus able to

determine instantaneous fluid distribution across the cross-section, for instance, of a pipe. The following pictures show the three-dimensional representation of a slug flow and the results of the visualization of different flow regimes of a air-water vertical flow.

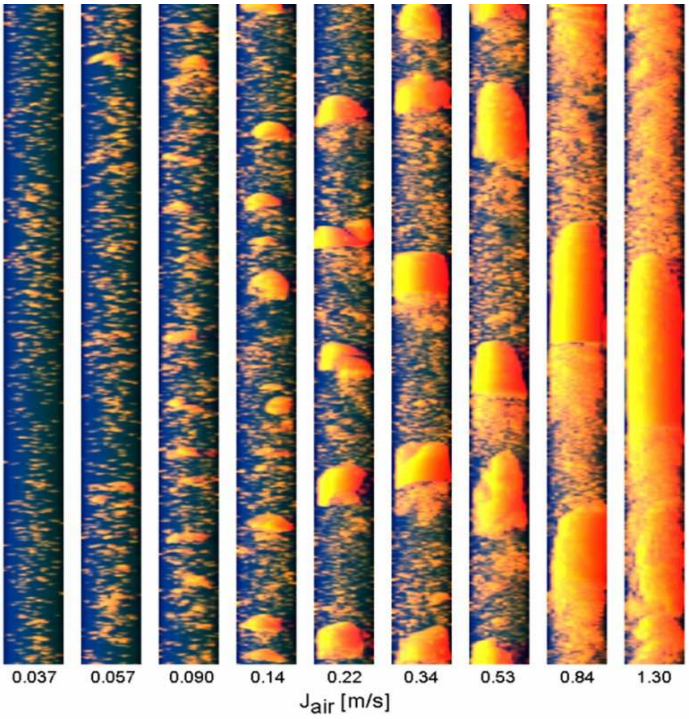

Fig.4.18: 3D-Visualization of data acquired with a wire-mesh sensor in a vertical test section of air-water flow at the TOPFLOW test facility [4.65]

Wire-mesh sensors can be manufactured depending on application requirements in diversity of different cross-section geometry and operating parameters. Newest wire-mesh sensors can be employed in a environmental conditions range of up to 286 °C and 70 bar [4.66]. Associated electronics for signal generation and data acquisition achieves a maximum temporal resolution of 10,000 Hz for the 16 x 16 wire mesh design and of 2500 Hz for the 64 x 64 wire mesh design.

Data processing

The data of a wire-mesh sensor consist of a time sequence of digitally codes conductivity values for each mesh point.
The sensor output is a 3-D matrix *V(i,j,k)* proportional to the local fluid conductivity. The indexes *i* and *j* refer to transmitting wires and to receiving wires respectively, while *k* is the time index. The first step of data processing is the determination of absolute conductivity values or alternatively an assignment of the relative conductivity values to the corresponding phase that is present in the flow.
The signal is normalized taking into account the single-phase reference matrix. The signal normalization can be considered as an approximation of the local void fraction value, if a linear relationship between conductivity and void fraction and a reference area equal to the square of the wire pitch p are assumed.

$$V^*(i,j,k)=\frac{V(i,j,k)-V_l(i,j)}{V_g(i,j)-V_l(i,j)} \tag{4.60}$$

where V_l and V_g are the time averaged values of the signals with the pipe filled with water or air at the beginning of the test.
The obtained result is the conductivity or phase distribution in the measurement plane at a contiguous sequence of temporal sampling points.
From the normalized signal the local instantaneous void fraction is derived taking into account the location of the wires with respect to the pipe. The points of the grid, that are located near the wall, are analyzed taken into account the wall influence, while the points, that are located outside the cross section of the pipe are excluded from the analysis; so the local instantaneous void fraction is calculated as:

$$\alpha(i,j,k)=\frac{V^*(i,j,k)-1}{a(i,j)}+1 \tag{4.61}$$

where *a(i,j)* is the geometrical weight factor, evaluated as s/p^2; where p^2 represents the reference area of each measurement point, and *s* is the fraction of the area that is inside the pipe cross section.
The value of *a(i,j)*, is equal to one if the reference area is totally inside the pipe area, while it is lower than one if the measuring point is located near the boundary, Fig.4.19.

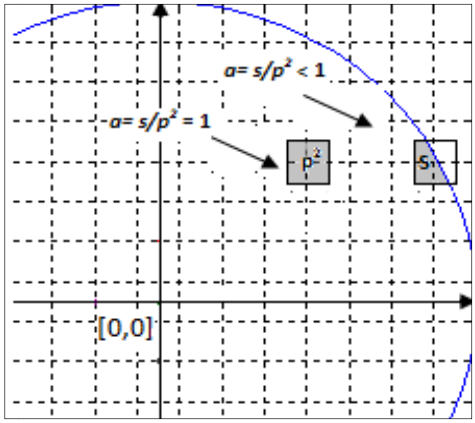

Fig.4.19: Reference area of the WMS measuring points

From the analysis of the time history of the local void fraction, many information can be extracted and used to characterize the flow.

Many flow parameters, such as gas volume fraction or bubble size distribution, are encoded in these data but must be extracted with appropriate processing algorithms (see [4.62] and [4.63]).
From data of gas-water two-phase flows it is possible to compute axial and radial gas fraction profiles and the integral gas fraction by proper integration of the gas fraction over certain cross-section areas.
For the determination of gas bubble size distributions from the raw data special data analysis algorithms were developed that can identify single bubbles by means of a filling algorithm

and compute volume and equivalent bubble diameters accordingly. Further, it is possible to measure the velocity distribution of the gas phase by the placement of two wire-mesh sensors with a small axial spacing in the flow. Since the conductivity distribution reaches the second sensor with only minor spatial structure modifications with a time shift that is determined by the flow velocity after having passed the first sensor, we can obtain the local velocity values within the measurement cross-section from a computational cross-correlation analysis of the two sensor signals.

The detailed analysis of the flow investigation by means of the WMS is reported in chapter 5.

Calibration

The linear dependence between the void fraction and the conductivity of the mixture needs the knowledge of two limit values: the conductivity as measured with the pipe filled with liquid only and the conductivity measured with the pipe filled with gas only. The liquid conductivity is dependent on the temperature and the temperature is varying during the transient experiment. It is therefore necessary to calibrate the instrument in order to take into account the changes in this limit value:

- It is possible to perform a calibration of the sensor reading for a completely filled pipe as a function of the water temperature. A fast thermocouple mounted close to the sensor is then necessary to provide the correction of the limit value.
- If there is a two-phase flow permanently present at each crossing point of the sensor, short-term PDFs (probability density functions) of the measured raw data can reveal the signal levels for liquid and gas without an explicit calibration. The position of the maxima in the PDF can be used as calibration values.

Accuracy

Errors of the wire-mesh sensor measurements for the gas fraction are mainly caused by the pitch of the wires and the distance of the wire planes.
Comparative measurements between the wire-mesh sensor and other research methods supplied information on the accuracy of the measurement technique and the evaluation algorithms for the experimental determination of these flow parameters. An air/water flow with gas volume fraction ranging from 0 to 100% shows that the deviations between wire-mesh sensor and gamma measurements are limited to ± 5% [4.62]. Comparative measurements between wire-mesh sensor and an X-ray tomography were also performed for air/water flow [4.67]. It was found that, the accuracy of the gas volume fraction averaged over the flow cross-section depends on the two-phase flow regime.
Differences in the absolute void fraction were determined for bubbly flows in the range of ± 1%, while a systematic underestimation of -4 % was observed for slug flows.

5. TWO-PHASE FLOW INVESTIGATION WITH WMS

5.1 Introduction

In a gas-liquid flow, since the interfaces are deformable, there are in principle infinite ways in which the two-phase can be distributed within the flow. Because the interface distribution depends on the mechanical and thermal dynamic equilibrium, the parameters that govern the occurrence of a given flow pattern are numerous: the most important ones are the phases superficial velocity and the fluid properties (density, viscosity, surface tension, etc.), the pipe geometry/inclination and the flow direction (upward, downward, co-current, counter-current).

One of the main features of horizontal pipe flow compared to vertical flows is the tendency to the flow stratification, due to the gravity force. The gas phase tends to migrate towards the upper part of the channel while the liquid flows rather in the lower part of the channel owing to density difference, regardless of the flow pattern. In horizontal gas-liquid flow the flow can be classified in four general flow patterns: stratified flow, bubble flow, slug/plug flow and annular flow. Each flow pattern can be also divided in sub-categories: stratified flow in smooth and wavy flow, intermittent flow in slug and plug flow and annular flow in smooth, wavy and mist flow.

Several experimental techniques have been proposed for the characterization of the flow patterns and for the measurement and modeling of the flow parameters [5.1]-[5.4]. One of the most import parameters that are used to characterize the two- phase flows is the void fraction, that is a dimensionless quantity indicating the fraction that is occupied by the gaseous phase, in a defined volume, or in the cross section, or in a defined line (chordal void fraction). The void fraction can also be evaluated as the instantaneous value or as an average value. The definition of the averaging time is not a trivial task and depends on the flow characteristic itself. The Wire-Mesh Sensors (WMS), based on the measurement of the local instantaneous conductivity of the two-phase mixture, are used for a high-speed visualization of a gas–liquid flow as well as for the measurement of void fraction profiles, bubble size

distributions and gas velocity distributions [5.5]-[5.8]. The WMS is able to measure directly the conductivity between pairs of crossing wires, so that the space and time resolution can be high. In the present work, the WMS has been used to investigate the air-water flow in a horizontal Plexiglas pipeline (D_i=19.5 mm), for several flow patterns. The local, chordal, cross-sectional void fraction are estimated from the sensor data. The flow evolution in time and space is analyzed and the characteristics for all the flow patterns are extracted by means of a statistical analysis. The dependence of the signals on the measured fluid dynamic quantities are discussed.

5.2 WMS geometry

The sensor used in the present work has been manufactured by Teletronic Rossendorf GmbH [5.10]. The sensor working principle is the measurement of the conductivity of the fluid. Because air and water have different electrical properties (water is highly conductive while air has a very low conductivity) the measurement of the conductance can be analyzed to detect the presence of each phase in the channel. The WMS (Fig.5.1) consists of two planes of parallel wire grids (16x16) that are placed across the channel at a short distance from each other (1.5 mm); the wires of both planes cross under an angle of 90°.

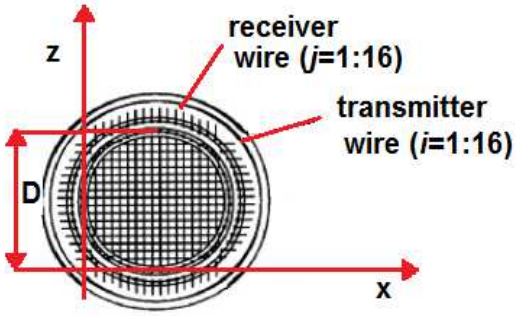

Fig.5.1: Scheme of the WMS

The sensor has been designed to cover the cross section of a channel having a 19.5 mm inner diameter; the wires have a diameter D_{wire} of 70 μm and a pitch p equal to 1.3 mm, so that only the 5.4% of the pipe section is occupied by the sensor. The measuring grid allows a spatial resolution of the order of the pitch length and it is possible to analyze the evolution of the investigated flow pattern, as the time resolution is rather high (up to 10000 frames/s).

5.3 Horizontal flow pattern characterization

The horizontal gas-liquid flow can be classified in four general flow structures: stratified flow, bubbly flow, slug/plug flow and annular flow. Each flow pattern can also be divided in sub-categories: stratified flow in smooth and wavy flow, intermittent flow in slug and plug flow and annular flow in smooth, wavy and mist flow. Analyzing the macroscopic structure of the flow, for different flow patterns, a characteristic shape of the void fraction vertical profile can be defined. The reference system is fixed in the bottom wall of the pipe with the coordinate z ranging from 0 to D, where D is the inner pipe diameter.

Stratified flow

A stratified flow is characterized by the complete separation of the two-phases in gas and liquid streams, due to gravity effects. Liquid tends to flow along the bottom of the tube and gas along the top part. From a qualitative point of view it is possible to distinguish three regions: liquid region, interface region and gas region. The amplitude of the interface regions and the relative void profile depend on the amplitude of disturbance waves.
The vertical chordal profile is given by:

$$V^*(i,j,k) = \begin{cases} 0 & z/D < h^* \\ 1 & z/D > h^* \end{cases} \qquad (5.1)$$

$h^* \pm \Delta h^*$ is the position of the interface, where the local void fraction ranges from 0 to 1.

Bubbly flow

This flow pattern is characterized by the flow of bubbles, having the reference length (d_b) much lower than the pipe diameter, dispersed in a continuous liquid phase. Due to the gravity effect, the bubbles tend to concentrate in the upper part of the pipe, so the local void fraction increases with z reaching the maximum in the upper half section of the pipe. If the bubble dimension is smaller than the distance between the measuring planes (1.5 mm), the local value of the void fraction is lower than one due to the simultaneous presence of gas and water in the measuring region. As the bubbles transit time is d_b/v_b (where v_b is the bubble velocity), the local void fraction changes with a frequency equal to the bubble frequency $f_b = d_b/v_b$.

Slug/Plug flow

The slug flow is characterized by a succession of slugs of liquids separated by large gas bubbles whose diameter approaches that of the pipe. The slug unit consists of the slug body, having a length L_s, and of a stratified region (or bubble region) having a length L_b. The slug body propagates along the pipe with a velocity v_s higher than the film velocity, producing an entrainment of gas from the film region to the slug body (aeration). As the structure of the slug flow is almost identical to that of plug flow, the two regimes are classified as a single flow pattern, and the flow is called "intermittent". For the slug / plug flow, due to the intrinsically intermittent nature of the flow, the modeling of the void fraction vertical profile requires consideration about the transit times and the shapes of slugs and plugs. Two profiles, related with the two characteristic times $\tau_s = L_s/v_s$, $\tau_b = L_b/v_b$, can be defined, considering that

$$\tau_{tot} = (\tau_s + \tau_b) = (L_s + L_b)/J_{tot} \qquad (5.2)$$

where J_{tot} is the total superficial velocity of the flow.

Annular flow

An annular flow is characterized by the presence of a continuous liquid film at the wall surrounded by a central gas core (gas continuous phase) containing a variable amount of entrained liquid droplets (liquid dispersed phase). The flow is symmetric with respect to the pipe vertical axis, while the liquid film strongly depends on the superficial velocity of the phases and is asymmetric due to the gravity effect in horizontal flow. Under the hypothesis of fully developed flow, it is theoretically possible to define the liquid film region, the interface region and the core region. The void fraction in the core region can be different from one, depending on the reached equilibrium between the drops entrainment and deposition rate.

5.4 Experimental facility and test matrix

The experimental facility consists of the feed water loop (tap water with conductivity of about 620 μS is used), the feed air loop and the test section. The liquid flow rate is measured by means of an electromagnetic flow meter in a range of 0.9-36 m^3/h with a ±0.5% r.v. accuracy value. Lower values of the water flow rate are measured by means of rotameters in the ranges of 0-100 l/h and 100-400 l/h with an accuracy value of ±2% r.v.. The air flow rate is measured by means of different rotameters for the different ranges (100-500 Nl/h, 1000-5000 Nl/h and 6300-63000 Nl/h) with a ±2% f.s.v. accuracy value.
A pressure gauge and a thermocouple near the flow meter allow for the correction of flow meter readings to compensate for variation in air density and for the calculation of the mass flow rate entering the test section.
The standard volumetric flow rate is evaluated by eq.5.3.

$$Q(p_0,T_0) = Q_{ASA}(p,T)\sqrt{\frac{p}{p_0}\frac{T_0}{T}} \qquad (5.3)$$

Where p_0 and T_0 refer to standard conditions.
The mass flow rate is then calculated using the air density (evaluated under Standard Conditions).
The test section consists of a 19.5 mm diameter and 7 m long pipe. The WMS is installed at L/D = 192 from the entrance, between two Plexiglas pipes having a length of 600 mm.

In the present tests the liquid flow rate W_l ranges from 0.0056 kg/s to 0.78 kg/s while the air flow rate W_g ranges from 0.083 g/s to 22.5 g/s; the flow quality ranges from 0 to 0.73 and the superficial velocity ranges from 0.15 to 31.94 m/s for air and from 0.019 to 2.62 m/s for water; the pressure ranges from atmospheric pressure to 3.7 bar. The temperature is equal to 20 ± 2°C. The comparison between the observed flow patterns and the prediction by the Baker's [5.14] is reported in Fig.5.3, while the comparison with the Mandhane's map [5.15] prediction is shown in Fig.5.3. The test flows are identified by the phases mass fluxes ($G_g = W_g/A$, $G_l = W_l/A$, where A is the pipe cross section) and superficial velocities (J_g , J_l).

The flow is discharged at atmospheric pressure. The experimental test section is equipped with two quick closing valves (QCV) that allow the measurement of the volumetric void fraction in a length of 1300 mm.

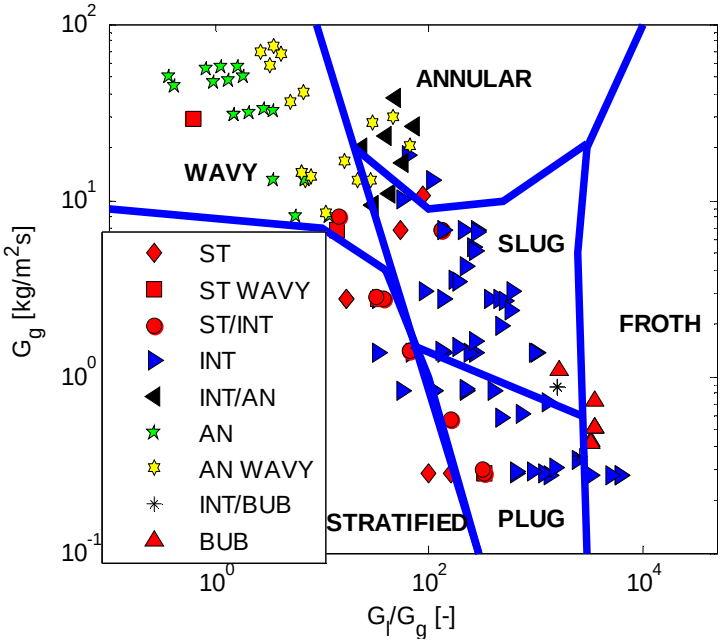

Fig.5.2: Comparison between Baker's Map flow patterns prediction and present observations. Legend: ST=Stratified, INT=Intermittent, AN=Annular, BUB=Bubble

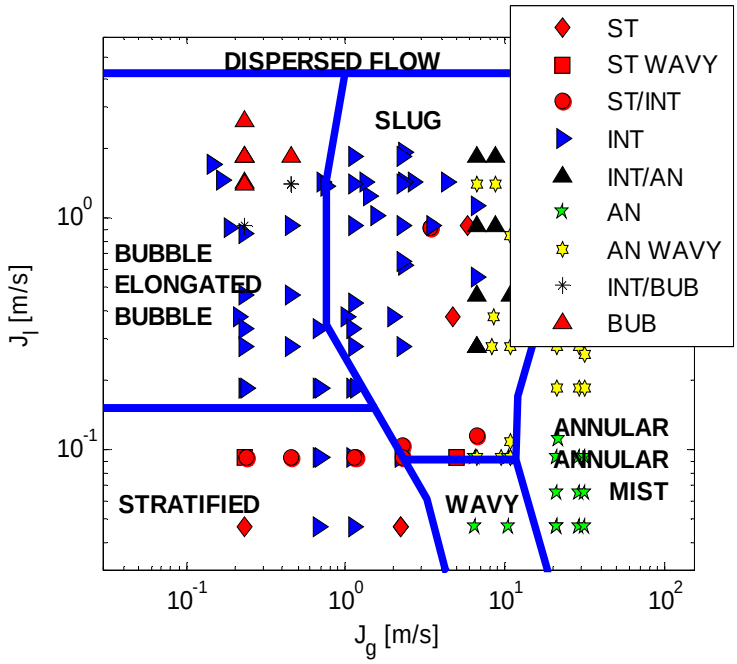

Fig.5.3: Comparison between Mandhane's Map flow patterns prediction and present observations. Legend: ST=Stratified, INT=Intermittent, AN=Annular, BUB=Bubble

In Fig.5.2 and Fig.5.3, the legend represents the classification of the flow performed by visual observation:

- the annular wavy (AN WAVY) and the stratified wavy (ST WAVY) flows identify flow characterized by a wavy interface compared with annular (AN) or stratified (ST) flows characterized by a flat interface.
- ST/INT is used for the flows in which the flow pattern is stratified but the liquid waves start to evolve in slugs increasing their amplitude;
- INT/AN is used for the intermittent annular flow; the flow is pulsed but the liquid phase is distributed along the pipe wall in a wavy film;
- INT/BUB is used for the intermittent bubbly flow; the flow is pulsed but the dimension of the bubbles is much lower than the pipe diameter; the gas phase is dispersed (non homogenously) in the continuous liquid phase.

5.5 Experimental methodology and signal processing

The WMS sensor signals are acquired by means of WMS200 electronics and processed in Matlab® environment. The output *V(i,j,k)*, is a 3-D matrix of digital signals proportional to the local fluid conductivity. Starting from the reference instruments equations, described in 4.6.5, the developed signal processing scheme has been structured in order to obtain the desired two-phase flow parameters. First of all the signal is normalized taken into account the single-phase reference matrix. The normalized time history signal of each mesh point is calculated by means of eq. 4.61

A fundamental task for the flow analysis is then the choice of the signal acquisition frequency and of the observation time. A high acquisition frequency allows the detection of fast phenomena while a long observation time allows us to detect slow phenomena. For flow pattern classification analysis, we focus the attention on the macroscopic flow objects (plug, slug, bubbles, droplets, waves, etc..) having a length L_o, that propagate along the pipe with a velocity v_o, and with a sensor observation time $\tau_o = L_o / v_o$.
At the first step, the local time series void fraction at each measuring point (i,j) is analyzed by means of normalized histograms.
The local instantaneous void fraction α has been obtained with an acquisition frequency f_{acq} equal to 1250 Hz for a total observation time T_T equal to 20 s, so that the value of k ranges from 1 to k_T, where k_T is the total number of measured frames, that can be expressed by the eq.

$$k_T = f_{acq} \cdot T_T \tag{5. 4}$$

and the corresponding time is

$$t = k \cdot \frac{T_T}{k_t} \tag{5. 5}$$

The selected acquisition frequency (1250 Hz) is sufficient to detect and characterize objects having a minimum space length equal to

$$L_{\min} = \frac{2u_{\max}}{f_{acq}} \tag{5. 6}$$

As the flow velocity *u* ranges from 0.26 m/s to 32 m/s, the minimum length at lower velocity is of the order of 0.5 mm, while at higher velocity is of the order of 50 mm. In the present study, the flow is characterized in terms of macroscopic phenomena, that can be considered as deterministic ones, while the microscopic phenomena are considered as stochastic phenomena and are evaluated by means of a statistical analysis. The selected observation period (20 s) allows the analysis of phenomena having a characteristic frequency higher than 0.1 Hz.

5.5.1 Time average local void fraction

The signal normalization can be considered as an approximation of the local void fraction value, if a linear relationship between conductivity and void fraction and a reference area equal to the square of the wire pitch *p* are assumed. The mesh points near the pipe wall refer to a fraction of the square section area. A matrix of weight, *a(i,j)*, takes into account the reference area: associating at each crossing point the square section equal to p^2 (where *p* is the 1.3 mm pitch), the weight is evaluated as one if the reference area of the point is inside the pipe cross section and as s/p^2 (*s* is the fraction of the area inside the pipe) if a portion, or the total of the reference area of the point is outside [4.62].
Then the local instantaneous void fraction is derived from eq. 4.61.
From the time history of the local void fraction the time average value $\alpha(i,j)$) and the variance σ_α *(i,j)* are calculated as:

$$\alpha(i,j) = \frac{1}{k_T} \cdot \sum_{k=1}^{k_T} \alpha(i,j,k) \tag{5. 7}$$

$$\sigma_a(i,j) = \left[\frac{1}{k_T} \cdot \sum_{k=1}^{k_T} (\alpha(i,j,k) - \alpha(i,j))^2 \right]^{1/2} \tag{5. 8}$$

The standard deviation distribution analysis is used to derive the amplitude of the interface oscillations in stratified flow. In slug flow the variance distribution allows one to obtain information concerning the amplitude and the frequency of the pulsating flow.

Finally the average cross-section value $\alpha(k)$, is calculated as:

$$\alpha(k) = \frac{1}{\sum_{i=1}^{16}\sum_{j=1}^{16} a(i,j)} \cdot \sum_{i=1}^{16}\sum_{j=1}^{16} \alpha(i,j,k) \cdot a(i,j) \tag{5. 9}$$

The time history of the average void fraction is characterized by the time standard deviation and by the normalized histograms.

5.5.2 Time history analysis

From the evaluated local void fraction, the instantaneous chordal profiles are derived in order to analyze the time evolution of the phases distribution. The vertical profiles in the center line of the pipe (index j=8) are used to evaluate the characteristic times and the characteristic shape of the void fraction profiles for the different flow conditions.

In the most general case, the local void fraction can be considered as the sum of two components: deterministic and stochastic.
The deterministic component is representative of the time evolution of the macroscopic structures of the flow, while the stochastic component represents the random fluctuation of the parameter and it is characterized by the related standard deviation. The local void fraction in each point of the sensor grid has been characterized by the signal histogram.

The histograms are obtained by using a number of groups given by the Kendal-Stuart [5.11] grouping guide and give information about the probability density function (PDF) of the local void fraction.
The analysis of the normalized histograms, that are evaluated for each measuring point and for the total observation time, allows us to define if a deterministic or a stochastic behavior characterizes the flow.
In Fig.5.4 the normalized histograms along the central chord (j=8) are shown at three different flow velocities. The ratio J_g/J_l is $9\cdot10^{-2}$, 1.18 and 122 for the case (a), (b) and (c) respectively. Depending on the phases velocity combination, the flow assumes a stochastic behavior (Fig.5.4 (a-c)) or a deterministic behavior (Fig.5.4 (b)). In Tab.5.1 the corresponding local mean void fraction values and the parameter σ/α_{mean}, where σ is the standard deviation of the signal and α_{mean} is the average void fraction, are shown; the parameter σ/α_{mean} is an index of the fluctuation of the signal. If a stochastic behavior is observed the mean value of the void fraction can be considered as representative of the flow, while in case of deterministic behavior further analysis is required.

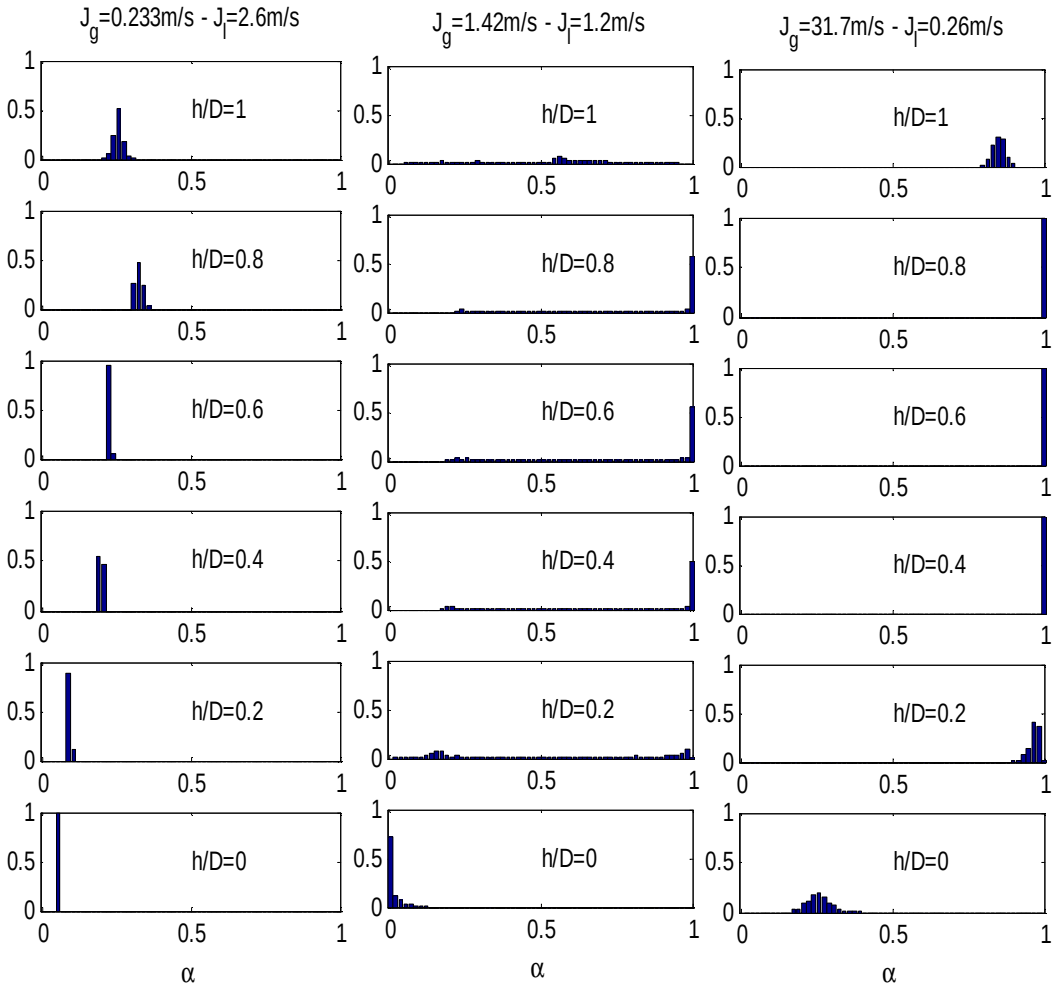

Fig.5.4: Normalized histograms along *j*=8 at different flow velocities.

	(a) J_g **= 0.23 m/s-** J_l **= 2.6 m/s**		**(b)** J_g **= 1.42 m/s-** J_l **= 1.2 m/s**		**(c)** J_g **= 31.7m/s -** J_l **= 0.26 m/s**	
h/D	α_{mean}	σ/α_{mean}	α_{mean}	σ/α_{mean}	α_{mean}	σ/α_{mean}
0	0.051	0.02	0.0126	1.76	0.256	0.156
0.2	0.089	0.043	0.535	0.643	0.966	0.016
0.4	0.195	0.024	0.766	0.391	0.997	0.001
0.6	0.224	0.011	0.804	0.353	0.999	0.0002
0.8	0.322	0.038	0.819	0.318	0.998	0
1	0.252	0.057	0.524	0.455	0.851	0.023

Tab.5.1: Local average void fraction and standard deviation values along *j*=8 at different flow velocities

For non intermittent flows, the standard deviation value of the local void fraction is small, and the flow can be characterized with a unique void fraction profile.

If the normalized histogram is not a Gaussian curve and a quasi periodic behavior is observed for the macroscopic structures of the flow, the characteristic times and the

characteristic profiles have to be derived. The analysis of the histograms and of the parameter σ/α_{mean} have been analyzed for different flow conditions as reported in reference [5.18].

In order to analyze the time evolution of the flow (and the related void fraction profiles) in terms of deterministic component, a moving average of the void fraction time values has been performed using a time interval τ. The correct time interval depends on the flow conditions, and it is chosen in such a way to obtain a Gaussian distribution of the void fraction fluctuations. In the present work, a value of the moving average time τ equal to 0.4 s has been chosen, in order to have, with the acquisition frequency of 1250 Hz, a representative sample of the void fraction and the required Gaussian distribution of the fluctuations.

Once the average time interval is defined, every average profile has been characterized from the statistical point of view by the root mean square profiles and the variation in time of the chordal profile has been analyzed considering the evolution of the parameter *M(t)*, that is defined as the sum along the chord of the difference between the moving average local void fraction evaluated at the time *t* and at the time *t*-Δt:

$$M(t) = \sum_{i=1}^{16} \left(< \alpha(i, j, t) > - < \alpha(i, j, t - \Delta t) > \right) \tag{5. 10}$$

where the corresponding time *t* is

$$t = \frac{k}{f_{acq}} \tag{5. 11}$$

and Δt is equal to $1/f_{acq}$.

M(t) is an indicator function, used to evaluate the void fraction profile distortion between two different times, *t*-Δt and *t*, at different flow conditions (J_g, J_l).
For a void fraction profile constant in time, characterized by null stochastic fluctuations, the function *M(t)* is equal to zero. If the stochastic component is not zero but it is distributed homogenously along the analyzed chord, it is observed that the local histograms are centered on the mean local value of the void fraction, and the mean values evaluated at the time *t*-Δt and at the time *t* are characterized by a difference equal or lower than σ. If the value of the standard deviation is small the void fraction chordal profile is characterized by small time distortions and the flow can be classified steady state.

In such condition the maximum value of *M(t)*, evaluated using the eq. 5.10, can assume a maximum value equal to 16σ. For the water and air single-phase flow the local value of the standard deviation was about 0.006; for this condition the standard deviation value represents the noise of the WMS signal acquisition chain. So that the maximum value of the *M(t)* in steady state conditions is evaluated of the order of 16*0.006= 0.096. Considering this reference value, the threshold for the classification of the two-phase flow void fraction profile has been selected equal to 0.1.

Higher values of *M(t)* are observed when the local void fraction (evaluated as the mean value in the time interval Δt) is characterized by sharp variations along the analyzed chord.
Starting from the evolution in time of the *M(t)* parameter it is possible to determine the time interval in which the profile is constant and the time interval in which is changing.
The analysis of this function allows the identification of the characteristic times of the flow and of the void fraction profiles that characterize the flow. The chordal profiles at the chosen time are then analyzed and used to characterize the flow pattern in terms of time evolution and characteristic shape and parameters. This methodology allows us to recognize the flow pattern in those conditions in which the direct observation is not possible and the flow velocities are unknown, by characterizing the flow and defining the shape of the void fraction profiles and their evolution in time.

5.6 Results: average cross-sectional void fraction

The average void fraction for each run is evaluated by using the eq. 5.7 and is compared with the volumetric void fraction that is measured by the quick closing valves (QCV) method; because of the intermittence of the flow the void fraction measurement by QCV method is repeated several times for each flow rates combination in order to get a representative mean value. Fig.5.5 presents the comparison of the measured void fraction as a function of the experimental flow quality between the QCV and WMS methods. Compared to the QCV void fraction, the WMS void fraction shows a higher dispersion in the range of intermittent flow and it is in good agreement at very high void fraction when the flow becomes annular. Moreover the WMS gives lower values of void fraction at flow quality higher than 0.01 and higher values at flow quality lower than 0.001. It must be observed also that the volumetric void fraction is an average value along the test section; it is measured at the entrance of the test section, where the flow is not completely developed and the effect of L/D is fundamental to characterize the flow [5.12]-[5.13].

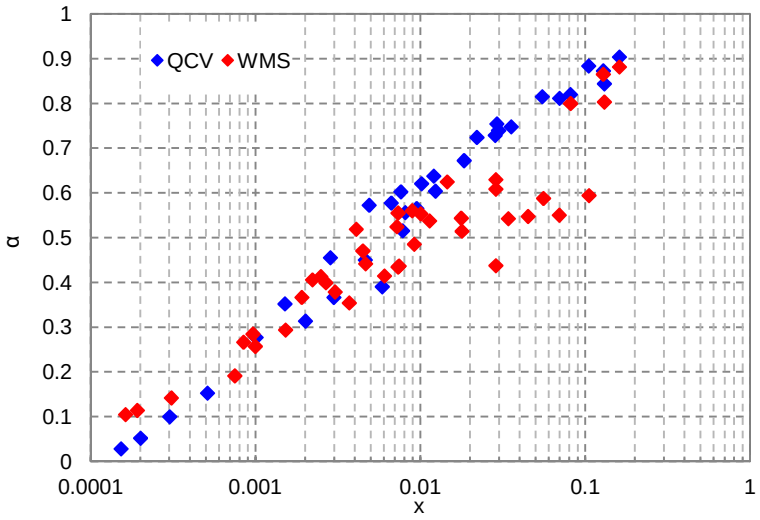

Fig.5.5: Average void fraction measured using the QCV method and the WMS method

5.7 Results: average cross-sectional void fraction time analysis

As shown in Fig.5.6, Fig.5.7 and Fig.5.8, the time evolution of the mean cross-sectional void fraction has been analyzed by means of the normalize histograms and by means of the frequency analysis.

In Fig.5.6 the average cross-section void fraction time evolution is presented for five different two-phase flow conditions. From the comparison of the flow evolution at different superficial velocity different regimes can be identified. Fig.5.6 (a) shows the average cross section void fraction for stratified flow: a constant value of the void fraction is not reached due to interface wave oscillations.
By increasing the phases mass flow rate the flow becomes intermittent. As shown in Fig.5.6 (b), (c) and (d) several sub-regimes can be distinguished depending on the superficial velocity of the liquid and gas phase.
A typical slug unit, according to [5.3], consists of a liquid slug zone of length L_s and an elongated bubble zone of length L_f. with a liquid film under the long gas bubbles (stratified zone): because of the velocity of slugs two transit times $\tau_s=L_s/v_s$ and $\tau_f=L_f/v_f$ are defined. In Fig.5.6 (b) many features of other flow regimes are shown: aerated slugs can be observed, small bubbles in the wavy liquid layer at the bottom of the tube and dispersed water droplets in the gas phase appear.
At higher superficial gas velocities, Fig.5.6 (c), the flow pattern is identifiable as slug flow: the time evolution is characterized by elongated liquid slugs and stratified flow zones with low interface oscillations. By increasing the gas flow rate, the frequency of the slugs strongly increases, as shown in Fig.5.6 (d). This flow regime is more turbulent than the elongated bubble flow regime: the slugs increase in velocity and become shorter. At air superficial velocities higher than 3 m/s the liquid flow tends to produce a very thin film also in the upper wall, while the interface in the lower part of the cross-section becomes strongly wavy and the flow having these characteristic can be classified as annular-wavy.

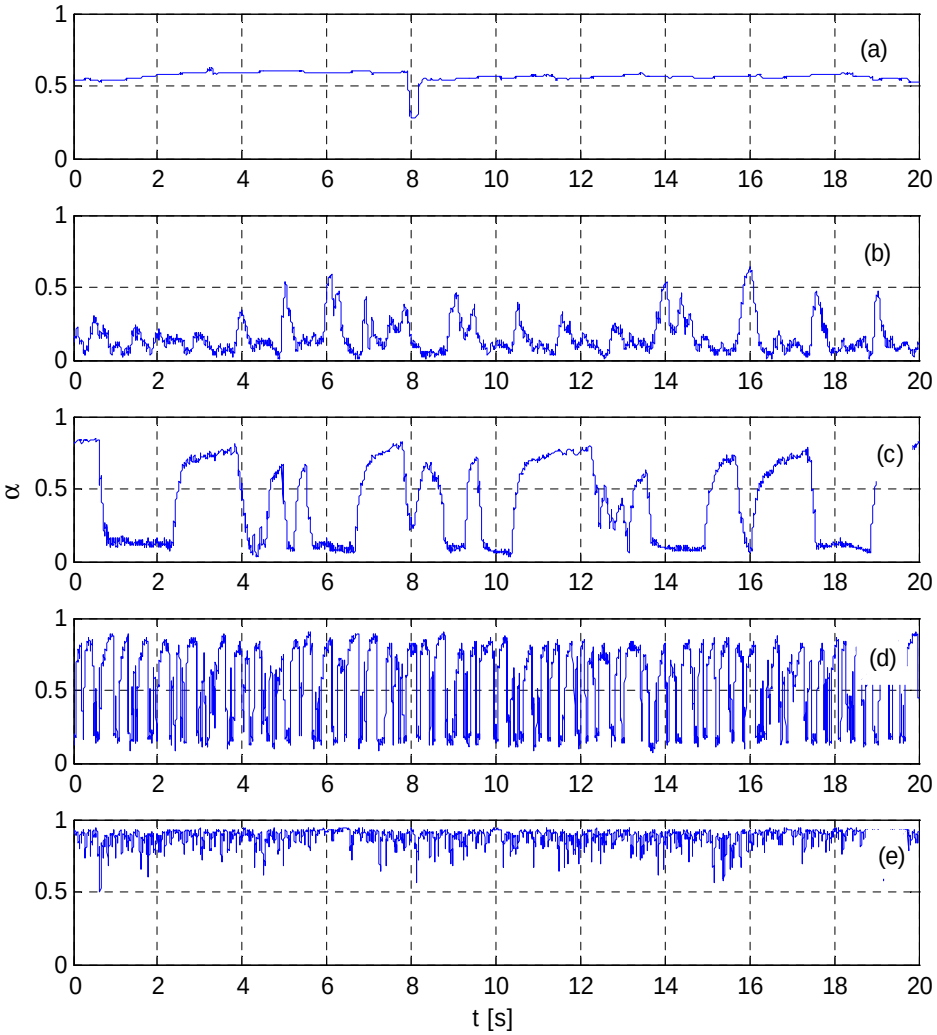

Fig.5.6: Time evolution of the average cross-section void fraction. (a): Jg = 0.23 m/s, Jl = 0.05 m/s, (b): Jg = 0.14 m/s, Jl = 1.71 m/s, (c): Jg = 0.71 m/s, Jl = 1.42 m/s, (d): Jg = 1.33 m/s, Jl = 1.42 m/s, (e): Jg = 10.5 m/s, Jl = 0.05 m/s

For lower air and water velocities, Fig.5.7 (a), the normalized histogram is a distorted unimodal function centered in the mean void fraction value; for intermittent flow, Fig.5.7 (c), the normalized histogram is clearly a bimodal function with the two maximum at very low (0.1) and high (0.7) void fraction; the lower void fraction values are still the most expected value.

For the flow conditions of Fig.5.7 (d) the normalized histogram is still a bimodal function, but in this case the expected value of the void fraction is 0.8: the annular-wavy flow, is determined by a function shaped as unimodal with the maximum probability at very high void fraction ($\alpha > 0.9$).

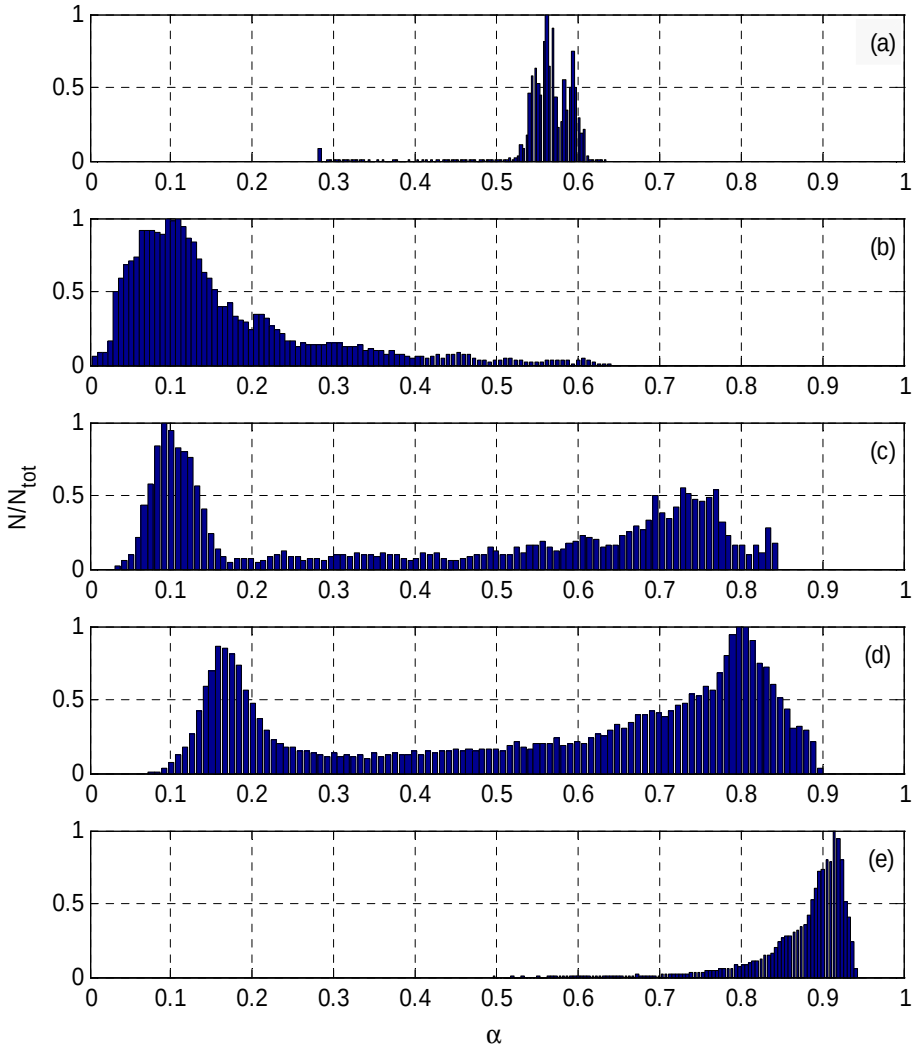

Fig.5.7: Histogram of the average cross-section void fraction. (a): J_g = 0.23 m/s, J_l = 0.05 m/s, (b): J_g = 0.14 m/s, J_l = 1.71 m/s, (c): Jg = 0.71 m/s, J_l = 1.42 m/s, (d): J_g = 1.33 m/s, J_l = 1.42 m/s, (e): J_g = 10.5 m/s, J_l = 0.05 m/s

The Fast Fourier Transform (FFT) MATLAB® algorithm has been used to extract the signal ampitude at different frequencies, as shown in Fig.5.8.
The analysis allows the identification of the characteristic spectrum for the different flows: (a) and (e) diagrams corresponding to bubbly and annular flow respectively, are characterized by a flat spectrum, while for intermittent flows, such as (c) and (d) diagrams, one or more characteristic frequency can be identified.

The performed analysis showed that the mean cross-sectional void fraction can be used to classify the flow pattern in a rather objective way by means of the normalized histogram and the frequency spectrum analysis, but is not sufficient to investigate the internal structure and the phases distribution.

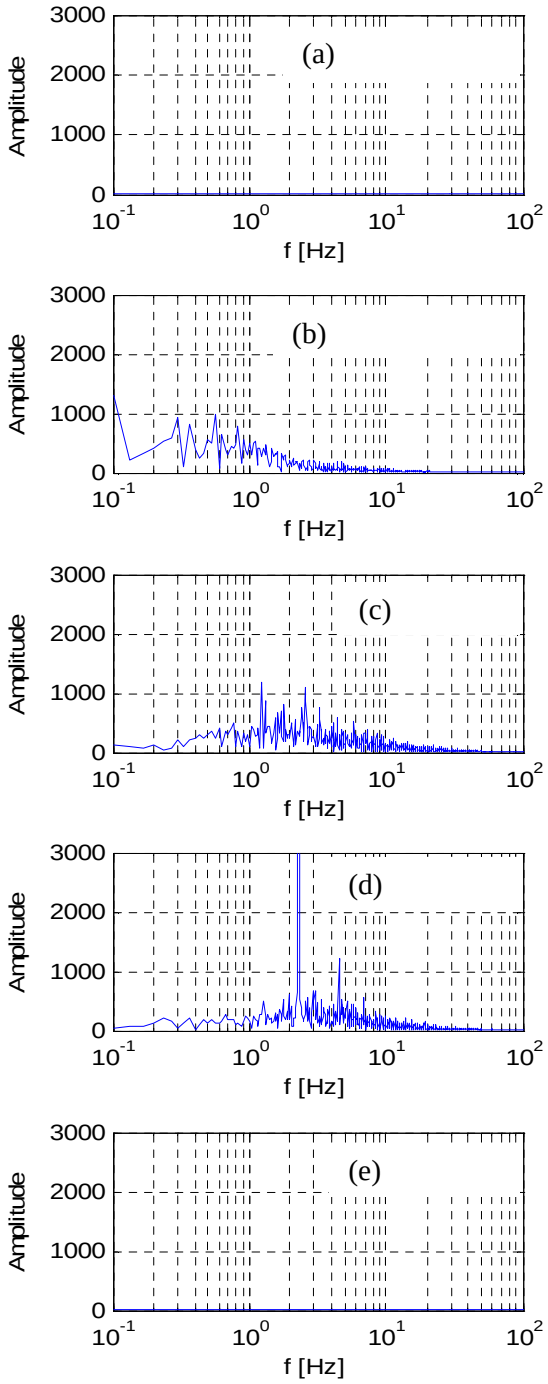

Fig.5.8: Frequency analysis of the average cross-section void fraction. (a): Jg = 0.23 m/s, Jl = 0.05 m/s, (b): Jg = 0.14 m/s, Jl = 1.71 m/s, (c): Jg = 0.71 m/s, Jl = 1.42 m/s, (d): Jg = 1.33 m/s, Jl = 1.42 m/s, (e): Jg = 10.5 m/s, Jl = 0.05 m/s

5.8 Results: *M(t)* time history and flow classification

The void profiles corresponding to *j=8* are reported for selected cases in order to evaluate the influence of the phases velocity during the time flow evolution and the phases distribution.

To obtain a characteristic shape of the flow that can be related to the superficial flow velocity the moving average profiles have been evaluated.
In Fig.5.9 the time evolution of the parameter *M(t)* is plotted for different air and water superficial velocities. The optimum time interval, used for the moving average profiles, has been chosen as the minimum averaging time, that allows us to maximize the time period in which *M(t)* is zero. The time history of *M(t)* is strongly dependent on the superficial velocities for both frequency and amplitude, so it is possible to extract the profiles that characterize the flow for different time periods.
If the amplitude is lower than a threshold value the flow can be characterized by the mean profile and the correspondent standard deviation (Fig.5.9 (a)), and it is classified as "non intermittent" or "non periodic profile" flow; while for higher amplitudes (*M(t)* higher than 0.1 in absolute value, as it has been shown in paragraph 5.5.2, a number of profiles depending on the time history have to be analyzed. In this case the flow evolution can be divided in two categories, namely "quasi periodic profile" (Fig.5.9 (b)) , and "non periodic profile with high noise" (Fig.5.9 (c)): the profile is classified as "quasi periodic" if there is a time period in which the profile doesn't change significantly, while it is classified as "non periodic high noise" if the absolute value of *M(t)* is higher than the threshold value and the local flow is characterized by a chaotic behavior. For the "high noise" profile, in which the value of the *M(t)* is continuously changing, the time evolution is characterized by the mean profile, that is evaluated adopting the observation time of 20 s, and by the relative standard deviation.
For the "quasi periodic" profile at least two characteristic profiles with the related times are derived considering the time periods in which *M(t)* is near zero and the time periods in which the flow is evolving and *M(t)* is higher than zero.

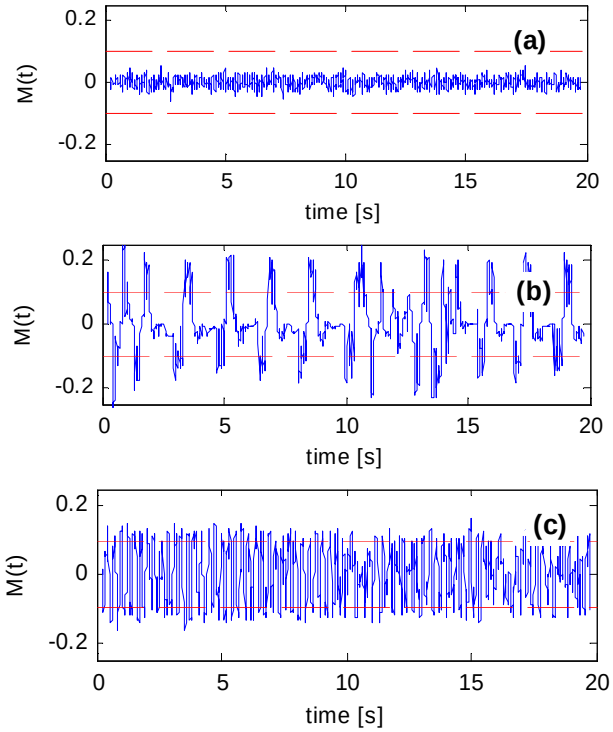

Fig.5.9: *M(t)* time evolution at j=8. (a) J_g =0.23 m/s - J_l=1.86 m/s, (b) J_g =2.26 m/s - J_l =0.65 m/s, (c) J_g =8.73 m/s - J_l =1.86 m/s

For classification purpose and considering the time interval that has been adopted to perform the moving average, the limit value has been chosen of the order of 0.5 s: the profile is considered as "quasi periodic" if the profile doesn't change significantly for a period higher than 0.5 s. If the water superficial velocity (J_l) is lower than 0.5 m/s and the air superficial velocity (J_g) is lower than 10 m/s the profile evolution is characterized by a quasi periodic behavior; if the air velocity is increased up to values higher than 10 m/s and the water velocity values are lower than 0.5 m/s, the amplitudes related to the profile change evolution parameters are lower than the threshold value and then the flow can be characterized by a single profile shape. If the value of the air velocity is lower than 10 m/s and the water velocity is higher than 0.5 m/s the evolution of the parameter *M(t)* is characterized by a high noise and by an amplitude higher than the threshold value; but for further increase of the water velocity the amplitude tends to decrease and an amplitude lower than 0.1 has been detected for water superficial velocities higher than 1.4 m/s and air superficial velocities lower than 0.5 m/s.
In Fig.5.10 the classification of the void fraction profile time behavior is shown in the Mandhane's map.

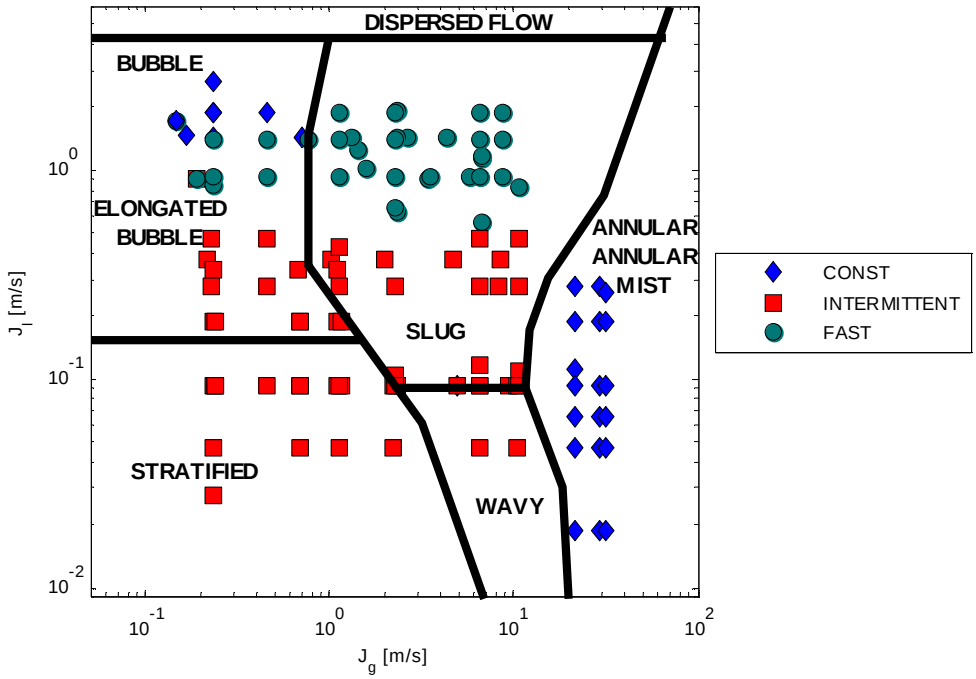

Fig.5.10: Flow characterization results compared with the Mandhane's Map [5.15] flow pattern classification

The characteristics of the flow, that have been identified by means of the analysis of the *M(t)* time evolution, are in good agreement with the flow pattern classification performed by Mandhane [5.15]. Moreover the analysis of *M(t)* gives relevant information concerning the time evolution of the void fraction profiles.

5.9 Results: analysis of the void fraction profiles

From the analysis of the parameter *M(t)* time evolution, the flow characteristic profiles are derived and qualified in terms of shape and flow parameters. In Fig.5.11 the characteristic void fraction chordal profile is shown for two different flows, that are characterized by low amplitude values of *M(t)*. In Fig.5.11 (a) the typical profile of a horizontal bubbly flow is shown, while in Fig.5.11 (b) the flow can be classified as annular. All the profiles are evaluated at *j*=8.

Considering the flow of Fig.5.11 (a), the parameters that have to be defined in order to classify it are: the height of the stratified region, the mean value of the void fraction in the bubbles region, the mean value of the void fraction and the related standard deviation in the stratified region, and finally the mean value of the void fraction in the upper part of the pipe, that is close to the wall. In order to characterize the annular flow the parameters like the liquid film thickness, the interface position, the average void fraction in the core region can be derived from the void fraction profile (Fig.5.11 (b)).

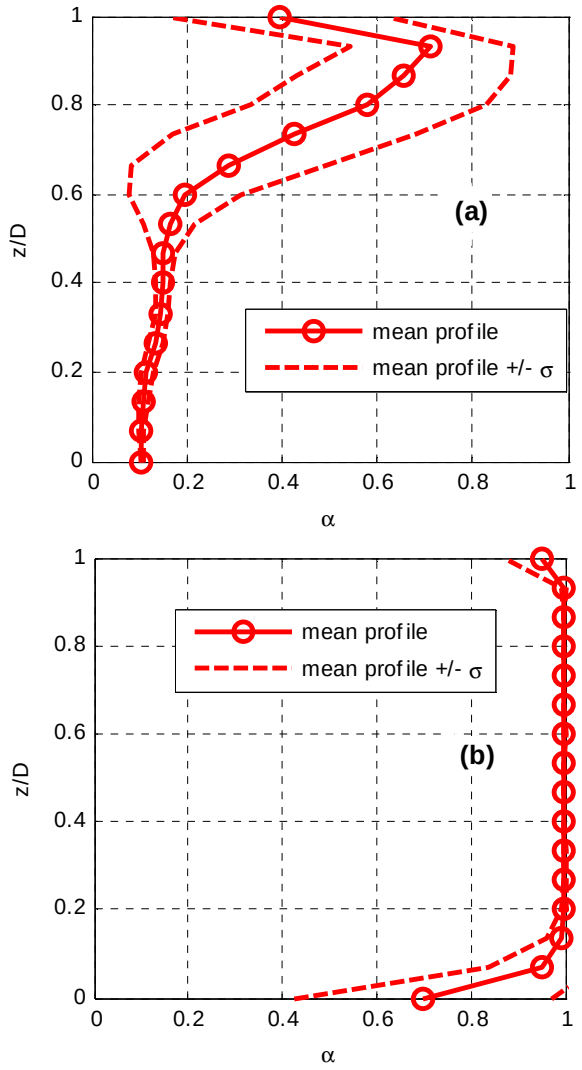

Fig.5.11: Characteristic void fraction chordal profile for non-intermittent flows. (a) J_g =0.23 m/s – J_l =1.86 m/s, (b) J_g=29.3 m/s – J_l =0.05 m/s

The frequency spectrum of the flow classified also as “non periodic with low noise”, that is evaluated in points of the grid that are representative of the flow (Fig.5.12), shows that the energy of the signal is different along the chord, but a predominant characteristic frequency is not observed.

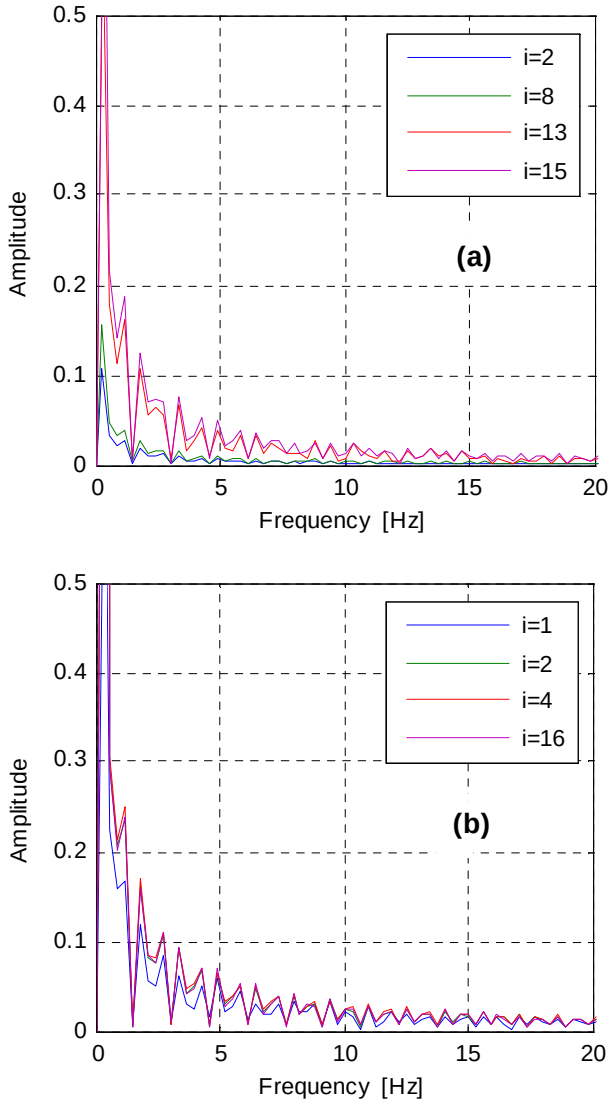

Fig.5.12: Frequency spectrum for non-intermittent flows. (a) J_g=0.23 m/s – J_l =1.86 m/s, (b) J_g=29.3 m/s – J_l=0.05 m/s

If the flow is fast intermittent or “non periodic with high noise” (Fig.5.13) the stochastic/deterministic behavior of the profile change is analyzed by means of the probability density function in each measuring point of the chord: the mean profile, the standard deviation profile and the time period are derived. Then the profile is characterized in terms of shape parameters and in terms of their oscillation amplitudes. The characteristic profile is calculated as the mean time profile (Fig.5.13).

For flow classified as “non periodic with high noise”, the frequency spectrum shows the presence of characteristic frequencies in the range between 20 and 40 Hz as in the case that is analyzed in Fig.5.14.

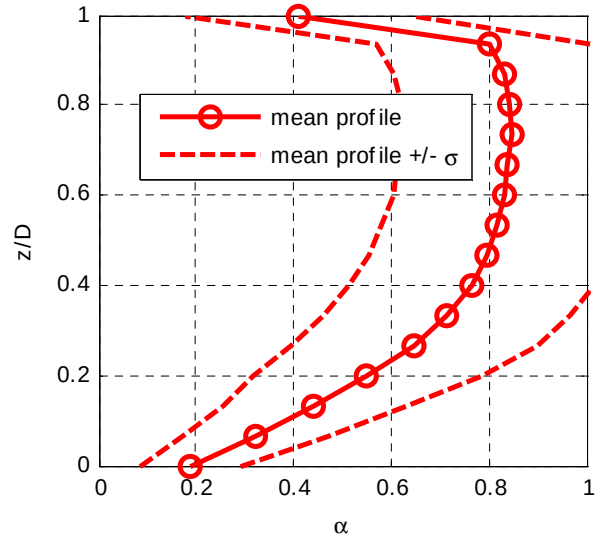

Fig.5.13: Void fraction profile analysis for “non periodic with high noise” flow at Jl =1.86 m/s - Jg =8.73 m/s

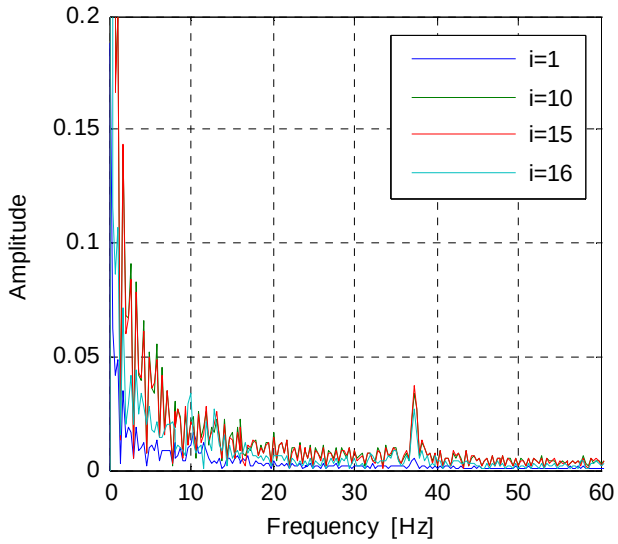

Fig.5.14: Frequency spectrum for Jl =1.86 m/s - Jg =8.73 m/s

If the flow is classified as “quasi-periodic” (Fig.5.15), the profile evolution during the two characteristic periods (absolute value of *M(t)* higher than zero or near zero) is analyzed. The changing profile period is analyzed, in terms of profile evolution (profiles at *M(t)* min and max and corresponding times), while the mean profile and the variation amplitude are used for the second period. The flow is then described at least by two characteristic profiles and by the characteristic time of each one. This flow is typical of intermittent flows, such as slug flow. The red line (diamonds) refers to the slug region profile, while the blue line (circles)

refers to the bubble region profile of the slug unit; the dashed lines represent the ($\alpha_{mean} \pm \sigma$) profile; in Fig.5.15 it is also reported the slug and bubble total residence time.
The characteristic frequencies are in the range from 0 to 20 Hz, as it is shown in Fig.5.16.

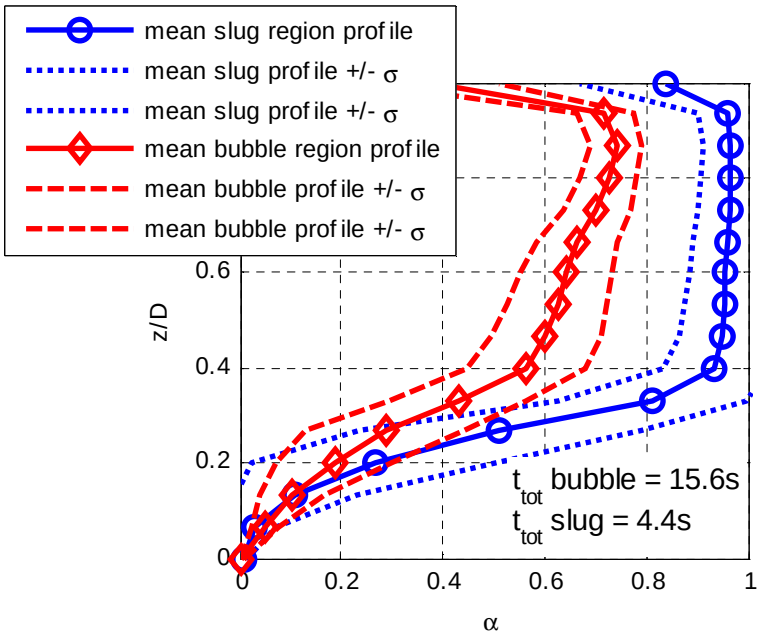

Fig.5.15: Void fraction profile analysis for the "quasi periodic" flows at Jl =0.65 m/s - Jg =2.26 m/s

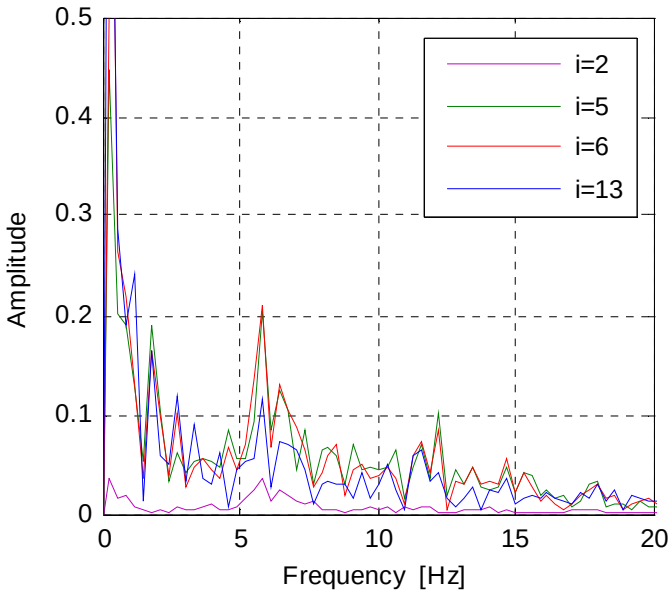

Fig.5.16: Frequency spectrum for Jl =0.65 m/s - Jg =2.26 m/s

5.10 Results: void fraction profile shape dependence on the phases velocity

In the following figures the dependence of the void fraction profile shape (at *j*=8) on the phases velocity is analyzed for the flows that are classified as "quasi periodic": two characteristic void fraction profiles, corresponding to the slug and bubble regions, are analyzed as a function of the ratio J_g/J_l (Fig.5.17). Concerning the slug region profiles, the effect of the liquid velocity increase is the reduction of the peak of the void fraction profile, and the tendency to a more homogeneous chordal profile, while the effect of the air rate increase is the reduction of the stratified region thickness due to the entrainment of bubbles within the upper region. The bubble region is characterized by a stratified liquid thickness that decreases by increasing the air velocity; a thin liquid film in the upper region of the channel with a thickness that increases with the liquid flow rate is detected by the sensor. The value of the void fraction in the bubble region approaches unity at the lowest water velocities, but tends to decrease at water velocity higher than 0.8 m/s.

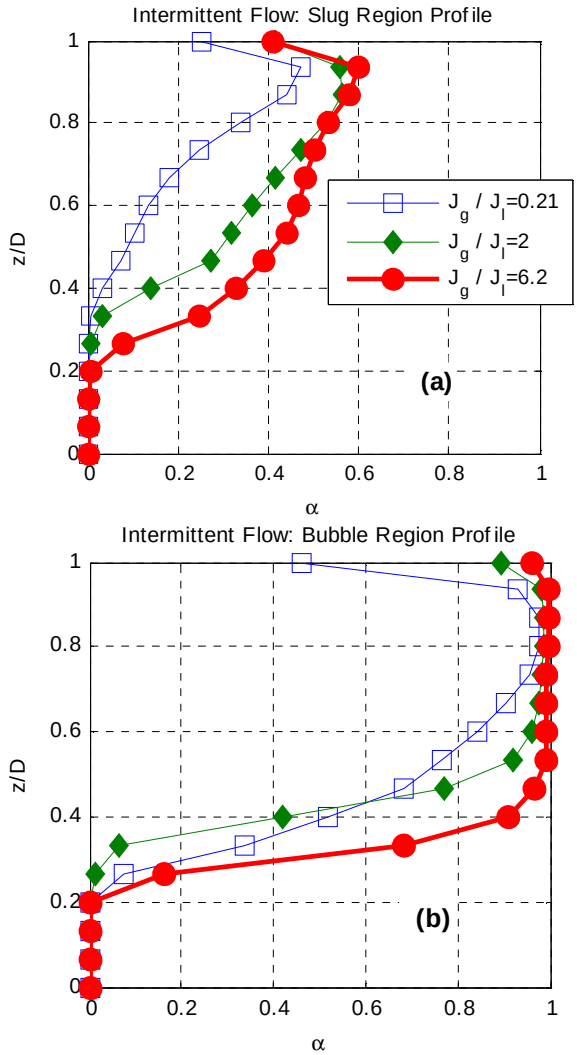

Fig.5.17: "Quasi periodic" void fraction profiles dependence on the ratio J_g/J_l for slug region(a) and bubble region (b)

In the following figures the velocity dependence of the characteristic profiles for the flows that can be classified as ”non periodic with low noise” and “non periodic with high noise” is shown. Fig.5.18 presents the profile evolution that is obtained by increasing the liquid flow rate, at three air flow rates (2.33 m/s, 11 m/s, 21.21 m/s). At lower air velocity and at water velocity lower than 2 m/s the profiles show a peaked shape, with the peak localized in the upper region of the pipe where the gas phase is concentrated due to the gravity force. By increasing the air flow rate the flow tends to become more symmetric with respect to the pipe center and the typical shape of an annular flow is reached.

At air velocities ranging from 4 m/s to 10 m/s the liquid entrainment in the core region is detected and the thickness of the liquid film either at the top cross section region or at bottom one is higher (Fig.5.18 (b), Fig.5.19 (b) and (c)). In Fig.5.19 the profiles at three water velocities (0.09 m/s, 0.93 m/s and 1.86 m/s) and at different air velocity are presented. The characteristic shape is reported in Fig.5.19 (a) for lower water velocity: stratified and annular flows occur with a liquid film thickness that decreases by increasing the air flow rate.

At higher water velocity the evolution from bubble flow to annular flow is shown in Fig.5.19 (b and c); the air flow rate increase causes an increase of the void fraction and a reduction of the liquid film thickness both in the upper and lower region of the pipe: it tends to flat the profile in the central region, resulting in a more symmetric profile. At higher water velocity (Fig.5.19 (c)) the upper liquid film region seems to be unaffected by the air flow rate, while the void fraction value in the lower region is higher than the liquid reference value (α=0), due to the air entrainment inside the liquid film.

The profiles that are obtained for bubble flow allow some important considerations: the bubble flow is characterized, for the present test conditions, by a void fraction distribution that strongly depends on the gravity force (peaked profile) and the maximum value of the void fraction along the chord is reached near the channel top and ranges from about 0.4 to 0.75 depending on the phases velocity combination. A liquid film in the cross section upper region has been detected by the sensor for all tested flow conditions.

If the liquid velocity increases the flow tends to homogenize with a void fraction at the channel bottom higher than zero while the maximum void fraction value decreases. By increasing the air velocity the mean chordal void fraction increases and the profile flattens evolving in annular flow. The transition to the annular flow seems to coincide with a shift of the void fraction maximum value towards the centre of the pipe. Where the air velocity is lower than 11 m/s the core region of the annular flow is characterized by a value of the void fraction lower than one, while at higher velocity the value is zero.

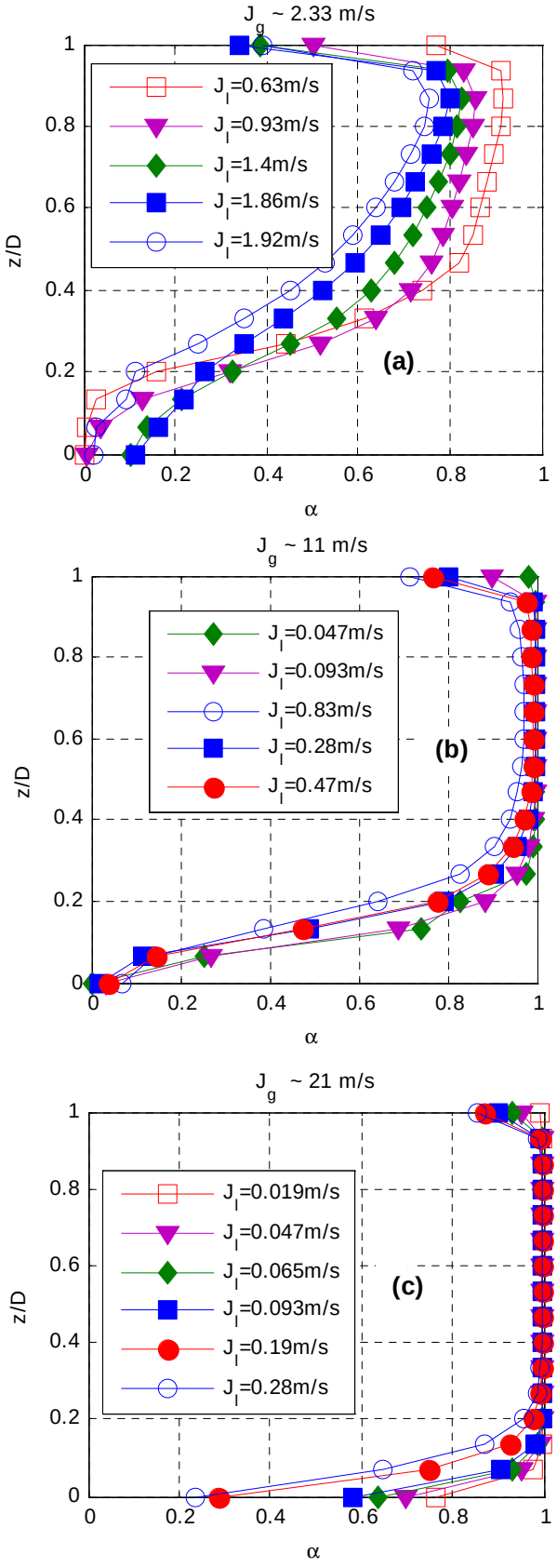

Fig.5.18: Void fraction profiles at different air velocity: (a) J_g=2.33 m/s, (b) J_g =11 m/s, (c) J_g =21.21 m/s

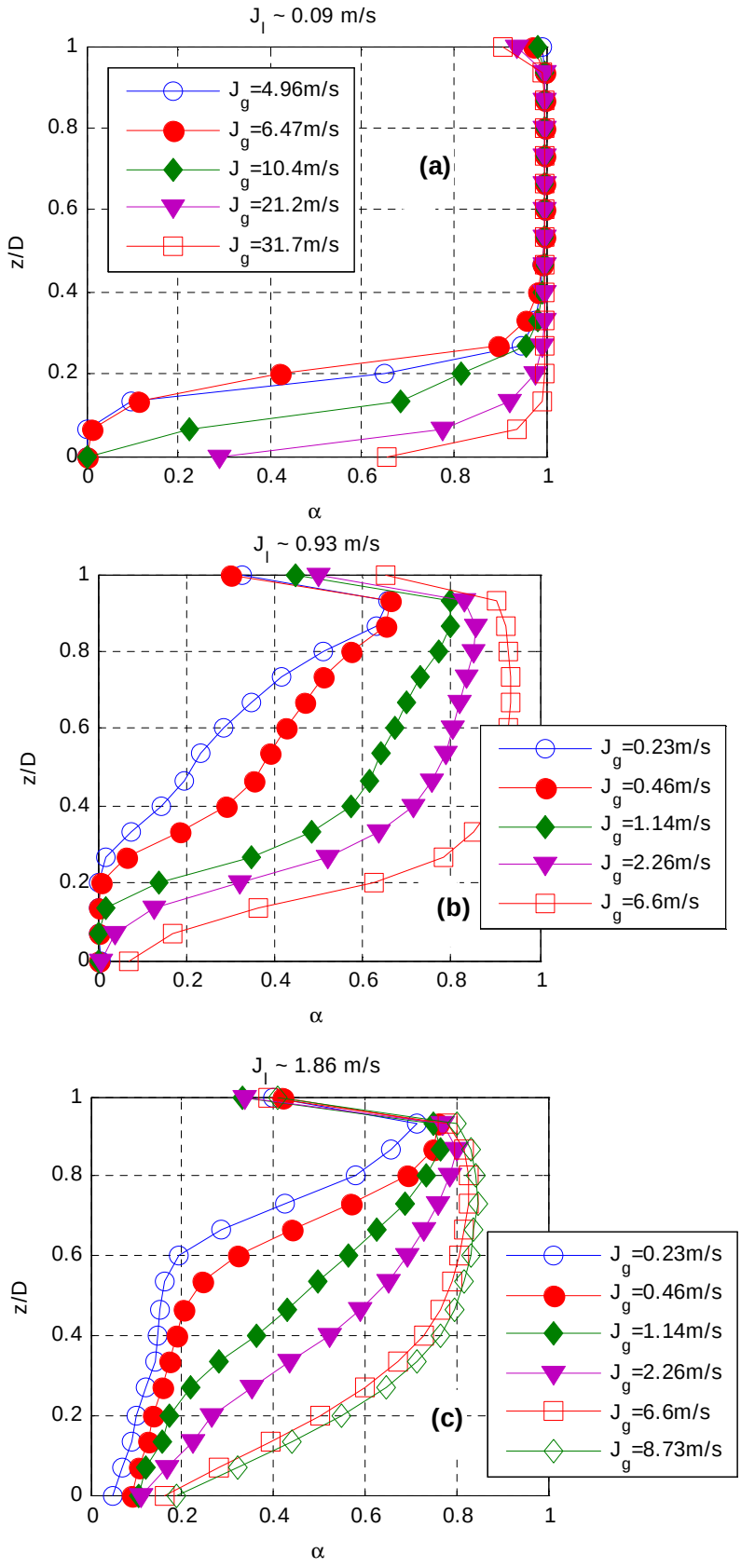

Fig.5.19: Fig. 14 Void fraction profiles at different water velocity: (a) J_l =0.09 m/s, (b) J_l =0.93 m/s, (c) J_l =1.86 m/s

5.11 Interface time evolution and liquid level

From the analysis of the time chordal profile at j=8, the air-water interface evolution is derived. A threshold value, $a(i,j,k)$=0.1, is chosen to define the interface, and by a simple algorithm the mean liquid level $h_l(t)$ in the pipe is reconstructed as reported in Fig.5.20, Fig.5.21 and Fig.5.22. For a given gas velocity and very small liquid velocity slugs are observed with a relative high frequency ($1/T$ >8 s). As shown in Fig.5.20 and Fig.5.21, following a passage of the slug the liquid level drops to the lowest values, as the liquid in the stratified flow is swept up by the slug, enabling the cycle to repeat. Moreover, as the superficial liquid velocity increases the number of roll waves and the slug frequency increase. The h/D values obtained from the sensor signal do not always reach a value of unity when a slug passes because of the presence of gas bubbles.
In Fig.5.22 the interface evolution at very low liquid flow rate is presented. In this case the effect of the increasing gas flow rate is the interface perturbation, and the transition through stratified and annular wavy flow. The presence of the liquid film in the upper part of the tube is not clearly detected by the sensor because the film is very thin due to gravity effect.

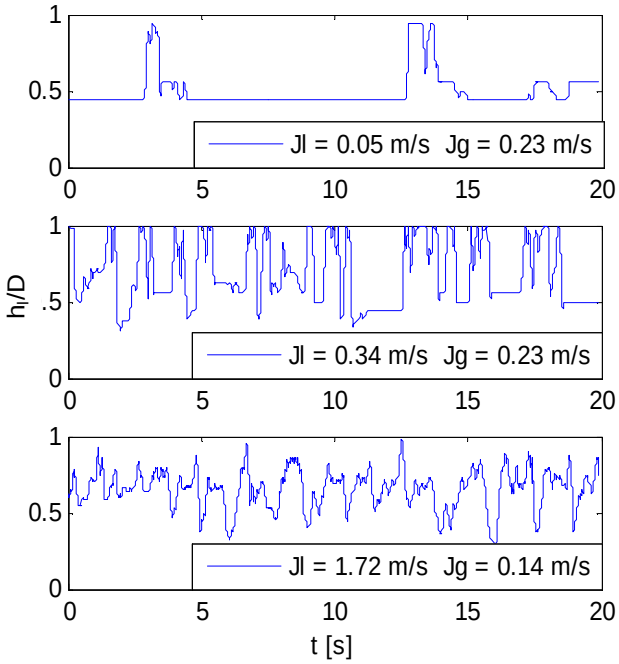

Fig.5.20: Air-Water interface time evolution for J_g=0.23 and J_g=0.14 m/s and J_l from 0.05 to 1.72 m/s

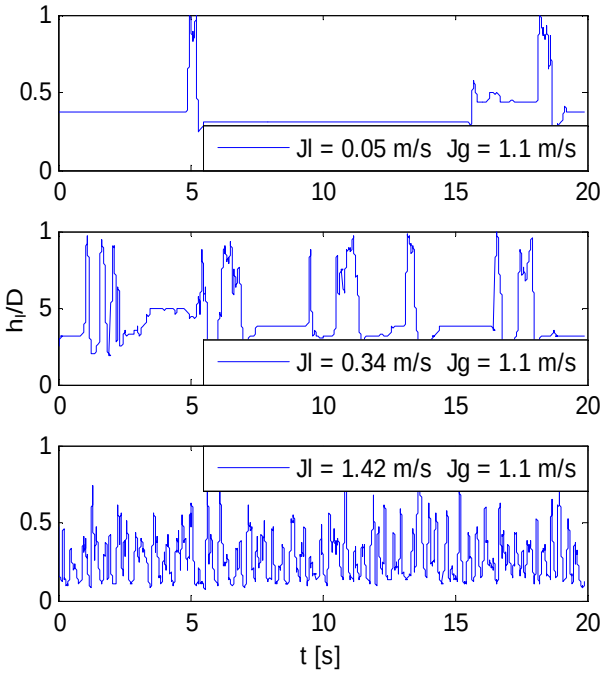

Fig.5.21: Air-Water interface time evolution for J_g=1.1 m/s and J_l from 0.05 to 1.42 m/s

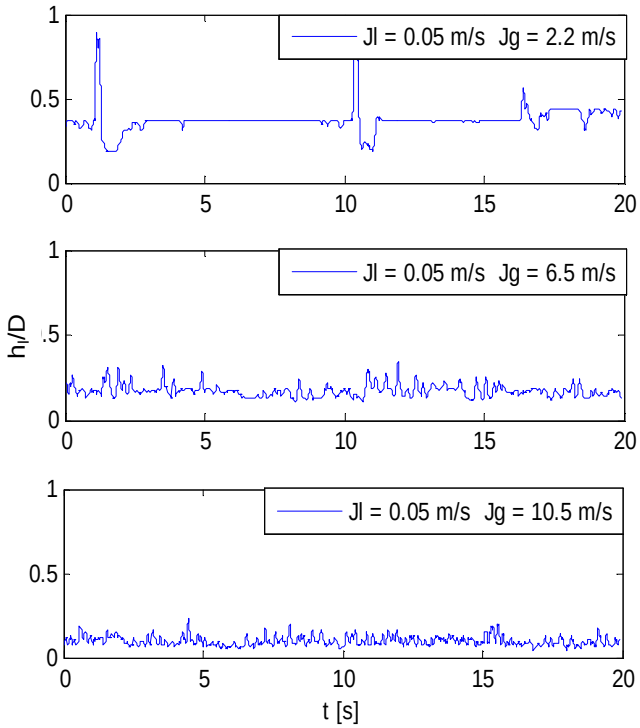

Fig.5.22: Air-Water interface time evolution for J_g = 2.2, 6.5, 10.5 m/s and J_l = 0.05 m/s

The analysis of the interface evolution allows the identification of the minimum liquid level h_{min}. Fig.5.23 shows h_{min} as a function of the phases superficial velocity: in the tested range h_{min} significantly decreases with increasing superficial gas velocity (logarithmic law) and slightly increases with increasing superficial liquid velocity. At lower superficial gas velocities, the h_{min} significantly depends on the liquid velocity, while such dependence is

poor when J_g>2 m/s.

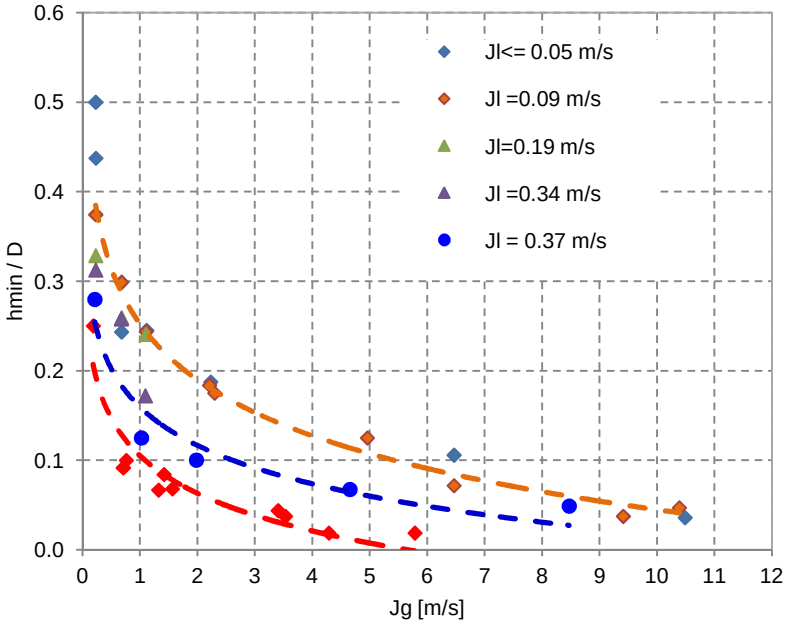

Fig.5.23: Minimum liquid level as a function of air and water superficial velocity

5.12 Intermittent flow characterization

From the WMS signal analysis described in the previous paragraph a model able to classify the different flow patterns has been developed. In the present paragraph the methodology developed to classify and characterize the intermittent flow is described.

The histogram and the frequency spectrum of the mean cross sectional void fraction are used to identify the different sub-regimes of the intermittent flows.

In Fig.5.24 the normalized histogram (left column) and the frequency spectrum (right column) of three intermittent flows, obtained with different combinations of the phases superficial velocities, are shown.

The mean cross sectional void fraction histograms of intermittent flows, are characterized by a bimodal shape (due to the intermittence), in which the peaks position and value depends on the superficial velocity of the two phases.

The flow reported in Fig.5.24 (a), obtained with J_l=1.13 m/s and J_g =6.66 m/s, is characterized by a primary peak localized at high void fraction (α=0.8) and by a secondary peak at low void fraction (α=0.3). A relative noisy frequency spectrum with three different characteristic frequencies has been highlighted from the curve in the right column of Fig.5.24 (a).

The flow shown in Fig.5.24 (b), obtained with J_l=0.93 m/s and J_g =1.14 m/s, is instead characterized by two equivalent peaks localized at α=0.1 and α=0.7. A single characteristic frequency is detected at these flow conditions.

The third example, reported in Fig.5.24 (c), obtained with J_l=1.4 m/s and J_g =1.14 m/s, shows an opposite behavior compared with the flow of Fig.5.24 (a): the primary peak is localized at low void (α=0.2) and the secondary peak is localized at α=0.7. Also for this flow, at least two characteristic frequencies can be identified.

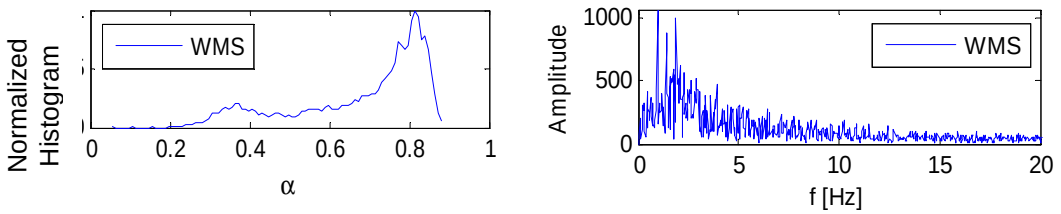

(a) Jl=1.13 m/s – Jg =6.66 m/s

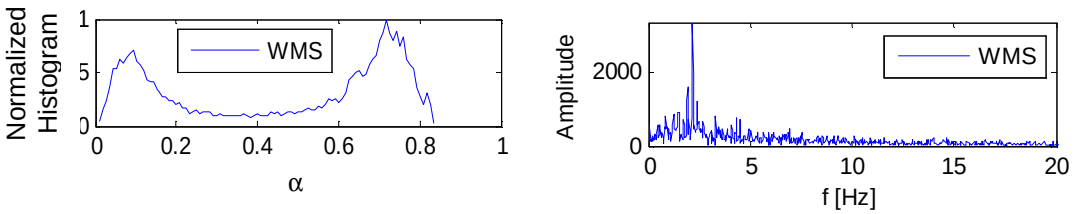

(b) Jl=0.93 m/s – Jg=1.14 m/s

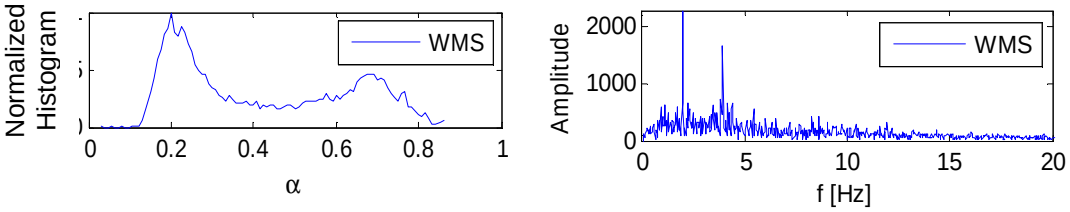

(c) Jl=1.4 m/s – Jg=1.14 m/s

Fig.5.24: Normalized histogram and frequency spectrum. (a) Jl=1.13 m/s – Jg =6.66 m/s, (b) Jl=0.93 m/s – Jg=1.14 m/s, (c) Jl=1.4 m/s – Jg=1.14 m/s

The intermittent flow has been classified in compliance with the histogram shape and plotted in the Baker's map, as shown in Fig.5.25. The analysis shows that the histogram shape is strictly related with the velocity of the phases, and can be used to distinguish between the tree different sub-regimes.

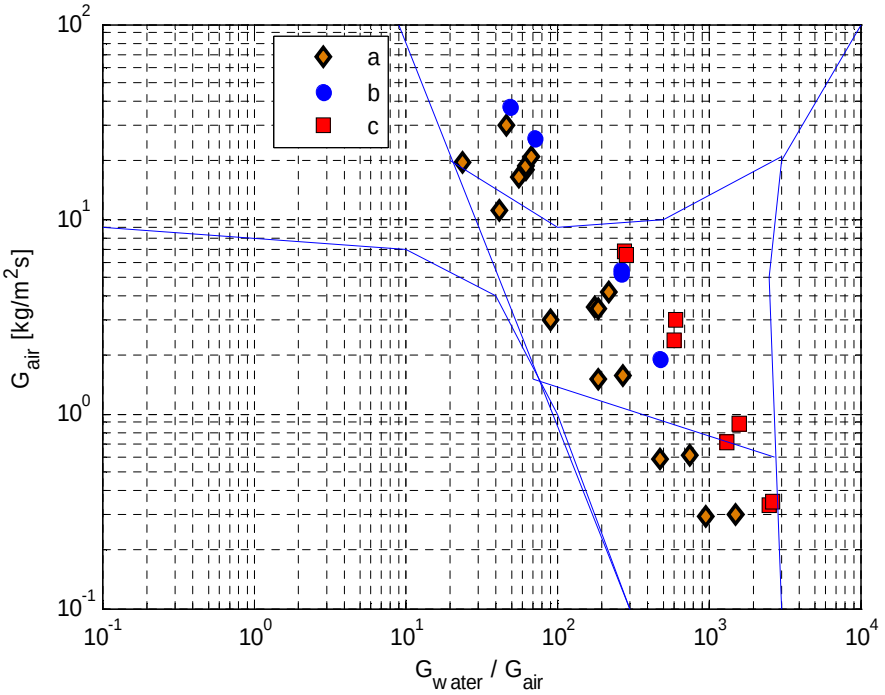

Fig.5.25: Intermittent flow sub-regimes classification

In Fig.5.26, the characteristic frequencies (corresponding to the maximum energy contents in case of two or more characteristic frequencies) are represented as a function of the liquid superficial velocity. The characteristic frequency increases with the liquid flow rate, so that can be represented in non-dimensional parameter using the Strouhal number *St*, as a function of the volumetric void fraction of the liquid phase β_l (Fig.5.27):

$$St = \frac{f \cdot D_p}{J_g} \tag{5. 12}$$

$$\beta_l = \frac{J_l}{J_{tot}} \tag{5. 13}$$

The *St* number shows a linear dependency on the β_l flow parameter, and the sub-regimes identified by means of the histogram shape (flow classified as (a), (b) and (c)), are identified by different characteristic frequencies: the group (c), appears for β_l higher than 0.4 and shows the highest characteristic frequencies, while the group (a) that is observed at relative lower velocities is characterize by lower values of the characteristic frequencies.

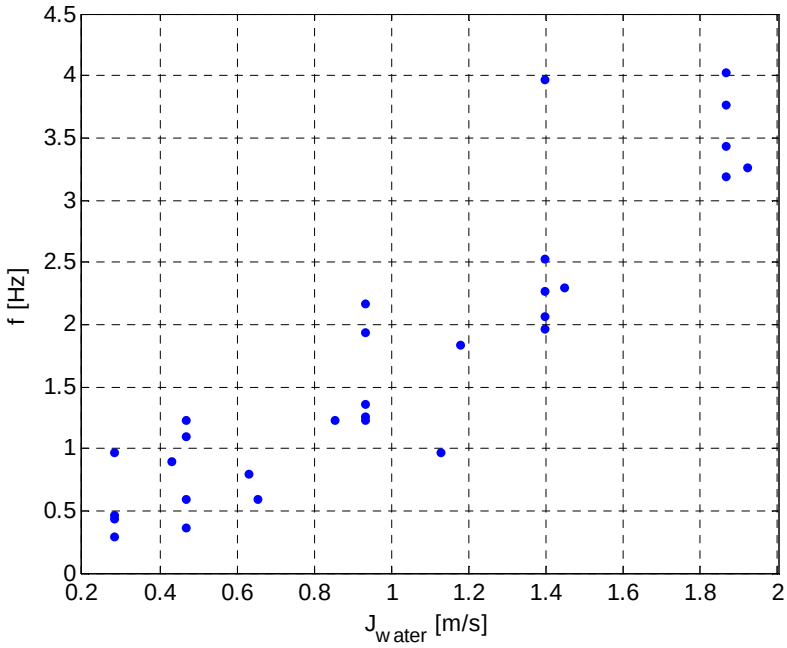

Fig.5.26: Characteristic frequencies of intermittent flows

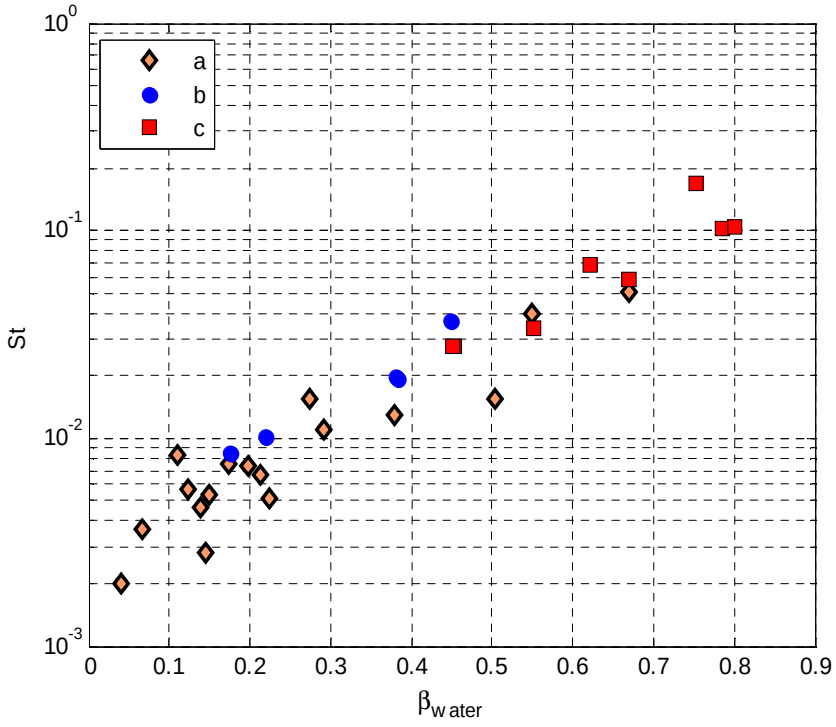

Fig.5.27: Intermittent flows Strouhal number as a function of the liquid volumetric fraction

5.13 Bubbly flow characterization

In the present paragraph, the results of the experimental work carried out to analyze the response of the WMS in a horizontal air-water bubbly flow are shown. The effect of the gravity and of the pipe wall on the void distribution is analyzed and discussed as well as the effect of the superficial velocities of the phases on the void fraction profiles shape.

In the present analysis the superficial velocity ranges from 0.23 to 0.5 m/s for air and from 0.9 to 3.7 m/s for water. With a pressure ranging from 0.98 to 2.6 bar depending on the flow conditions.

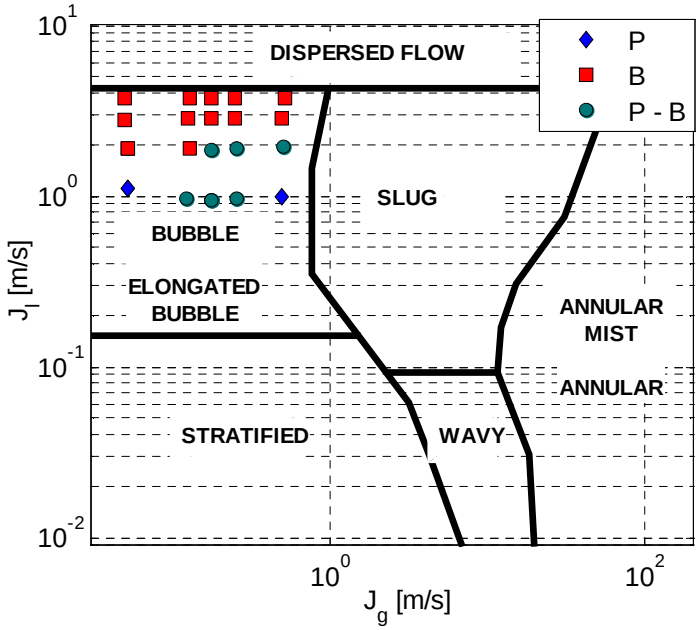

Fig.5.28: Experimental bubbly runs plotted on the Mandhane's map.

The methodology developed to characterize the flow evolution and to extract the flow characteristic void fraction profiles, along the vertical axis of the pipe cross-section, has been described in the paragraph 5.5 and reported in [5.16][5.17][5.18]. In the present work we focus the attention on a limited range of phases velocities, in order to investigate the internal structure of the bubbly flow.
The developed methodology is extended to all the measuring points of the WMS grid, in order to evaluate the symmetry of the flow with respect to the axis of the pipe cross-section in horizontal and vertical directions, as well as the effect of the pipe wall on the void distribution. First of all, the local history of the void fraction is analyzed by means of the normalized histograms. Then the void fraction chordal profiles are extracted from the sensor signals in order to analyze the phases distribution inside the channel at different superficial velocity of the two phases.

The bubbly flow is characterized by a mean cross sectional void fraction lower than 0.3; for higher values the transition to plug flow occurs. In order to determine the flow pattern inside the channel, the direct observation is supported by the signal time evolution analysis. In the present work, the flow is classified as bubbly flow if the measured void fraction ranges

between low and high values with a frequency higher than p/J_{tot}, where $J_{tot}=J_l+J_g$ is the total superficial velocity of the mixture and p is the grid pitch. An example of the void fraction time evolution is reported in Fig.5.29, for two different combination of phases velocities. The time history shown in Fig.5.29 (a) refers to a plug flow; this is clear from the picture in which the time history is plotted between 0 and 0.5 s. In bubbly flow the void fraction change rapidly and almost randomly in time, as for the flow shown in Fig.5.29 (b), while in this case a deterministic evolution of the void fraction, with a relative long time in which the local void fraction does not change is highlighted.

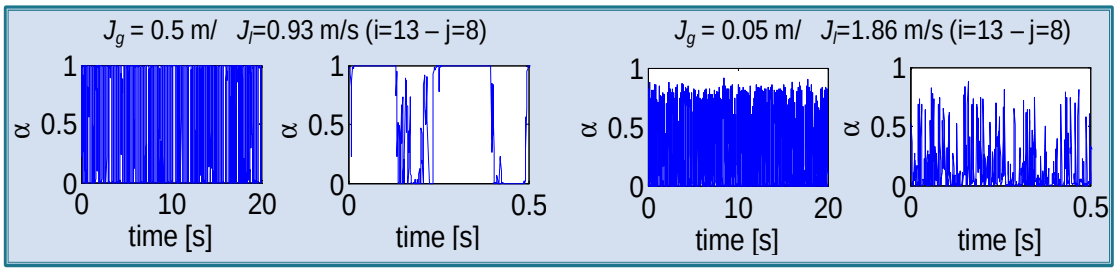

(a) **(b)**

Fig.5.29: Void fraction time evolution at the point (13, 8) of the WMS grid at J_l = 0.93 and J_g = 0.5 m/s (a) and J_l = 1.86 and J_g = 0.05 m/s (b)

Once the flow is classified, the void fraction chordal profiles are analyzed for the different flow conditions, as shown in the following pictures.
In Fig.5.30 the phases distribution for the flow at J_l=0.93 m/s and J_g=0.5 m/s is shown, while Fig.5.31 and Fig.5.32 present the void distribution for the flows characterized by J_g=0.05 m/s and J_l=1.86 m/s and J_l=2.79 m/s. For each flow condition the time history of the vertical profile at j=8, the mean cross-sectional void fraction distribution and the void fraction profiles, for the symmetrical chord (3-14, 5-12, 8-9), along the vertical (index j) and the horizontal (index i) direction are reported. The points outside the pipe have been excluded from the analysis.

Analyzing the pictures in Fig.5.30-Fig.5.32, some important information concerning the void distribution can be highlighted: first of all the comparison of the symmetrical chords allows us to conclude that the flow is symmetric with respect to the vertical pipe axis. Moreover the vertical profile of the void fraction is strongly affected by the gravity/buoyancy effect and shows an upper region peaked profile. The value of the peak reaches a maximum in the chords nearest to the vertical axis of the pipe (j=8-9), while the comparison of the void chordal profiles at j=3, j=5 and j=8, shows that the void fraction peak moves toward the upper pipe wall: at j=3 the peak is localized at d/D=0.7, while at j=8 it is located at 0.9.

The flow classified as plug flow (Fig.5.30) is characterized by a deterministic time evolution of the void fraction, with the lower part of the pipe (up to j=6) always covered by the liquid phase, while in the upper part of the pipe, large bubble of gas (plugs) are spaced out by slugs of liquid.
The void distribution for the flows classified as bubbly is quite different, depending on the liquid velocity. At relative low water velocity, Fig.5.31, the gas phase is totally confined in the upper part of the pipe, with the pipe cross-section up to the index j=12, totally covered by

the liquid phase. At higher liquid velocity, Fig.5.32, the flow tends to homogenize and the gas bubbles are entrained in the liquid phase, so that the stratification effect, due to the gravity, is less evident. In this case the vertical chordal profile, is not more characterized by a peaked profiles, and the void fraction appears almost constant on the cross-section.

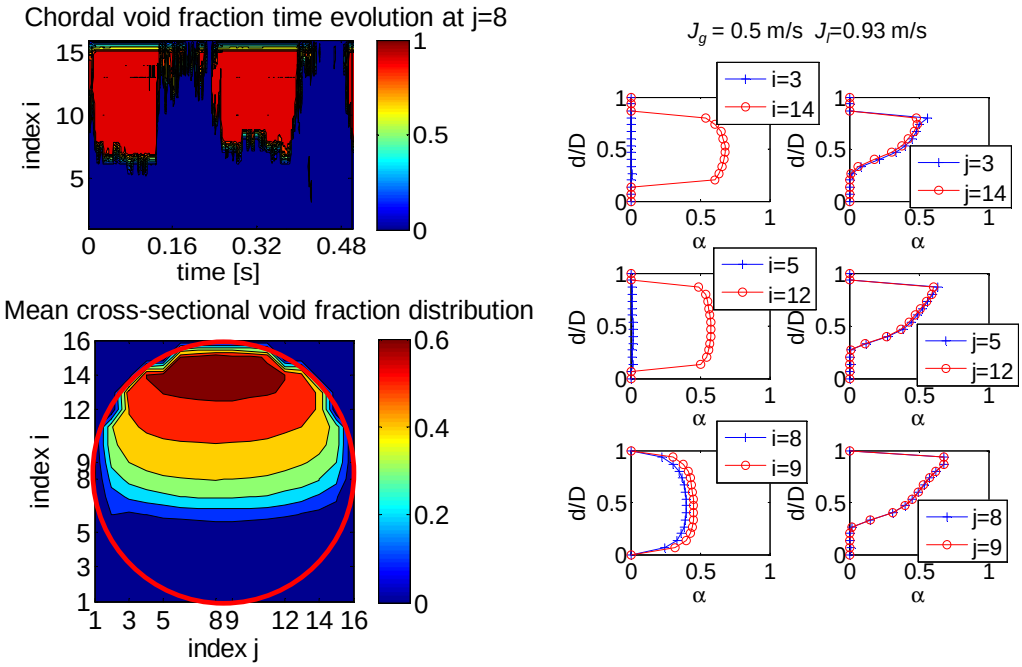

Fig.5.30: Plug flow example: J_l=0.93 m/s and J_g=0.5 m/s

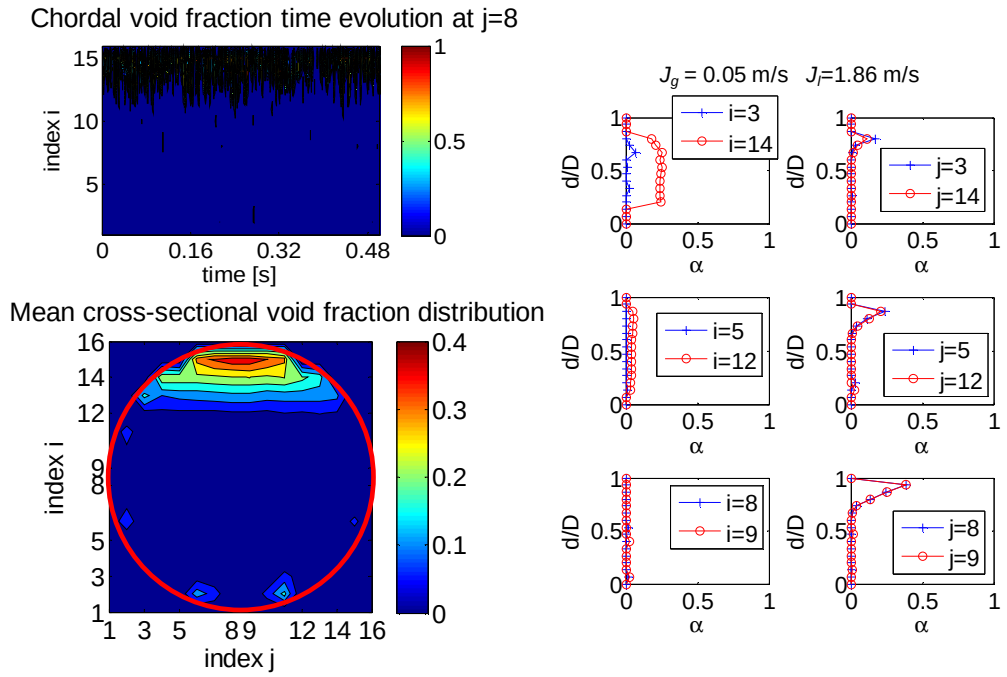

Fig.5.31: Bubbly flow example 1: J_l=1.86 m/s and J_g=0.05 m/s

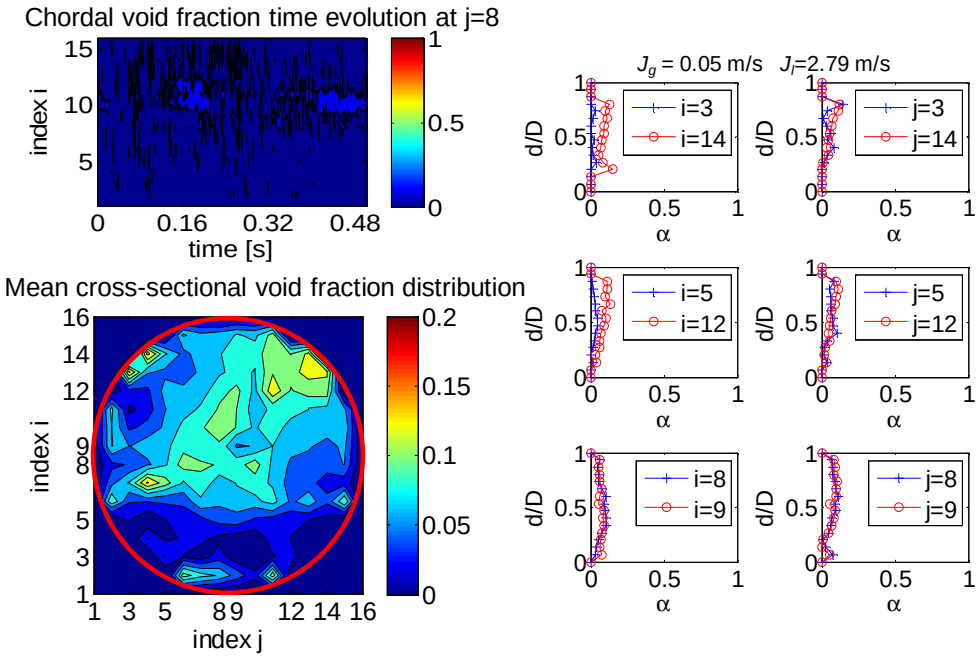

Fig.5.32: Bubbly flow example 2: J_l=2.79 m/s and J_g=0.05 m/s

The comparison of the chordal profiles at different superficial velocities combinations of water and air, is pointed out in Fig.5. 33 and Fig.5. 34. In Fig.5. 33 the effect of the superficial velocities on the vertical profiles is shown, while in Fig.5. 34 the influence on the horizontal profiles is reported. The combination of three different air superficial velocities (J_g=0.05,0.17 and 0.5 m/s) and four different water superficial velocities (J_l=0.93, 1.86, 2.79 and 3.72 m/s) is shown.

For water velocities lower than 2.79 m/s and air velocities lower than 0.17 m/s (Fig.5. 33 (a)-(b) and Fig.5. 34 (a)-(b)) the characteristic peaked profile along the vertical direction is observed, with a maximum void fraction that can reach a value also higher than 0.7 in the upper region of the pipe. The effect of the water flow rate increase is the homogenization of the phases distribution, with the void fraction characterized by a flat profile along the different chords.

By increasing the air flow rate up to 0.5 m/s the void fraction tends to increase in the lower part of the pipe, as shown in Fig.5. 33 (c) and Fig.5. 34 (c). The profile shape is smoothed, without any modification on the position of the peak. In that condition the effect of the water velocity is the change of the maximum value of the void fraction: higher value of the superficial water velocity corresponds to lower value of the peak void fraction value.
Moreover, in every tested condition the maximum value of the void fraction is localized in centre line of the pipe (j=8 and j=9) at i=14, as pointed out in the curves of Fig.5. 34.
.

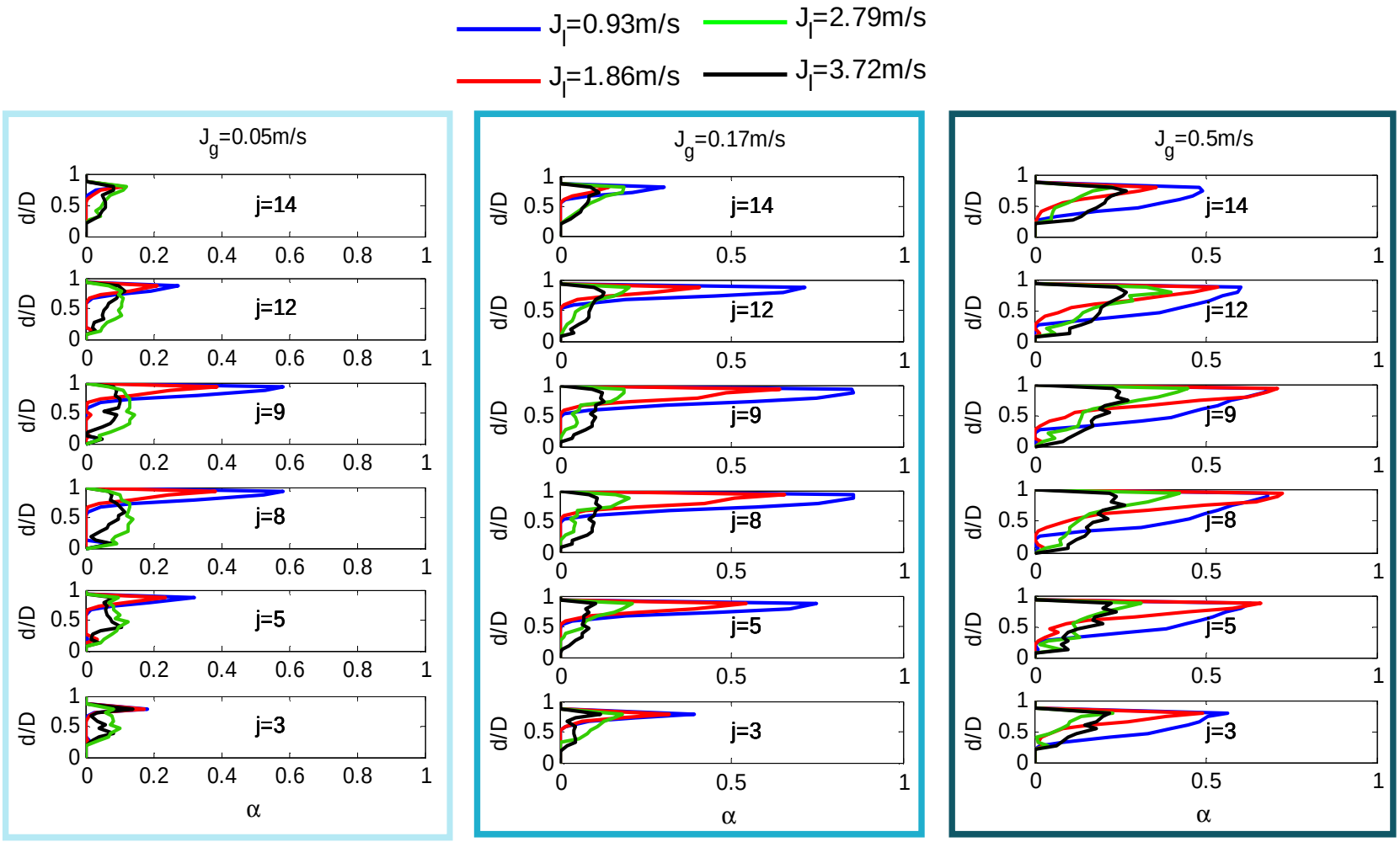

Fig.5. 33: Velocities dependency: Vertical Profiles

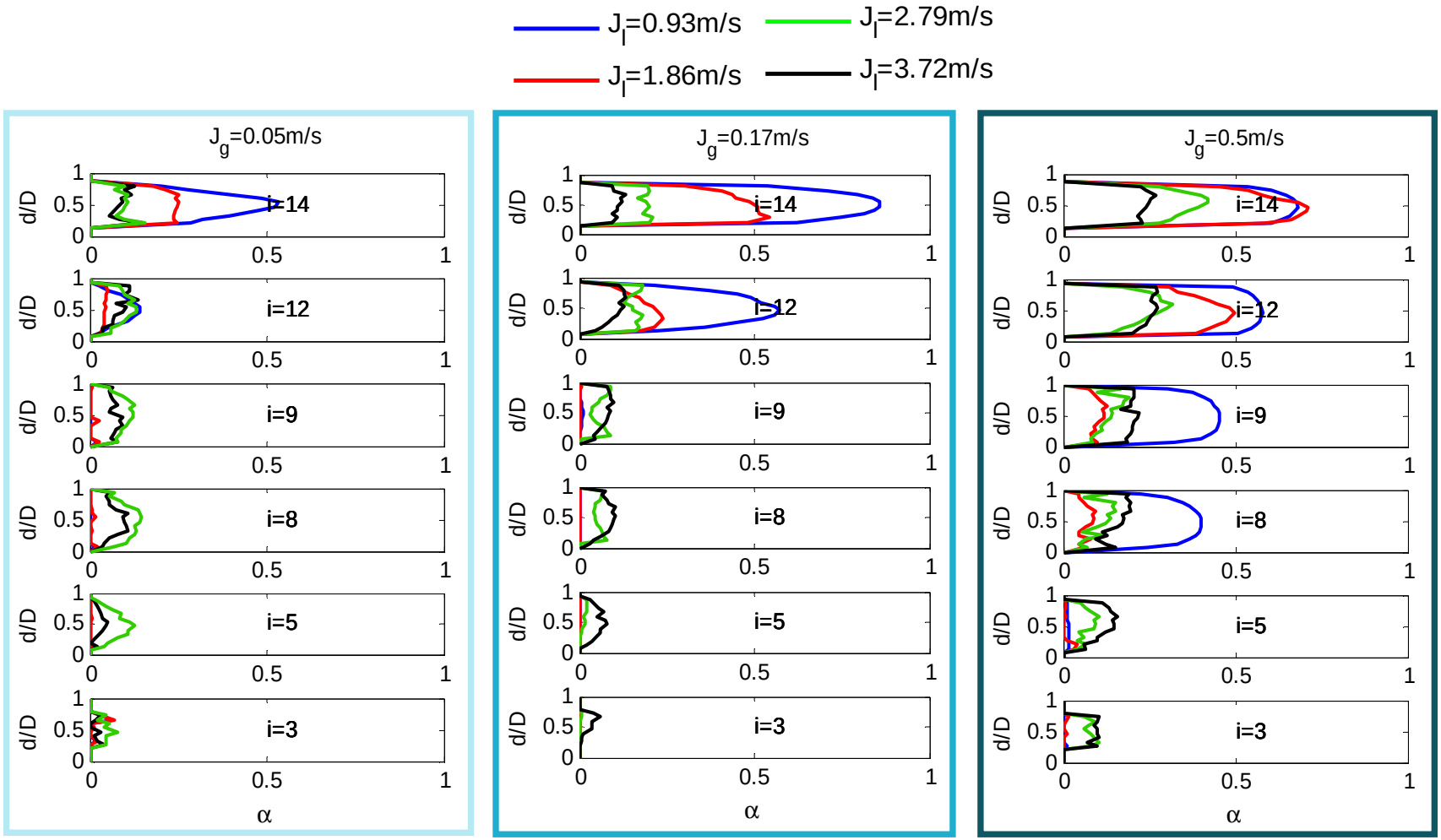

Fig.5. 34: Velocities dependency: Horizontal Profiles

5.14 Conclusions

Air-water experiments have been performed in a horizontal Plexiglas pipe, having an internal diameter of 19.5 mm and a total length of about 6 m. The superficial velocities of the two-phases range from 0.14 to 32 m/s for air and from 0.019 to 3.79 m/s for water, corresponding to almost all the horizontal flow patterns, from stratified to annular flow. In the present work a WMS has been adopted to characterize the air-water two-phase flow: local, chordal, cross-section void fraction values are derived from the sensor data.

The developed methodology for the analysis of the Wire Mesh Sensor signals allows the identification of the flow pattern and the flow characterization in terms of void fraction profiles and characteristic times. From the analysis of the time evolution of the local void fraction and of the parameter *M(t)* it is possible to characterize the flow in terms of the void fraction profile shape and other parameters like phases distribution, liquid level, mean void fraction in the different pipe regions, characteristic frequencies.

The obtained results give important information about the phase distribution inside the pipe, as the local and time average void fraction, the interface evolution, and the transit time of slugs or plugs.

Moreover the presented signal processing methodology allows the investigation of the internal structure of the flow at different velocities of the phases.

From the analysis of the WMS signals the phases distribution in a horizontal pipe under bubbly flow condition has been derived and the asymmetry of the flow as well as the shape of the void fraction profiles have been shown by means of the void chordal profiles.

The evolution of the void fraction profiles has been related to the superficial velocity of the two-phases (J_g and J_l) and the flow evolution in time and space has been analyzed and discussed, showing that such methodology is useful to identify and characterize the two-phase flow patterns.

6. SPOOL PIECE TURBINE AND DRAG DISK

The SP made up of a turbine flow meter (TFM) and a drag disk (DD), usually coupled with a densitometer, is one of the most analyzed instruments combination during the first experimental tests for nuclear reactor. Models available in literature are Volumetric [6.1]-[6.2], Rouhani [6.3] and Aya [6.4]. The first two are simple, while the Aya model is more accurate.
Hardy [6.5] demonstrated that the turbine flow-meter response is sensitive to the variation in the flow pattern. For the low values of liquid flow rate, the velocity detected by the turbine is lower than the single-phase air flow. The turbine response is dominated by the water velocity and the introduction of liquid tends to slow down the flow-meter. Only in the case of annular-mist flow regime, the turbine response is dominated by the air flow.
The aim of this study is the experimental and theoretical analysis of a SP made up of an axial turbine flow meter and a drag disk, horizontally installed in a test section operating with air-water flow, under different flow conditions and different flow patterns.
The experimental data allowed the construction of an operating map of the SP and the performed analysis allows the evaluation of the mass flow rates of the phases in the mixture with relative errors and the prediction of the flow pattern and other quantities important to characterize the flow.

6.1 First experimental campaign

6.1.1 Characteristics of the SP

The SP consists of the series TFM- DD and of the connected straight pipes.
The TFM used here, has been produced by Hoffer, while the DD has been produced by Ramapo (Tab. 6.1). The internal diameter of the SP is 21 mm. Upstream and downstream of the turbine, there are two straight pipe lengths of 345 mm (15. D) and 145 mm (7 D).

The DD is installed with an upstream straight pipe length of 450 mm (18 D) and a downstream straight pipe length of 217 mm (8.7 D). The characteristics of the two instruments are shown in Tab. 6.1.
The total length of the SP is 1360 mm, with the instruments nominal lengths of about 100 mm.
The SP is installed between two horizontal pipes, made of transparent Plexiglas, having a length respectively of 600 mm and 1000 mm and an internal diameter of 21 mm, for the flow visualization upstream and downstream of the SP.
The two-phase flow is discharged at atmospheric pressure. The pressure in the test section is between 1 bar and 2.5 bar depending on the flow rates.
The turbine flow meter generates, via a magnetic pickup, a sinusoidal low-level electrical signal, whose frequency is proportional to the angular velocity of the rotor of the axial turbine.
A linear frequency-voltage converter has been developed in order to measure the turbine signal in the range between 100-10000 Hz, with a proportional factor equal to 0.001 Volt/Hz.
The electronics of the target flow meter produces, by a strain gage, a signal in the range between 0-10 V, corresponding to the force that the fluid flow applies to the target. Conversion is linear, and the declared force factor is:

$$k = \frac{S}{V_{al} F} = 0.595 \frac{V}{(V * Kg_f)} \qquad (6.1)$$

where: S is the electric signal in Volt, V_{al} is the supply voltage of the Wheatstone bridge, F is the force expressed in kg due to the interaction between target and fluid.

Characteristics (Water flow)

TURBINE FM	HOFFER mod: HO 1X1-4-60-G-HT-MS	**DRAG DISK**	RAMAPO Mark V
Diameter:	nominal value: 1" (D_i = 21 mm)	Diameter:	nominal value: 1" (D_i = 21 mm)
N° of blades :	5	Target:	ACR-484 F
Flow Rate Linear Range:	15-230 l/m	Target Section:	A_t=1,187 cm^2
Repeatability Range:	8-285 l/m	Materials:	Sensing element: Inconel X-750. Housing: T304 S.S.
Overrange:	150% of max flow rate (intermittent)	Flow Rate Range:	5.4 – 54 Lt/min
Linearity:	±0,5%	Pressure Range:	345 bar (max)
Temperature Range:	-270°C- 270°C (Standard)	Temperature Range:	-55°C – 345°C
Pressure Drops:	4-5 psi (0.276 – 0.345 bar)	Force Factor (K):	0.595 V/V/Kg
Materials:	316/316L stainless steel	Straight pipe lengths:	18 D (upstream) , 8.7 D (downstream)
Straight pipe lengths:	15.5 D (upstream) , 5.8 D (downstream)	Force Transducer Syst.	Strain gage Wheatstone bridge circuit (R= 265 Ω)

Tab. 6.1: SP DD and TFM: Instruments characteristics

6.1.2 Experimental facility, test section and instrumentation

The test section where the SP is installed is part of the facility shown in Fig.6.1.
The main components of the facility are, the feed water loop, the feed air loop, described in the paragraph 5.4 and schematically reported in Fig.6.1, and the instruments used to measure air and water single-phase flow rate, pressure and temperature.
Air and water mixture is prepared in a chamber (D_i = 50 mm, L = 52 mm) where air enters along the axial direction and water along the radial pipe direction through a hole drilled in the mixer wall (D_i = 3/8"); a bronze porous component can also be used for the water side inlet.
The absolute pressure in the mixer is measured by means of the absolute pressure transducer Rosemount 3051/1, operating in the range between 0.5-10 bar.
The mean pressure of the test section is the mean pressure between the pressure in the mixer (inlet pressure) and the atmospheric pressure (outlet pressure).
The SP instruments signals (Turbine and Drag Disk flow meters) and the pressure signals are gathered by a National Instruments DAQ system (NI USB-6218) using the LabView® environment.

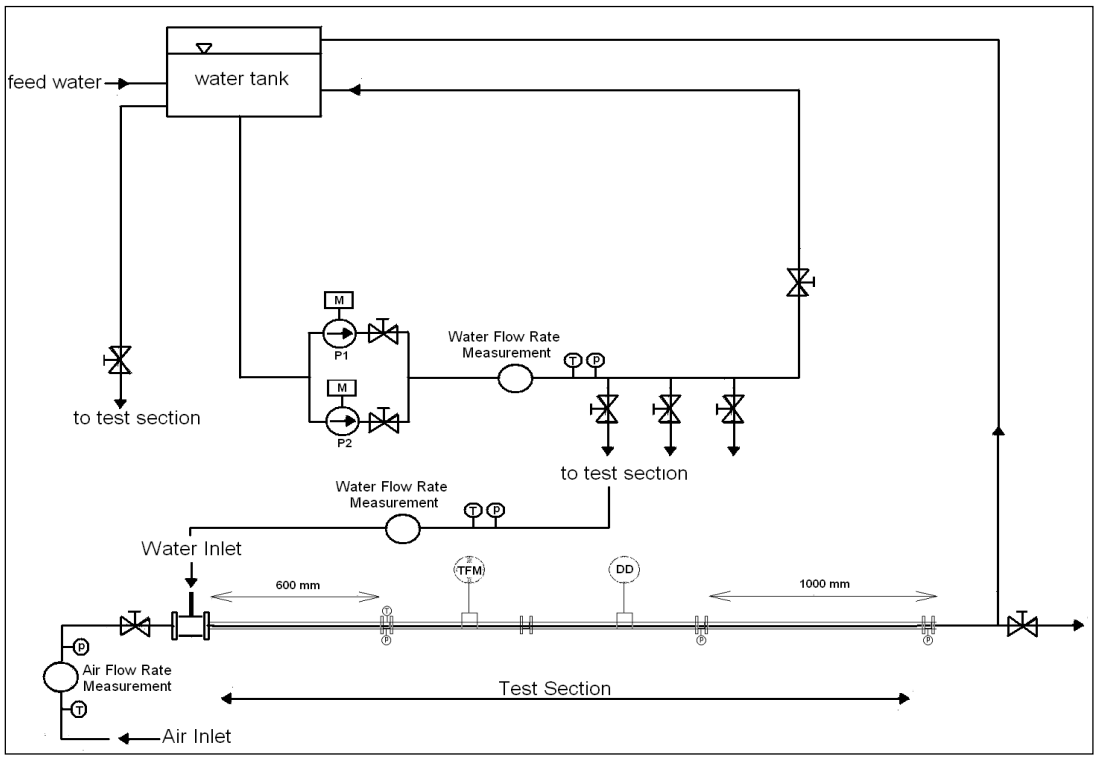

Fig.6.1: Experimental facility

6.1.3 Single-phase flow

In order the verify the calibration curves, a series of measurements in single-phase flow have been performed for air (0.005-0.014 kg/s) and water (0.13-0.50 kg/s).
The turbine-meter is essentially a turbine rotor which rotates as the fluid passes through its blades, and in single-phase flow the output is used to calculate the fluid velocity and the volumetric flux (eq. 4.1).

In the experimented water flow rate range, the parameter K_T has been found constant and equal to 0.0382 Hz/(l/h).
The turbine operating range is between 900 and 9000 l/h; because the air volumetric flow rate is varied between 6300 and 35000 l/h, the device is not working under optimal conditions. The mean air calibration parameter has been found equal to 0.02 Hz/(l/h).
The drag disk is a very simple device capable of measuring the force exerted by the fluid flow on a portion of the pipe cross section (eq 4.9).
According to the eq. (4.9) the calibration curves are found proportional to the flow rate squared (parabolic curve) both for water and for air.
Comparing the calibration curves of air and water, for the experimented mass flow rates, the drag coefficient is the same for both (Fig.6.2) and the product $K_D \cdot C_D$ is equal to 25.5.
Concerning the turbine device, due to the very different velocity fields of water and air, the calibration curves are characterized by two different calibration coefficients (Fig.6.3).
K_T for air is smaller than K_T for water at the same value of the Reynolds number; this is probably due to the increased bearing friction torque, that occurs in the turbine within the velocity field of air experimented here.

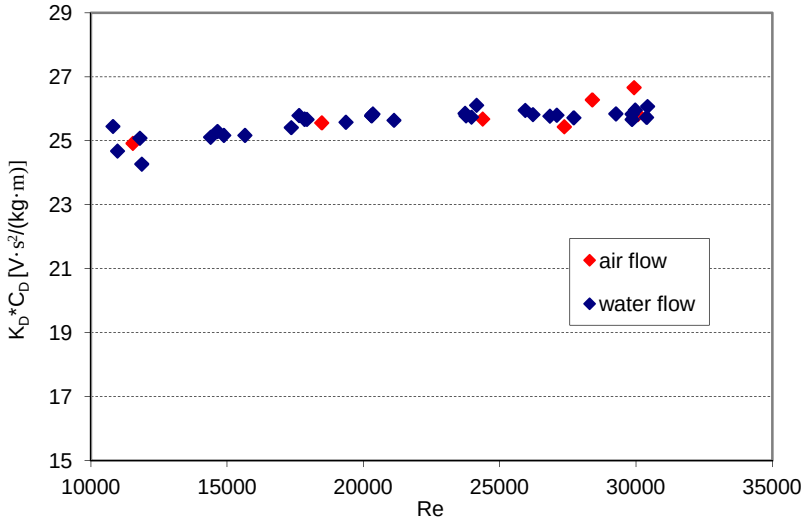

Fig.6.2: Drag calibration coefficient vs. Re number in single-phase flow

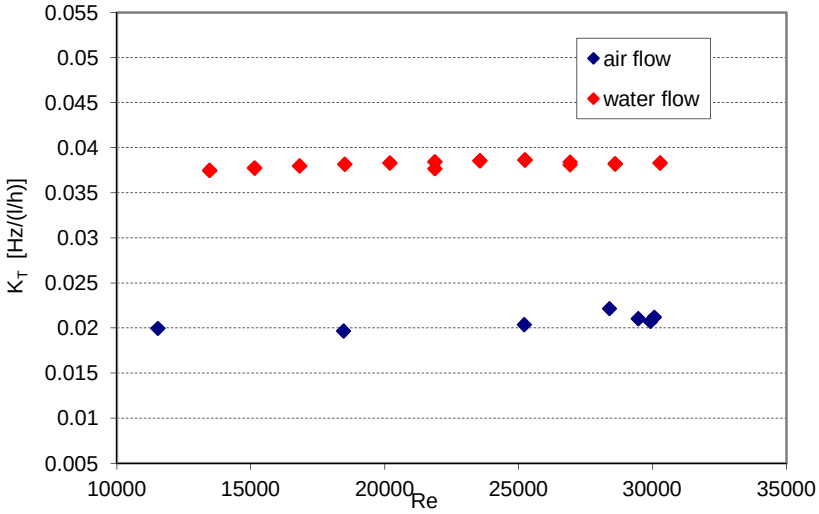

Fig.6.3: Turbine calibration coefficient vs. Re number in single-phase flow

6.1.4 Two-phase flow: experimental data

Two-phase flow measurements are performed using two different set-ups; in the first one the water flow rate is changed, keeping the air flow rate constant, while, in the second one, the air flow rate is changed keeping constant the water flow rate.
The water flow rate ranges between 0.055 and 0.3 kg/s, while air flow rate ranges between 0.005 and 0.013 kg/s. 40 runs have been performed in the first set, using 5 different air flow rates, and 20 runs in the second set using 4 different water flow rates. For each test the signals of the turbine, of the drag disk and of the absolute pressure are gathered with their relative standard deviation.
Fig.6.4, Fig.6.5 and Fig.6.6 show the experimental results. The pressure in the mixer, for each water flow rate, increases with the air flow rate (Fig.6.4); a most relevant increase occurs increasing the water flow rate and keeping constant the air flow rate (Fig.6.4). Each experiment is performed discharging the mixture into an atmospheric environment, downstream of the test section. The Plexiglas pipe allows the visualization of the flow upstream and downstream of the SP; the flow patterns observed downstream have been stratified for W_g lower than 0.0109 kg/s and annular-wavy for W_g higher than 0.0109 kg/s. They are typically pulsed flows, that have been characterized in term of mean value, standard deviation and probability density function (PDF), and in the frequency domain with the power spectral density function (PSD), using 20000 measurement points and a sampling frequency of 1000 readings per second.

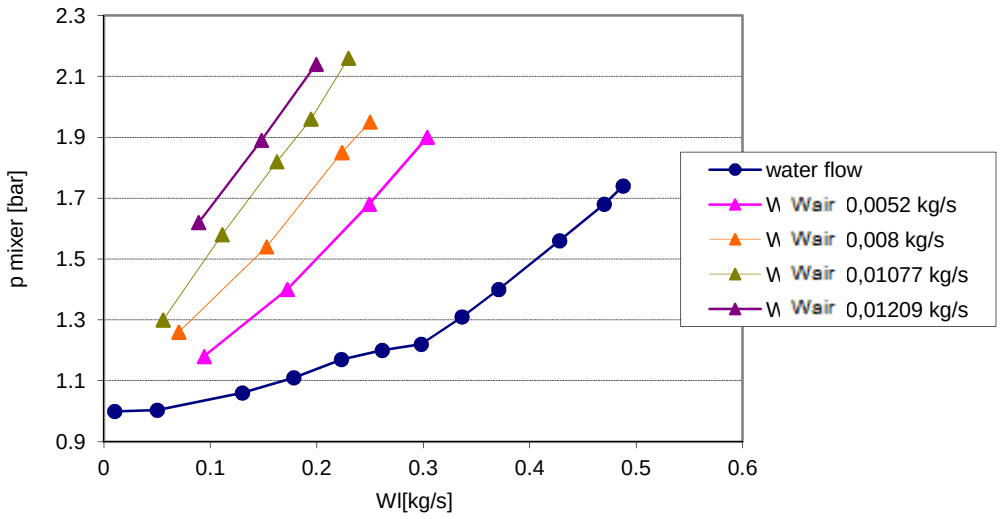

Fig.6.4: Mixer pressure variation as a function of the water and air flow rates

From a physical point of view, the signals of drag and turbine are proportional respectively to the force transferred by the mixture to the target and to the rotation velocity of the rotor of the turbine.
It is noted that, in the tested range, with a fixed air flow rate and increasing the water flow rate, the speed of rotation of the turbine decreases (Fig.6.5).
This effect is significant for flow rate higher than 0.0096 kg/s, since in these conditions the volumetric flow variation is significant.
For lower flow rates, the experimental results highlight a behavior that, in first approximation, is due to a volumetric flow roughly constant or slightly increasing.

Fig.6.6 shows the drag disk electric signal as a function of the water flow rate and parameterized as a function of the air flow rate. It is interesting to notice that the force, and then the momentum, that the flow transfers to the target rises with the water flow rate, and more consistently with the increasing of the air flow rate.
This can be explained by the increased velocity of the liquid that is entrained from the film to the gas stream.

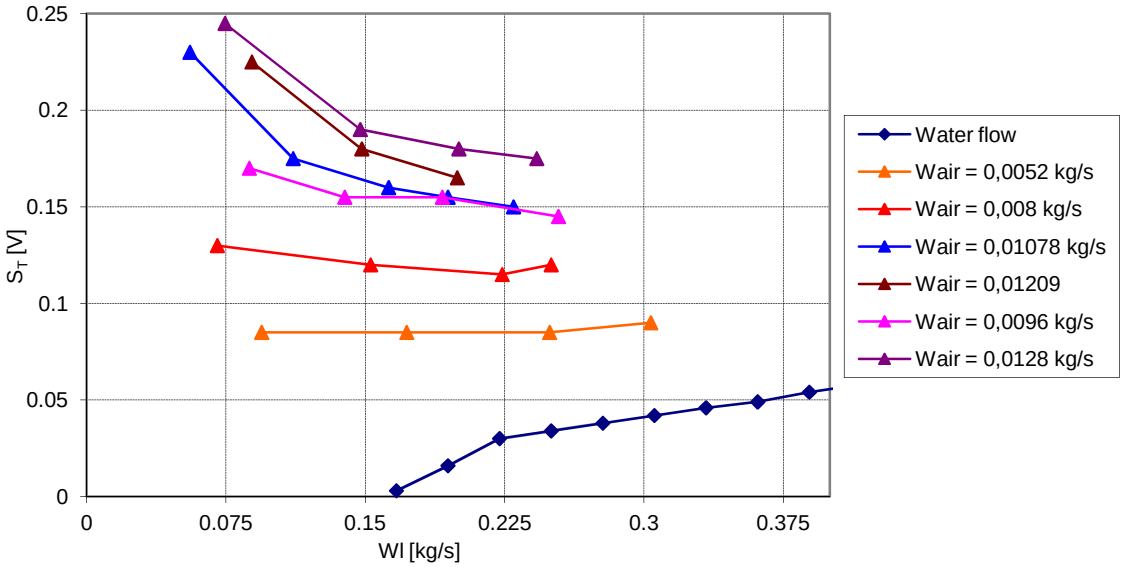

Fig.6.5: Turbine Electric Signal vs. mass flow rate in two-phase flow

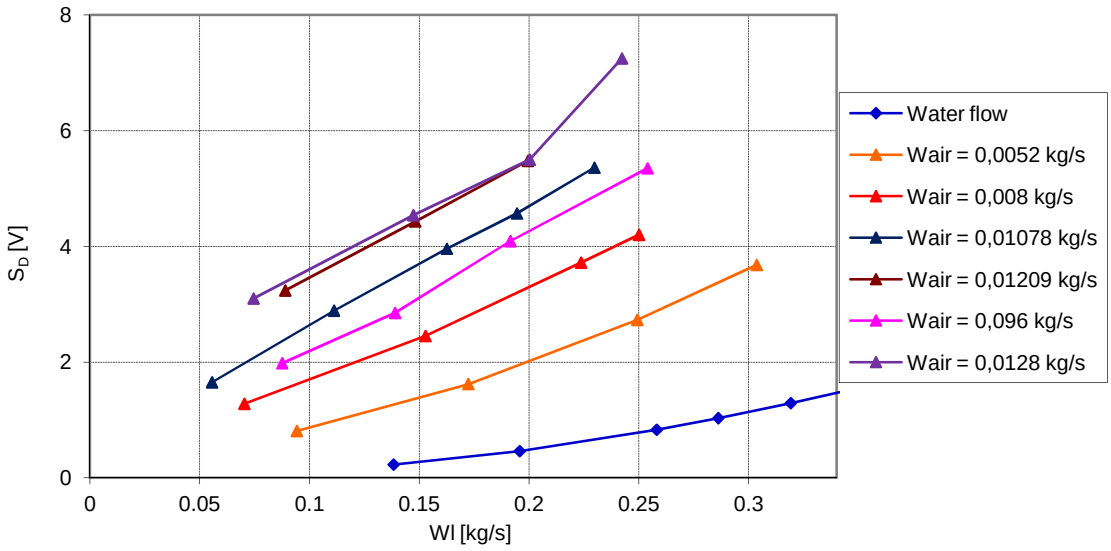

Fig.6.6: Drag Disk Electric Signal vs. mass flow rate in two-phase flow

6.1.5 Model of the SP

Representing the electrical signals of the two instruments in a single graph the operation map of the SP is obtained (Fig.6.8).
The joint measurement of pressure, drag signal and turbine signal, allows to reconstruct the flow rate of water and air univocally using the graphs of Fig.6.8 and Fig.6.7.

The SP signals are correlated in order to take into account the pressure effect in the test section:

$$S^* = \frac{S_D}{S_T} \cdot \frac{\rho_g(p_o, T_o)}{\rho_g(p, T)} \qquad (6.\ 2)$$

The ratio calculated using eq. 6.2 allows us to group in a curve the value of S^* as a function of the water flow rate normalized with the maximim measured flow rate:

$$W^* = \frac{W_l}{W_{l\_\max}} \qquad (6.\ 3)$$

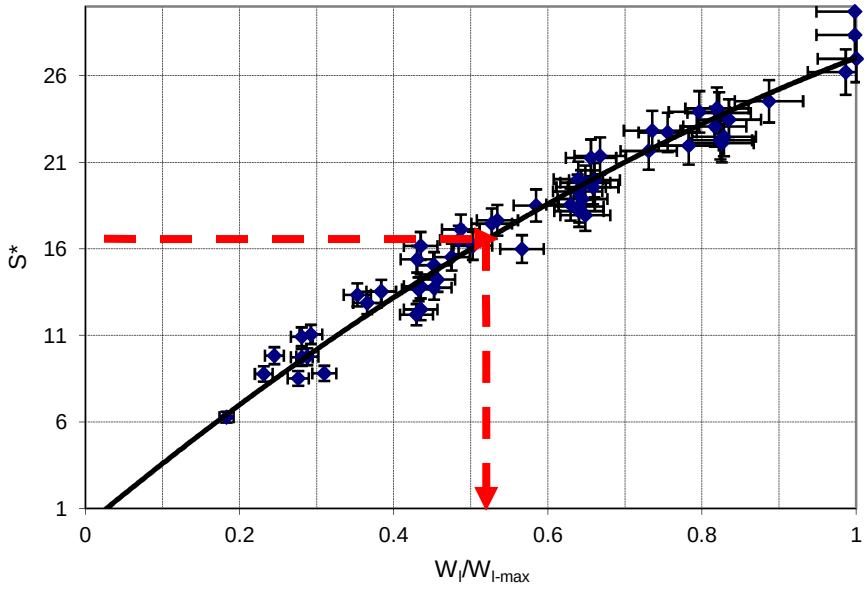

Fig.6.7: S* as a function of dimensionless water flow rate

Using the curve shown in Fig.6.7 and the graph of Fig.6.8, it is possible to evaluate the mass flow rate of the two phases. An example of graphical mass flow rate estimation is reported in Fig.6.7 and Fig.6.8.

The estimated value of S^* can be used in order to evaluate the liquid flow (red arrow in Fig.6.7); then the knowledge of the liquid mass flow rate, togheter with the knowdlege of the TFM and DD signals, allow us to entering in the graph of Fig.6.8 and to identify the curve related to the actual air flow rate.

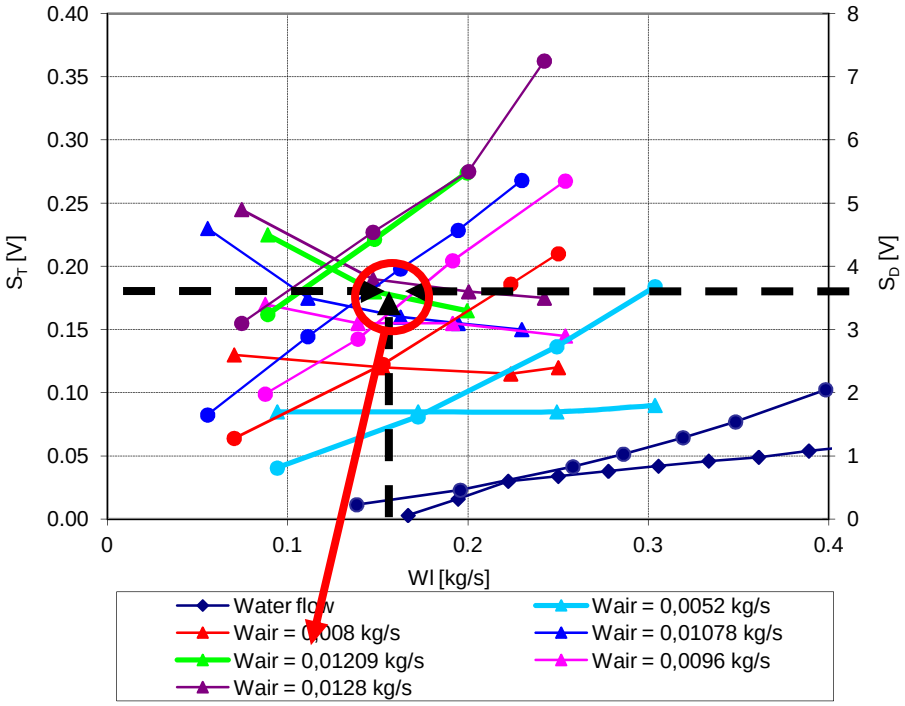

Fig.6.8: SP Map, Symbols: Turbine Signal =▲. Drag Signal = ●.

In Fig.6.9 the liquid flow rates obtained with the best-fit curve are compared with the measured water flow rates.

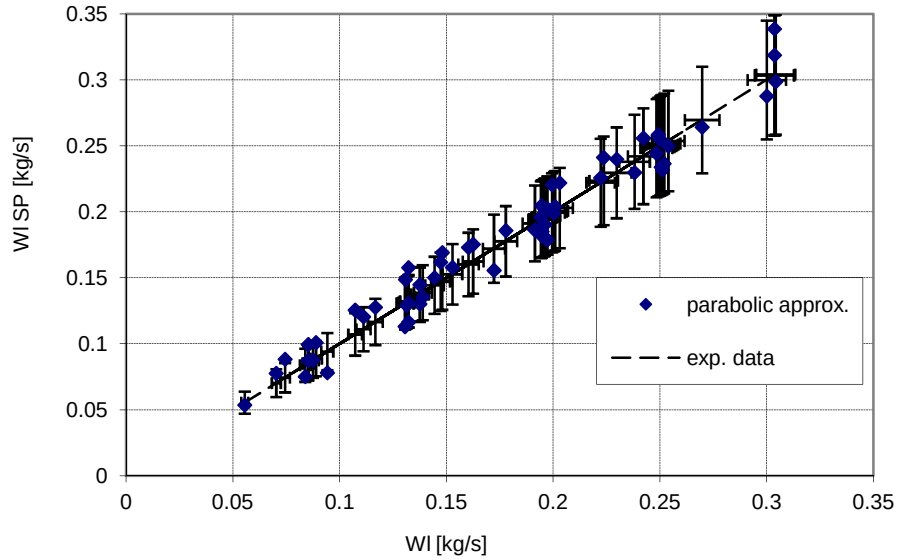

Fig.6.9: W_l SP vs. Experimental W_l. Error bar: y =±15% of Experimental W_l

Using the proposed procedure, the liquid flow rate is estimated with an accuracy of 10% for the 74% of the experimental data. The lower flow rates are characterized by the greatest deviations but the 91% of the data is evaluated with an uncertainty lower than 15%.
The accuracy of the estimated air flow rate is then given by the sum of the liquid flow rate error and the errors introduced reading the charts.

The experimental signals shown in the figures are mean values characterized by the standard deviations presented in Fig.6.10.

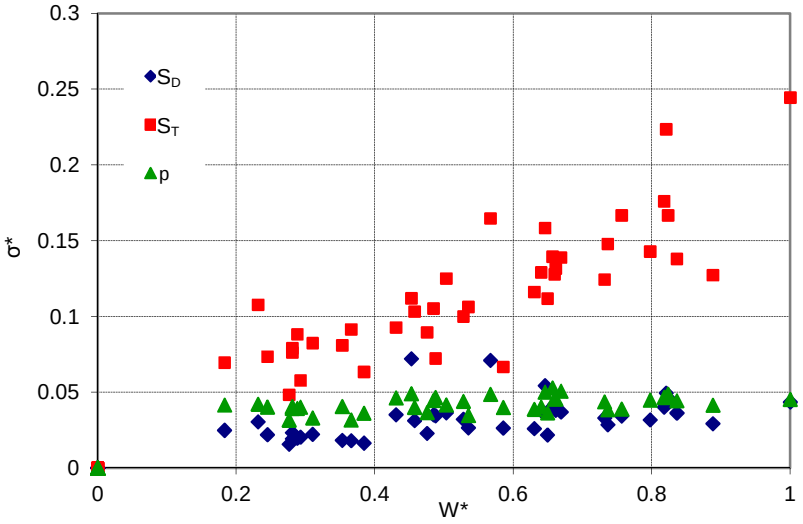

Fig.6.10: Standard deviation of electric signals

It can be observed that the standard deviations (normalized with respect to electrical signals) are contained for drag disk and pressure signals, while are more consistent for the turbine signal; in this case the standard deviation increases with the flow rate. This is probably due to the fact that, for intermittent flow, the turbine flow meter is able to follow the flow speed variations with a sensitiveness larger than the drag disk.
The signal analysis allows us to characterize the intermittence of the flow in terms of characteristic frequencies. It is important to highlight that, for low liquid flow rate, the electric signal is not periodic, but increasing the value of the liquid flow rate, keeping constant the air flow rate, the signal increases in amplitude and frequency; the characteristic frequency increases also with the air flow rate, although more slowly.

The variation in the flow structure is highlighted also by the histogram of turbine and drag signals (Fig.6.11): the Gaussian, that characterized the signal dispersion at low water fluid flow, evolves in a bimodal function for increasing water flow rate.
It is possible to conclude that the analysis of the time signal variation, together with the frequency analysis (Fig.6.12), gives important information that can be used to predict the flow pattern.

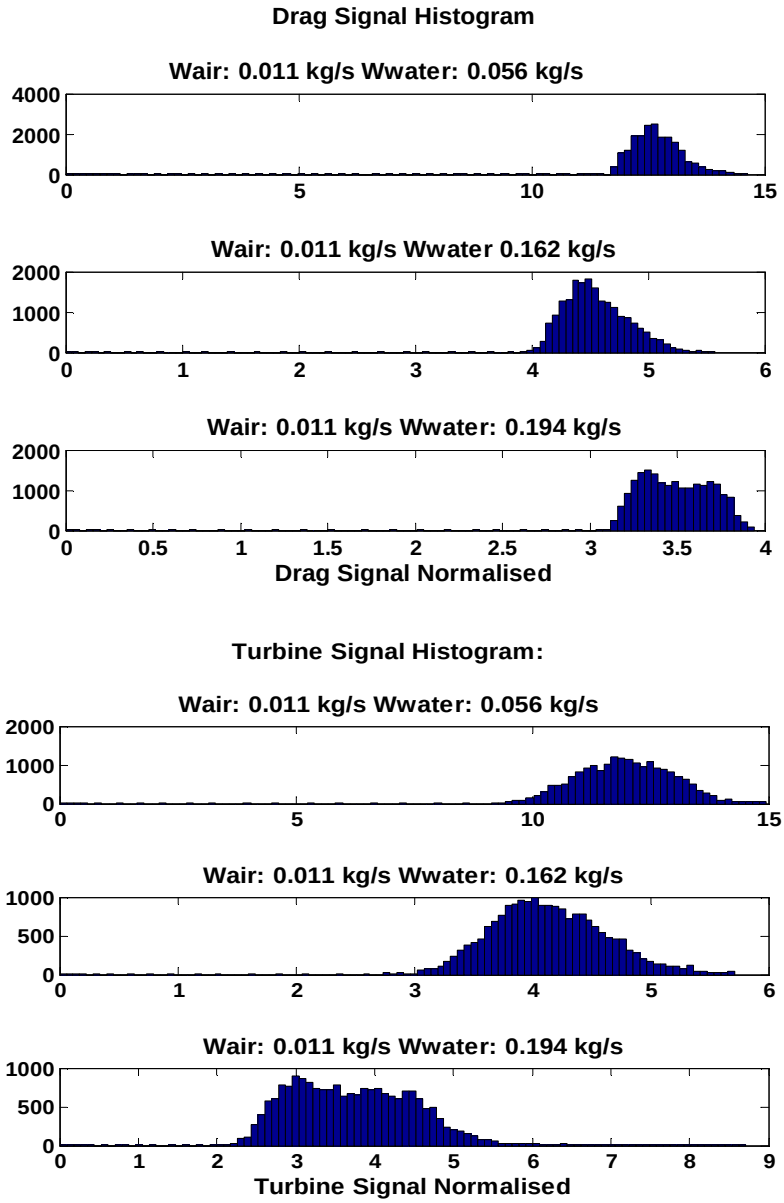

Fig.6.11: Signal Histograms

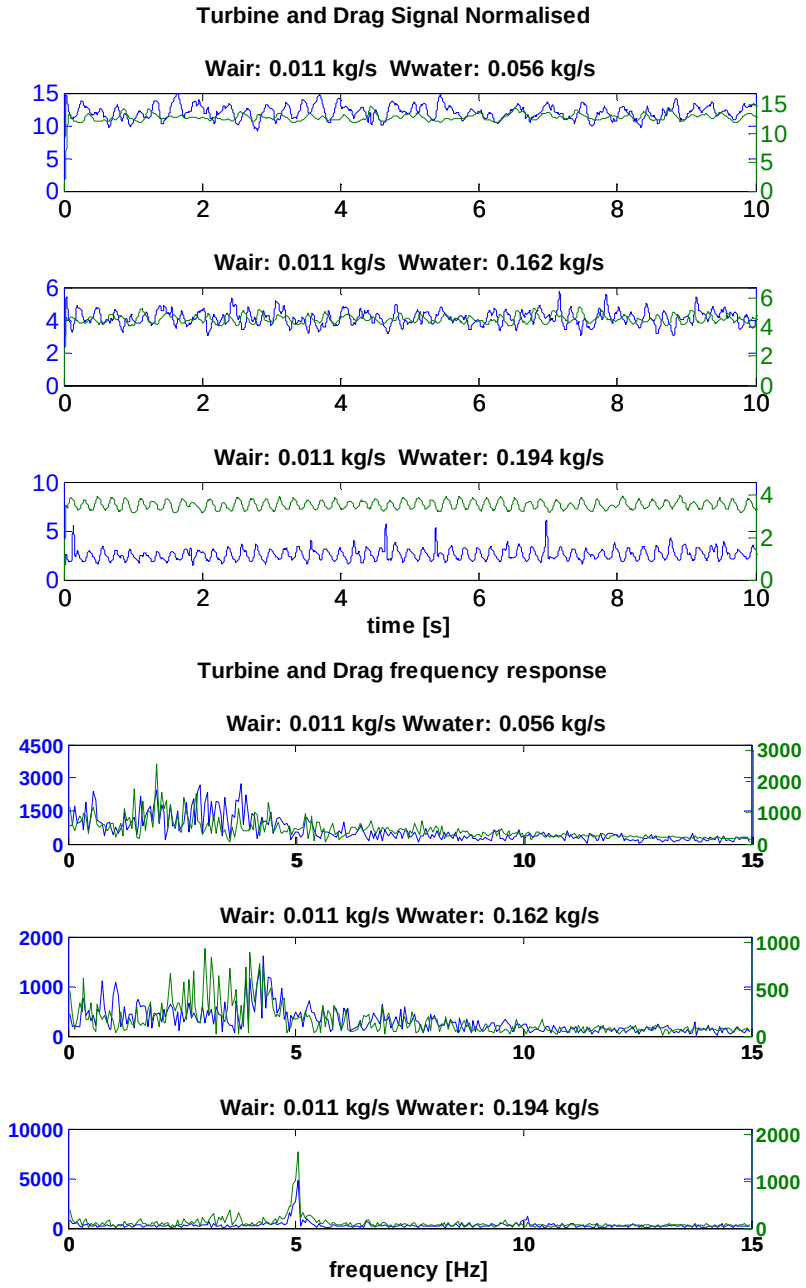

Fig.6.12: Time and Frequency Signal Analysis

A theoretical model, suitable for describing the SP operation, is represented by a set of relations that, based on turbine and drag electric signals, is able to evaluate the mass flow rates of the two phases of the mixture.

The Aya's model [6.4] allows the estimation of the mass flow rate of dispersed two-phase flow (with the gas velocity higher than the liquid velocity (Slip condition)) by using the electric signals of a SP constituted by: a densitometer, a drag disk, and a turbine meter.

Combining the equations of the two instruments equation (TFM: eq. 4.7 and DD: eq. 4.11) and the information concerning the void fraction, it is possible to evaluate the mass flow rate of the two phases.

The model proposed by Aya requires as input the turbine and the drag signals, as well as the two-phase mixture density.

To estimate the void fraction an additional information concerning the slip ratio *S* is required (eq. 3.12).
Thom [6.7] gives the *S* value as a function of the pressure and of the phases density ratio (Fig.6.13).
In this work the ratio between water density and air density ranges between 480 and 780, then the slip value can be estimated between 3 and 5.
Using these values of the Slip ratio, a parametric application of the Aya model is proposed in order to evaluate the difference between the experimental mass flow rates and the flow rates calculated using the model.
The results of the analysis are presented in Fig.6.14; the Aya's model is able to predict the mass flow rates of the phases with an error of the 15%.

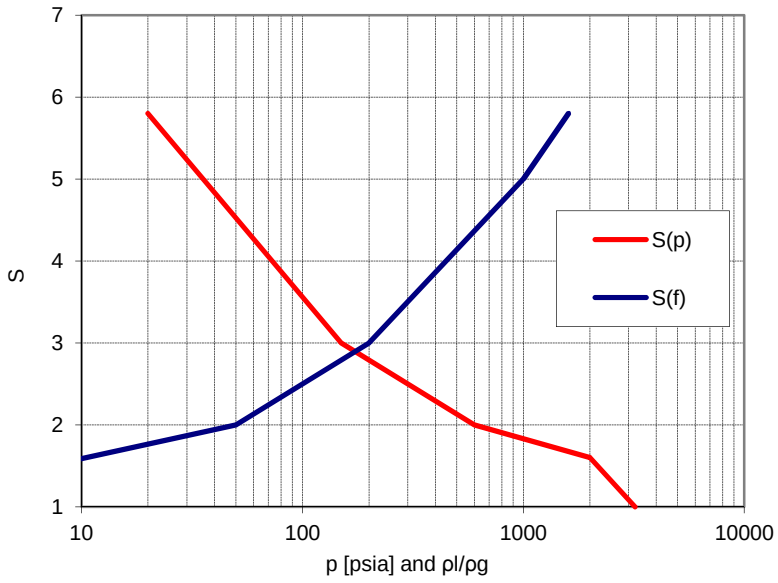

Fig.6.13: Slip ratio determined experimentally by Thom [6.7]

Fig.6.14 (a) shows that the Slip value decreases with the air flow rate; the reduction is probably due to the fact that at low air flow rate the flow pattern is stratified and then the velocity differences between the phases is high. Increasing the air flow rate, the percent of the liquid flow rate entrained and dragged in the gaseous core raises, and then the mean liquid velocity approach the mean air velocity.
Concerning the SP analysis, the flow can be divided in 3 operating region: annular flow with high slip ratio (low water flow rate), annular flow (with high water and air flow rate) and stratified flow at high water flow rate.

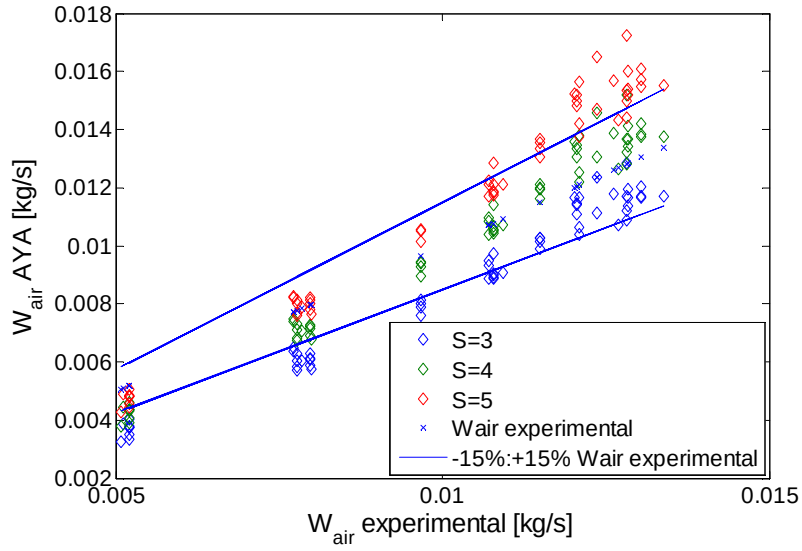

(a)

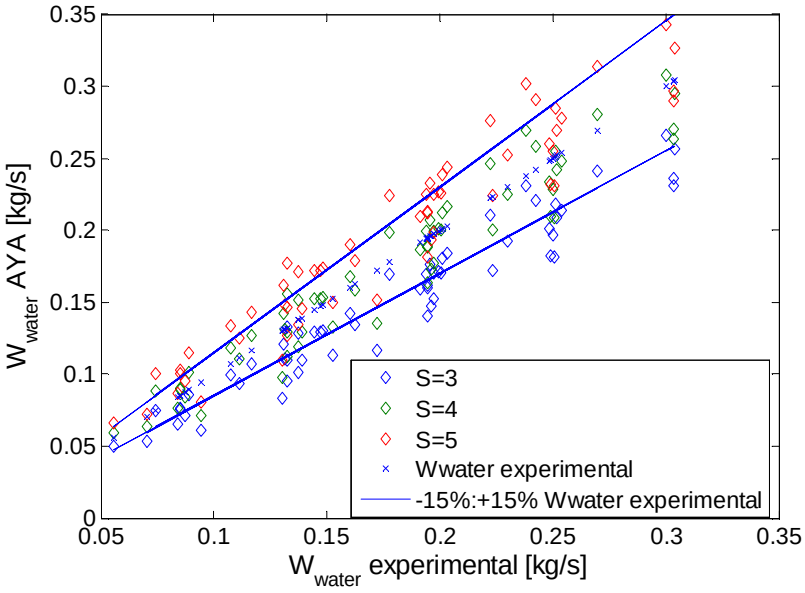

(b)

Fig.6.14: W_g and W_l calculated through the Aya's model

6.2 Second experimental campaign

The analysis and the processing of the electric signals of the SP described in 6.1, allowed the characterization of the flow in terms of flow pattern and mass flow rates of the two phases. The analysis highlighted also the fundamental role of the pressure concerning the flow pattern and the void fraction value of the mixture.
In order to improve the knowledge of the instruments, and complete the study concerning the present Spool Piece, a new analysis has been carried out using a Spool Piece made up of 3 instruments.
The aim of this study is the experimental and theoretical analysis of horizontal air-water flow using a Spool Piece consisting of a turbine, a drag disk and an impedance probe to measure the flow rate and the void fraction; the pressure and the temperature are also measured.
The experimental data are used to establish an operating map of the SP, able to evaluate the mass flow rates of the phases in the mixture by means of the Aya's model, with the related errors.

6.2.1 Test section

In Fig.6.15, the position of the instruments along the test section is shown: 1- Impedance probe, 2- Turbine and 3- Drag Disk.

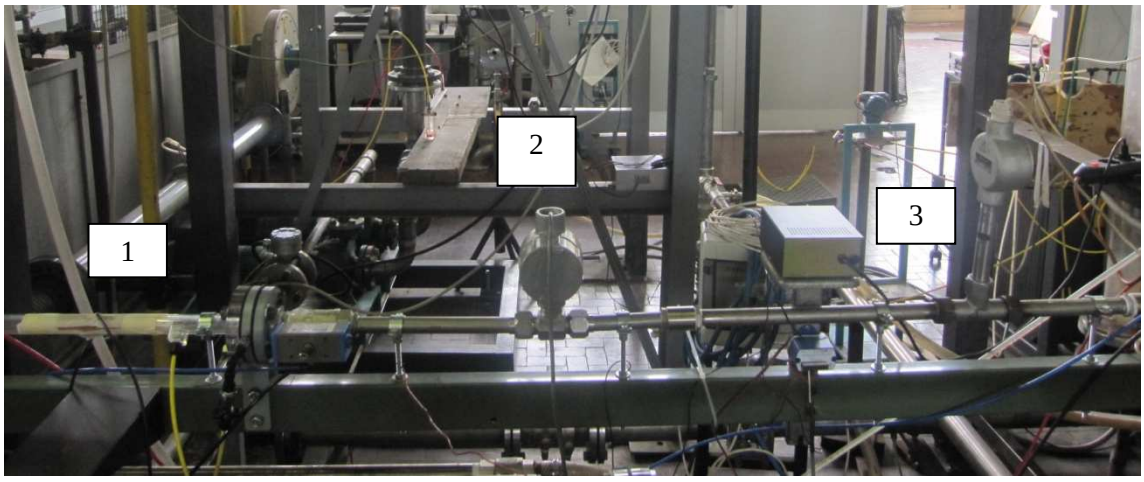

Fig.6.15: Experimental test section and SP instruments

The same water feed loop described in 6.1 has been used there. For high water flow rate (higher than 400 l/h), the water flow rate is provided using the pumps; in this case water enters the test section axially, through a pipe of 21 mm that connects the main loop to the feed water loop.
Lower water flow rates are obtained using both the potential energy of the water that is stored inside the tank (flow rate lower than 100 l/h), and by means of the pumps (flow rate lower than 400 l/h). In this case, water enters the test section radially, through a pipe of 10 mm that connects the mixer to the feed water loop.
The air flow rate is provided by the air net (flow rate lower than 5000 Nl/h at p=6 bar), or by means of a compressor (flow rate lower than 35000 Nl/h at about atmospheric pressure).
The test section, which has a total length of 4800 mm, is made up of the SP installed between two Plexiglas pipes having a length of 1200 mm. In the second Plexiglas pipe two

quick closing valves (QCV) have been installed in order to measure the mean volumetric void fraction. Other two QCV have been installed in the SP section.

6.2.2 Turbine Flow Meter

The turbine, manufactured by Hoffer, is inserted between an upstream length of 290 mm (15 D) and a downstream length of 180 mm (about 8.6 D).
The present model of the Hoffer turbine flow meter differs from that one described in 6.1 due to the incorporated microprocessor. The preamplifier accepts the input from the flow meter. The Preamplifier applies amplification, low-pass filtering, and wave-shaping to the input signal. The wave shaping function converts the signal into a square-wave before sending it to the Microcontroller.
The Microcontroller, PCA183, accepts the square-wave output of the preamplifier and performs all the calculations that are required to control the Loop Driver. After measuring the frequency of the square-wave, the Microcontroller computes the flow rate.

6.2.3 Single-phase Turbine Flow Meter calibration

The water single-phase calibration curve is shown in Fig.6.16, based on the experimental curve the water single-phase parameter K_T has been calculated equal to 2100 $V \cdot s/m^3$.

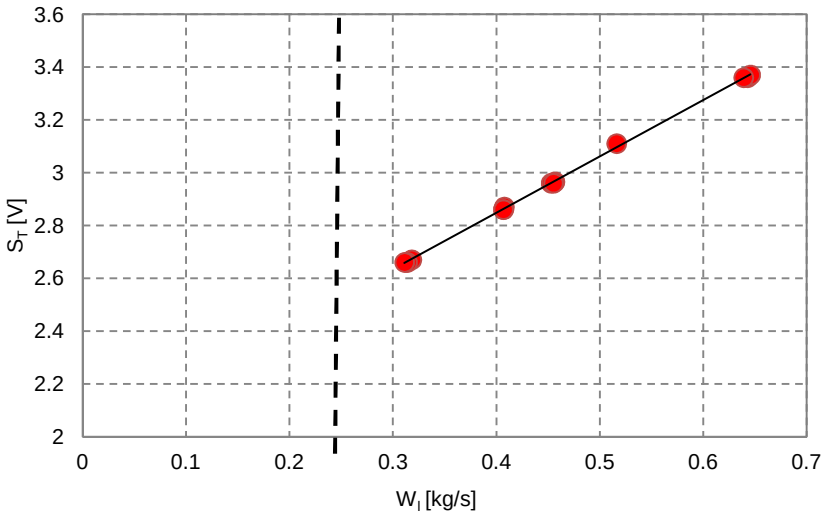

Fig.6.16:Turbine signal [V] vs. mass flow rate of water [kg/s]. Single-phase (water)

The dotted line (Fig.6.16) indicates the minimum water flow rate (single-phase flow) where the turbine is designed to work. The operating range is 900-13600 l/h or 0.25-3.8 kg/s. In this range the output signal is related linearly to the mass flow rate of the fluid.
The single-phase air coefficient is not evaluated in the present experimental campaign, due to the instable behavior of the turbine flow meter for air flow in the experimented range.

6.2.4 Drag Disk

The same instrument described in 6.1 has been used.

6.2.5 Impedance Probe

The impedance probe, installed in the SP, consists of two concave externally mounted electrodes having a length of 166 mm and a width of 18 mm. The two electrodes are installed at 180° along the axial length of the pipe (one electrode in the pipe bottom and one in the upper part of the pipe)
Because of the presence of water (conductive fluid) and because of the excitation frequency used (167 kHz), the system cannot be considered as purely capacitive. Then the equivalent impedance is given by a resistive component (R) and a capacitive component (X_C):

$$Z_{eq} = R + jX_C \tag{6. 4}$$

The model of the system (wall + fluid phases' distribution) has to be analyzed as an electrical system constituted by a network of resistances and capacitances connected in series and/or in parallel. The values of R and C depend on electrical properties of the materials and also on the geometry of the system.

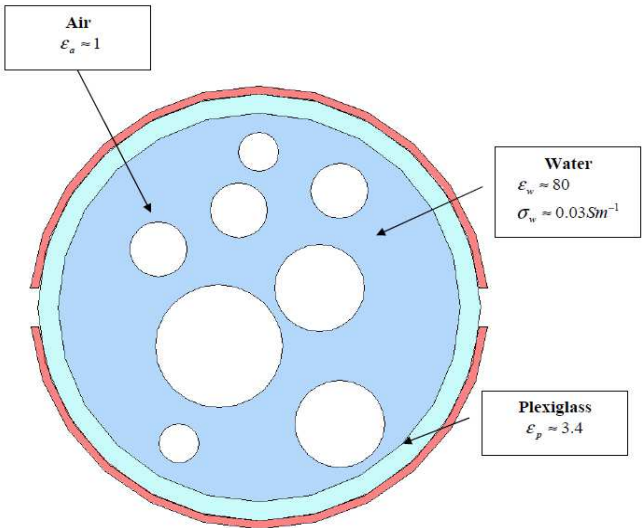

Fig.6.17: Scheme of the measurement cross-section and electrical properties of the materials

Fig.6.18 and Fig.6.19 show the electrical schemes adopted to generate an analogical electrical signal function of the impedance probe.
It consists on a signal which provides a sine wave, 5Vpp/167kHz applied to one of the two electrodes. The output signal (voltage between the electrodes) is sent to an amplifier, a full wave rectifier and a low pass filter (100Hz) and then sent, by the National Instruments DAQ system, to the computer.

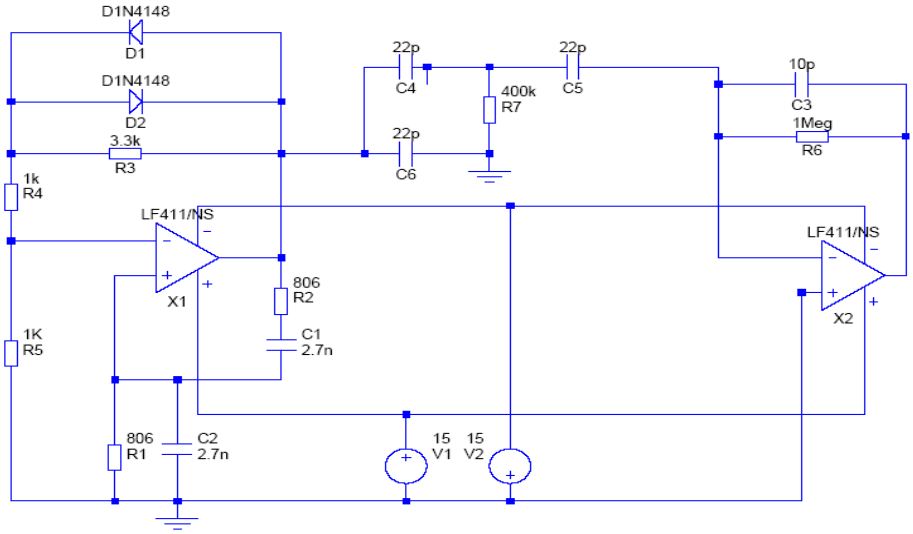

Fig.6.18: Electrical scheme. Oscillator

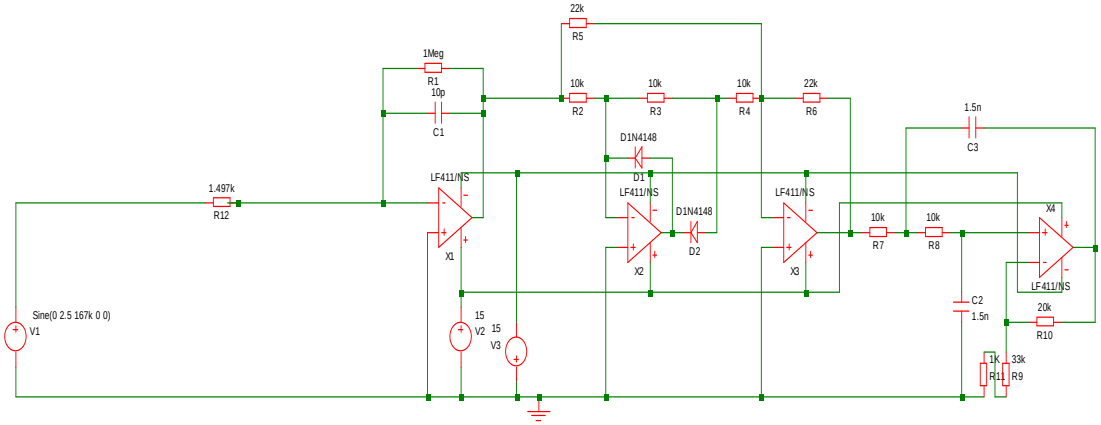

Fig.6.19: Electrical scheme. Measurement system

6.2.6 Measurement methodology and experimental flow rate range

In the present experimental campaign, the water flow rates range between 0.0632 and 0.6 kg/s and the air flow rates between $9.1 \cdot 10^{-5}$ and $4.4 \cdot 10^{-3}$ kg/s.

The mixture of air and water is prepared in a mixer pipe (D_i = 21 mm) where air enters along the radial direction and water along axial and/or radial pipe direction.

Single-phase flow rates are measured before the inlet section (pressure and temperature in the rotameter are measured for each run in order to correct the volumetric air flow rate).

In the test section, the absolute pressure at the inlet of the SP is measured using an absolute pressure transducer Rosemount 3051/1 operating in the range between 0.5-10 bar. Hence, pressure drops in the SP and in the second or first Plexiglas section have also to be measured.

The SP instrument signals (turbine, drag disk, impedance probe) and the pressure signals are gathered with a National Instruments DAQ system (NI USB-6218) using LabView® environment. The signals are acquired for 30s, using a sample frequency of 1kHz.

At each run the volumetric void fraction is measured by means of the QCV technique after the signal acquisition. The volumetric void fraction is measured 5-10 times at the same flow condition in order to have a sufficient statistics.

6.2.7 Two-phase flow experimental results

Impedance Probe

The tests provided data points for 0.2<α<0.9. The observed flow patterns have been related with the measured void fractions: bubbly and slug flows are confined to low-range flow quality with void fractions ranging between 0.2-0.45 and 0.45-0.7 respectively, while annular flow has been observed in such flows characterized by a void fraction ranging between 0.7 and 0.9.
The impedance probe analysis has been performed comparing the signal with the experimental volumetric void fraction measured by means of the QCV technique (Fig.6.20).

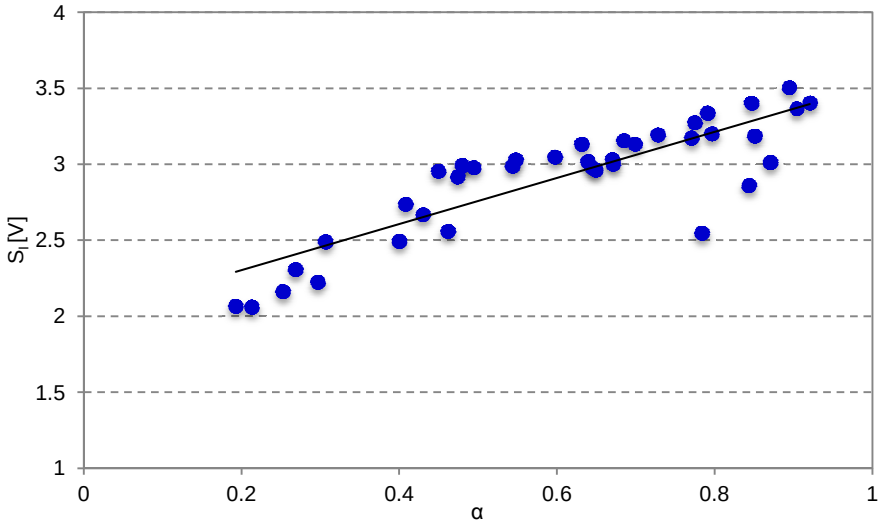

Fig.6.20: Impedance vs. void fraction

A linear relationship between impedance signal and volumetric void fraction can be used for the points of Fig.6.20. The linear regression curve is given by:

$$S_I = 1.5505 \cdot \alpha + 2 \qquad (6.5)$$

characterized by a correlation coefficient $R^2 = 0.80277$.

The relative error is shown in Fig.6.21.

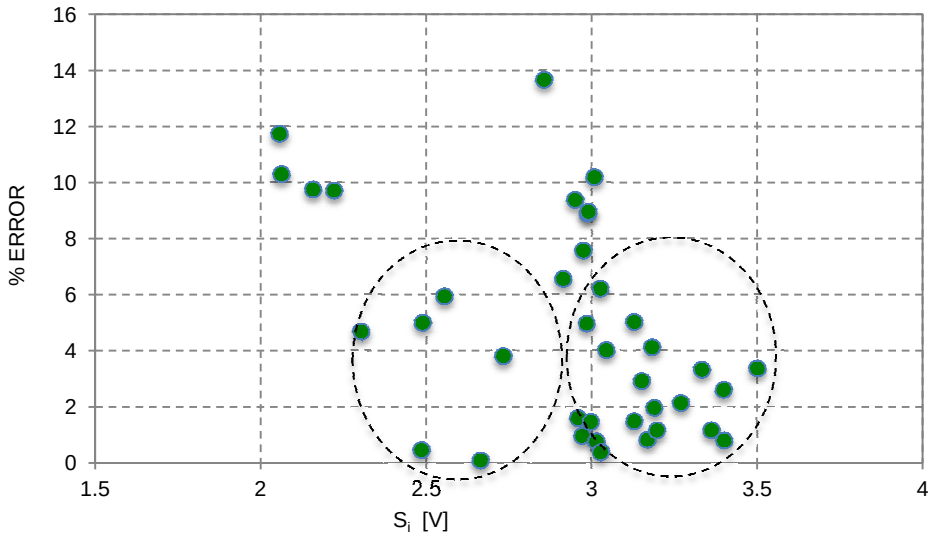

Fig.6.21: Void fraction estimation errors

The analysis of Fig.6.21 allows the identification of the flows characterized by higher estimation errors: the samples are divided into groups depending on the flow pattern and for each group a new linear regression is obtained (Tab.6.2 and Fig.6.22).

Flow pattern	Expression	R^2
Bubbly/Plug/Intermittent	$SI[V] = 2.9496 \cdot \alpha + 1.4553$	0,8634
Annular	$SI[V] = 1.2631 \cdot \alpha + 2.3049$	0,8632
Slug	$SI[V] = 1.7624 \cdot \alpha + 1.8511$	0,8417
Stratified/Slug (High velocity)	$SI[V] = 6.3363 \cdot \alpha - 2.4034$	0,8888

Tab.6.2: S_I [V] – α linear best fit equations for different flow patterns

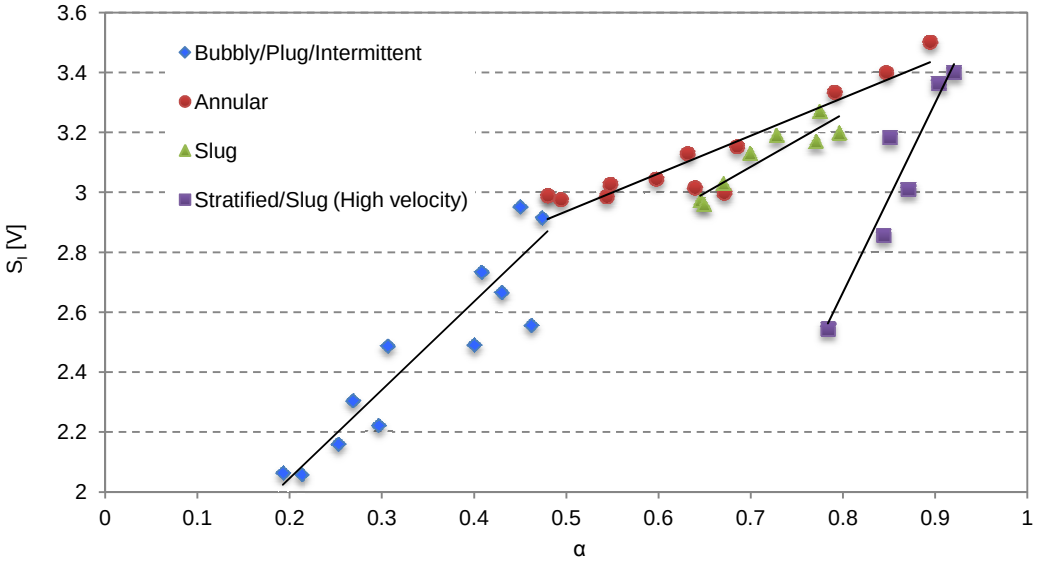

Fig.6.22: S_I [V] vs. experimental void fraction. Parameterized by flow pattern

With the same aim, in Fig.6.23 the comparison between experimental and estimated void fraction is reported. The performed analysis allows the estimation of the void fraction with a maximum error lower than 14%.

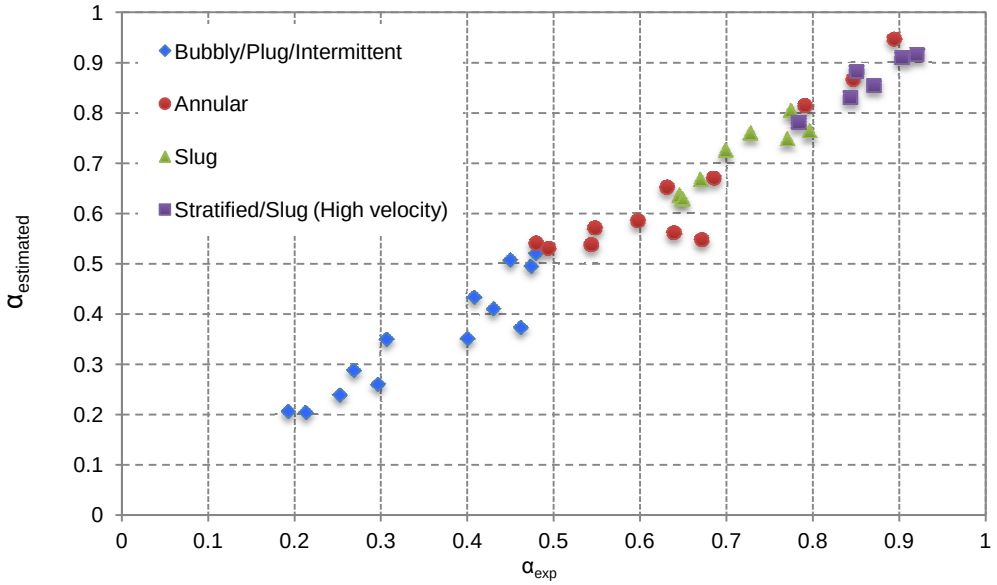

Fig.6.23: Experimental void fraction vs. estimated void fraction

Turbine Flow Meter

The dependency of the TFM signal on the mass flow rate of the phases is analyzed in Fig.6.24.

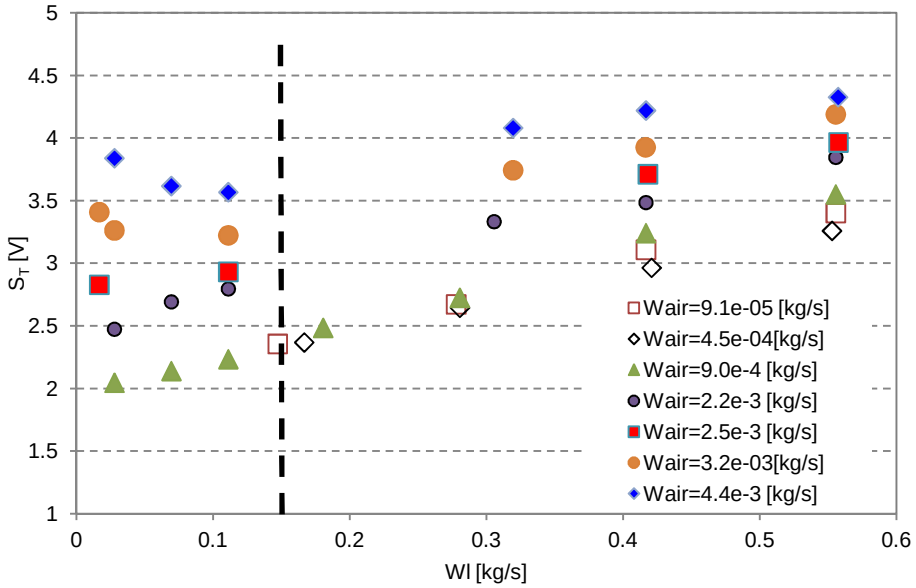

Fig.6.24: S_T [V] vs. water mass flow rate [kg/s]. Parameterized by air mass flow rate [kg/s]

Depending on the fraction of air/water mass flow rate and therefore depending on the void fraction, there are important differences in the response of the turbine flow meter. It can be noticed the non-linear behavior at lower water flow rate. The turbine is designed to work for water single-phase flow rates between Q_l=900-13600l/h or W_l=0.25-3.8 kg/s; in two-phase flow conditions this range appears to be extended at lower mass flow rate values, and the linear behavior is extended up to 0.15 kg/s.

The non linear behavior is evident for air mass flow rates higher than $2.53 \cdot 10^{-3}$ kg/s; at these air flow rates a decreasing signal is highlighted for mass flow rate of water lower than 0.15 kg/s, while an increasing signal corresponds to water flow rates higher than this threshold value. For lower values of the air flow rate the signal increases with a monotonic behaviour.

Drag Disk

As described for the turbine flow meter, also for the drag disk the signal dependency on the mass flow rate of the two phases has been analyzed as shown in Fig.6.25.
The quadratic relationship between mass flow rate and sensor signal is observed at all the experimented flow rates. The signal of the drag disk tends to increase with both the air flow rate and water flow rate.

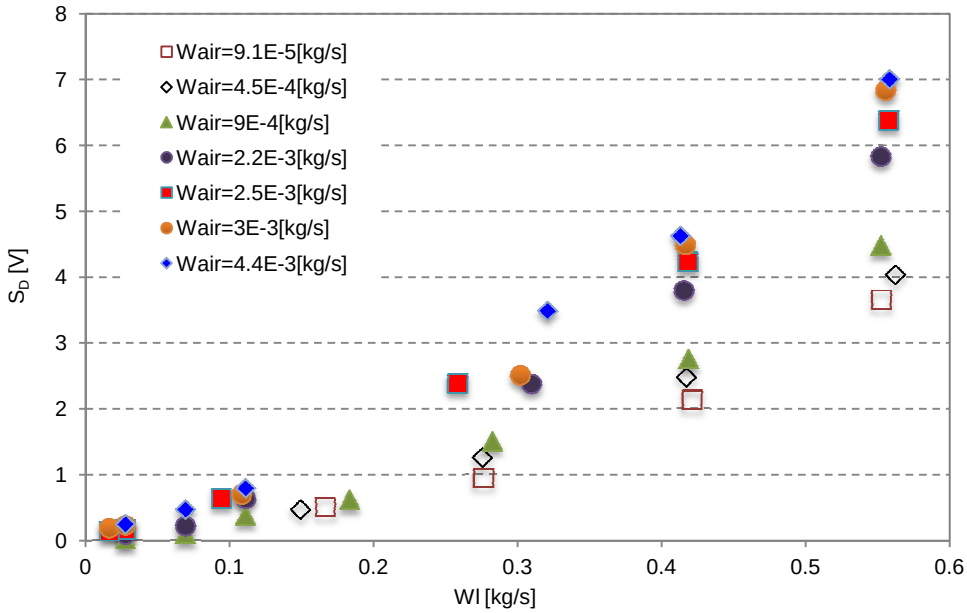

Fig.6.25: S_D [V] vs. water flow rate [kg/s]. Parameterized by air mass flow rate [kg/s]

6.2.8 Aya's model

The Aya's model has been used, to calculate the mass flow rate of the two phases, adopting in this case a turbine coefficient equal to the water single-phase flow coefficient, and evaluating the void fraction by means of the developed model of the impedance sensor. In the following, a critical analysis of the results is presented.

Fig.6.26 shows that most of the points calculated with the model of Aya are in the range of 15% of error, which means that the data has been obtained correctly.
In Fig.6.27 the comparison between the experimental water mass flow rate and the values estimated by the Aya's model is shown.

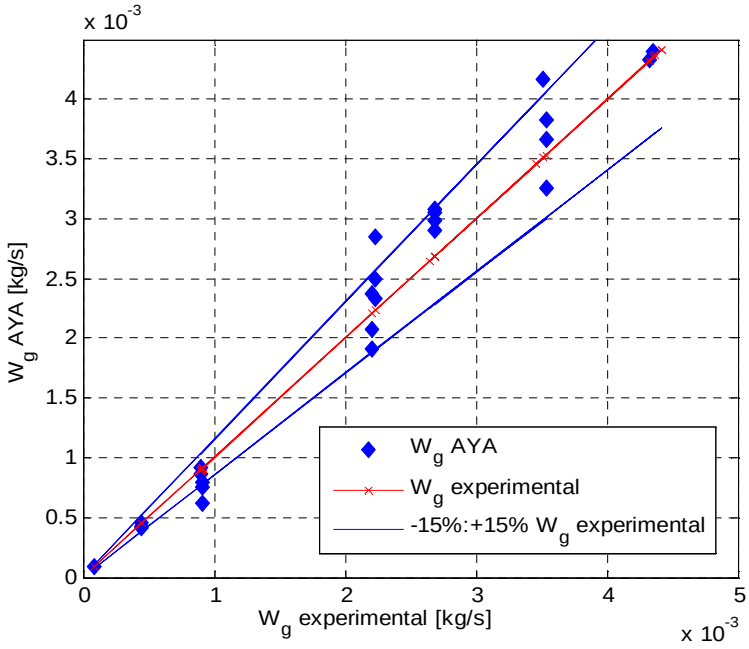

Fig.6.26: W_g experimental vs. W_g Aya's model

.

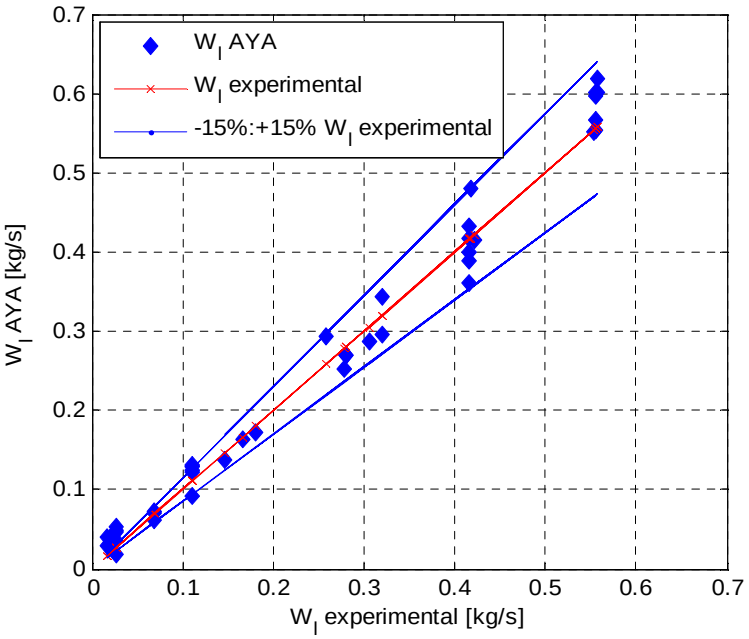

Fig.6.27: Wl experimental vs. Wl Aya's model

Also in this case for the 70% of the runs the mass flow rate is estimated with an accuracy of 15%. The larger errors are observed for the lower values of the mass flow rate, where the effect of the air flow rate value is more relevant.

6.3 Conclusions

In the first experimental campaign the SP made up of a turbine flow meter and a drag disk has been analyzed under annular and stratified annular air-water two-phase flow. The analysis and the processing of the electric signals of the SP, allowed to characterize the flow in terms of flow pattern and mass flow rates of the phases.
Although in the test section a void fraction measurement device is not present, the proposed method allows us to evaluate the mass flow rate of air and water in the two-phase mixture, with an accuracy of 15%, in the experimented range. The analysis of the signal time evolution shows that important information concerning the flow pattern can be extracted from it and then a model of the SP that takes into account this information can be developed.
The parametric analysis, performed by the Aya's model, has shown that, in the tested operating range, the knowledge of the flow pattern, and then of the void fraction, is indispensable to evaluate the two-phase flow parameters.
In the second experimental campaign, the SP has been completed with the third instrument able to measure the void fraction of the flow. The impedance sensor signal has been analyzed as a function of the flow parameters and the signal has been compared with the experimental volumetric void fraction measured by means of the QCV technique. The analysis shows that in the present configuration a linear relationship between void fraction and impedance sensor can be used, but the knowledge of the flow pattern is fundamental for a proper signal interpretation.
The experimental data have been used to construct an operating map of the SP, able to evaluate the mass flow rates of the phases in the mixture, with the relative errors, and to predict the flow pattern.
Compared with the first experimental campaign the new data cover a wider range of flow superficial velocities, corresponding to different flow pattern from bubbly to annular flow.
The existence of a non-linear area in the response of the turbine when working with single-phase flow at low water flow rate has been highlighted; if the measurement range is extended to the non-linear region in two-phase flow, a different behavior and performance of the Spool Piece has been noticed.
Moreover, the present analysis has highlighted the strong influence of the electronics of the instruments on the behavior of the Spool Piece; in particular, considerable differences have been marked in the response of the turbine flow meter, using analogic signal conditioning or digital signal conditioning.

The measurement of the void fraction allows the use of the Aya's model in all the experimented range, obtaining the mass flow rate of the phases with an accuracy of 15% in the 75% of the cases.

7. SPOOL PIECE: VENTURI FLOW METER AND WIRE MESH SENSOR

In the previous analysis the SP made up of three instruments has been modeled and tested and the fundamental role of the void fraction measurement has been highlighted. The second SP analyzed is made up of two instruments: a Venturi Flow Meter (VFM) and a WMS. The possibility to develop a SP made up of only two instruments is a fundamental task for an industrial facility because a lower number of instruments allows the reduction of costs, complexity and space requirements. On the other hand, it requires the introduction of theoretical or empirical models able to compensate for the lacking of information. As the response of a meter in a two-phase flow tends to be highly sensitive to the flow pattern, to the upstream configuration and flow history, one of such instruments has to be able to measure the void fraction. Wire Mesh Sensors (WMS), based on the measurement of the local instantaneous conductivity of the two-phase mixture, are used for the evaluation of local void fraction, bubble size distributions and gas velocity distributions. The WMS has been used, in different geometry and for different configurations, to study mean cross-section void fraction and gas profile evolution [7.1].

The calculation of fluid flow rate by reading the pressure drop across a pipe restriction is perhaps the most commonly used flow measurement technique in industrial applications. Compared with single-phase flow, the pressure drops in two-phase flow increase due to the interaction between the gas and the liquid phase; for this reason the value of the effective two-phase mass flow rate must be estimated using available correlations derived from experimental data or semi-empirical models.

In the present chapter, the results of the experimental work carried out to analyze the response of a SP made up of a VFM and a WMS are shown. The SP has been tested in a horizontal test section for air-water flows in a large range of phases mass flow rates. The methodology for the signals interpretation, the developed model of the SP for the phases mass flow rates estimation and the results are presented and discussed.

7.1 Experimental facility and test matrix

The test section described in the chapter 6 has been modified with the insertion of the second SP Fig.7.1. It consists of a 19.5 mm diameter and 7 m long pipe. The SP is installed at L/D = 192 from the entrance; the WMS is installed between two Plexiglas pipes having a length of 600 mm, while the VFM is installed between two Plexiglas pipes having a length of 500 mm and 490 mm upstream and downstream respectively. The inlet pressure ranges from atmospheric pressure to 4 bar depending on the experimental conditions. The flow is discharged at atmospheric pressure. The experimental test section is equipped with two quick closing valves (QCV) that allow the measurement of the volumetric void fraction in a length of 1300 mm.

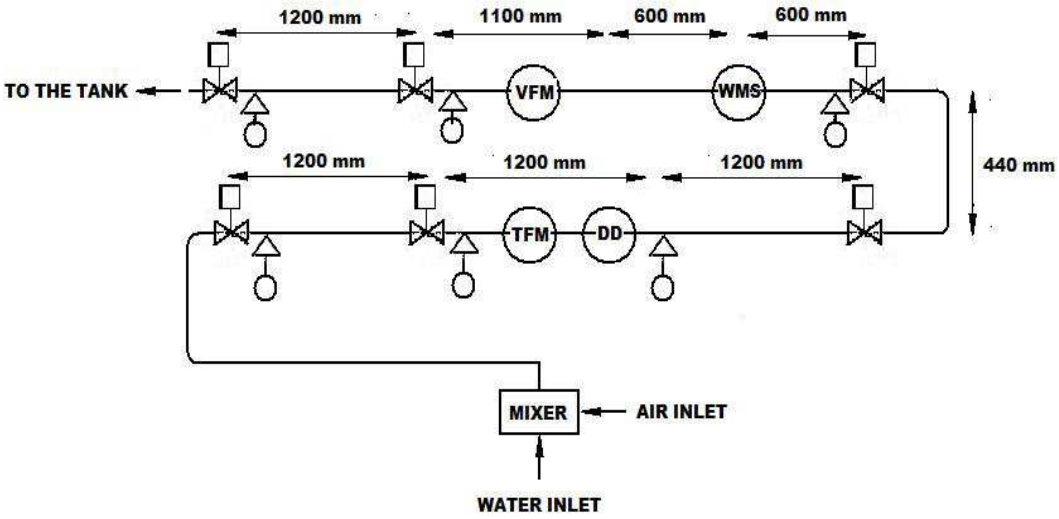

Fig.7.1: Test section schematic

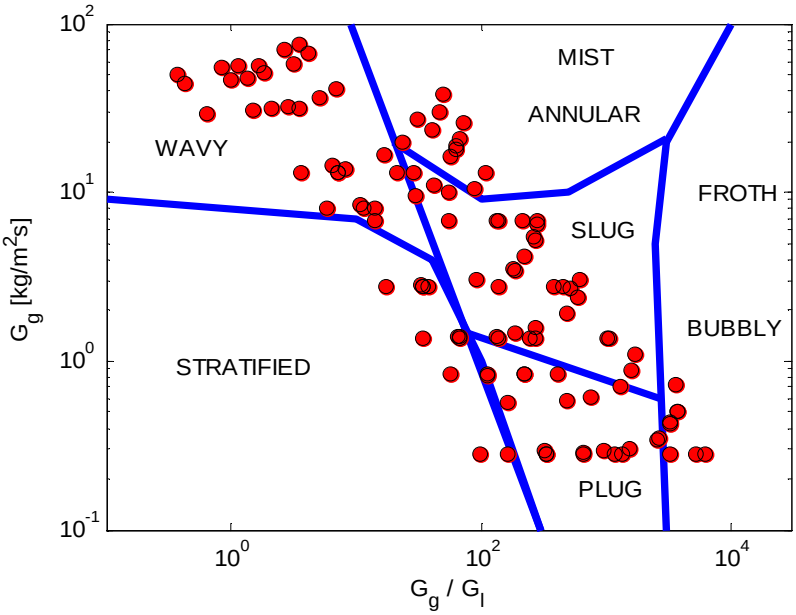

Fig.7.2: Baker's Map [7.4] prediction of Flow Patterns

The pressure drop in the VFM is measured by means of two differential pressure transducers having two different working range: -40÷40 mbar and 0÷1250 mbar. The instruments signals

are acquired in a LabView® environment by the National Instruments DAQ (Digital AcQuisition) system (NI USB-6218). The WMS signals are instead acquired by means of the sensor software, synchronizing the measures through a trigger. The signals have been acquired using a frequency f = 1250 Hz for all the instruments for a total acquisition time of 20 s. Instruments characterization in single-phase flow of air and water has been performed. Two-phase experiments have been carried out at water temperature of about 20 °C. The flow quality ranges from 0 to 0.73 and the superficial velocity from 0.14 to 32 m/s for air and from 0.019 to 2.62 m/s for water. The typical observed flow patterns were stratified flow, intermittent flow (slug and plug) and annular flow. The population of samples ranges over different flow patterns and it is more representative of intermittent flow regime and annular wavy flow regime. From visual observation and maps results (Fig.7.2) it also clear that some runs have been performed in transition regimes.

7.2 Spool Piece

7.2.1 Wire Mesh Sensor geometry and signal processing

As described in chapter 4, the basic working principle of the sensor is the measurement of the conductivity of the fluid. Because air and water have different electrical properties (tap water is high conductive while air is very low conductive) the measurement of the conductance can be analyzed to detect the presence of each phase inside the pipe.
The sensor used in the present work has been described in the paragraph 5.2. The WMS sensor signals are acquired by means of WMS200 electronics and processed in Matlab® environment.
The output signal *V(i,j,k)* is analyzed in order to obtain the mean cross sectional value of the void fraction, that is used to model the response of the VFM.

The local instantaneous void fraction (eq. 4.60 - 4.61) has been obtained with an acquisition frequency f_{acq} equal to 1250 Hz for a total observation time T_T equal to 20 s, so that the value of k ranges from 1 to k_T, where k_T is the total number of measured frames, equals to $f_{acq} \cdot T_T$.

The averaged time cross-sectional void fraction is obtained by averaging over the observation time and over the measuring section:

$$\langle \alpha \rangle = \frac{1}{k_T} \sum_{k=1}^{k_T} \frac{1}{A_p} \sum_{i=1}^{16} \sum_{j=1}^{16} \alpha(i, j, k) \qquad (7.\ 1)$$

where A_p is the pipe cross section.

7.2.2 Experimental void fraction analysis

The experimental void fraction has been then compared with different literature correlations, in order to define an analytical relation between the experimental values of α-x.

The curves of Fig.7.3 represent the void fraction dependency on the flow quality expressed by the correlations of Lockhart-Martinelli, Baroczy, Chisholm and Wallis, reported in Tab.3.1.

From the comparison shown in Fig.7.3 it can be concluded that the Lockhart-Martinelli correlation and Wallis correlation give a good estimation of the experimental data at flow qualities higher than 10^{-2}; while, the estimation accuracy decreases for lower flow quality values.

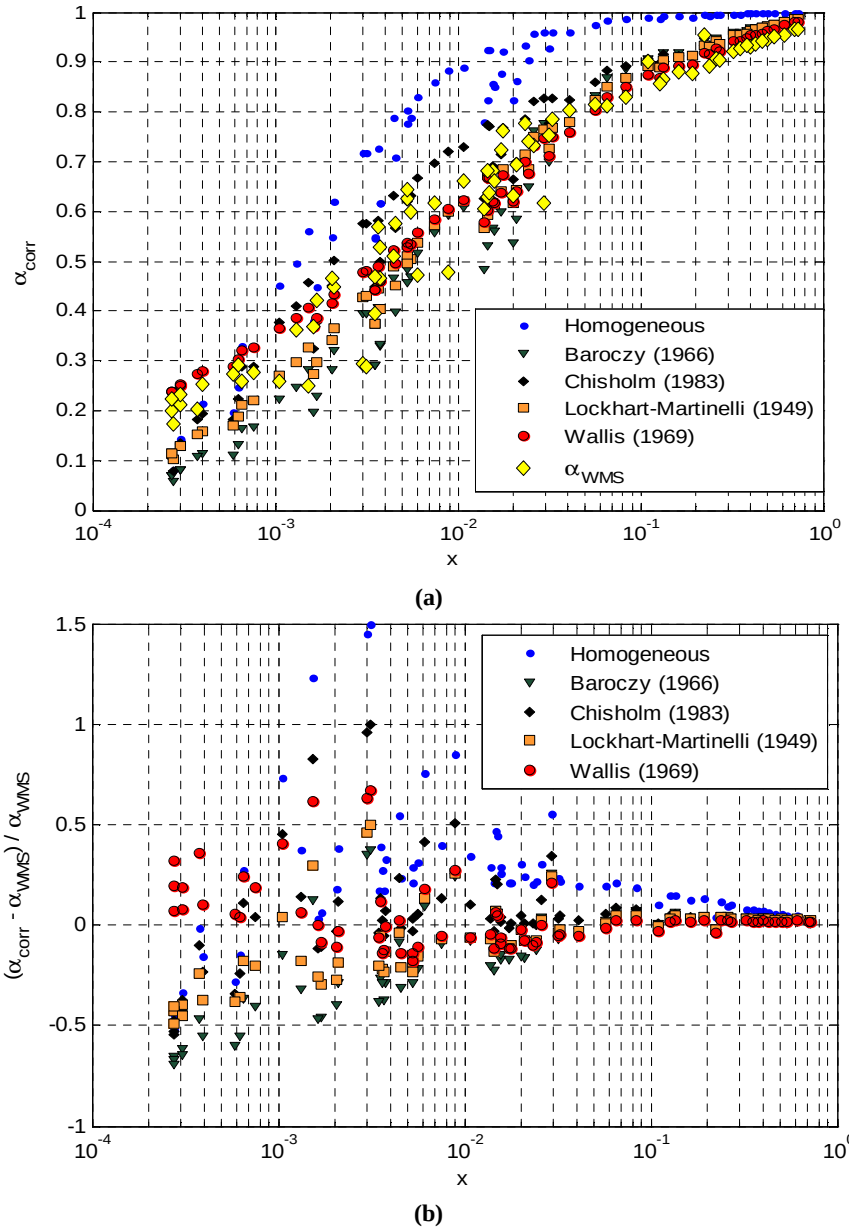

Fig.7.3: x-*α* correlations (a) and relative deviations from WMS void fraction values (b)

7.2.3 Venturi Flow Meter

The characteristics of the tested Venturi flow meter are shown in Tab.7.1.

Type Herschel (Fluid: Water)		
D_1	26	mm
D_2	10.251	mm
B	0.394	-
Δp	68.6 (700)	mbar (mmH_2O)
W_{water}	300	g/s
$L_{upstream}$	500	mm
$L_{downstream}$	490	mm

Tab.7.1: VFM Data

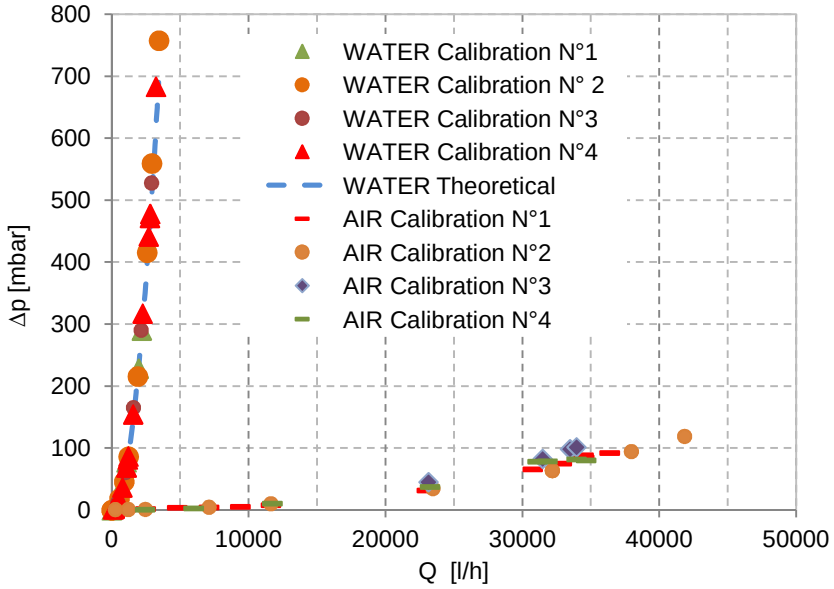

Fig.7.4: VFM single-phase calibration

The calibration results are shown in Fig.7.4 and Fig.7.5 where the discharge coefficient, obtained in air and water single-phase flow, is represented as a function of the Reynolds number.

The experimental discharge coefficient has been found equal to 0.94 in water flow and 0.97 in air flow, at Reynolds numbers higher than 15000 and shows a fast decrease for lower values.

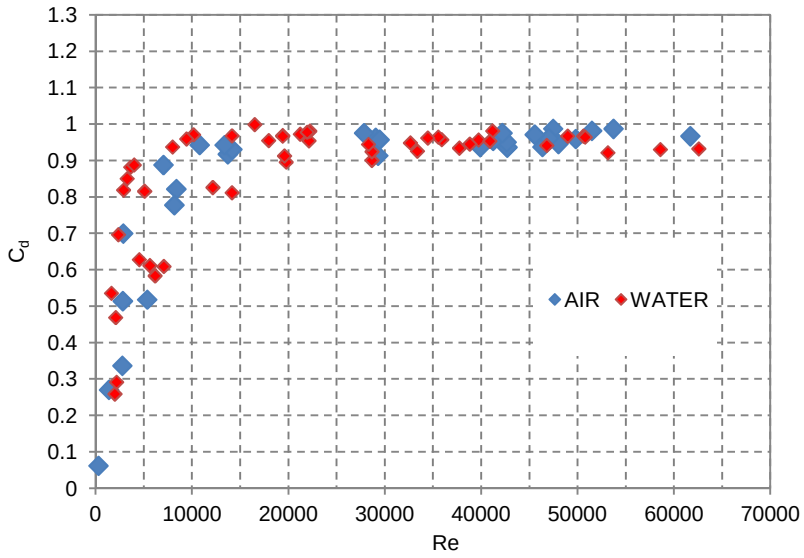

Fig.7.5: Single-phase VFM discharge coefficient

With reference to the eq. 4.17 and 4.18, considering the value of Y and F_a equal to one, the two parameters, that have to be defined, are the two-phase discharge coefficient and the two-phase density.

The VFM *reference density* has been evaluated analyzing the instrument response in terms of estimated flow rate and comparing the discharge coefficient obtained in single-phase flow and the discharge coefficient obtained in two-phase flow characterized by the three densities: Homogeneous density, Separated flow density, Momentum density.

The density obtained with the three models is reported in Fig.7.6 as a function of the flow quality.

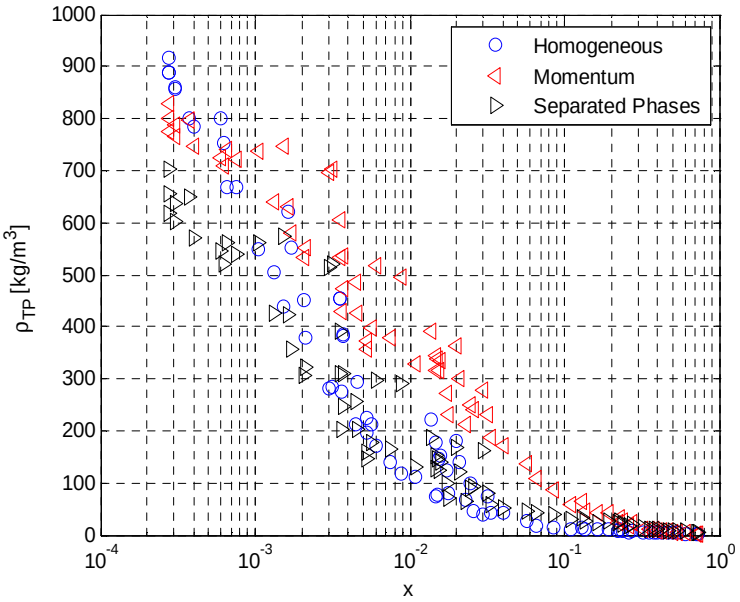

Fig.7.6: Two-phase flow density, calculated with theoretical models as a function of the flow quality

Introducing the calculated densities in eq. 4.17 and imposing the value of $C_{d\text{-}TP}$ to one, it is possible to estimate the total mass flow rate of the mixture. In Fig.7.7 the comparison between the experimental total mass flow rate and the three estimated values is shown.

As shown in Fig.7.8, the related two-phase flow discharge coefficients, evaluated by eq. 7.2

$$C_{d-TP} = \frac{W_{tot}}{F_a \cdot Y \cdot A_2} \cdot \left(\frac{\left(1-\beta^4\right)}{2\rho_{TP}\Delta p_{TP}} \right)^{0.5} \qquad (7.\ 2)$$

are characterized by different dispersion ranges. The coefficient evaluated considering the momentum density shows a very low *standard deviation*, and a behavior similar to the single-phase flow coefficient.

The analysis allows us to conclude that the *reference density* for the VFM is momentum density, defined in the paragraph 3.2, and this density is used to analyze the VFM response.

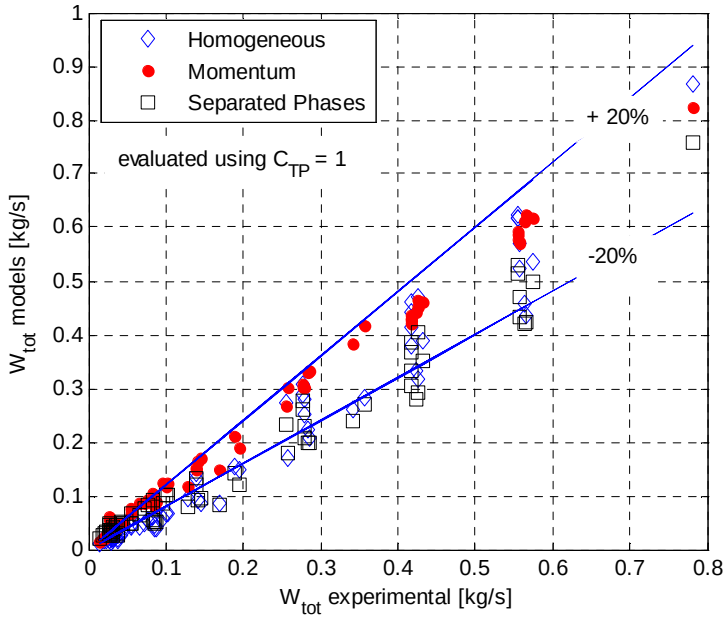

Fig.7.7: Experimental two-phase Wtot vs. Wtot evaluated by the analysis on the VFM with different density definitions

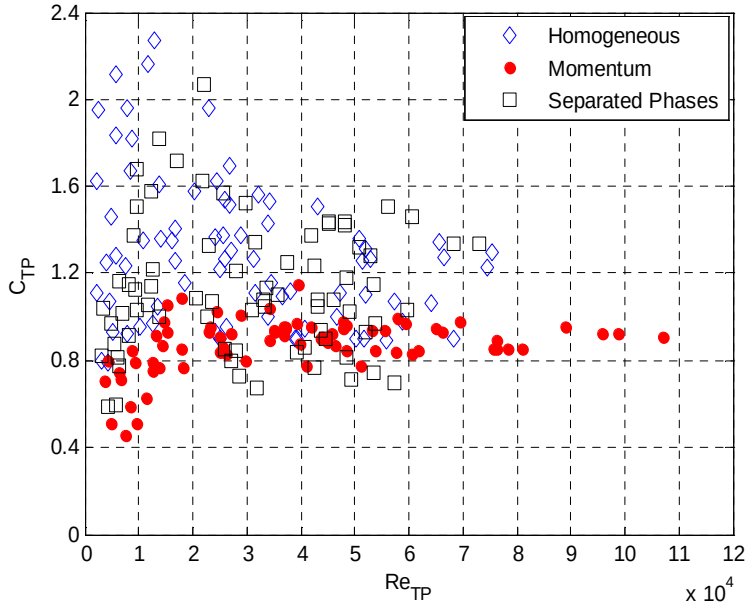

Fig.7.8: Effect of the two-phase flow density definition on the VFM discharge coefficient

In order to estimate the density, the void fraction value must be known; then the output of the WMS becomes an input for the VFM signal interpretation. The two-phase flow discharge coefficient is then evaluated, based on the experimental data (Fig.7.9) and the dependence of the parameter $C_{d\text{-}TP}$ on the two-phase Re number has been modeled as (Fig.7.10):

$$\begin{cases} C_{d-TP} = a + b \cdot \sqrt{\dfrac{10^{c}}{\mathrm{Re}_{TP}^{\ d}}} & \mathrm{Re}_{TP} < 1.5 \cdot 10^{4} \\ C_{d-TP} = 0.91 & \mathrm{Re}_{TP} > 1.5 \cdot 10^{4} \end{cases} \qquad (7.\ 3)$$

with the parameters evaluated on the basis of the experimental data: *a=1.1, b=0.6, c=3.5* e *d=1*.
The Reynolds number has been defined as:

$$\mathrm{Re}_{TP} = \frac{G_{TP} D_p}{\mu_{TP}} \qquad (7.\ 4)$$

and the dynamic viscosity μ, in accordance with the two-phase momentum density equation (Tab.3.2), has been defined as:

$$\mu_{TP} = \left[\frac{x^2}{\alpha \mu_g} + \frac{(1-x)^2}{(1-\alpha)\mu_l} \right]^{-1} \qquad (7.\ 5)$$

The two-phase flow discharge coefficient shows a higher dispersion compared to the single-phase value. In single-phase flow it takes into account the phenomena of the wall flow detachment at the inlet of the divergent section; in two-phase flow the presence of the interface between the two phases complicates the physical interpretation of this correction coefficient. Moreover it is strongly affected by the value of the density, that is strongly related to the phases distribution along the VFM.

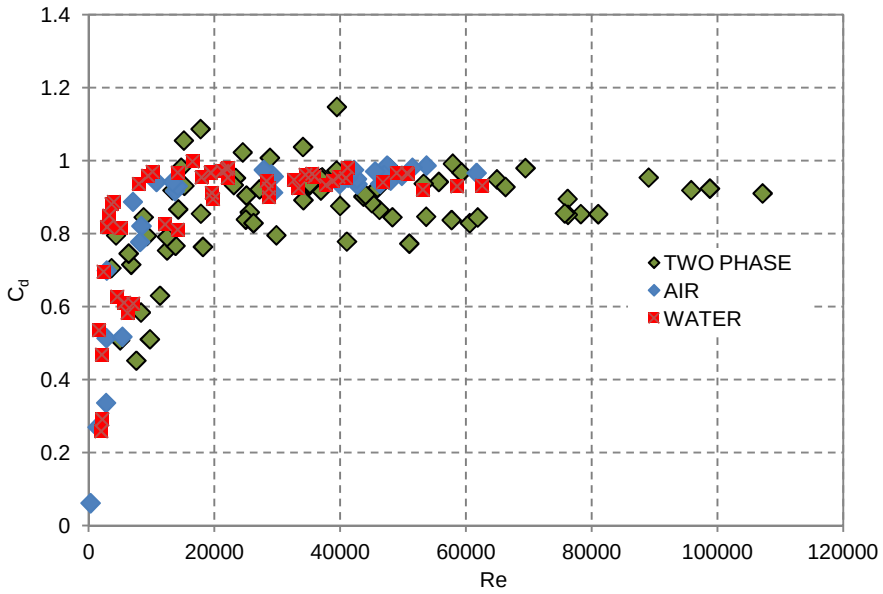

Fig.7.9: VFM discharge coefficient. Experimental single and TP flow

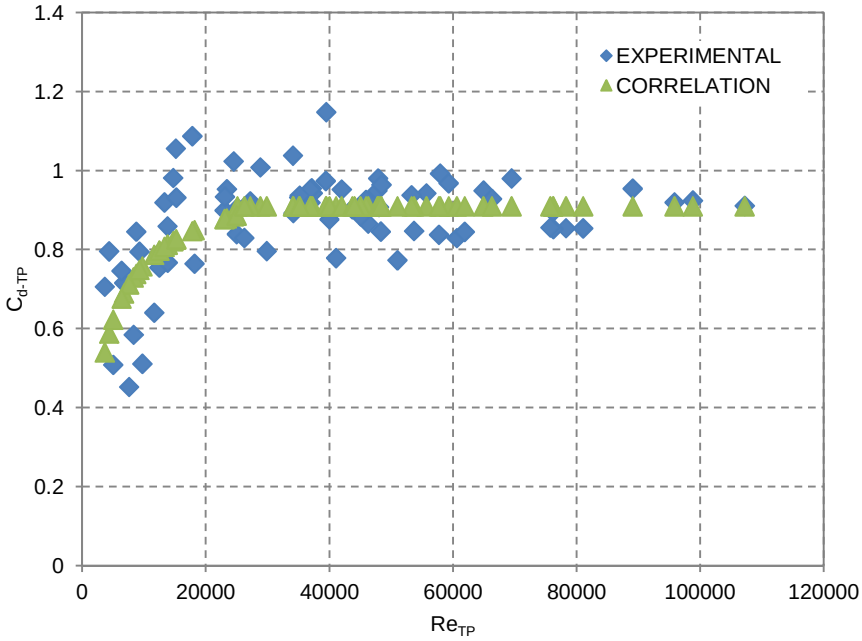

Fig.7.10: VFM discharge coefficient. TP flow correlation

The experimental pressure drops of the VFM have been analyzed in order to highlight the dependence on the superficial velocities of the phases. The Δp value increase is shown in Fig.7.11 as a function of the two phases superficial velocities. The regular behavior of the increasing curves suggests that a model of the instrument, depending on the phases velocities, can be developed in order to avoid the use of the discharge coefficient correlations, for the mass flow estimation. The apparent lack of information between J_g = 3 m/s and J_g = 6 m/s is due to the non complete superimpositions ranges of the air mass flow meters.

In Fig.7.12, the pressure drops in the VFM are expressed in terms of two-phase flow multipliers. The multipliers $\Phi^2_{l,g}$ has been evaluated as the ratio between the two-phase flow pressure drop and the single-phase pressure drop at the same phase mass flow rate (eq. 4.20)

In the x-axis the experimental Lockart-Martinelli parameter, that is evaluated as the ratio between liquid and gas VFM pressure drops, is reported.

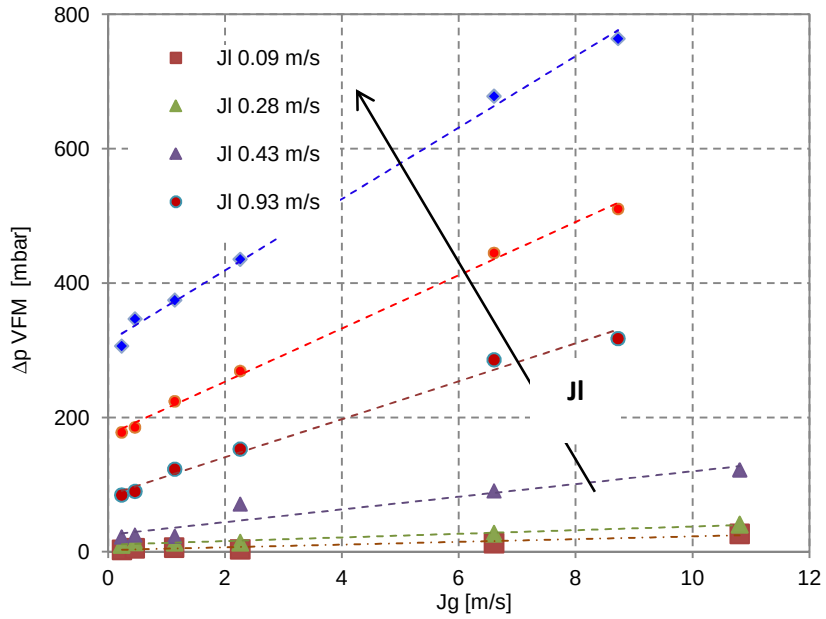

Fig.7.11: Experimental VFM pressure drops as a function of phases superficial velocities

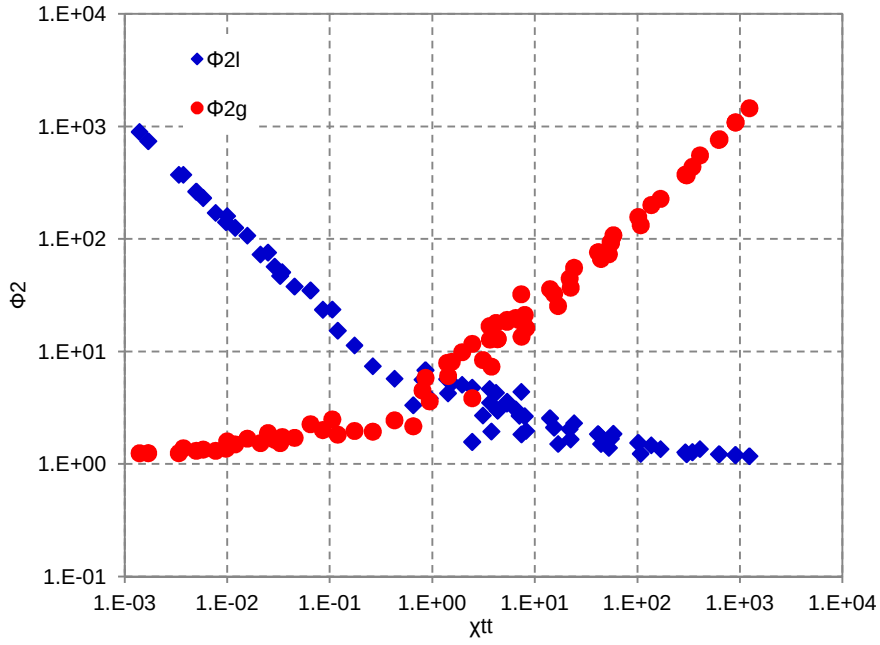

Fig.7.12: VFM pressure drops two-phase multipliers

In Fig.7.13 the curves show the VFM pressure drops as a function of the liquid superficial velocity and parameterized with the mixture flow quality. The curves behavior highlights that the VFM is strongly affected by the value of the flow quality, as three regions, having three different curves slopes, can be identified for flow quality lower than 0.005, between 0.01 and 0.05 and between 0.1 and 1.

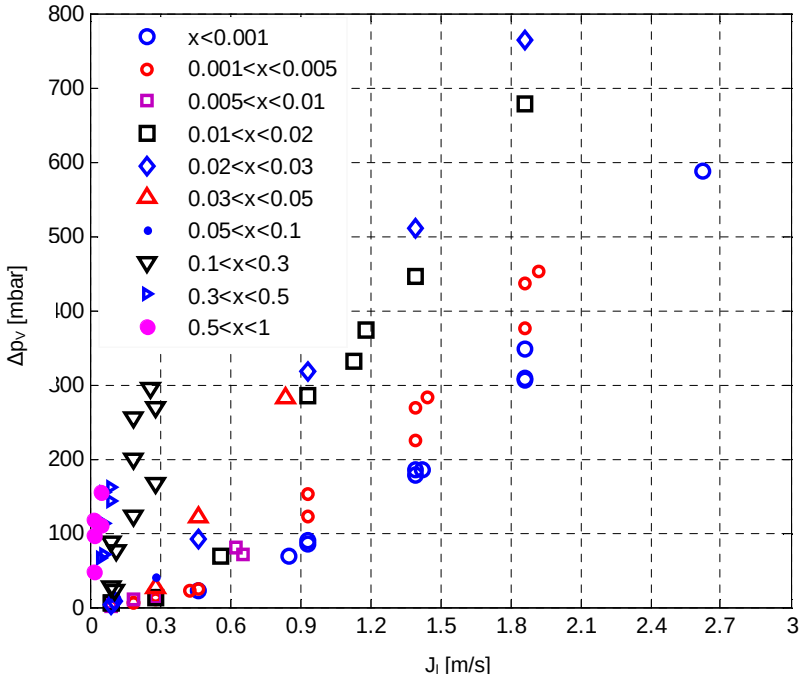

Fig.7.13: Cadute di pressione bifase nel Venturi: dipendenza dal titolo

7.3 Spool Piece model

The SP model consists of a set of equations that, based on the measurement of the VFM pressure drop, and on the measurement of the void fraction in the WMS, together with the measurement of pressure and temperature of the fluid, allows the estimation of the mass flow rate of the phases in the test section:

$$\begin{cases} x = f_1(\alpha) \\ J_l = f_2(\alpha, \Delta p_{VFM}, p) \\ J_g = f_3(\alpha, \Delta p_{VFM}, p) \end{cases} \qquad (7.6)$$

In the present work, an iterative approach is adopted for the estimation of the mass flow rates of the two phases. The model input are the void fraction, the pressure drop in the VFM, and the properties of air and water that are evaluated at the working pressure and temperature. An initial guess value for the flow quality is introduced. Using a x-α correlation the void fraction is calculated and the flow quality value is iterated till the error between the void fraction calculated and the void fraction measured by the WMS is lower than a threshold value (10^{-4}). When the required accuracy is reached, the two-phase flow Reynolds number and the discharge coefficient are calculated in a new iterative loop, where for the first iteration $C_{d\text{-}TP}=C_{d\text{-}l}$ is assumed. When the convergence is got ($W_{TP,i}-W_{TP,i\text{-}1}<10^{-4}$) the mass flow rate are calculated for the two phases. For the *x-α* correlation used in the calculation, the Lockhart-Martinelli correlation (Tab.3.1) has been modified, based on the experimental data:

$$\begin{cases} \alpha = \left[1 + 0.2 \cdot \left(\frac{1-x}{x}\right)^{0.6} \cdot \left(\frac{\rho_g}{\rho_l}\right)^{0.36} \cdot \left(\frac{\mu_l}{\mu_g}\right)^{0.07}\right]^{-1} & x < 1 \cdot 10^{-3} \\ \alpha = \left[1 + 0.28 \cdot \left(\frac{1-x}{x}\right)^{0.6} \cdot \left(\frac{\rho_g}{\rho_l}\right)^{0.36} \cdot \left(\frac{\mu_l}{\mu_g}\right)^{0.07}\right]^{-1} & 10^{-3} \le x \le 6 \cdot 10^{-2} \\ \alpha = \left[1 + 0.45 \cdot \left(\frac{1-x}{x}\right)^{0.6} \cdot \left(\frac{\rho_g}{\rho_l}\right)^{0.36} \cdot \left(\frac{\mu_l}{\mu_g}\right)^{0.07}\right]^{-1} & x > 6 \cdot 10^{-2} \end{cases} \quad (7.7)$$

The comparison between the original correlation, the modified correlation and the void fraction value obtained from the WMS signal analysis is shown in Fig.7.14.

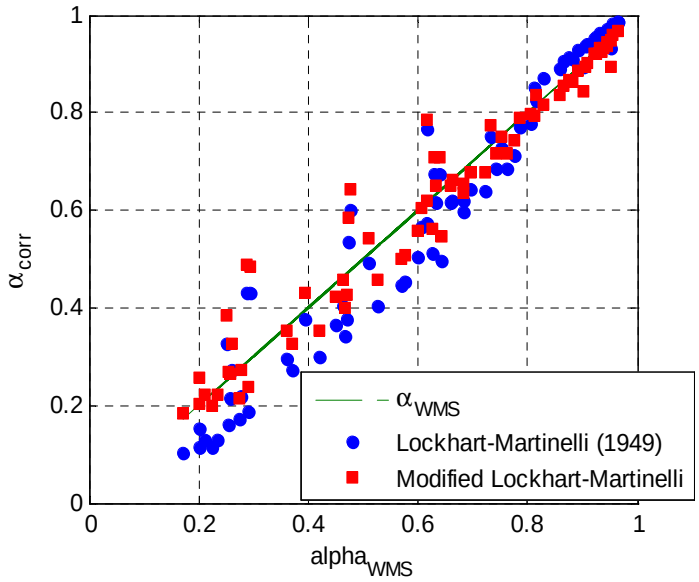

Fig.7.14: Comparison between WMS void fraction and correlations

7.4 Results

The developed SP Model has been applied to the experimental data in order to derive the mass flow rate of the phases. In Fig.7.15, the flow quality, that is estimated by the SP model, is compared with the experimental value obtained by the phases flow rate measurements. The accuracy of the model has been evaluated as the degree of closeness of the estimated quantity to the experimental value; and the estimation error is considered the distance between the estimated quantity and the experimental value.

The flow quality is estimated with an error lower than 20% for the flows in which the quality was higher than 0.1, and the error is lower than 10% for 72% of the runs. For flow qualities lower than 0.1 the estimation error increases and is lower than 50% for 90% of the cases. The estimated mass flow rates are shown in Fig.7.16 (water flow rate), and Fig.7.17 (air flow rate).

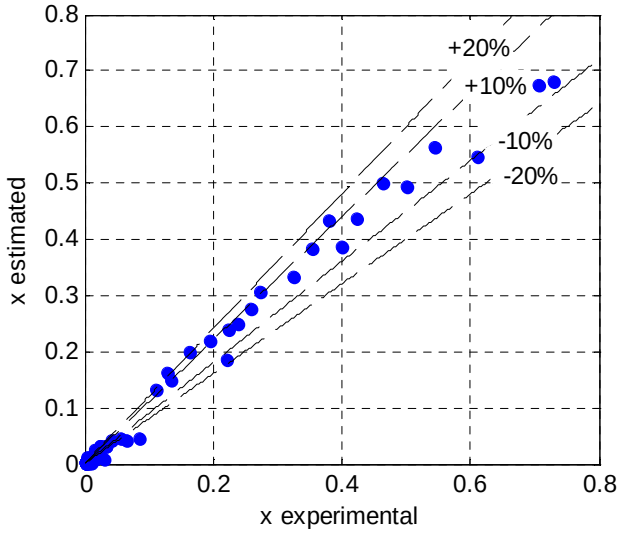

Fig.7.15: Experimental flow quality vs. SP flow quality

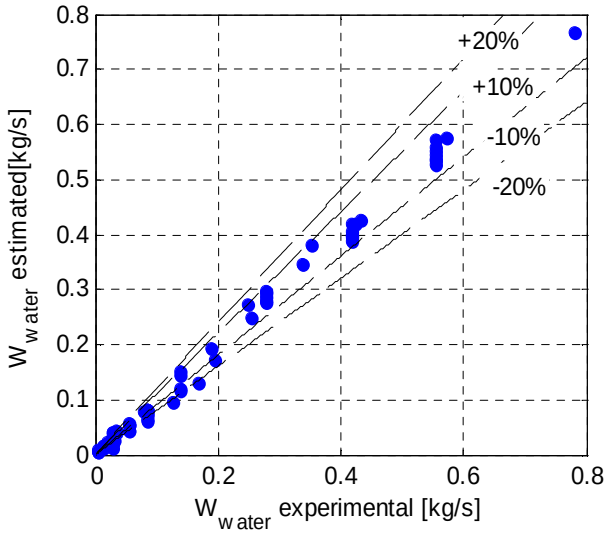

Fig.7.16: Experimental mass flow rate vs. SP mass flow rate for water phase

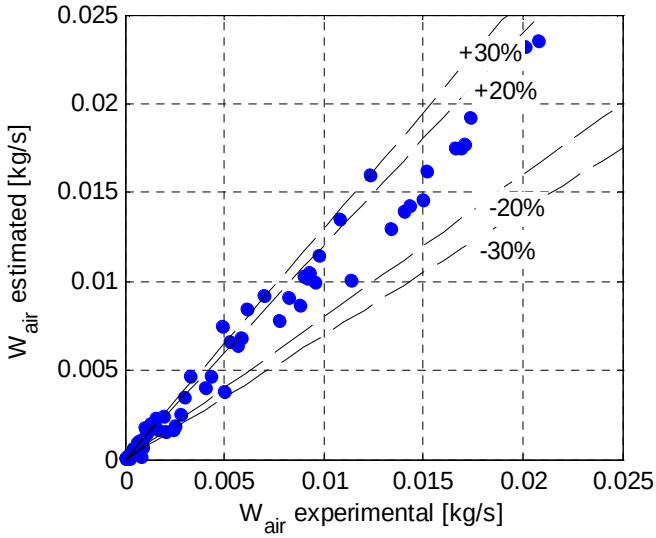

Fig.7.17: Experimental mass flow rate vs. SP mass flow rate for air phase

The total mass flow rate is estimated with an error that in 73.3% of the cases is lower than 10% and in 84% of the cases is lower than 20%. The highest estimation errors concern the air flow rate; in fact it is more affected by the errors in the quality estimation and in the total mass flow rate estimation due to the small values of this parameter. In this case the error is lower than 30% for the 73.3% of the cases. The highest errors have been obtained for the flows characterized by an intermittent behavior (slug/plug flow patterns). Moreover the intermittent flow has been realized in a region where the VFM discharge coefficient is strongly dependent on the Re number; and an error on the estimation of $C_{d\text{-}TP}$ produces obviously an additional error on the mass flow rate estimation.

7.5 Conclusions

The analysis of the signals and the developed model of the SP, made up of a VFM and WMS, allow the estimation of the mass flow rate of the phases in air-water horizontal flows with a good accuracy in a large range of flow conditions (J_g = 0.14 - 32 m/s and J_l = 0.019 - 2.62 m/s), with observed flow patterns ranged from stratified flow to intermittent flow (slug and plug) and annular flow.

The VFM response has been modeled by defining the two-phase flow discharge coefficient, $C_{d\text{-}TP}$, and its Re dependency. A modified Lockart-Martinelli correlation for x-α, able to represent the WMS experimental data, has been developed and included in the SP model.

By means of the developed signal analysis the mass flow rate has been estimated with an error lower than 10% in the 73.3% of the cases. Moreover the estimation error is considerably lower for the flow characterized by high values of quality and void fraction. In this range, with reference to facility SPES3 test conditions, the error in the mass flow rate estimation is always lower than 10% and 20% for water and air respectively.

8. ELECTRICAL CAPACITANCE SENSOR CHARACTERIZATION IN VERTICAL ANNULAR FLOW

In this chapter the analysis of the electrical sensor designed at the SIET laboratories [8.4][8.5][8.6] for the measurement of the void fraction in the SPES-3 break lines is described.

The sensor has been developed with the aim to be inserted in a SP for the measurement of the mass flow rate of the phases. The range of interest of the flow parameters in the SPES3 facility, in steady state and transient conditions, has been investigated by means of the RELAP-5 code [8.15] and for each line the range of measurement of the different parameters has been identified; the simulations show that in a relative long period of the transients, the two-phase flow corresponds to an annular flow pattern, characterized by very high void fraction and high flow velocity, so that the selected instruments of the Spool Piece must be sensitive to the flow in such conditions.

With the present sensor (Electrical Capacitance Probe – ECP), the impedance measurements are taken from a multi-electrode sensor surrounding the pipe wall. The working principle consists of sending a sinusoidal signal to an electrode and measuring the output signal in the other electrodes. This procedure is repeated for all the other electrodes pairs until a full rotation is completed to get a set of measurements. The concentration of each phase can be evaluated from the electrical permittivity values of each phase.

The drawback of the ECP is the relatively low spatial resolution, since the phases distribution reconstruction is based on measurements at the periphery of the sensor. This problem is stressed in presence of an annular flow as the liquid film at the wall creates a preferential path for the electric field lines that shields the core region and makes the sensor poorly sensitive to the void fraction. In order to address this drawback a sensor, consisting of nine external electrodes and an internal one, has been designed and developed.

The sensor design and the experimental characterization at very high void fraction and in presence of annular air/demineralized-water flow are described. The possibility to obtain

information about other thermal-hydraulic parameters is also discussed and an evaluation of the response of the sensor at the variation of the flow pattern has been carried out.
Concerning the annular flow pattern a large number of experimental and theoretical studies have been performed by several authors (see the references of Bennett et al. [8.9], Hewitt and Roberts [8.18], Ishii and Mishima [8.19], Hazuku et al. [8.17]). The flow pattern can be described in a simplified model as a liquid film flowing on the wall of the tube and a gas phase flowing in the center (core flow): some rate of the liquid phase is entrained as small droplets in the gas core. As the liquid flow rate is increased, the droplet concentration in the gas core increases and the droplet coalescence occurs leading to large lumps or streaks as wispy liquid inside the gas core. It is hypothesized that the occurrence of agglomeration is due to a fundamental instability of the gas-droplet core flow: if positive wave growth coefficients are present, the system is classified as unstable and belongs to the wispy-annular flow regime [8.18], while fully stable systems are classified as belonging to the annular flow regime.
The annular flow is quite difficult to be observed using ordinary visualization techniques since the liquid film in this regime tends to screen the core region. The study investigates also the use of the ECP sensor to detect the phase distribution inside the core region of the annular flow.

8.1 Electrical Capacitance Probe (ECP)

The sensor (ECP) has been developed by the SIET Company, and consists of 10 electrodes: 9 external and one internal (Fig.8.1). The internal and the external diameters of the Plexiglas pipe, where the probe is mounted, are 80 mm and 90 mm respectively. The external electrodes (steel stripes of 400 mm length and 5 mm width) are spaced with 22.5° angle only on a half-circumference of the pipe, due to the vertical flow symmetry. The angle corresponds to an external chord of 17.56 mm and an internal chord of 15.6 mm. The sensor geometry has been developed in half of the pipe circumference as the symmetry of the vertical flow has been verified. The main purpose of the sensor is the evaluation of the effect of the angular electrode distance on the output signal.
The external electrodes are pasted on the Plexiglas pipe and are welded with the conductor that allows the link with the electronic part, while the internal electrode is connected through a metallic support to the outer pipe wall (Fig.8.2).
The electrodes are connected in an electronic circuit by several reed relays and two insulation transformers, in order to prevent common mode disturbances. The reed relays technology has been selected for their simplicity and their features: very small closing and opening time, very high resistance when open, very small resistance when closed, very small electrical capacity and long life.
Each external electrode is connected, at the upper and lower extremity, to two reed relays to activate, in a predefined sequence, the excited electrode and the measuring one; the internal one is connected only in the upper extremity and it is always used as measuring electrode, when the corresponding reed relay is activated.

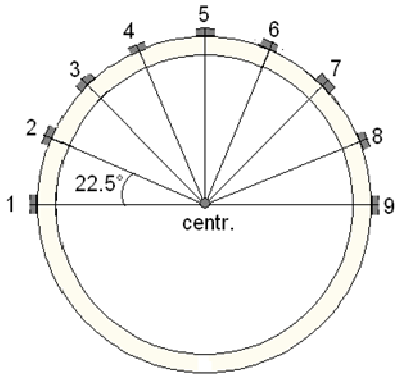

Fig.8.1 Schematic of the ECP

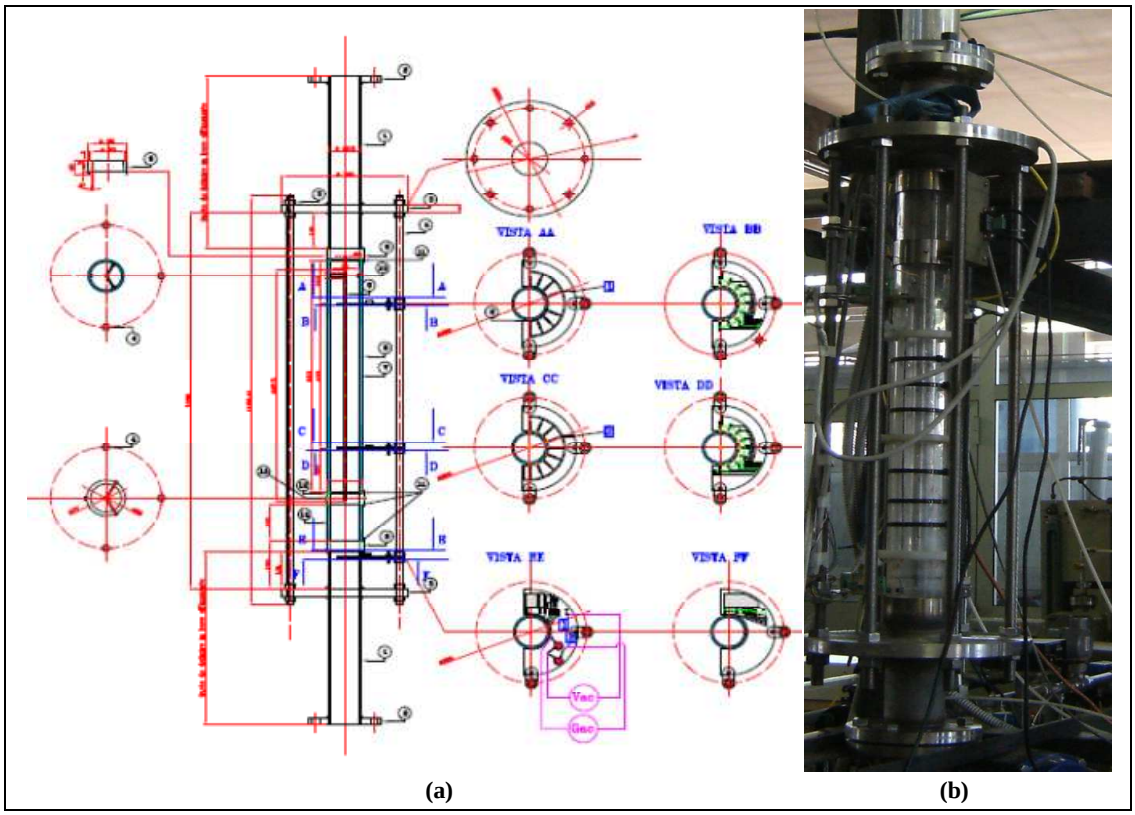

(a) **(b)**

Fig.8.2: SIET ECP Sensor. Design sheet (a) and picture (b)

8.2 First experimental campaign

8.2.1 Experimental facility and test section

The experimental facility consists of the feed water and the feed air loops equipped with instruments to measure the single-phase flow parameters (flow meter, temperature and pressure). The water mass flow rate is measured by a rotameter, while the air flow rate is measured by a calibrated orifice flow meter; whose accuracy is 2% full scale value.
The facility, that is shown in Fig.8.3, consists of a 4 m long, 80 mm inner diameter vertical pipe. The test section is transparent (Plexiglas) in order to visualize the flow pattern. Air enters axially the test section and water flow is injected axially by means of a porous bronze;

the mixing zone is located at 400 mm from the test section inlet (Fig.8.3). The 2.5 m long test section is equipped with two pneumatic quick closing valves (QCV) to measure the volumetric void fraction; the uncertainty associated with the void fraction measurement has been estimated as $\Delta\alpha = \pm\ 0.0012$.
Downstream of the upper valve the two phases are separate in a tank at atmospheric pressure. Experiments are carried out at a constant water temperature of 20°C, and the absolute pressure is measured at the inlet of the test section by a pressure transducer Rosemount 3051/1.

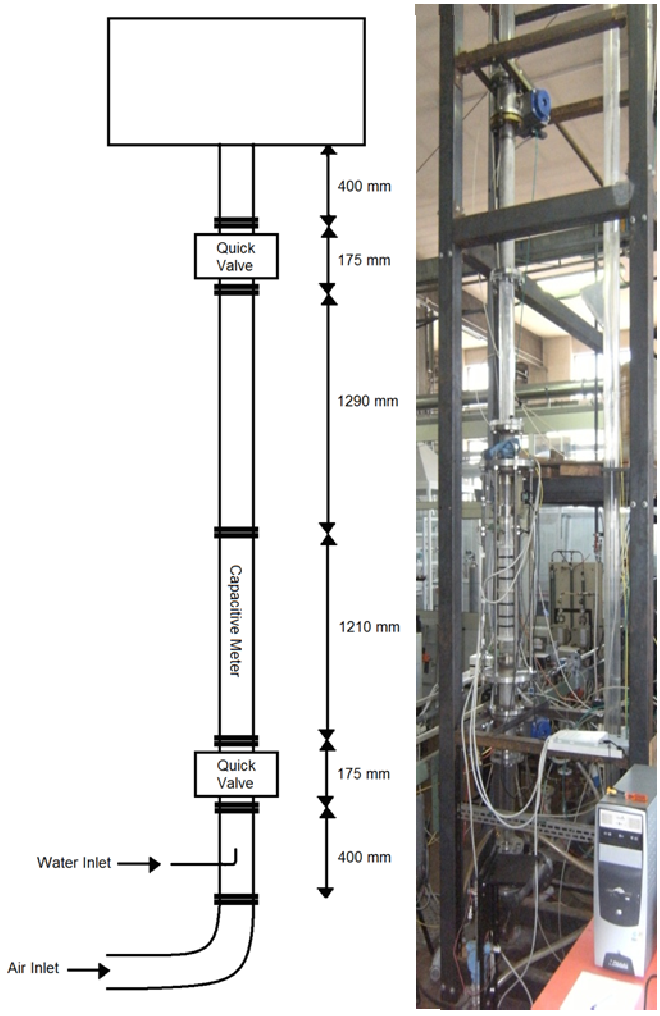

(a) **(b)**

Fig.8.3: Experimental facility: test section schematic (a) and picture (b)

The presence of the internal electrode (whose length is 400 mm and diameter is 5 mm) in the center of the pipe affects the mechanisms of the dispersed flow; a liquid film has been observed on it. Okawa et al. [8.20] have shown in their experiments that the deposition rate of droplets was markedly increased if the present flow obstacle was placed inside the flow channel and the deposition rate was approximately 1.5 times larger than the deposition rate with no obstacle. The presence of the central obstacle, together with a higher diameter and the coaxial liquid injection can affect the waves in the liquid film and the droplet coalescence in the core region also at rather low liquid superficial velocities.

8.2.2 Experimental methodology and signal acquisition

The signals from the sensor are acquired by using the NI USB-6259 DAQ (Data AcQuisition), and are managed using a LabView® program. The predefined measurement sequence is read and the corresponding reed relay is activated by using a 5 V DC signal. The excitation signal is sent to the electrodes (sinusoidal signal with an excitation frequency f_{ex} = 25 kHz and an amplitude of 5 V) and the output signal is sampled using a frequency f_{ac} of 250 kHz; the RMS (Root Mean Square) value corresponding to 2000 samples is acquired. The excitation frequency has been chosen considering that the experiments are carried out with demineralized water; in this case the sensor output signal is directly proportional to the fluid capacitance.
The measurement sequence is defined as follows: the external electrodes are excited in sequence and for each one the output signal of the other external electrodes are read; after that scan the output signal relative to the central electrode is acquired for each excited external electrode. For every couple of electrodes the sampling time of RMS value is about 33 ms; so that the total scanning time depends on the selected measurement sequence. Before each set of experimental runs the static values of the signals for air and water are measured. Then, for each run, the mass flow rates of water and air are fixed and when the flow is steady state, the pressure value and the signals from the ECP sensor are acquired. At the end of the measurement sequence the volume averaged void fraction is measured by means of the quick closing valves technique.

8.2.3 Experimental data range

In order to evaluate the response of the sensor at high void fractions, corresponding to annular flow, a mixture of air and demineralized water is introduced in the test section. The mass flow rate ranges from 0.094 to 0.15 kg/s for air and from 0.002 to 0.021 kg/s for water, corresponding to a void fraction higher than 95%. The tests have been performed at atmospheric pressure. The volumetric void fraction (measured with QCV technique) increases with gas superficial velocity J_g and decreases with J_l, as shown in Fig.8.4.

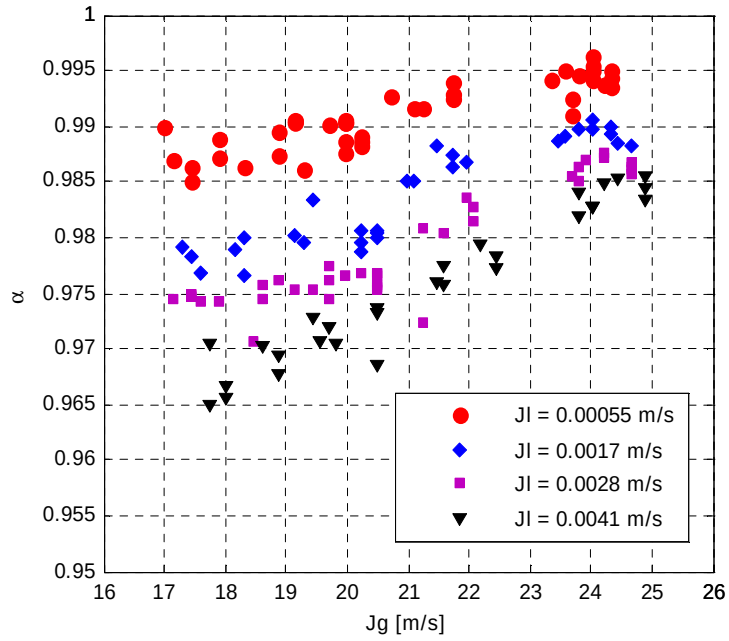

Fig.8.4: Experimental volumetric void fraction as a function of water and air superficial velocities

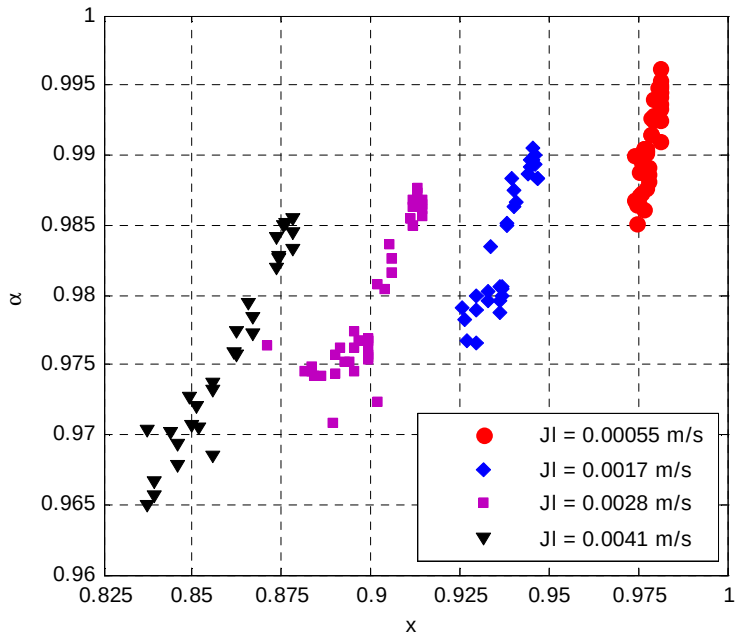

Fig.8.5: Experimental volumetric void fraction as a function of the flow quality at different water superficial velocity

Fig.8.5 shows the volumetric void fraction as a function of the flow quality: a small flow quality variation at constant J_l corresponds to large void fraction variations, while the slope of the void fraction versus x increases as J_l decreases.

8.2.4 Electrical Capacitance Probe experimental results

The first ECP qualification step is the characterization of the sensor for single-phase conditions; so, before each test, measurements with air and demineralized water have been carried out in order to evaluate the signal noise level and to normalize the signals for two-phase flows; the single-phase measurements are used to determine the electrodes shape function of the sensor. In Fig.8.6 the RMS signals measured between the electrode 1 and the other external electrodes are presented, as a function of the value of the angle θ between the electrodes. The measured RMS value is proportional to the electrical capacitance between the measuring electrodes; it also depends on the excitation frequency and on the resistance that is different between air, water and two-phase mixture, also with demineralized water. As it is shown in Fig.8.6, the signal variation range is very limited due to the presence of the quite large Plexiglas thickness (5 mm) and to the absence of any signal amplification.

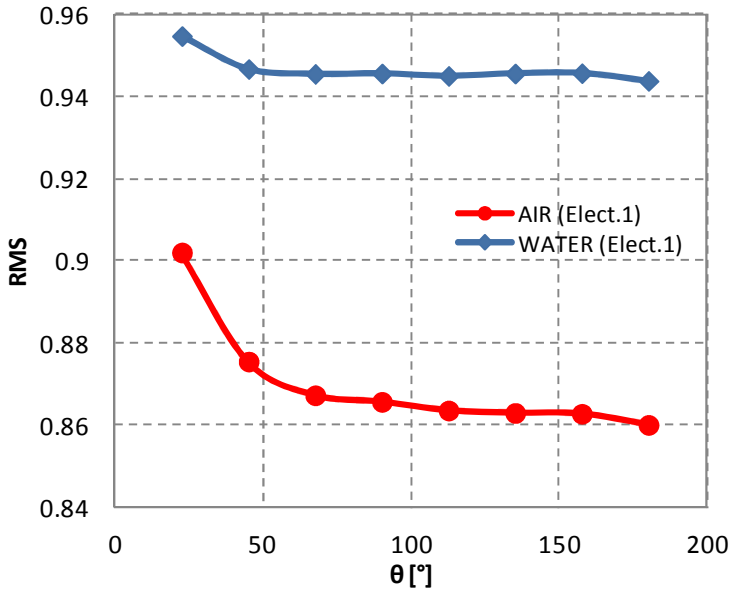

Fig.8.6: Single-phase ECP signals as a function of the angle θ for the excited electrode 1

Moreover, the theoretical ratio between the water electrical permittivity and the air electrical permittivity, that is equal to 80, is reduced, in the practical case, to a value from 1.05 to 1.1 depending on the electrodes distance. The ratio is lower at θ=22.5° due to the strong influence of the wall. The angle dependence is higher for the signal measured in air flow, while it seems limited for single-phase water flow.
For each electrodes combination the ratio RMS_g/RMS_l shows a rather high repeatability. The ratio of the two phases RMSs, obtained by the measurements between the external electrodes, as a function of the angle θ is shown in Fig.8.7.

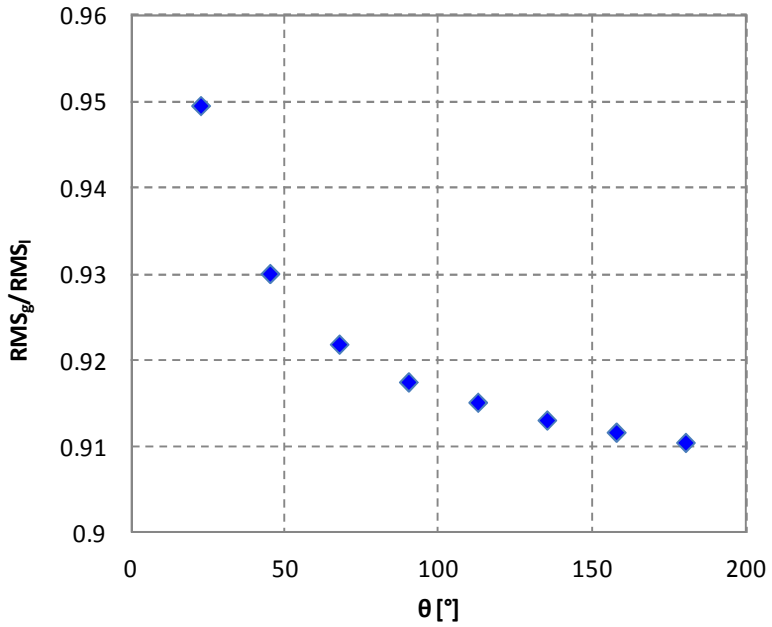

Fig.8.7: Single-phase ECP signals ratio as a function of the angle θ, for the excited electrode 1

The analysis of the signals of the central electrode shows a higher sensitivity due to the direct contact of the probe with the mixture. In this case the mean RMS_g/RMS_l ratio is equal to 0.582 ± 0.002.
In order to take into account the single-phase signal variations, the two-phase flow measured values are normalized as follows:

$$V_{ij}^{*} = \frac{RMS_{TP-ij} - RMS_{l-ij}}{RMS_{g-ij} - RMS_{l-ij}} \qquad (8.\ 1)$$

where the subscript *ij* identifies the measuring electrodes combination.
Because of the physical differences between the internal and external electrodes response, the signal of external and internal electrodes has been analyzed separately.

External electrodes signals

In order to evaluate the behavior of the sensors as a function of the mean void fraction, only the *i-j* combination signals are considered (deriving the mean value and the standard deviations); while, in order to evaluate the interface phenomena in the liquid film and in the core region, the time dependent signals have to be considered (an example is reported in Fig.8.8 for the electrodes combination 1-2 and test volumetric void fraction α equal to 0.977 (a) and 0.995 (b)). The signals evolution is shown in Fig.8.8: the single-phase signal is very stable in time, so that the two-phase flow signals fluctuation can be related to the dynamic evolution of the flow; the third digit of the RMS has to be considered in order to take into account the film and the core flow dynamics. In Fig.8.8 the signal has been compared with water or air depending on the nearest mean RMS value.

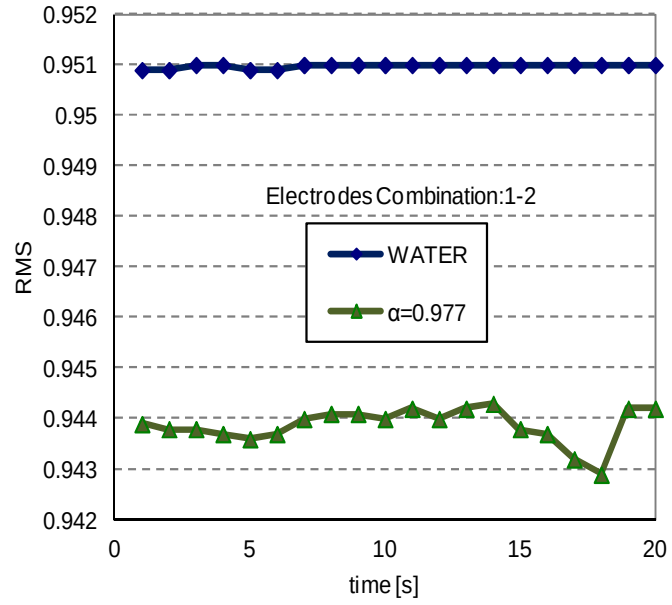

(a)

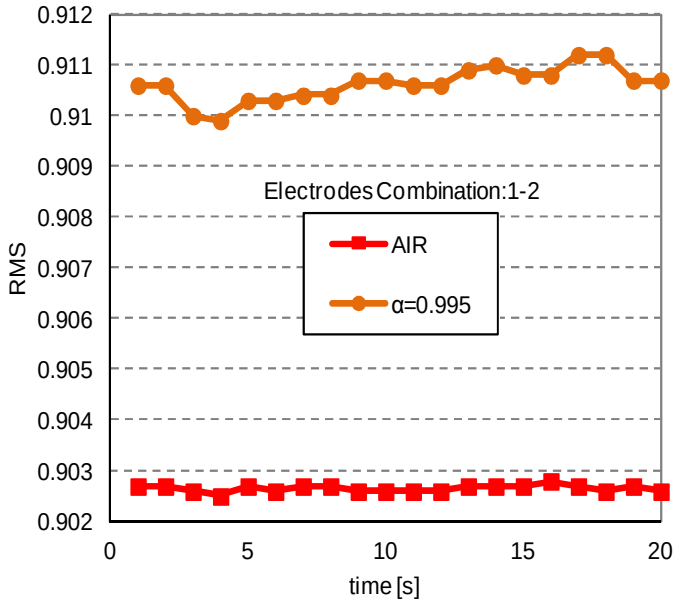

(b)

Fig.8.8: RMS time evolution for 1-2 electrodes combination compared with the single phases RMS time evolution: a) α = 0.995 ; b) α = 0.977

Each combination is analyzed in terms of dependence on the fluid-dynamic quantities (experimental void fraction, superficial velocities of air and water) and geometry parameters (θ). A typical set of curves is reported in Fig.8.9 and Fig.8.10. The sensor is sensitive to very little variation of the void fraction and this variation is detected from all the measuring electrodes combinations. As reported in the following pictures the normalized signal V_{ij}* is a function of angle θ, liquid film thickness δ and volumetric void fraction α (measured by the QCV technique).

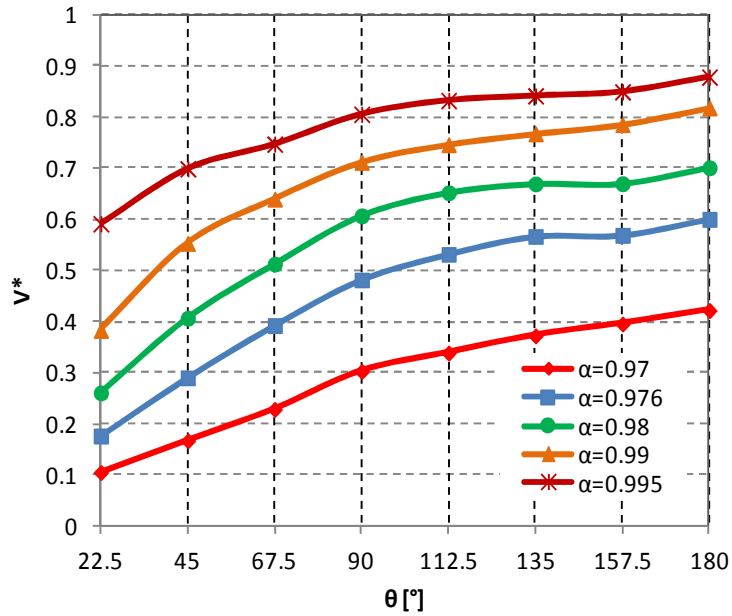

Fig.8.9: Normalized signal Vij* for i=1 and j=2- 9 as a function of angle θ for different experimental volumetric void fractions α

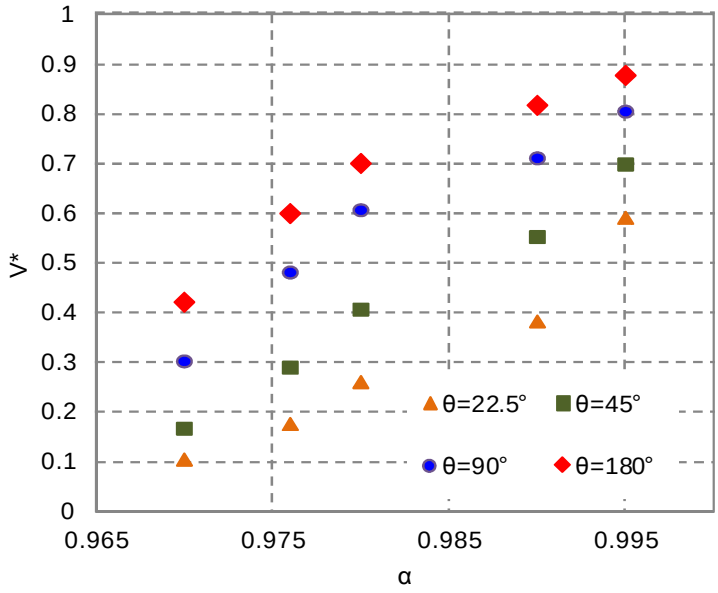

Fig.8.10: Normalized signal Vij* as a function of the experimental volumetric void fraction α for different angles θ

The relationship between the capacitance and the void fraction depends on the dielectric values of the two phases, but also on the surfaces of the sensors, on the separation distance between the two electrodes and on the voltage distribution inside the measurement volume, that in turn depends on the phases distribution.

As regards the flow pattern, it is possible to develop a qualitative model for the signal variation: in annular flow the measurements taken from the external electrodes are not very sensitive to the core region flow, because the preferential path of the electrical field lines is located in the continuous liquid film. The analysis of the signal shows that the measurement, taken between close electrodes (θ=22.5°), is affected by the presence of the liquid film because the measured volume is that relative to the liquid film zone, while the electrodes

having higher distances are partially affected by the core region. In the hypothesis of axial symmetric flow, and in order to evaluate the sensor sensitivity to the mean void fraction variation, all the signals measured between electrodes, placed at the same angular distance, are used to evaluate the average normalized signal at the angle θ. The average signals measured between electrodes at 22.5°, 45°, 90° and 180° are presented in Fig.8.11 as a function of the volumetric void fraction measured by the QCV technique. V_{ij}* , evaluated by means of the eq. 8.1, increases with θ at constant void fraction, and approaches the air value at higher angular distance. No significant difference has been found between the signals of electrodes at 90° and 132.5° and at 157.5° and 180°.

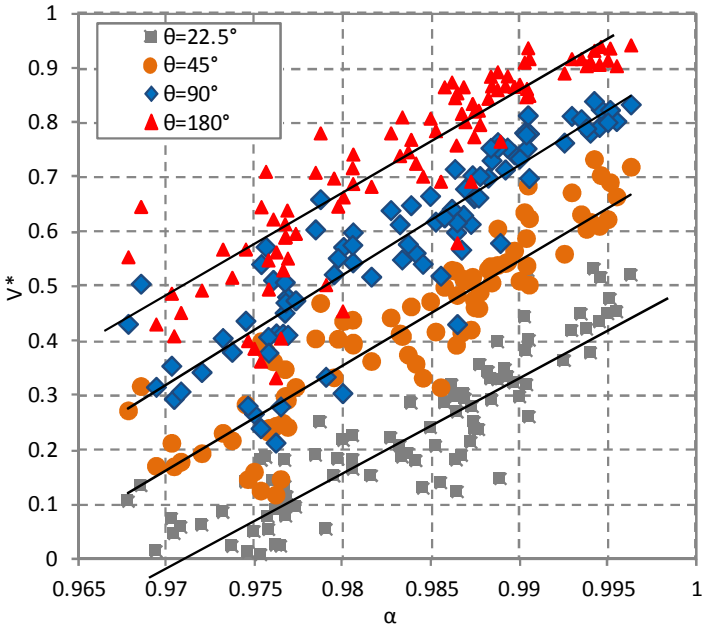

Fig.8.11: Mean signal measured in the external electrodes as a function of the experimental volumetric void fraction α

The best fit curves of the signals reported in Fig.8.11 are parallel for angles higher than 45°, while for the angles equals to 22.5° and 45° the signal dependence is different, due to the larger effect of the Plexiglas wall and of the liquid film thickness.

Central electrode signals

The signal of the central electrode, that is in direct contact with the fluid, is sensitive to the mean cross section void fraction and could be directly related to the measured void fraction and to the amount of liquid droplets in the core region.
In Fig.8.12, the mean signal measured between the central electrode (j=10) and the external electrodes (i=1:9), is represented as a function of the experimental void fraction, measured by means of the QCV technique: the signal depends linearly on the void fraction at values higher than 0.98 and it is characterized by a higher standard deviation at lower values. In the tested range, the observed flow pattern is annular, with a rather low turbulence at the film interface, for liquid superficial velocities lower than 0.00152 m/s, while at higher water mass flow rates and void fraction values lower than 0.98, the flow pattern tends to become more turbulent with a greater mass of liquid that is entrained inside the core region as previously discussed.

The annular flow pattern is more regular at higher experimental void fraction as it is shown in Fig.8.12.

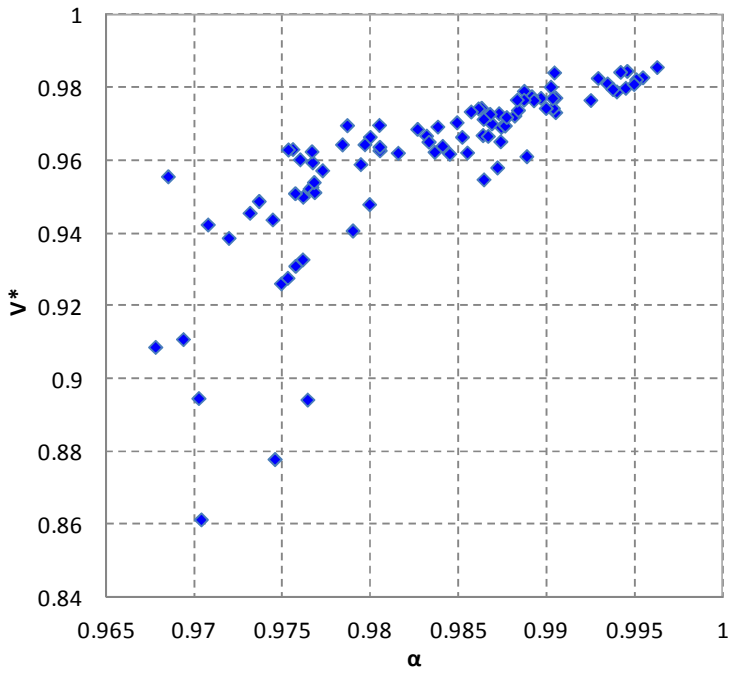

Fig.8.12: Mean signal measured in the central electrode as a function of the experimental volumetric void fraction α

8.2.5 Annular flow model and signals interpretation

Due to the symmetry of the flow, the annular flow regime in a vertical channel can be analyzed in a simplified scheme as a liquid film region and a core region. The liquid film is characterized in terms of film thickness, frequency and amplitudes of the waves at the liquid-gas interface, while the core region is characterized in terms of the mean void fraction value. By increasing the air flow rate, the liquid entrainment from the film to the gas core increases, while by increasing the water flow rate the amplitude of the waves increases and the flow tends to become more turbulent with a higher fraction of the water phase that is entrained in the core region and with an irregular wavy film flow.
In order to analyze the experimental results, some relevant flow parameters have been expressed by means of a simplified model. The parameters evaluated with the model are then used to interpret the sensor signals. In an annular flow, the void fraction can be written as:

$$\alpha = \alpha_c \cdot (1 - \alpha_d) \tag{8. 2}$$

where

$$\alpha_d = \frac{A_d}{A_c} \tag{8. 3}$$

$$\alpha_c = \frac{A_c}{A} = 1 - \alpha_f \tag{8. 4}$$

A_c is the core region area, α_d is the cross-section fraction occupied by the droplets in the core, α_c is the fraction of the pipe cross section occupied by the core region and α_f is the fraction of the pipe cross section occupied by the film region. Then the value of α_c is an indirect index of the liquid film thickness.

Ishii and Mishima [8.19] derived the criteria for the onset of entrainment based on the balance of the forces acting on the waves, to characterize the interface evolution in annular flow. The fraction of the liquid flux flowing as droplets (E_∞) is derived by Ishii and Mishima [8.19] and Hazuku et al. [8.17] as:

$$E_\infty = \tanh\left(7.25 \cdot 10^{-7} \cdot We^{1.25} \cdot \mathrm{Re}_f^{0.25}\right) \tag{8. 5}$$

Where the Weber number is:

$$We = \frac{\rho_g \cdot J_g^2 \cdot D}{\sigma}\left(\frac{\rho_l - \rho_g}{\rho_g}\right) \tag{8. 6}$$

and the Reynolds number is:

$$\mathrm{Re}_f = \frac{\rho_l \cdot J_l \cdot D}{\mu_l} \tag{8. 7}$$

where ρ_g , μ_g, J_g and ρ_l, μ_l, J_l are the density, the dynamic viscosity and the superficial velocity of air and water respectively, and σ is the surface tension.

In the present tests the liquid Reynolds number Re_l ranges from 44 to 332 and the Weber number *We* ranges from 2200 to 7000.

In a pure annular flow the liquid flows only in the film region, so the maximum value of liquid film thickness $\delta_{\max}$ is evaluated from the measured void fraction as:

$$\alpha = \frac{\left(D - 2 \cdot \delta_{\max}\right)^2}{D^2} \tag{8. 8}$$

Under the hypothesis of pure annular flow the liquid film velocity U_l and the core gas velocity U_g are evaluated as:

$$U_g = \frac{J_g}{\alpha} \tag{8. 9}$$

$$U_l = \frac{J_l}{1-\alpha} \tag{8. 10}$$

In Fig.8.13 the liquid film thickness is shown as a function of the superficial velocity of the two phases. Actually this model is valid for pure annular flow, but by introducing the correction due to the entrainment (Fig.8.14), the core gas fraction is evaluated more

correctly. The velocities of the phases are corrected assuming the same liquid droplets velocity as of the gas in the core region:

$$U_g = J_g / (\alpha_c - \alpha_d) \tag{8. 11}$$

$$U_l = (1 - E_\infty) \cdot U_f + E_\infty \cdot U_g \tag{8. 12}$$

$$U_f = (1 - E_\infty) \cdot J_l / (1 - \alpha_c) \tag{8. 13}$$

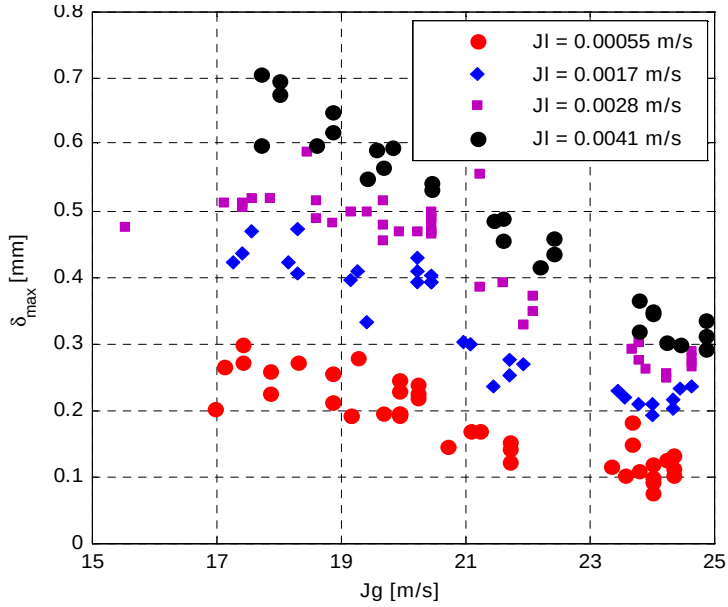

Fig.8.13: Maximum film thickness (eq. 8.8) as a function of the experimental water and air superficial velocity

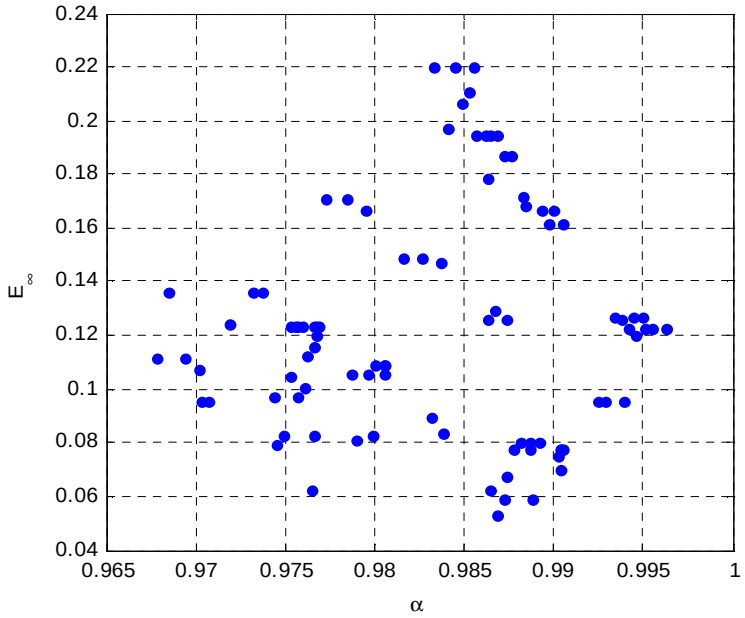

Fig.8.14: Equilibrium entrainment (eq. 8.5) as a function of the experimental volumetric void fraction α

The velocity of the two phases is shown in Fig.8.15 and Fig.8.16.

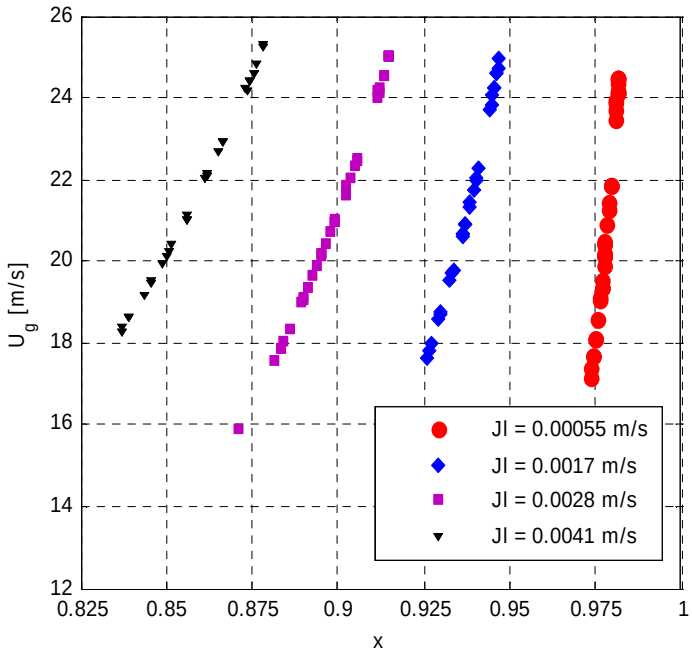

Fig.8.15: Air velocity as a function of the experimental flow quality (eq. 8.11)

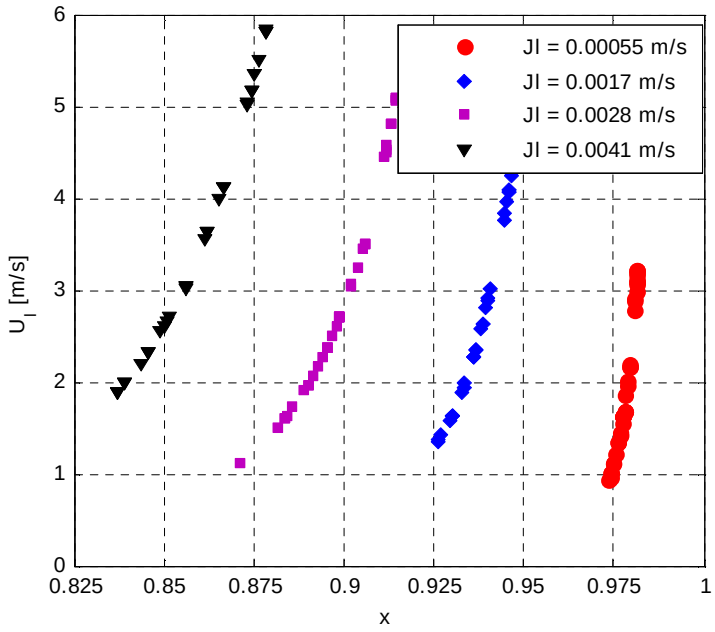

Fig.8.16: Water velocity as a function of the experimental flow quality (eq. 8.12)

In Fig.8.17, the derived slip ratio ($S=U_g/U_l$) is shown as a function of the flow quality, at different liquid superficial velocity.

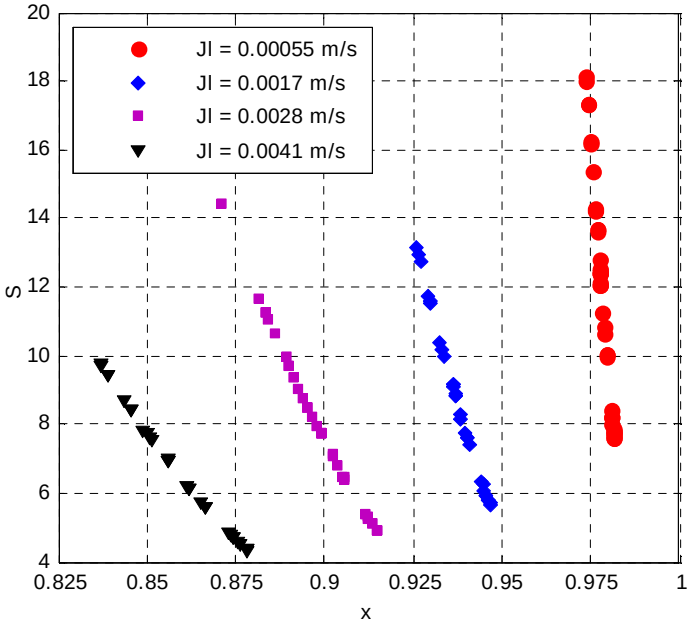

Fig.8.17: Slip ratio S= Ug /Ul (evaluated on the basis of the Ishii's model) as a function of the experimental flow quality

The liquid film thickness is corrected, as shown in Fig.8.18, taking into account the amount of liquid that is entrained into the core region:

$$\alpha_c = \frac{(D - 2 \cdot \delta)^2}{D^2} \qquad (8.\ 14)$$

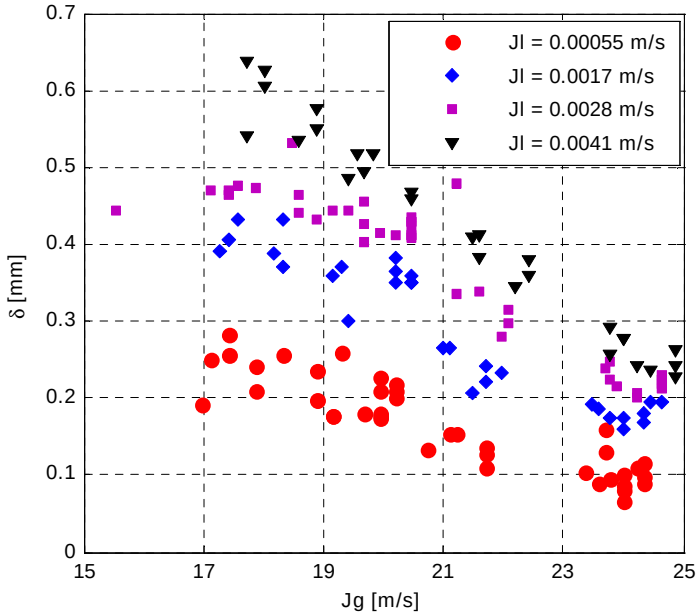

Fig.8.18: Corrected mean film thickness as a function of the experimental water and air superficial velocities

In order to analyze the dependence of the sensor signals on the measured void fraction, the data of the different electrodes combination are related to the liquid film thickness δ by means of the core void fraction α_c, and to the liquid fraction in the core region by means of

the droplets fraction α_d. A model correlating the probe signals to the two-phase flow parameters, as α_c, α_d, J_l, J_g, pressure p, geometry and fluid parameters is required. For an axial symmetrical two-phase flow at constant pressure and temperature a simple model with two parameters and two signals (from an external electrode and from the central one) can estimate the film thickness, the liquid core droplet fraction and the void fraction. In Fig.8.19 the signals measured in the central electrode are shown as a function of the core fraction; the flow pattern characteristics, from rather regular to more disturbed annular flow, are clearly detected. In Fig.8.20, the same signal is evaluated as a function of the droplets fraction: the internal probe is more sensitive than the external ones to the effect of the liquid and gas velocity change.

In the future the direct measurement of the local liquid film thickness and of the frequency of the film waves will be performed and their influence will be considered in the signal analysis.

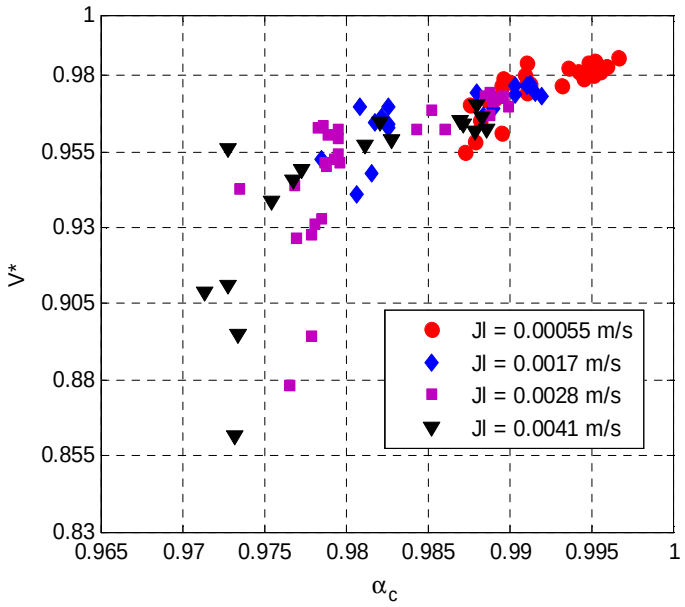

Fig.8.19: Normalized average signals of central electrode, as a function of the core void fraction (evaluated on the basis of the Ishii's model)

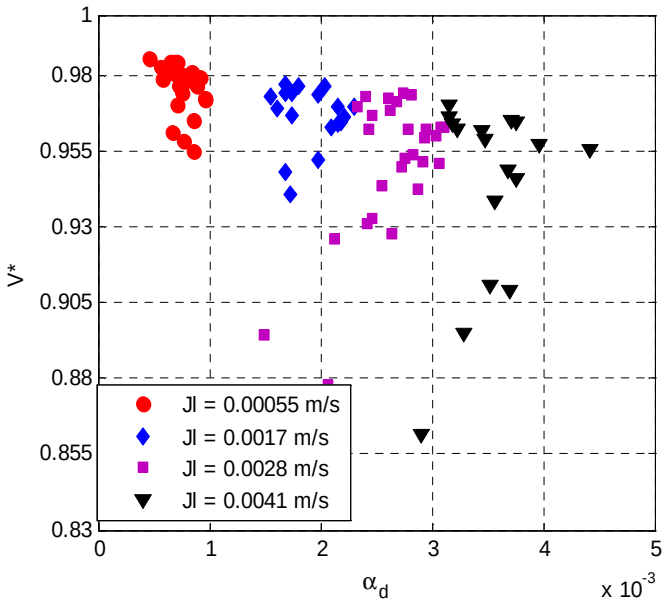

Fig.8.20: Normalized average signals of the central electrode, as a function of the core droplets fraction (evaluated on the basis of the Ishii's model) at the different experimental liquid superficial velocity

Fig.8.21 presents the evolution of the signals with the film thickness, evaluated using the Ishii model, for the different measuring angles. A linear dependency is highlighted for all the angles.

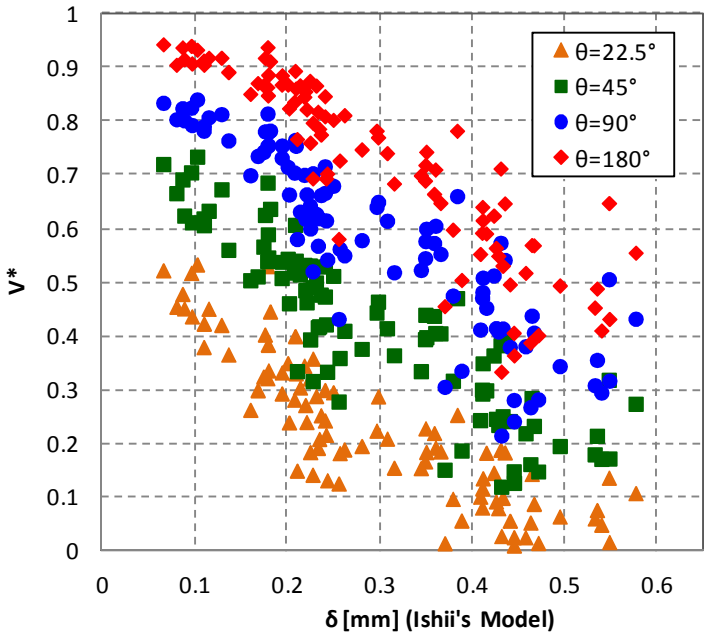

Fig.8.21: Average signal measured in the external electrodes as a function of the liquid film thickness (evaluated on the basis of Ishii's model).

8.3 Second experimental campaign

8.3.1 Test section and instrumentation

The test section described in 8.2.1, has been modified in order to insert the VFM described in the chapter 9.
After the ECP (paragraph 8.1), having a total length of 1210 mm, the VFM is installed between two straight pipes of 1290 mm upstream and downstream respectively. The absolute pressure is measured at the inlet of the test section. The fluid temperature is measured at different location of the test section by means of thermocouples (accuracy of ±0.5°C).

8.3.2 Data acquisition

The instrument signals (single phases flow parameters, pressures and temperatures in the test section) are acquired by means of a NI DAQ, using the LabView® software. The acquisition time was equal to 30 s with an acquisition frequency of 1250 Hz. The ECP signal acquisition has been improved in order to have a faster response of the sensor, suitable to be used in transient analysis. The signal are acquired with a dedicated DAQ in LabView®, synchronizing the acquisition with the other test section instruments.
The electrodes measurement combinations (81) and sequence is defined in the LabView program, together with the number of samples (2000), used to perform the RMS value and the acquisition frequency (250 kHz). The sequence is defined to excite the electrodes from 1 to 9 and to read the outputs from the receiving external electrodes; then the 9 lectures related with the central electrode are performed. The time required to acquire the 2000 samples for each measuring combination is equal to 33 ms, corresponding to a total acquisition time of a measuring cycle of 2.7 s. For each flow condition 10 cycles are acquired, in order to evaluate with a good statistics the mean value of the RMS and the related standard deviation.

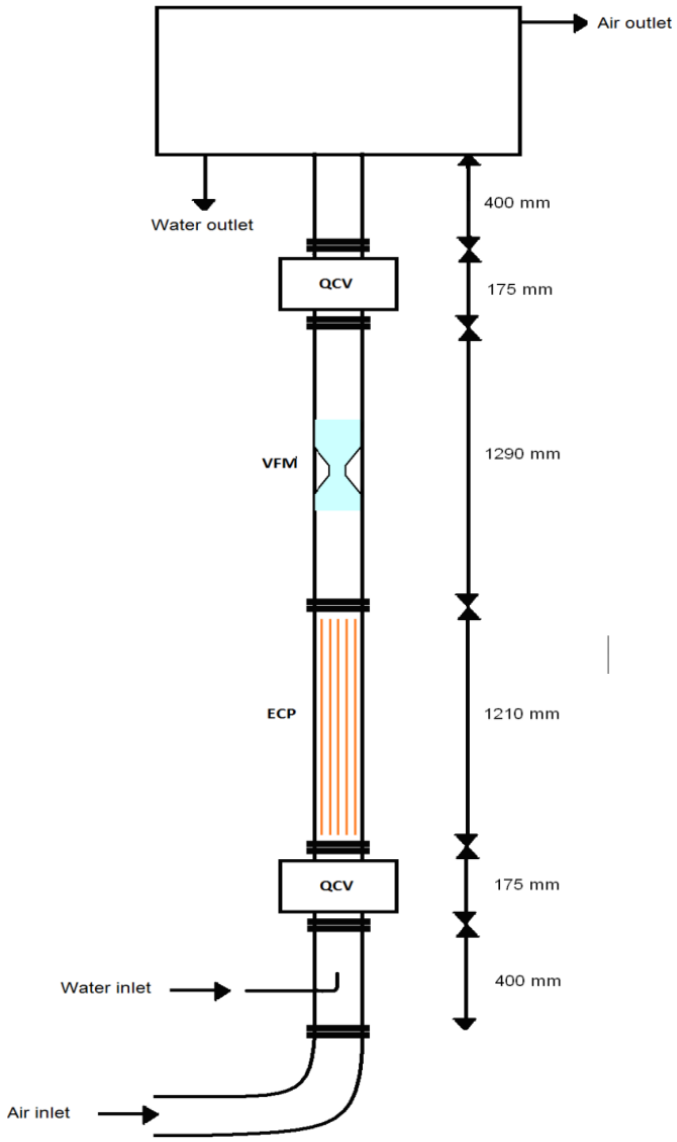

Fig.8.22: Vertical Test Section schematic

8.3.3 Experimental matrix

The experiments have been carried out fixing the mass flow rate of the two phases at the inlet of the test section. The air superficial velocity ranged between 14 and 18 m/s while the water superficial velocity ranged between 0.0008 and 0.005 m/s, so that the flow pattern was annular and the corresponding void fraction is higher than 0.97, while the flow quality ranges from 0.78 to 0.96.

For the tested superficial velocities range the variation of the void fraction (measured by QVC technique) is shown in Fig.8.23. The small variation of this parameter is due to the very small values of the liquid superficial velocities. In the present work the value of $\rho_l J_l$ is much smaller than $\rho_g J_g$. The liquid superficial velocity range has been chosen in order to obtain the annular flow pattern in the test section; considering the experimented air flow velocities, higher values of the liquid superficial velocities involve the presence of a counter-current flow.

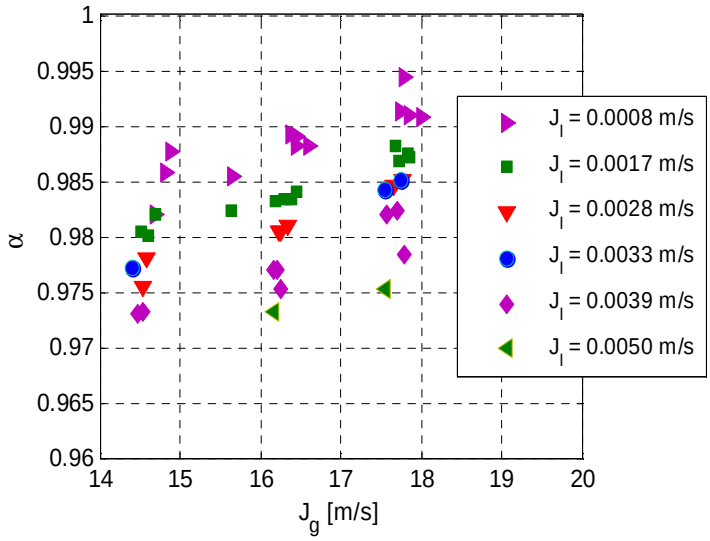

Fig.8.23: Void fraction as a function of the superficial velocity of the two-phases

In Fig.8.24 the void fraction is represented as a function of the flow quality.

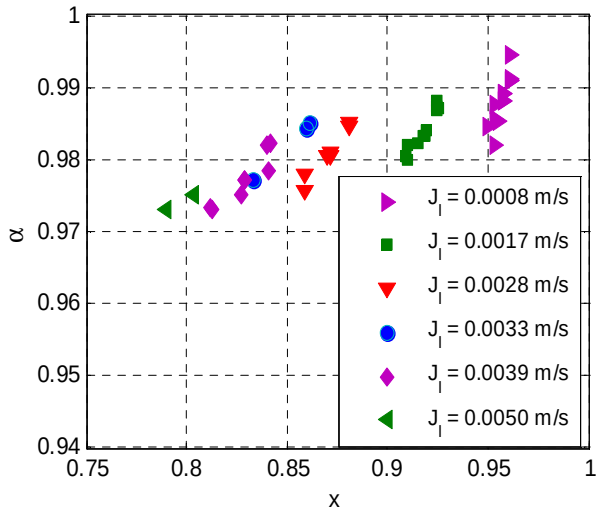

Fig.8.24: Void fraction as a function of the flow quality

The experimental points reported in Fig.8.24 show that the x-α relation, in the present conditions, is not a unique curve, but strongly depends on the slip ratio *S* defined in the paragraph 3.2.

The annular flow parameters, evaluated by the Ishii model [8.19], are shown in Fig.8.25 and Fig.8.26.

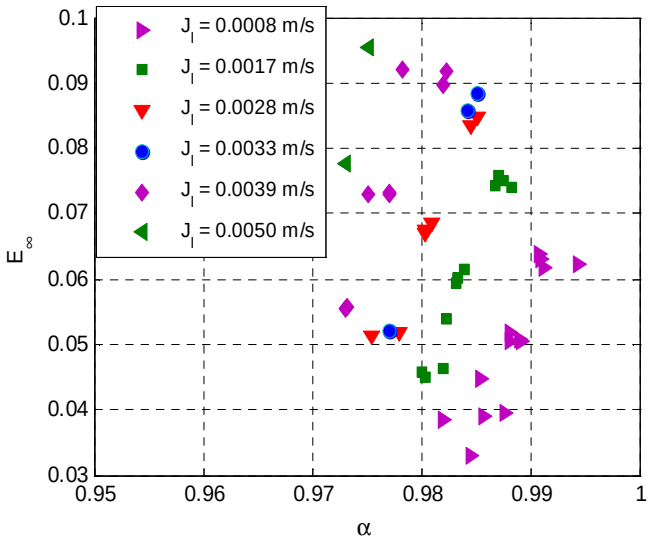

Fig.8.25: Entrainment (Ishii model) as a function of the QCV void fraction measurement

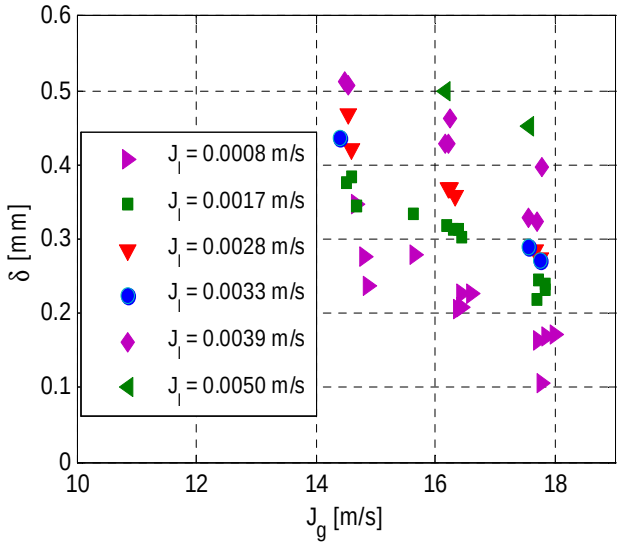

Fig.8.26: Liquid film thickness (Ishii model) as function of the phases superficial velocities

8.3.4 Numerical analysis of the ECP in annular and dispersed two-phase flow

The ECP response has been studied by means of a FEM analysis, able to evaluate the sensitivity of the sensor to the void fraction variation in the measurement volume.
The FEM analysis allows the evaluation of the capacitance associated with the different measuring electrodes, for the different phases distributions, by means of the electrical field resolution in the control volume.
The electrical field has been obtained solving the Laplace equation, eq. 8.15, imposing the Dirichlet boundary conditions:

$$\nabla^2 V = 0 \qquad (8.\ 15)$$

V=0 grounding electrode

V=5 excited electrode
Once the potential field is calculated, the capacitance value for each electrodes coupling can be evaluated by means of eq. 8.16:

$$Q = C\Delta V \qquad (8.\ 16)$$

where Q is the charge accumulated at the electrodes surface.

The sensor geometry has been modeled in 2-D (Fig.8.27), respecting the real dimensions of the pipe inner and outer diameter and the electrodes width.
The electrodes material has been defined using the properties of a commercial stainless-steel, the pipe material is Plexiglas, while the two-fluid flow has been modeled using the electrical properties of air and demineralized water.

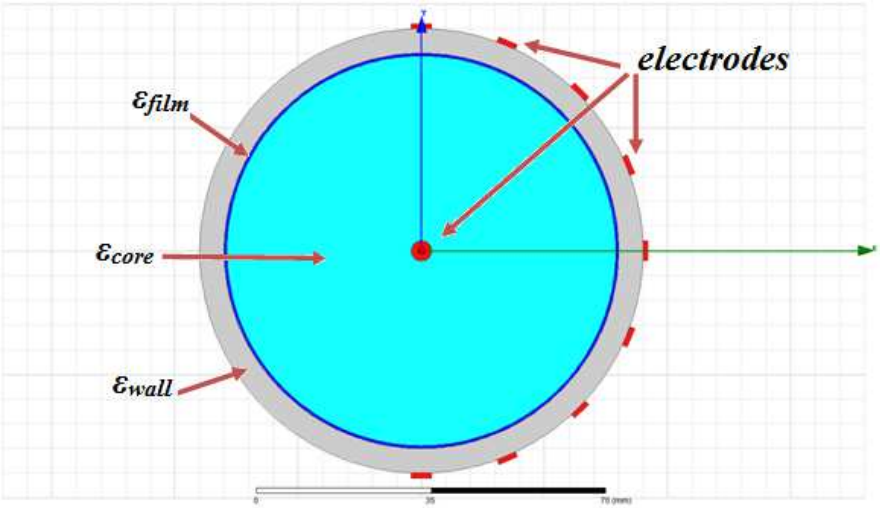

Fig.8.27: ECP numerical model schematic

The first analysis has been performed considering the pipe full of water and air respectively, in order to characterize the single-phase sensor response (sensitivity and measuring angle dependencies) and the signal attenuation due to the Plexiglas pipe thickness.

In Fig.8.28 the single-phase simulation results are shown. The theoretical ratio C_l/C_g, reported in Fig.8.28 (b), decreases from 80 ($\varepsilon_{water}/\varepsilon_{air}$ ~ 80) to a value that ranges between 1.64 and 3.14 depending on the measuring angle θ.

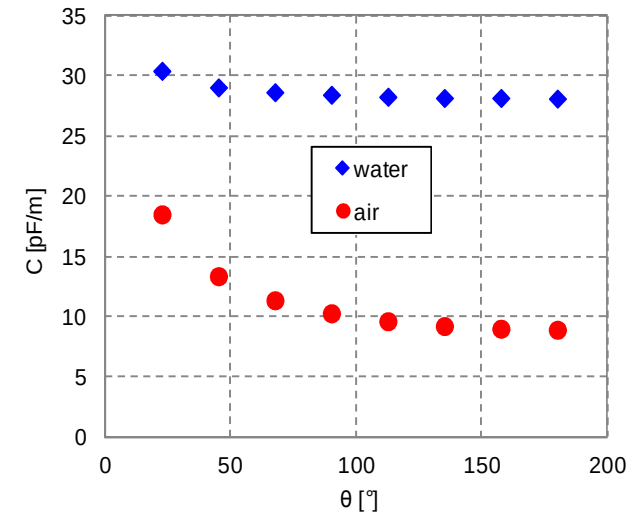

(a)

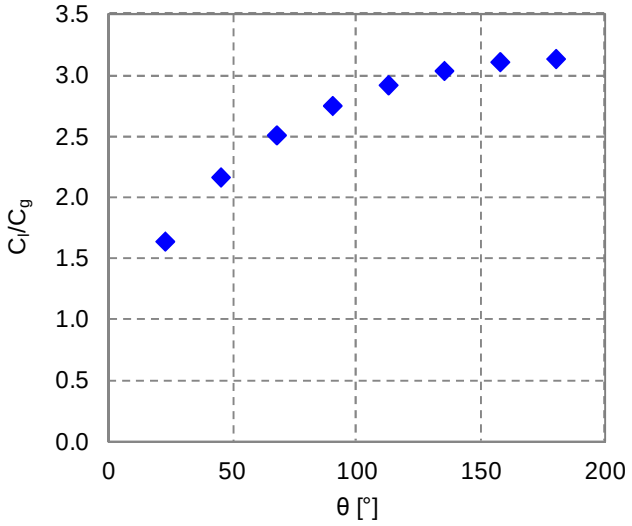

(b)

Fig.8.28: ECP numerical model: (a) single-phase sensor response, (b) water-air capacitance ratio, as a function of the measuring angle θ, for the external electrodes

The ratio C_l/C_g relate to the central electrode is instead equal to 5.41. The lower attenuation is due to the direct contact of the electrode with the fluid, so that in this case only a pipe thickness is interposed between the measuring electrodes.
The simulation highlights that the pipe thickness is responsible of a signal attenuation of more than 60% compared with the theoretical capacitance ratio. Moreover, in the real case, an additional signal attenuation due to the electrical wires and the electrical circuits must to be considered.

Concerning the two-phase flow simulations, the phases distribution has been modeled considering three different approaches:

- Homogeneous flow, with the mixture electrical properties evaluated by means of Maxwell's equation (eq. 4.38) as a function of the void fraction.
- Ideal annular flow without entrainment: modeled as fully separated phases distribution, with a thin and smooth liquid film at the pipe wall, characterized by the dielectric constant of the water phase, and a gas core region, characterized by the

dielectric constant of the air. The void fraction value is changed by changing the liquid film thickness.

- Annular flow with entrainment, with a thin and smooth liquid film at the pipe wall and a homogeneous mixture in the core region. In this case the void fraction value depends on the liquid film thickness and on the dielectric constant of the mixture in the core region.

The simulation results have been normalized as:

$$C_{ij}^{*} = \frac{C_{l,ij} - C_{TP,ij}}{C_{l,ij} - C_{g,ij}} \qquad (8.\ 17)$$

where $C_{l,ij}$ e $C_{g,ij}$ are the single-phase capacitance measurement for the different measuring electrodes (ij), and $C_{TP,ij}$ is the two-phase capacitance value.

The sensor response for homogeneous flow conditions is shown in Fig.8.29, while the results concerning the ideal annular flow without and with entrainment are reported in Fig.8.30 and Fig.8.31 respectively.

The numerical analysis highlights that the electrodes response strongly depends on the phases distribution. The same average cross-sectional void fraction value can gives different value of the sensor signal depending on the flow pattern. The simulated response of the ECP to an homogeneous flow shows very poor sensitivity and a signal saturation for the external electrodes characterized by a measuring angle higher than 72.5°, as shown in Fig.8.29 (a). At the same flow condition the response of the central electrodes appears to be a linear function of the void fraction (Fig.8.29 (b)). For annular flow conditions (Fig.8.30), the sensitivity of the external electrodes seems to increase, with a normalized value that ranges from about 0.4 to 0.72 for the distribution characterized by an average void fraction of 0.956, and from 0.75 to 0.95 for an average void fraction of 0.99.
Moreover the curves of Fig.8.30 (a) highlight that the higher sensitivity to the film thickness is achieved for the electrodes having a distance of 22.5°. For thin liquid film thickness, $\delta<0.3$mm the response depends on the core void fraction values, while for higher film thickness the electrodes are rather insensitive to the internal distribution.

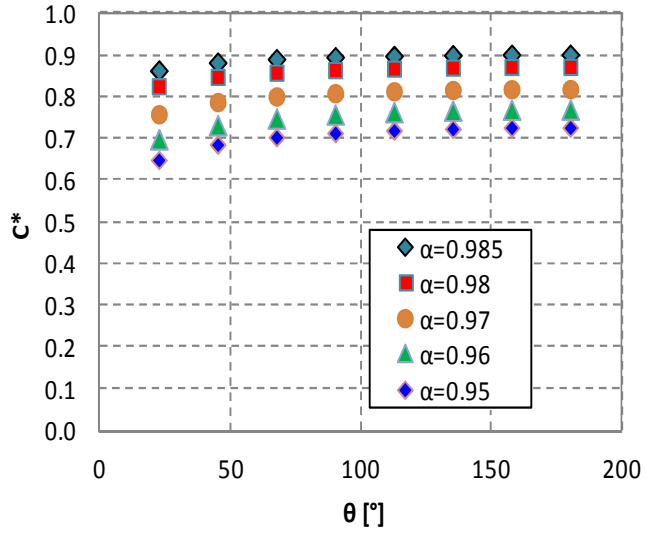

(a)

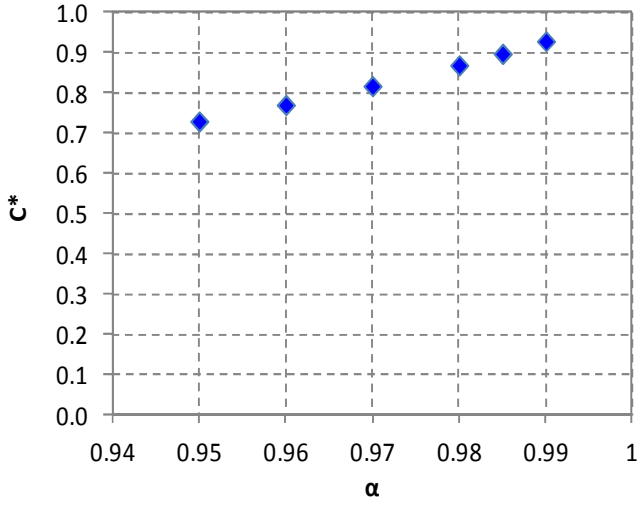

(b)

Fig.8.29: Homogeneus two-phase flow simulation. (a) External electrodes response. (b) Central electrode response

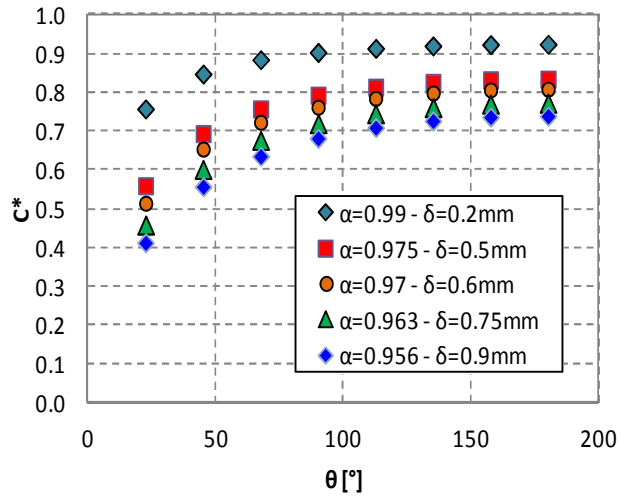

(a)

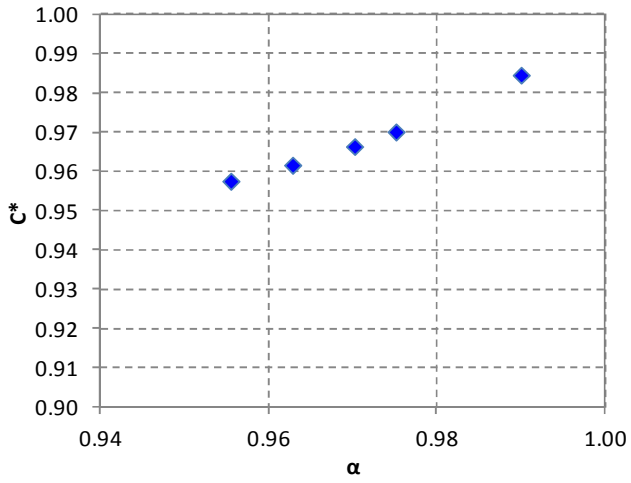

(b)

Fig.8.30: Ideal annular two-phase flow simulation without entrainment. (a) External electrodes response. (b) Central electrode response

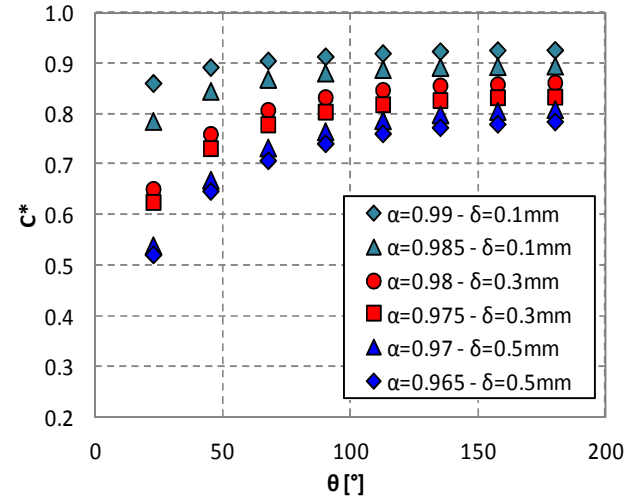

(a)

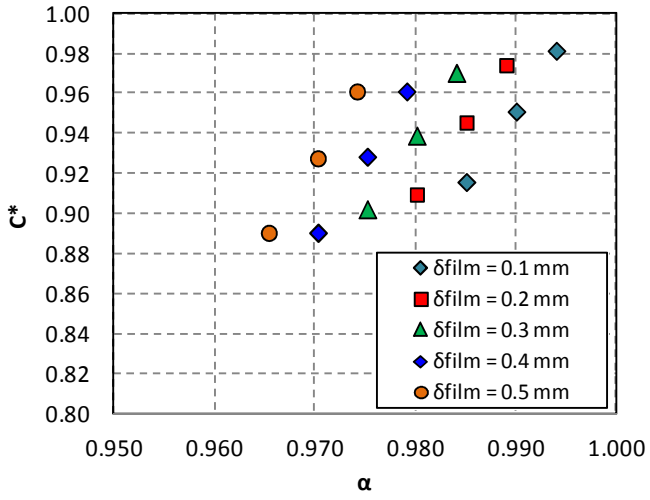

(b)

Fig.8.31: Ideal annular two-phase flow simulation with entrainment. (a) External electrodes response. (b) Central electrode response

The analysis of the central electrode (Fig.8.30 (b)) shows that also in this case the signal is linearly dependent on the average cross-sectional void fraction, but it is characterized by a strong sensitivity to the film thickness value, as shown in Fig.8.31 (b).

The performed numerical analysis allows the identification of the flow parameter that more affect the sensor signal, and allows the quantification of the sensitivity of the ECP at different flow conditions.
The analysis allows us to conclude that the identification of the phases distribution is fundamental for a proper signal interpretation.

8.3.5 Experimental single-phase calibration

As for the first analysis the sensor response for static single-phase conditions has been analyzed in order to evaluate the signal repeatability and the sensor sensitivity.
The results are compared with the numerical simulations.

In Fig.8.32 is reported the RMS values corresponding to the electrodes i=1 and j=2:9, as a function of the measuring distance θ, for air and water respectively, and the ratio RMS_l/RMS_g.
The curves measured at different times show the good repeatability of the signal, but highlight also the limited sensitivity of the sensor.

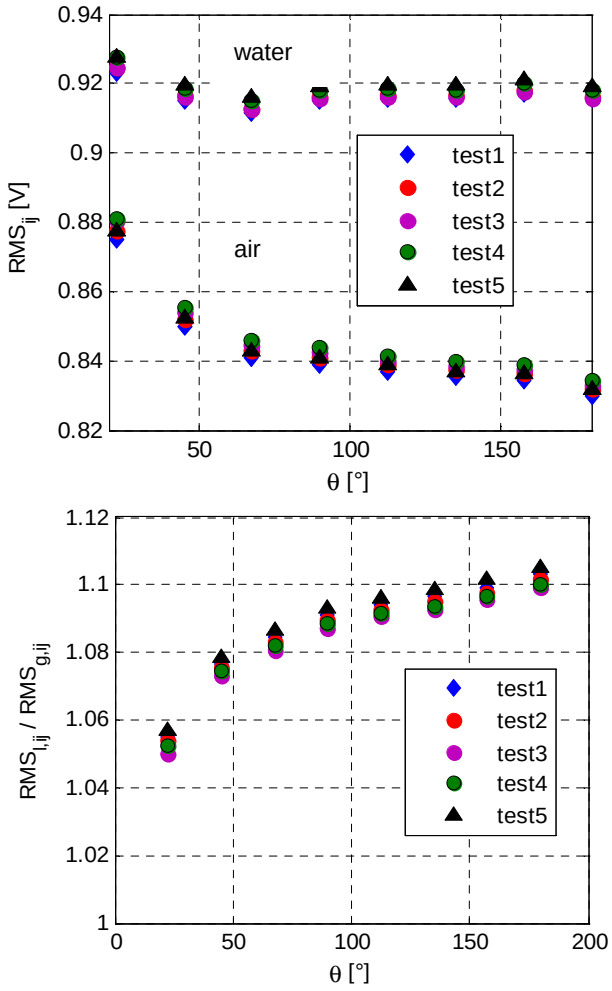

Fig.8.32: Single-phase ECP external electrodes response

The ratio RMS_l/RMS_g decreases from the theoretical value of 80 ($\varepsilon_{water}/\varepsilon_{air} \sim 80$) to a value that ranges between 1.05 and 1.1 depending on the measuring angle θ.
The signal is strongly influenced by the measuring angle under air conditions, while shows a limited variation under water conditions.
Concerning the central electrode, the average signal obtained from the nine measurements has been considered. In this case the ratio RMS_l/RMS_g has been found equal to 1.6 ± 0.1
The comparison between the experimental, RMS_l/RMS_g, and the numerical, C_l/C_g, results is reported in Fig.8.33. The comparison shows that the ECP signal is affected by constant external impedances that act to reduce the sensitivity of the sensor response, that must be reduced in order to develop an instruments suitable to be used in a SP.

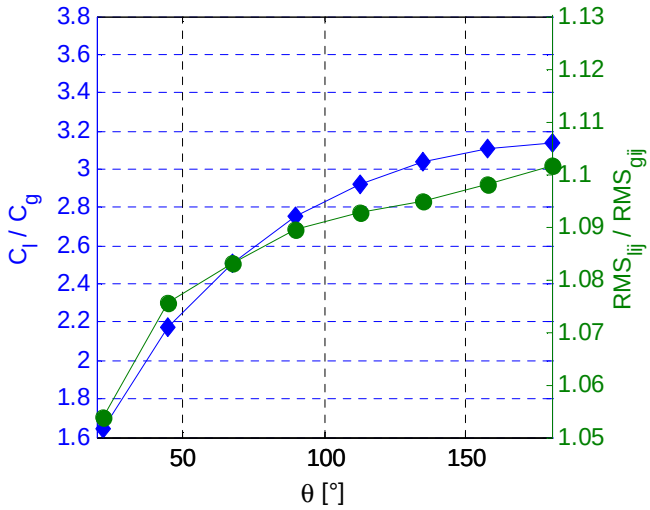

Fig.8.33: Comparison between experimental (RMS_l/RMS_g) and numerical (C_l/C_g) external electrodes response in single-phase conditions

8.3.6 ECP sensor response in two-phase flow conditions

The signal obtained under two-phase flow conditions is normalized as reported in eq. 8.1.
In the following figures the experimental signals are compared with the results of the numerical simulations, as a function of the fluid-dynamic parameters evaluated on the basis of the experimental measurements and the Ishii's model described in the paragraph 8.2.5.

External electrodes

In Fig.8.34 the comparison between experimental and numerical data is shown for the external electrodes characterized by a measuring distance of 22.5° and 180°.
In Fig.8.34 (a) the dependency on the void fraction is reported, while in Fig.8.34 (b) the dependency on the liquid film thickness is highlighted. The numerical simulations reported in the figures are identified with triangles, for the homogeneous flow, and diamonds for the ideal annular flow.
The comparison, performed using two different reference scales, shows a qualitative good agreement of the experimental data with the predictions.
Moreover the comparison shows that the electrode, characterized by a measuring distance of 180°, shows a very low data dispersion, a linear dependency on the mean cross sectional void fraction and a behavior in accordance with the numerical simulation, that highlights a similar behavior under homogeneous and annular flow. The electrode characterized by a measuring distance of 22.5°, instead, shows a higher dispersion, probably related to the strong sensitivity to the liquid film thickness and its dynamics. However, also in this case, the signal shows the same behavior of the simulated annular flow.
The performed analysis can be used to qualitatively understand the ECP response at different flow conditions, and allow us to conclude that the signal related to the electrodes at 180° can be used to directly estimate the average cross sectional void fraction, due to the low sensitivity to the phases distribution, while the measurement at 22.5° can be modeled in

order to extract information concerning the liquid film thickness and the core phases distribution.

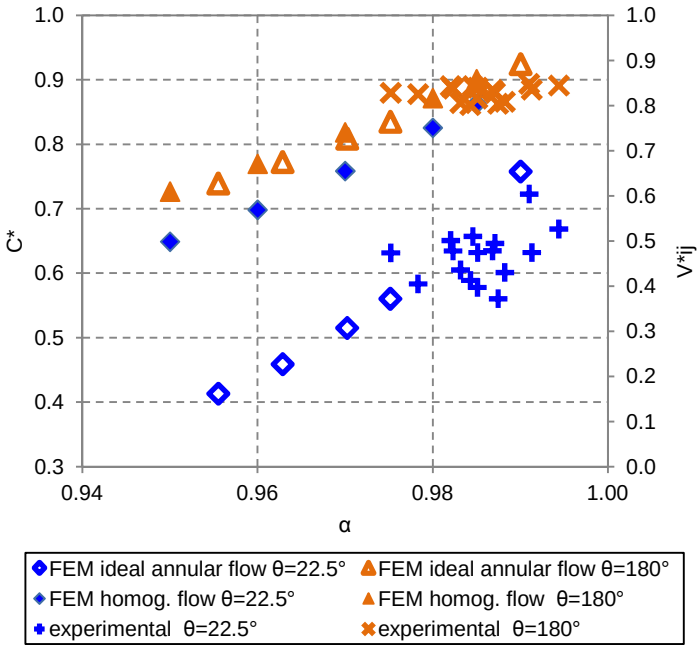

(a)

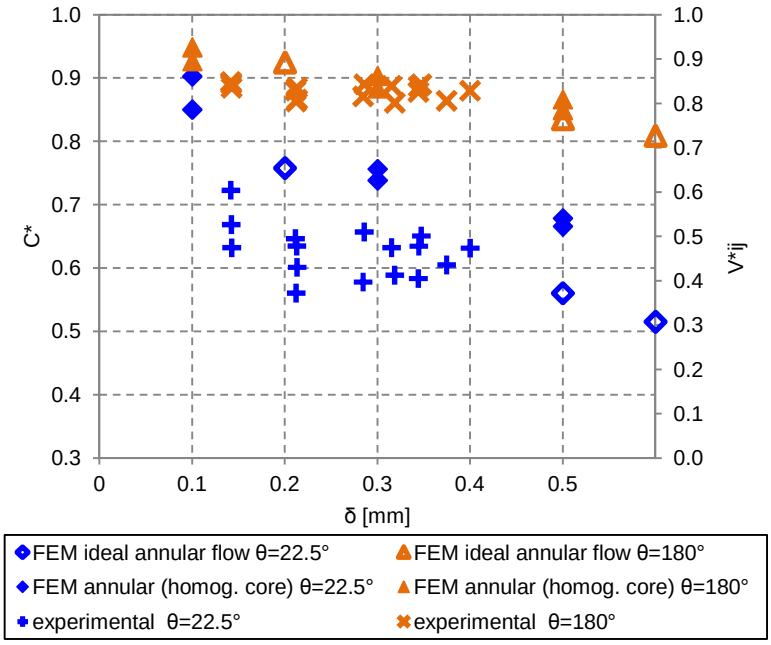

(b)

Fig.8.34: Comparison between experimental and numerical external electrodes results at 22.5° and 180° for two-phase flow. Void fraction dependency (a) and film thickness dependency (b)

Central electrode

In Fig.8.35 the comparison between numerical and experimental results for the central electrode is reported. In this case a unique scale is used, suggesting that the direct contact of

the electrode with the fluid allow the reduction of the effect of the external impedance on the measured signal.
Also in this case the comparison shows a good agreement between the experimental measurement and the simulations corresponding to the ideal annualr flow.

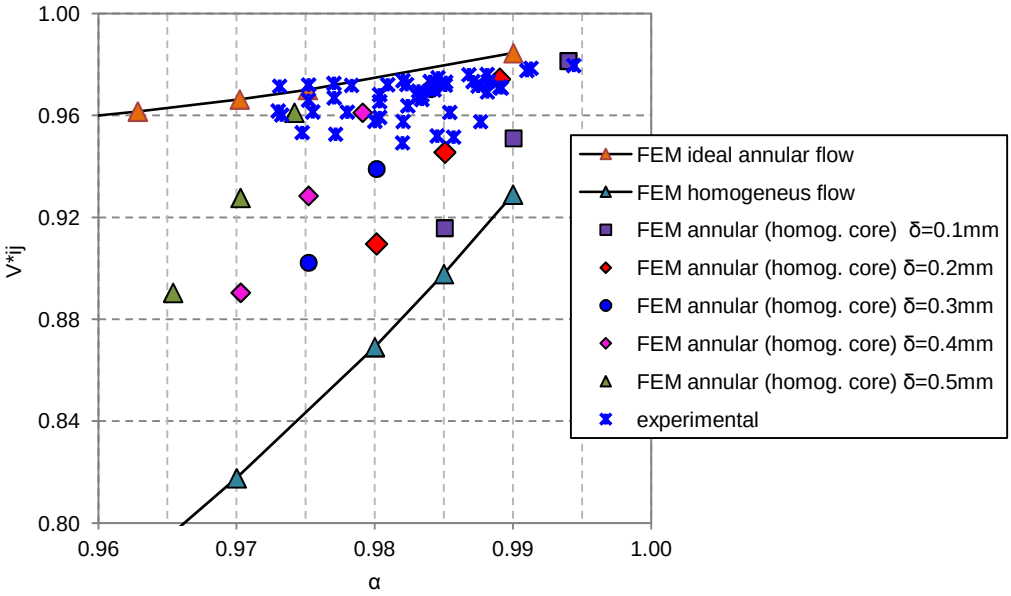

Fig.8.35: Comparison between experimental and numerical central electrode results under two-phase flow, as a function of the void fraction

8.4 Conclusions

The characterization of a new impedance void fraction measurement device, in vertical annular and annular-mist air-water flow, has been described in this chapter.
The Electrical Capacitance Probe (ECP), has been developed by the SIET Company, and consists of ten measurement electrodes, nine external and an internal one.
The presence of the internal electrode introduces a little flow disturbance, but allows one to obtain important information on the phase distribution inside the core region of the annular flow.
The response of the sensor has been characterized in terms of single-phase flow sensitivity and signal variation dependence; geometry and fluid-dynamic influences on the signal have been investigated. Although the sensitivity in single-phase flow is low, two-phase flow void fraction variations lower than 1% have been detected. The presence of the central electrode allows the evaluation of the average cross-section void fraction also in annular flow, where the liquid film is the principal cause of the sensor low sensitivity. The signal measured in the central electrode is linear with the void fraction for values higher than 98% and it is quite sensitive to the flow pattern: the flow pattern, from rather regular to more disturbed annular flow, has been clearly characterized in the first experimental campaign. The variation of the signal measured in the external electrodes has been related to the average liquid film thickness that is evaluated by means of the Ishii's model. The tests have shown the potentiality of this technology for the measurement of two-phase flow parameters at very high void fraction conditions (higher than 95%).

A FEM model of the sensor has been developed and used to investigate the ideal response of the ECP for different flow conditions. The numerical model allows the identification of the pipe wall thickness effect on the measured signal and the dependency of the capacitance on the fluid-dynamic parameters. The comparison with the experimental data showed a good agreement and highlights the possibility to use the numerical model to identify the possible sensor modifications finalized to increase the sensitivity under annular flow conditions.

The analysis concluded that the sensitivity of the sensor must be increased, in order to make the instrument suitable to be used for void fraction measurement with a good accuracy, but even if characterized by a low sensitivity, the analysis highlights the possibility to use this new impedance sensor in order to measure the mean cross sectional void fraction and the liquid film thickness for annular and annular-mist two-phase flow.

9. VENTURI FLOW METER IN VERTICAL ANNULAR FLOW

In the previous chapters the analysis of two different SP, in horizontal pipe configuration, has been described.
The analysis of the SP made up of a TFM and a DD, chapter 6, allows us to conclude that the information about the flow structure (void fraction and flow pattern) is fundamental for a proper interpretation of the instruments signals and then for the correct modeling of the SP.
Considering that for an industrial application the installation of a reduced number of instruments is important for both economical aspects and for space requirements, the second SP consists of only two instruments: a VFM and a WMS [9.1]. The analysis concluded that if the void fraction, and then the flow pattern, can be correctly identified, the two instruments can be used to evaluate the mass flow rate of the two phases with a good accuracy. A similar approach has been applied in a vertical test section, where a new VFM has been coupled with a new electrical sensor, Electrical Capacitance Probe (ECP). The VFM has been home designed (see ANNEX I) and has been built in Plexiglas in order to allow the visualization of the flow along the instruments. Because the analysis of the ECP sensor showed that the accuracy and the sensitivity of the system must be improved in order to use the sensor in the SP, in this chapter the analysis focus only on the VFM response and signal analysis.
The pressure drops in the VFM have been modeled as a function of the two phases superficial velocities in order to evaluate the effect of each phase on the total flow meter pressure drops. The predictions of the existing correlations are compared with the experimental pressure drops, and a formulation that predicts the experimental data is presented. Moreover the irreversible VFM pressure drops have been measured and analyzed. The experimental results have been modeled as a function of the flow quality and of the superficial velocities of the phases, showing that additional relevant information on the two-phase flow can be extracted from the test data [9.2].
In the last part of the work the characterization of the instrument is used to evaluate the mass flow rate of the two-phases with different approaches.

9.1 Test section and instrumentation

The test section, where the VFM is installed, is described in 8.3.1. The VFM is installed between two straight pipes of 1290 mm upstream and downstream respectively, after the ECP, paragraph 8.1, [9.3], having a total length of 1210 mm. The absolute pressure is measured at the inlet of the test section, while the VFM pressure drops are measured between the inlet and the throat sections and between the inlet and the outlet sections (irreversible pressure loss). The fluid temperature is measured at different location of the test section by means of thermocouples (accuracy of ±0.5°C).
The instrument signals (single phases flow parameters, pressures and temperatures in the test section) are acquired by means of a NI DAQ, using the LabView® software. The acquisition time was equal to 30 s with an acquisition frequency of 1250 Hz.

9.2 Experimental matrix

The experiments have been carried out fixing the mass flow rate of the two phases at the inlet of the test section. The air superficial velocity ranged between 14 and 18 m/s while the water superficial velocity ranged between 0.0008 and 0.005 m/s, so that the flow pattern was annular and the corresponding void fraction is higher than 0.97, while the flow quality ranges from 0.78 to 0.96.
The liquid superficial velocity range has been chosen in order to obtain the annular flow pattern in the test section; considering the experimented air flow velocities, higher values of the liquid superficial velocities involve the presence of a counter-current flow.

9.3 Venturi Flow Meter

The VFM used to perform the present analysis has been designed to operate in both fluid direction (symmetrical flow meter), with the angle of the convergent section equal to the divergent section angle (θ=21°), in order to be able to work in reverse flow conditions. The selected material, Plexiglas, allows the direct flow visualization along the instrument. Compared with the Herschel model the present VFM is characterized by a higher divergent angle (usually set to 15°), with lower manufacturing costs but also higher irreversible pressure drops, due to the flow separation. The geometrical characteristics of the experimented VFM are described in Tab.9.1 while the instrument is shown in Fig.9.1.

VFM Characteristics		
D_1	80	mm
D_2	40	mm
$\theta_{convergent} = \theta_{divergent}$	21	°
$L_{tot\_Venturi}$	340	mm
$L_{upstream}$	628	mm
$L_{downstream}$	628	mm

Tab.9.1: VFM Characteristics

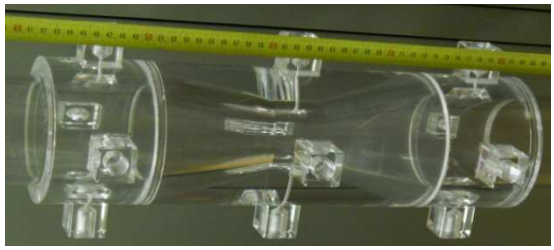

Fig.9.1: Venturi Flow Meter

The instrument single-phase behavior has been analyzed, as it is shown in Fig.9.2, in order to obtain the VFM discharge coefficient C_d (Fig.9.3) by using the experimental values of mass flow rate and pressure, and by adopting F_a and Y equal to one.

The Reynolds number dependency can be approximated by an exponential law of type:

$$C_d = a \cdot \mathrm{Re}^b \qquad (9.\ 1)$$

with the parameters a and b obtained from the experimental data (a=1.5054 and b=-0.0510). The Re number is evaluated as:

$$\mathrm{Re} = \frac{\rho U D_1}{\mu} \qquad (9.\ 2)$$

In single-phase flow the discharge coefficient value takes into account the phenomena of the wall flow detachment at the inlet of the divergent section; in two-phase flow, the presence of the interface between the two phases complicates the physical interpretation of this correction coefficient.

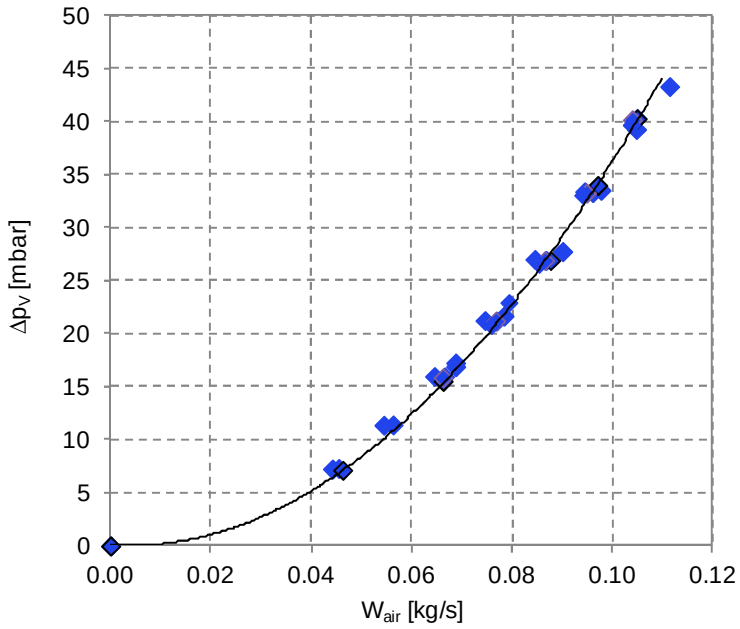

Fig.9.2: Single-phase flow calibration curves for the VFM

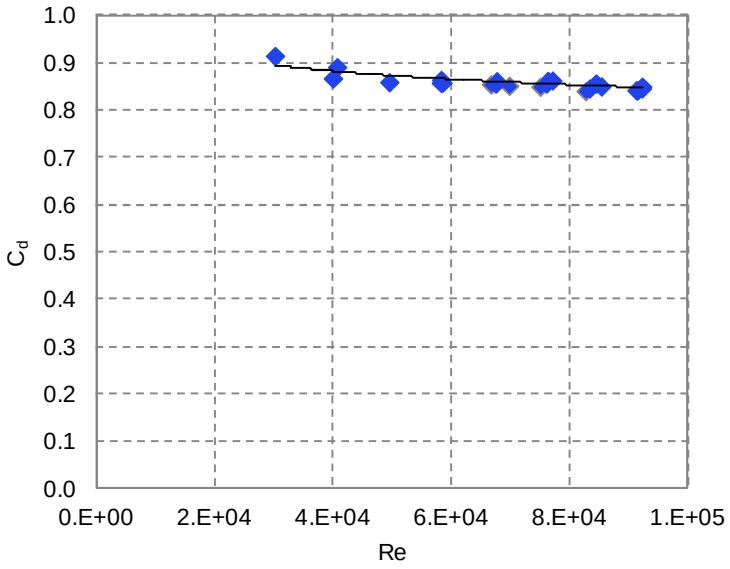

Fig.9.3: Experimental single-phase discharge coefficient

9.4 VFM modeling in two-phase flow

In chapter 7, as regards the SP constituted by a classical Venturi and a WMS [9.1], the VFM has been modeled by means of the definition of an equivalent two-phase flow density and by the two-phase flow discharge coefficient. The model has been applied in a flow quality range between 0 and 0.75.
In the present tests the flow quality ranges between 0.78 and 1, corresponding to void fraction higher than 0.95. Due to the limited range (annular flow), in the present case two different approaches can be used to investigate the flow and develop a model of the instrument that allows the estimation of the mass flow rate of the phases: the classic methodology based on the use of the discharge coefficient or the definition of a two-phase flow multiplier.

9.4.1 Two-phase flow discharge coefficient

As shown in the chapter 7, the response of a VFM in two-phase flow can be modeled considering the effect of the presence of the second phase on the discharge coefficient. Following this approach the VFM pressures drops can be related with the total mass flow rate of the mixture as:

$$W_{tot} = \frac{C_{d-TP} \cdot F_a \cdot Y \cdot A_2}{\sqrt{\left(1-\beta^4\right)}} \cdot \sqrt{2\rho_{TP}\Delta p_{TP}} \qquad (9.3)$$

where ρ_{TP} is the two-phase flow momentum density.
The use of this model requires the knowledge of the void fraction in the measurement section, and the discharge coefficient must be obtained from a preliminary calibration.

9.4.2 VFM two-phase flow multiplier

According to the approach described in the paragraph 4.5.2, the frictional pressure gradient of a two-phase mixture flowing in a pipe can be correlated to the single-phase pressure drop by means of the two-phase flow multiplier:

$$\frac{\left(-\frac{dp}{dz}\right)_{TP}}{\left(-\frac{dp}{dz}\right)_{g}} = \phi_g^2 \qquad (9.4)$$

where $-(dp/dz)_g$ is the frictional gas pressure gradient obtained by using the actual air phase flow rate for the two-phase flow. The two-phase flow multiplier is expressed as a function of the Martinelli parameter, eq. 4.21, and the two-phase pressure drops are then related to the two-phase flow multiplier, by means of empirical or semi-empirical correlations.

The experimental data are compared with the results of the Chisholm [9.4] correlation and Murdock [9.5] correlation, described in the paragraph 4.5.2.

9.5 Experimental Venturi Flow Meter behavior in two-phase flow

In Fig.9.4, Fig.9.5 and Fig.9.6 the experimental VFM pressure drops are plotted as a function of the flow conditions.
In Fig.9.4 the pressure drop dependency on the total mass flow rate is shown: the VFM pressure drop is a function of the mass flow rate of the two phases; introducing the ratio W_l/W_g, if this ratio is equal to zero the air single-phase flow is obtained, while increasing the fraction of water in the mixture an increase of the pressure drops is highlighted. The dependency on the superficial velocities of the two phases and the small effect due to the liquid flow rate is confirmed in Fig.9.5. In Fig.9.6 the two-phase pressure drop, normalized with reference to the gas single-phase pressure drop, is shown as a function of the gas superficial velocity: the two-phase flow value is very close to the gas single-phase flow value, with a maximum increase of about 7%.

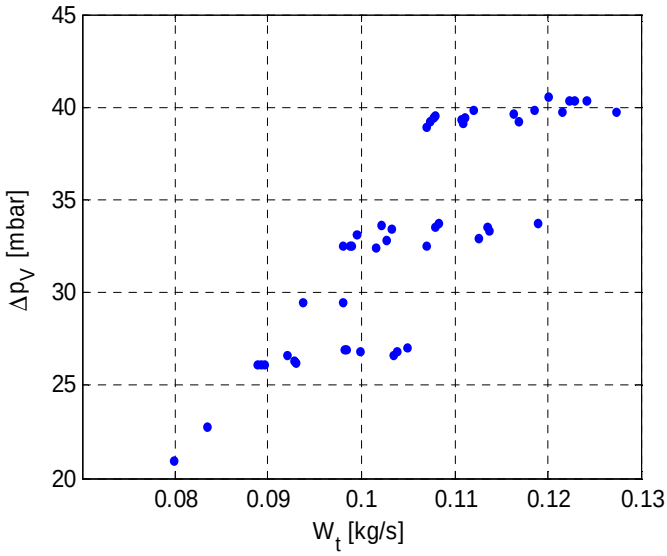

Fig.9.4: VFM pressure drop as a function of the total mixture mass flow rate

The pressure drop increase in presence of two–phase flow is caused by the interaction between the gas and liquid phases: liquid droplets accelerated by the gas, irreversible drag force work done by the gas phase accelerating the liquid film and frictional wall losses, determine the magnitude of the observed pressure drop increase.

The flow field is characterized and complicated by the continuous deposition and entrainment of liquid droplets along the Venturi length and by the presence of waves on the liquid film surface. The continuous deposition and entrainment process contributes to the overall pressure drop through the loss of momentum caused by the acceleration of the newly entrained droplets.

The surface waves produce an effectively roughened surface over which the gas flows increasing the momentum loss due to the interfacial shear stress.

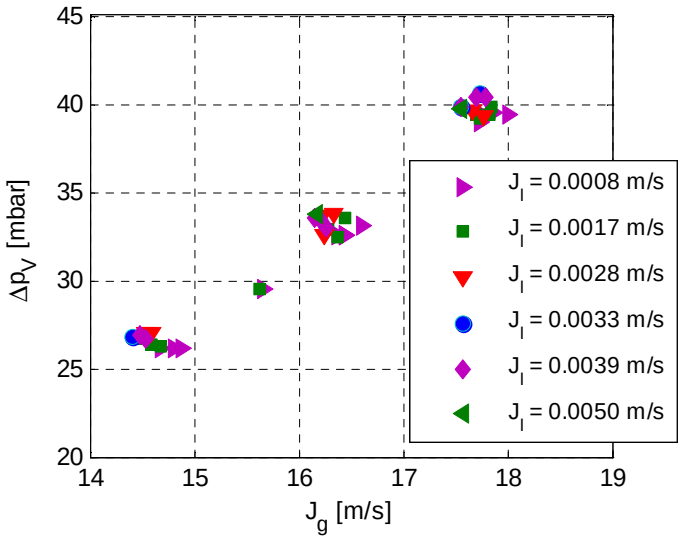

Fig.9.5: VFM pressure drop as a function of the two phases superficial velocities

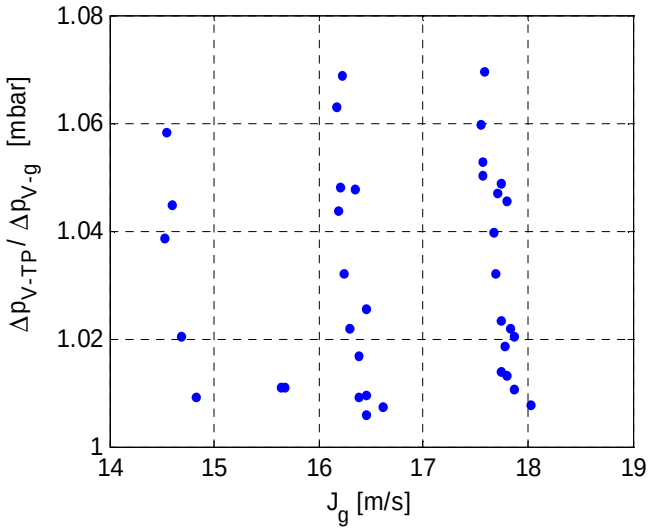

Fig.9.6: Normalized VFM pressure drop as a function of gas superficial velocity

By using the same approach described in the chapter 7, [9.1], the two-phase flow discharge coefficient $C_{d\text{-}TP}$ has been obtained. In Fig.9.7 the relation $C_{d\text{-}TP}$ – Re is reported.

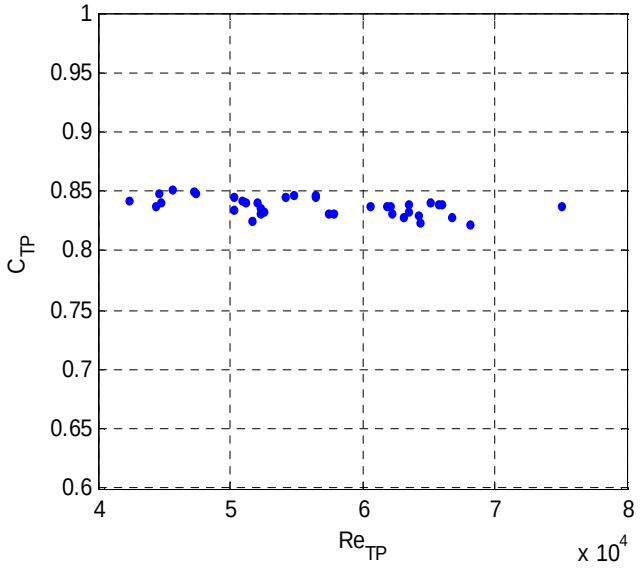

Fig.9.7: Two-phase flow VFM discharge coefficient as a function of the Re number

The Reynolds number dependency can be modeled, as for the single-phase flow, as:

$$C_{TP} = a \cdot \mathrm{Re}_{TP}^{b} \qquad (9.5)$$

where the constants a and b have been experimentally evaluated: a = 1.1938, b = -0.032.

On the ground of the previous considerations, the pressure drop in the VFM can be expressed also as a function of the single-phase pressure drop with a correction factor (a two-phase flow multiplier) that can take into account the presence and the effect of the liquid phase at different flow qualities. The two-phase flow multiplier can been written as:

$$\phi^2_{g,\mathrm{mod}} = 7.8 \cdot \chi + 1 \qquad (9.\ 6)$$

where the two constants have been obtained as best-fit of the present experimental data.
The two-phase flow multiplier values, evaluated by eq. 9.6, are compared with the correlations of Murdock, Chisholm and the present test data (Fig.9.8): the classical correlations under estimate the two-phase multiplier ϕ^2_g.

The experimental points dispersion can be justified by a change of the slip ratio value, that is considered constant in all the analyzed correlations. In Fig.9.9 the pressure drops evaluated with the new correlation are compared with the experimental values, showing a very good agreement and a calculation accuracy better than 5%.

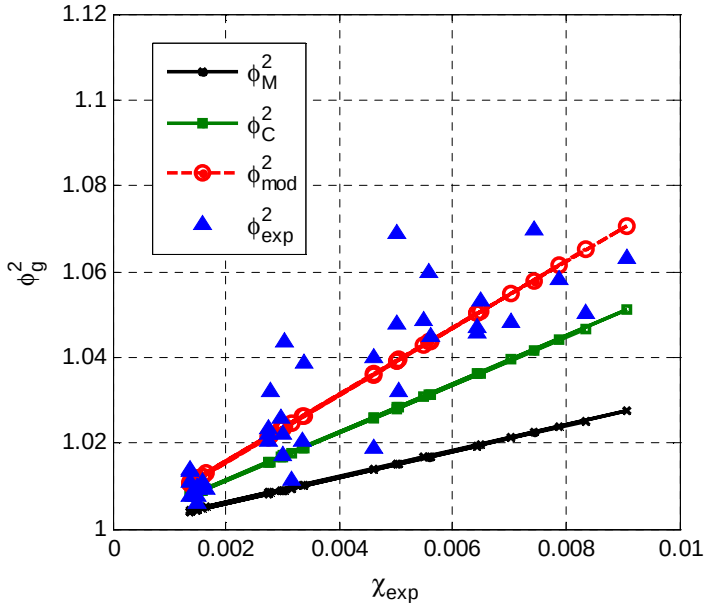

Fig.9.8: Two-phase flow multiplier: comparison between experimental data and correlations

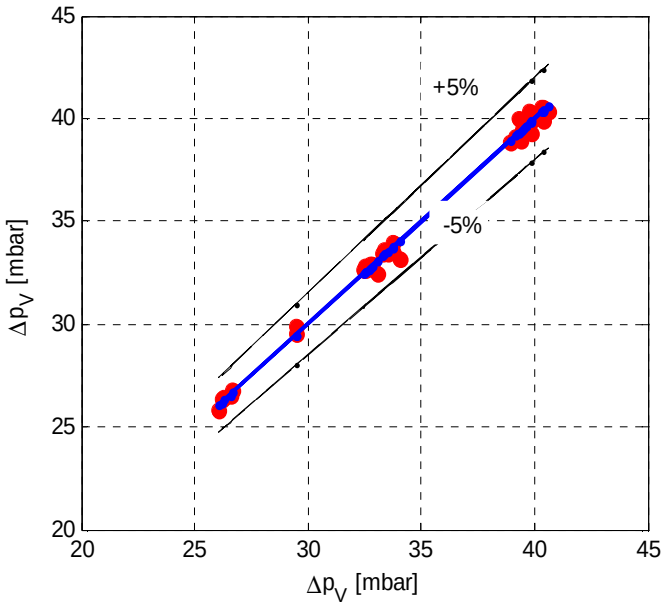

Fig.9.9: VFM pressures drops: experimental data vs. predicted values (eq. 9.6)

In the present work also the irreversible pressure losses, measured between the VFM inlet and outlet sections have been analyzed and correlated with the flow parameters. In the following pictures the dependency of the VFM irreversible pressure loss on the flow parameters is highlighted. The analysis of this component, that usually is not considered in two-phase flow models, allows us to understand better the effect of the dispersed phase in the two-phase pressure drops.

In Fig.9.10 the two VFM pressure drop components are shown as a function of the total mixture mass flow rate.

Fig.9.11 shows the irreversible pressure loss component with the pressure drop component measured between VFM inlet and throat sections. The circle points highlight the linear relation existing between inlet-outlet (irreversible component) and inlet-throat pressure drops in single-phase flow. The square points show that for an annular flow the relation between the two pressure components is not longer linear; the difference is clearly due to the liquid phase presence, so that the relation between the two components can be used to analyze the effect of the liquid flow rate and to estimate the liquid mass flow rate itself.

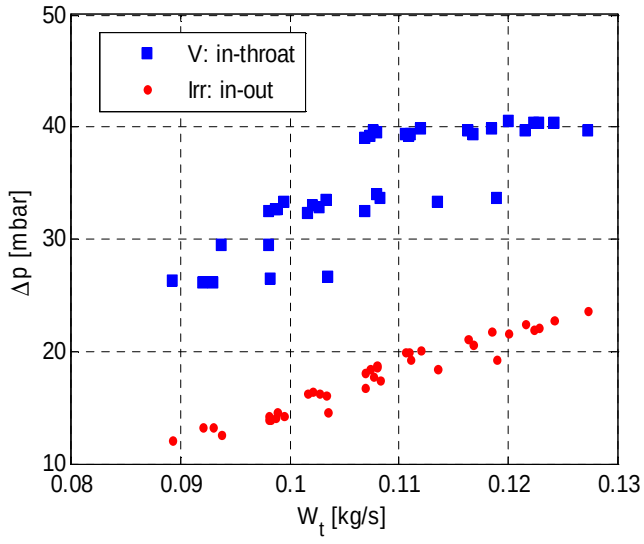

Fig.9.10: VFM pressure drop and VFM irreversible pressure loss vs. total mass flow rate

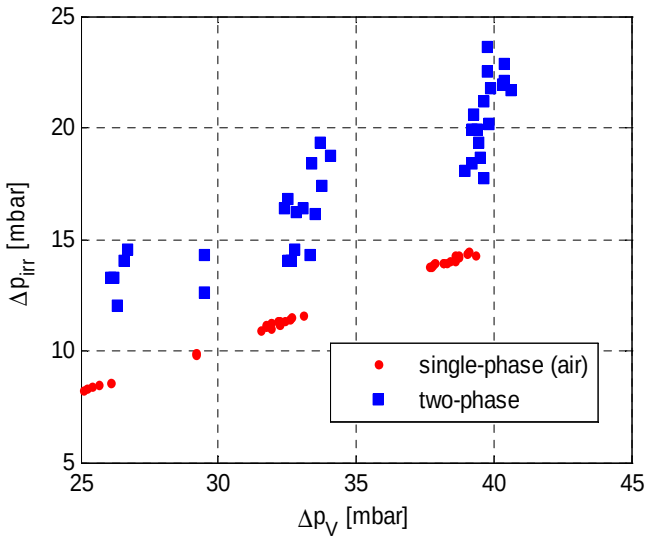

Fig.9.11: VFM irreversible pressure loss vs. VFM pressure drops

Fig.9.12 and Fig.9.13 show the dependency of the irreversible pressure loss on the superficial velocities of the phases and on the flow quality respectively. In Fig.9.13 the two-phase irreversible pressure loss is plotted as a function of the irreversible single-phase (air) component.

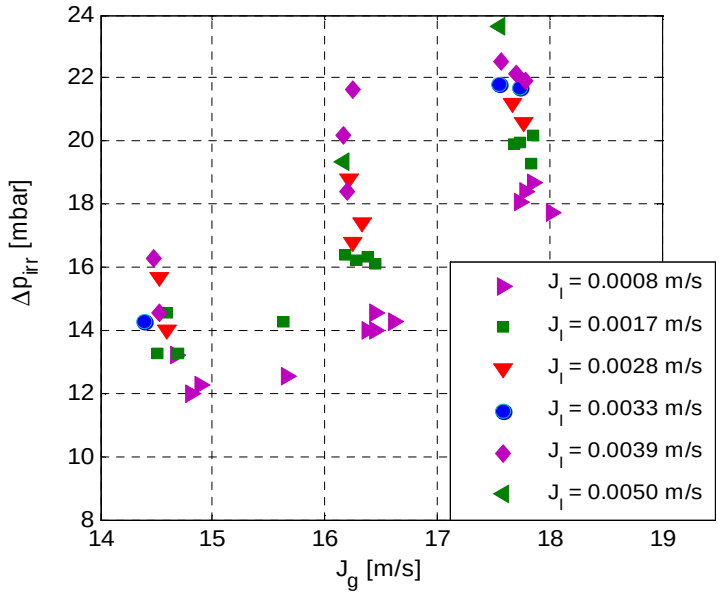

Fig.9.12: VFM irreversible pressure loss as a function of the superficial velocities of air and water

While, due to the liquid phase presence, the inlet-throat pressure drop increases of about 10%, if compared to the single-phase flow, the irreversible pressure loss increases from about 20% to 100% depending on the liquid flow rate.

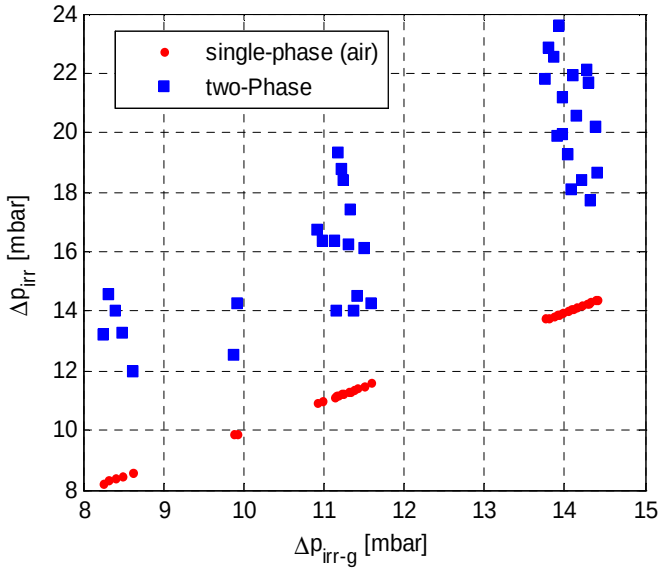

Fig.9.13: VFM pressure loss as a function of the air single-phase irreversible pressure loss

The previous analysis allows the derivation of a correlation able to describe the irreversible pressure loss change as a function of the flow rate of the two phases. The proposed correlation, developed for the present tested conditions, expresses the irreversible pressure

loss as a function of the gas superficial velocity and of the ratio between the liquid and the gas superficial velocities, highlighting the effect of the dispersed phase:

$$\Delta p_{irr} = k_1 \cdot \left(\rho_g J_g^{k_2}\right) \cdot \left(J_l / J_g\right)^{k_3} + k_4 \qquad (9.\ 7)$$

where J_g and J_l are the superficial velocity of air and water respectively. The following constants have been obtained from the best fit of the experimental data:
k_1 = 0.2096
k_2 = 2
k_3 = 0.13
k_4= -2.9786

The comparison between the predicted irreversible pressure loss and the test data is shown in Fig.9.14: the proposed correlation allows the estimation of the VFM irreversible pressure loss, in annular flow, at high void fraction, with an accuracy of 5%.

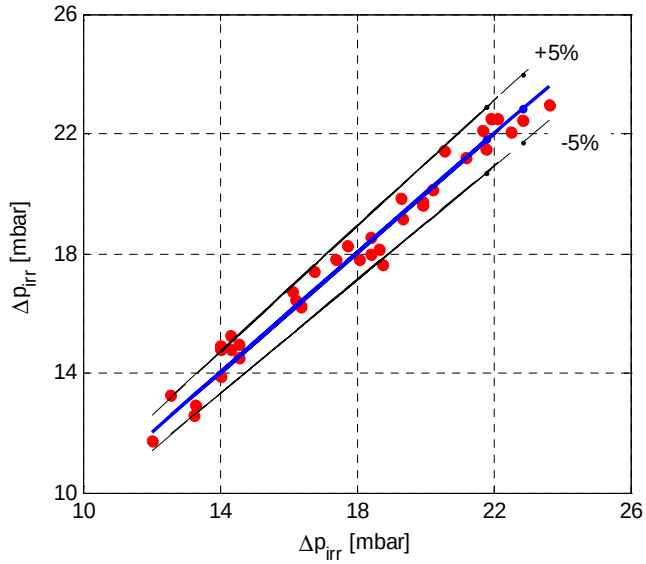

Fig.9.14: Experimental vs. predicted (eq 9.7) VFM irreversible pressure losses

9.6 Two-phase mass flow rate evaluation

For two-phase mass flow rate measurement purposes, as described in chapter 4, typically a set of instruments (Spool Piece - SP) must be installed. Each instrument of the SP has to be sensitive to the different properties of the flow (like momentum, velocity, density, void fraction) and the selection of the instruments depends strongly on the experimental conditions: pressure, temperature and phases velocities. Different instruments can be coupled in a SP, and the VFM, characterized by the absence of moving parts and by a smoother flow profile than the orifice plates, is one of the instruments more suitable to be installed in a wide range of industrial applications.
In single-phase flow the VFM allows the estimation of the mass flow rate from the pressure drop across the pipe restriction, but in presence of two phases the direct correlation between

pressure drops and mass flow rate is not possible, so that additional information and a model able to interpret the signals are required [9.1], [9.6],[9.7].
The use of the discharge coefficient requires the knowledge of the void fraction, that must be used to evaluate the mixture density and the Reynolds number, from which the discharge coefficient depends on.
In the present analysis this information is obtained by means of the QCVs, that measure the mean volumetric void fraction in the test section. Due to the integral nature of this information, the mean void fraction can differ from the local void fraction along the VFM, so that the accuracy of the model is limited.
Compared to the analysis proposed in chapter 7, [9.1], in the present model the introduction of the correlation x-α is avoided due to the information extracted from the measurement of the irreversible pressure losses. The two-phase flow parameters are estimated, using this approach, with the accuracy reported in Fig.9.15, Fig.9.16 and Fig.9.17.

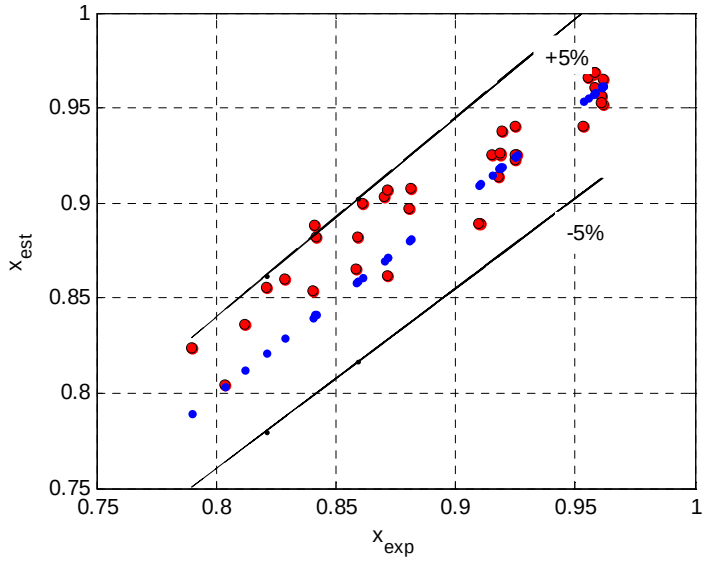

Fig.9.15: Estimated flow quality vs. experimental value. Discharge coefficient model

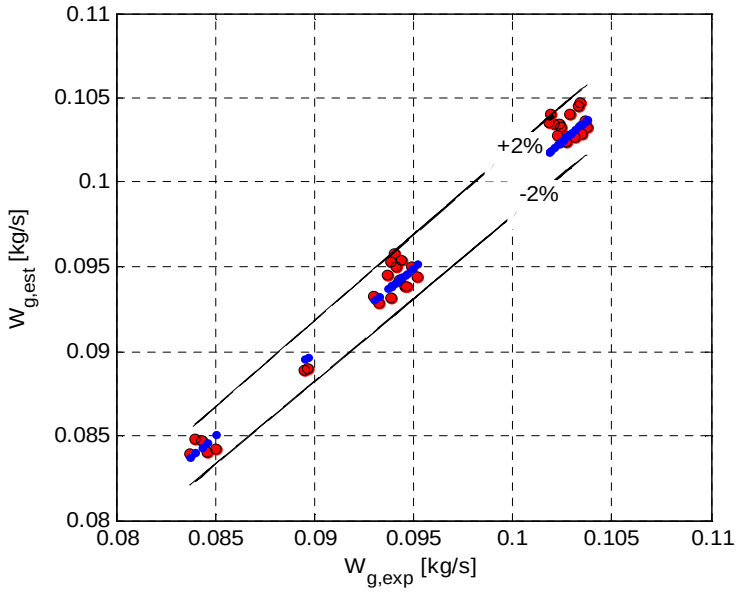

Fig.9.16: Estimated air mass flow rate vs. experimental value. Discharge coefficient model

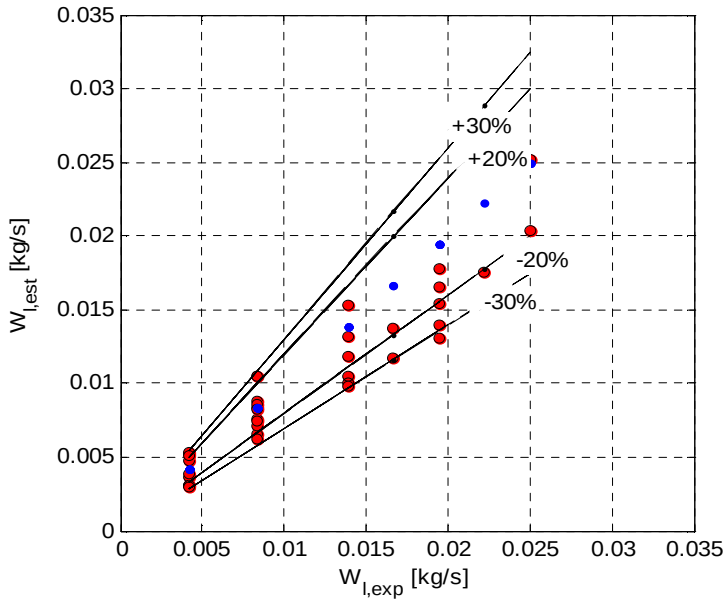

Fig.9.17: Estimated water mass flow rate vs. experimental value. Discharge coefficient model

In the tested limited flow ranges, because the flow pattern doesn't change, it is possible to derive the essential information from the signals of a VFM, avoiding the direct measurement of the void fraction.

In the model based on the evaluation of the two-phase flow multiplier, the closure equation is based on the measurement of the irreversible pressure losses and on the proposed correlation (eq. 9.7).

Using an iterative approach the flow quality and the mass flow rate of the two phases have been estimated by using only the acquired signals of the VFM and the information concerning the absolute pressure and the temperature of the flow. The flow quality is evaluated using eq. 9.6 correlation: an initial guess value of the parameter is used to evaluate the VFM pressure drops, and the iterative loop goes on until the estimated pressure drop reaches the experimental value. Then the mass flow rates of the two phases are estimated by using the flow quality value and the eq. 9.7 correlation. The reference signals have been obtained as the mean values of the 30 s acquisition time. In Fig.9.18 the estimated flow quality values are compared with the experimental data, obtained from the measurement of the single phases mass flow rate. The relative error is in each case lower than 5%.

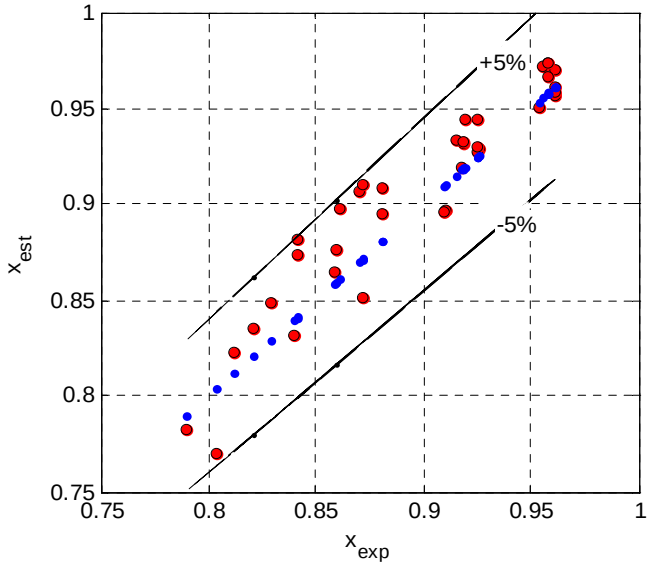

Fig.9.18: Estimated flow quality vs. experimental value. Two-phase flow multiplier model

In Fig.9.19 and Fig.9.20 the estimated mass flow rates of air and water are compared with the measured values: the air mass flow rate is estimated with an accuracy of 2%, while a lower accuracy characterizes the liquid flow rate prediction (the relative error is lower than 30% for all conditions).

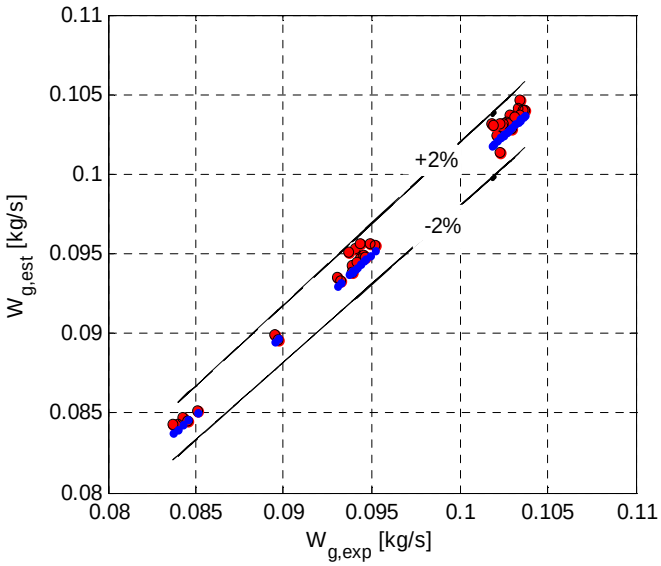

Fig.9.19: Estimated air mass flow rate vs. experimental value. Two-phase flow multiplier model

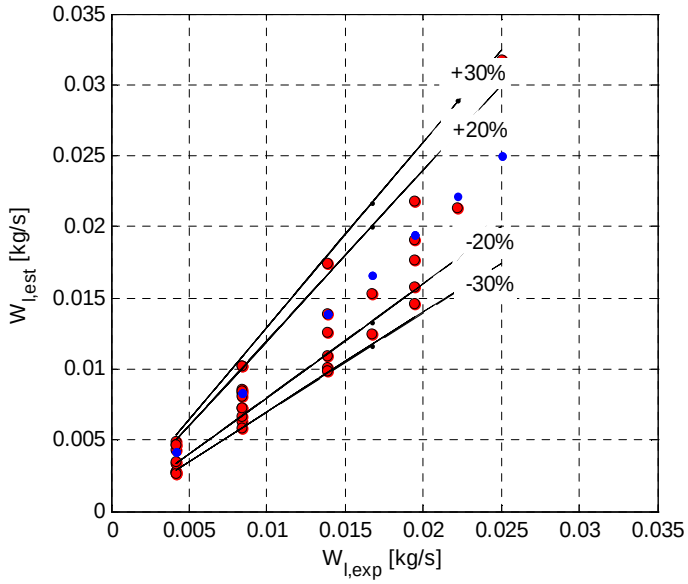

Fig.9.20: Estimated water mass flow rate vs. experimental value. Two-phase flow multiplier model

9.7 Conclusions

In the present chapter, the experimental investigation of a Venturi Flow Meter (VFM) in vertical upward annular two-phase flow has been performed. The dependency of the pressure drops, evaluated between the VFM inlet and throat and between the inlet and outlet sections (irreversible pressure loss), on the characteristic flow parameters (flow velocities, quality and void fraction) have been analyzed and discussed.

The analysis highlights that, from the measurement of the VFM irreversible pressure losses, important information can be extracted concerning the effect of the liquid dispersed phase on the total pressure drops. Due to the liquid phase presence, the inlet-throat pressure drop increases of about 10% compared to the single-phase flow, while the irreversible pressure losses increase from about 20% to 100% depending on the liquid flow rate. The proposed correlation describes the irreversible pressure loss change as a function of the flow rate of the two-phases, highlighting the effect of the dispersed phase.

Two different approaches for the mass flow rate measurement of the phases have been analyzed.
In the first one the model of the discharge coefficient of the VFM coupled with the void fraction measurement, performed by means of the QCVs, allowed us to estimate the two phases with an accuracy of 2% for air and 30% for water. The estimation accuracy can be improved measuring the void fraction near the VFM, in order to avoid the use of integral information, that are not always representative of the local flow conditions.

The second approach, has been developed in order to estimate the mass flow rate of the two phases, avoiding the direct measurement of the void fraction. This approach can be used, in very limited range of the flow parameters and only if the flow pattern is not changing. In these conditions, correlations describing the relation between velocities and VFM pressure

drops have been developed for the two pressure drops components. For both correlations, the prediction error is lower than 5%.
The developed model allows the evaluation of the flow quality of the mixture with an accuracy of 5% and the estimation of the mass flow rate of air and water with an accuracy of 2% and 30% respectively, showing that in particular conditions a single instruments can be used to estimate the mass flow rate also in two-phase flow.

ANNEX I: VFM DRAW

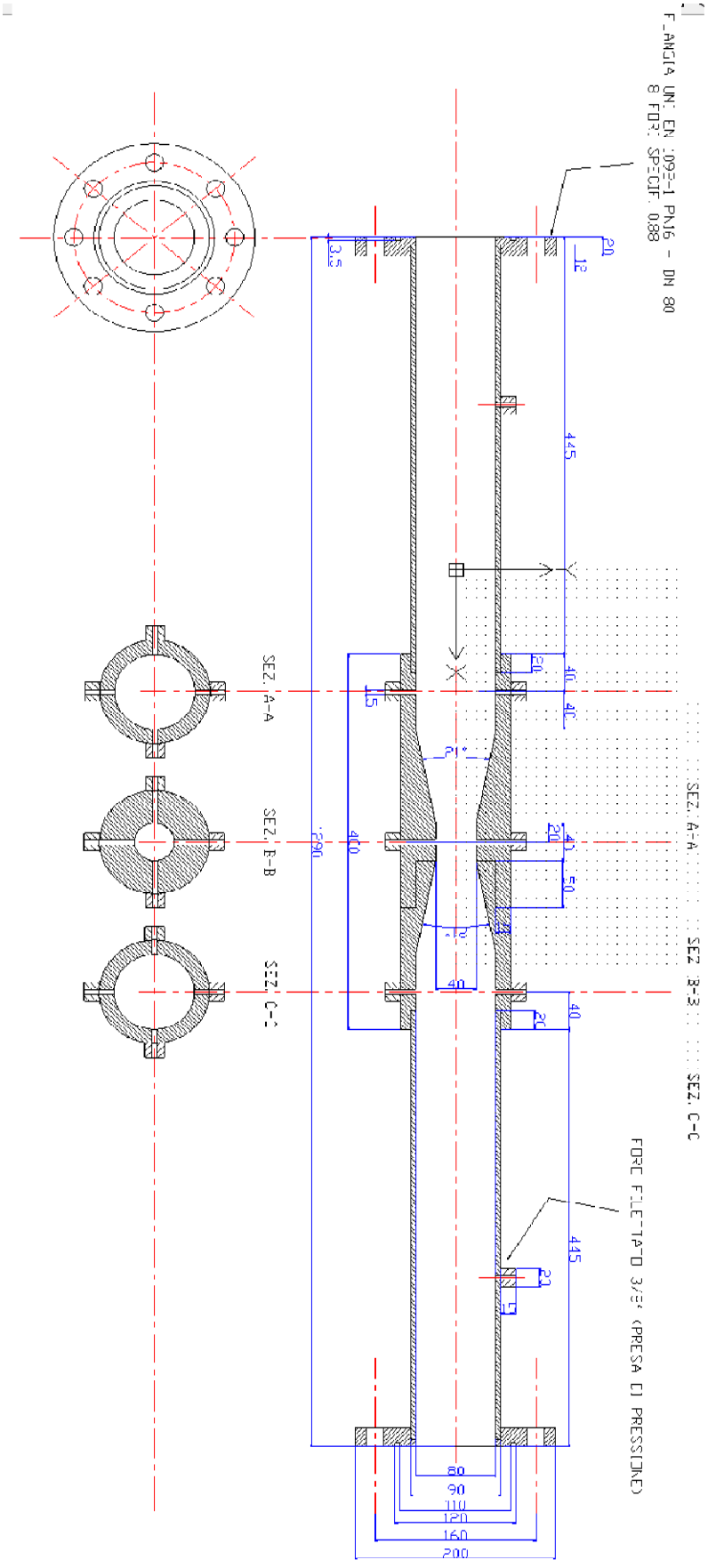

10. CONCLUSIONS

The developed research work focused on the development of special instrumentation and on the development of models, based on the analysis of experimental data, that are able to interpret the measurement signals for many possible two-phase conditions.
Two different measurement field, the internal flow structure investigation and the instrument modeling for phases mass flow rate reconstruction purposes, have been investigated.

Concerning the first field, the investigation of an horizontal two-phase flow has been performed by means of a Wire Mesh Sensor, as described in chapter 5. Local, chordal, cross-section void fraction values are derived from the sensor data in a wide range of phases superficial velocities, and a new signal methodology, able to characterize the flow in terms of phases distribution (flow patterns) and time evolution, has been developed. Moreover the methodology allows the extraction of important flow information, such as the local and time average void fraction, the interface evolution, and characteristic frequencies.
The evolution of the void fraction profiles has been related to the superficial velocity of the two-phases (J_g and J_l) and the flow evolution in time and space has been analyzed and discussed, showing that such methodology is useful to identify and characterize in detail the two-phase flow. The obtained results allowed us to improve the knowledge of the phases distribution in a horizontal flow and can be used to improve the modeling of the two-phase flow, both for measurement purpose and numerical analysis.

Concerning the second measurement field, a bibliographical research, on the available instrumentation for two-phase flow application, has been performed.
In the framework of the development of a SP able to measure the mass flow rate of the phases in the SPES-3 facility (nuclear safety experimental facility), that is currently under construction at the SIET laboratories in Piacenza (Italy), the candidate instruments have been defined considering the estimated flow range parameters.
The criteria that should be satisfied concern: range of measurement, dynamic response, installation requirements, materials/electrical compatibility with pressure and temperature conditions, flow velocity compatibility.

The selected instruments, described in the chapter 4 (TFM, DD, VFM and Impedance Probes) have been experimentally studied in different pipe configurations, and different models have been developed for each one. Different instrument combinations have been tested, and the performance of each one has been analyzed in terms of estimation of the mass flow rate of the two phases and two-phase flow parameters dependency.

In chapter 6 the SP made up of a turbine flow meter (volumetric device), a drag disk (momentum measurement device) and an impedance concave sensor (void fraction measurement device) has been analyzed under a wide range of flow conditions.
The experimental data have been used to construct an operating map of the SP, able to evaluate the mass flow rates of the phases in the mixture, with the relative errors, and to predict the flow pattern. The Aya's model has been used to estimate the mass flow rate of the two phases, obtaining an estimation accuracy of 15% in the 75% of the cases.

In chapter 7 the analysis of the signals and the developed model of the SP, made up of a VFM and WMS is reported. The developed methodology allow the estimation of the mass flow rate of the phases in air-water horizontal flows with a good accuracy in a large range of the flow conditions (J_g = 0.14 - 32 m/s and J_l = 0.019 - 2.62 m/s), with observed flow patterns ranging from stratified flow to intermittent flow (slug and plug) and annular flow.
The VFM response has been modeled by defining the two-phase flow discharge coefficient, $C_{d\text{-}TP}$, and its Re dependency. A modified Lockart-Martinelli correlation for x-α, able to represent the WMS experimental data, has been developed and included in the SP model.
By means of the developed signal analysis the mass flow rate has been estimated with an error lower than 10% in the 73.3% of the cases. Moreover the estimation error has been found considerably lower for the flow characterized by high values of quality and void fraction. In this range, with reference to facility SPES3 test conditions, the error in the mass flow rate estimation is always lower than 10% and 20% for water and air respectively.

In chapter 8, the analysis and the characterization of the impedance sensor (Electrical Capacitance Sensor – ECP, developed by the SIET company), consisting of 10 measurement electrodes (9 external and an internal one), in vertical annular and annular-mist flow, is described.
The response of the sensor has been characterized in terms of single-phase flow sensitivity and signal variation dependence. Geometry and fluid-dynamic influences on the signal have been investigated experimentally and numerically, by means of a FEM software. Although the sensitivity in single-phase flow is low, two-phase flow void fraction variations lower than 1% has been detected. The central electrode signal has been related to the average cross-section void fraction, difficult to measure with external electrodes, due to the presence of the wall liquid film, that act as a screen. The variation of the signal measured in the external electrodes has been related to the average liquid film thickness that has been evaluated by means of the Ishii model. The tests have shown the potentiality of this technology for the measurement of two-phase flow parameters at very high void fraction conditions (higher than 95%).

In the last chapter the modeling of a VFM, specifically designed by the candidate for two-phase flow investigation purpose, is described. The instrument has been analyzed in vertical

upward annular two-phase flow. The dependency of the pressure drops, evaluated between the VFM inlet and throat and between the inlet and outlet sections (irreversible pressure loss), on the characteristic flow parameters (flow velocities, quality and void fraction) have been analyzed and discussed.
The analysis highlights that, from the measurement of the VFM irreversible pressure losses, important information can be extracted concerning the effect of the liquid dispersed phase on the total pressure drops. A correlation for the VFM pressure drops and a correlation for the irreversible pressure losses have been developed. For both correlations, the prediction error is lower than 5%.
Two different approaches for the mass flow rate measurement of the phases have been analyzed.
In the first one the model of the discharge coefficient of the VFM coupled with the void fraction measurement, performed by means of the Quick Closing Valves (QCVs), allowed us to estimated the two phases flow rates with an accuracy of 2% for air and 30% for water.
The second approach has been developed in order to estimate the mass flow rate of the two phases avoiding the direct measurement of the void fraction. This approach can be used in a very limited range of flow parameters and only if the flow pattern is not changing. In that conditions, the developed correlations describing the relation between velocities and VFM pressure drops and irreversible pressure losses have been used to estimate the mass flow rate of the phases.
The developed model allows the evaluation of the flow quality of the mixture with an accuracy of 5% and the estimation of the mass flow rate of air and water with an accuracy of 2% and 30% respectively, and a standard deviation of 1%, 2% and 10% respectively, showing that in particular conditions a single instrument can be used to estimate the mass flow rate also in two-phase flow.

The thesis work showed that the measurement of two-phase flow quantities requires superior instrument performance. Performance parameters include accuracy, repeatability, resolution, rangeability, and dynamic response.
The choice of a meter to measure flow quantities in two-phase flow [4.4]depends on the purpose for which the measurement is made, whether an average or a local quantity is needed and on the accuracy required. The selection of the flow meter, and the related accuracy also depends on the nature of the flow field and the two phases involved.
The relative magnitudes of the instrumental length scales (pipe diameter for Venturi flow meters, drag plates area for drag disk, probe tip radius or probe plate area for impedance sensors, piezoelectric crystal diameter, wave length of the sensing radiation (whether electromagnetic or acoustic), etc.., compared with the length scale of the flow objects (drop or bubble diameters, film thickness, interface area, etc...), restrict the nature of the information provided by any device and hence affect how information are deduced and analyzed.

The performed research has allowed the identification of the advantage and drawbacks of the different instrument combinations, and the identification of the phases mass flow rate measurement accuracy achievable for each SP configuration.
The work has highlighted the complexity of the instruments selection and modeling, depending on the specific condition investigated.

Moreover the experimental analysis that has been performed with the different instruments, at different flow conditions and for different geometrical configurations, has allowed the investigation and the characterization of the air-water flow in a wide range of flow configurations and allowed the development of new correlations able to estimate two-phase flow parameters, such as void fraction and two-phase flow pressure drops.

In particular conditions, usually in laboratory experiments, in which the measurement errors must be further reduced, more sophisticate models able to couple the detailed physics of the instruments and the detailed physics of the flow, need to be developed, and more flow parameters need to be measured at different locations in order to evaluate the influence of the SP on the flow parameters them-selves, obviously increasing the complexity and the costs of the system.

For industrial installation purpose the best SP choice is also strongly influenced from economic considerations, including flow meter hardware cost (sensor, transmitter or conditioner, tubing, wiring), installation requirements (flanges, straight pipe lengths, taps), pressure drop (related to pumping costs), reliability, maintainability, and frequency of calibration; so that the optimum balance between cost and SP performance must be achived.

For the analyzed applications, the best instruments choise should be oriented to meters devoided of moving parts, such as VFM and impedance sensors, that allow the possibility to work in very different flow conditions without failures, and are characterized by a very good time response.
As futher work, the author suggests the development of a new system in which the two instrument (VFM and impedance sensor) could be incorporated (impedance probe installed along the VFM external wall), not only reducing the SP space requirement, but also allowing a more detailed information on the phase distribution inside the VFM. The information can be used todevelop a model of the sensor based on the balance equations of the two-phases inside the control volume. This model will allow a better interpretation of the signals and so a more accurate evaluation of the mass flow rates of the phases.

REFERENCES

Chapter 1

[1.1] Carelli M D, Conway L E, Oriani L, Petrović B, Lombardi C V, Ricotti M E, Barroso A C O, Collado J M, Cinotti L, Todreas N E, Grgić D, Moraes M M, Boroughs R D, Ninokata H, Ingersoll D T, Oriolo F, The Design and Safety Features of the IRIS Reactor, Nucl. Eng. Design, 230, pp. 151-167 (2004)

[1.2] SIET document 01 334 RT 07 Rev.1: Conceptual design of SPES3-IRIS facility Rev.1, September 2008

[1.3] Bertani C, De Salve M, Malandrone M, Monni G, Panella B, Mosetto A, SPES-3 Facility Analysis, reference data for postulated Accident Simulation, Criteria for general and special Instrumentation selection, Report RdS/2010/68 ENEA

[1.4] Bertani C, De Salve M, Malandrone M, Monni G, Panella B, State-of-Art and selection of techniques in multiphase flow measurement, Report RdS/2010/67 ENEA

[1.5] De Salve M, Monni G, Panella B, Turbine Flow Meter and Drag-Disk in Horizontal Air Water Flow. , In: UIT2011, Torino (Italia), 20-22 Giugno 2011. pp. 107-112

[1.6] De Salve M, Monni G, Panella B, A Model for a Spool Piece made up of Venturi and Void fraction Flow Meter in Horizontal Flow, In: ANS TRANS., vol. 108 , pp. 1013-1016. - ISSN 0003-018X, (2013)

[1.7] De Salve M, Monni G, Panella B, Horizontal Air-Water Flow Analysis with Wire Mesh Sensor. In: JoP, vol. 395, 012179-. - ISSN 1742-6588, (2012)

[1.8] Monni G, De Salve M, Panella B, Randaccio C, Electrical Capacitance Probe Characterization in Vertical Annular Two-Phase Flow. In: SCI TECHNOL NUCL INSTAL, vol. 2013, Article ID 568287, pp. 1-12. - ISSN 1687-6075, (2013)

Chapter 2

[2.1] Umminger K and Del Nevo A, Integral Test Facilities and Thermal-Hydraulic System Codes in Nuclear Safety Analysis, Science and Technology of Nuclear Installations, Vol 2012, Article ID 826732, 3 doi:10.1155/2012/826732

[2.2] Ferri R, Simulating capabilities of the SPES3 facility, Report RdS/2011/6

[2.3] Carelli M D, Conway L E, Oriani L, Petrović B, Lombardi C V, Ricotti M E, Barroso A C O, Collado J M Cinotti L, Todreas N E, Grgić D, Moraes M M, Boroughs R D, Ninokata H, Ingersoll D T, Oriolo F, The Design and Safety Features of the IRIS Reactor, Nucl. Eng. Design, 230, pp. 151-167 (2004)

[2.4] SIET document 01 334 RT 07 Rev.1: Conceptual design of SPES3-IRIS facility Rev.1, Sept. 2008

[2.5] SIET document 01 489 RT 09 Rev.0: SPES3-IRIS facility RELAP5 base case transient analyses for design support, Apr. 2009.
[2.6] SIET document 01 423 RT 08 Rev.0: SPES3-IRIS facility nodalization for RELAP5 Mod.3.3 code and steady state qualification, Jan. 2009.
[2.7] SIET document 01 525 ST 09 Rev.0: SPES3 - Two-phase Mass Flow Measurements: Technical Specifications, July 2010.

Chapter 3

[3.1] Collier J G and Thome J R, Convective Boiling and Condensation, Oxford science publications, 3th edition, 1996
[3.2] Ishii M, One-dimensional drift-flux model and constitutive equations for relative motion between phases in various two-phase flow regimes, Argonne National Laboratory, ANL-77-47, (1977)
[3.3] Ishii M and Hibiki T, Thermo-Fluid Dynamics of Two-Phase Flow, Springer, 2nd edition
[3.4] Rouhani S Z, Sohal M S, Two-phase flow patterns: a review of research results, Prog. nucl. Energy, 1983 11 219–259
[3.5] Melkamu A Woldesemayat, Afshin J Ghajar, Comparison of void fraction correlations for different flow patterns in horizontal and upward inclined pipes, International Journal of Multiphase Flow 33 (2007) 347–370
[3.6] Wallis G B, One-Dimensional Two-Phase Flow, McGraw Hill, 2nd Edition, New York, 1979.
[3.7] Zuber N, Findlay J, Average Volumetric Concentration in Two-Phase Systems, Trans ASME Jul Ht Transfer, Vol 87, p 453, 1969.
[3.8] Friedel L, Are the so called two-phase flow densities physical and real fluid-dynamic design variables in one-dimensional critical flow?, Journal of Loss Prevention in the Process Industries, Vol. 11, N 6, November 1998 , pp. 431-435(5)

Chapter 4

[4.1] Baker C R, Flow measurement handbook, Cambridge University Press, (2000)
[4.2] Miller R W, Flow measurement engineering handbook, McGrawHill, (1996)
[4.3] Bertani C, De Salve M, Malandrone M, Monni G, Panella B, State-of-Art and selection of techniques in multiphase flow measurement, Report RdS/2010/67 ENEA
[4.4] Hewitt G F, Measurement of two-phase flow parameters, Academic Press, (1978)
[4.5] Collier J G and Thome J R, Convective Boiling and Condensation, Oxford science publications, 3th edition, 1996
[4.6] Aya I , A Model to Calculate Mass flow rates and Other quantities of Two-phase flow in a Pipe with a densitometer, a drag disc, and a turbine meter, ORNL TM-47591, (1975)
[4.7] Chen N C J, Felde D K, Two-phase mass flux uncertainty analysis for thermal-hydraulic test facility instrumented spool pieces, ORNL, (1982)
[4.8] Hardy J E, Mass flow measurements under PWR reflood conditions in a downcomer and at a core barrel vent valve location, ORNL ,NUREG/CR-2710, (1982)

[4.9] Ohlmer E and Schulze W, Experience with CENG full-flow turbine meters for transient two-phase flow measurement under loss-of-coolant experiment condition, BHRA 2nd Int. Conf. on Multi-phase flow, London, (1985)
[4.10] Rouhani S, Application of the Turbine Type Flow Meters in the Measurement of Steam Quality and Void, presented at the Symposium on In-Core Instrumentation, Oslow, June 15, 1964.
[4.11] Anderson J L and Fincke J R, Mass flow measurements in air/water mixtures using drag devices and gamma densitometers. ISA Trans., (1980)
[4.12] Averill and Goodrich, Design and performance of a drag Disc and Turbine transducer. For LOFT Experimental Program, (1979)
[4.13] Chen and Felde, Two-phase mass flow uncertainty analysis for Therma-Hydraulic test facility instrumented Spool Piece. NUREG/CR-2544, (1982)
[4.14] Furrer M, Strumentazione, metodi e analisi impiegati per la misura della portata in massa in regime bifase. ENEA document, (1986)
[4.15] Ginesi, Chosing the best flowmeter, Chem. Eng., NY, 98(4):88-100, (1991)
[4.16] Kamath and Lahey, Transient analysis of DTT rakes. NUREG/CR-2151. and also in Nuclear Engineering and Design 65 343-367, (1981)
[4.17] Lahey R T, Two-phase flow phenomena in nuclear reactor technology. Quarterly report NUREG/CR-0233, (1978)
[4.18] Reimann, John and Moller, Measurement of two-phase mass flow rate: a comparison of different techiques. Int . Multiphase Flow Vol. 8, No. 1, (1981)
[4.19] Sheppard, Long, Tong, Apparatus for monitoring two-phase flow. ORNL report, 1975
[4.20] Turnage (1980): Two-Phase Flow Measurements with Advanced Instrumented Spool Pieces. NUREG/CR-1529
[4.21] Abdul-Razzak, Shoukri M, and Chang J S, Measurement of two-phase refrigerant liquid-vapor mass flow rate - part III: combined turbine and venturi meters and comparison with other methods, 1995.
[4.22] Johnson and Farroll S, Development of a turbine meter for two-phase flow measurement in vertical pipes, Flow Meas. Instrum., 1995.
[4.23] Shim T J, Dougherty and Cheh H Y, Turbine meter response in two-phase flows, Proc. Int. Conf. Nucl. Eng. - 4, **1** part B: 943-953, NY, NY:ASME, 1996.
[4.24] Hsu, Two-Phase Flow Instrumentation Review (1978)
[4.25] www.venturemeas.com
[4.26] Hardy and Smith, Measurement of two-phase flow momentum using force transducers, (1990)
[4.27] ISO 5167-1:4 :2003 (E)
[4.28] Lockhart R W and Martinelli R C, Proposed correlation of data for isothermal two-phase two-component flow in pipe *Chem. Eng. Prog.* 45 39-48, 1949
[4.29] Murdock J W , Two-phase flow measurement with orifices *J Basic Eng.* 84 419-33, 1962
[4.30] Chisholm D and Rooney D H, Research note: Two-phase flow through sharp-edged orifices J Mech. Eng. Sci. 16 353-55, 1974
[4.31] De Leeuw R , Liquid correction of venturi meter readings in wet gas flow In: North sea workshop paper 21, 1997
[4.32] Xu L, Xu J, Dong F and Zhang T, On fluctuation of the dynamic differential pressure signal of Venturi meter for wet gas metering Flow Meas. Instrum. 14 211-17, 2003

[4.33] Baroczy C J, A systematic correlation for two-phase pressure drop, AIChE reprint 37 presented at 8th National Heat Transfer Conference, Los Angeles, August
[4.34] James R, Metering of steam-water two-phase flow by sharp-edged orifices. Proc. Inst Mech. Engrs, 1965
[4.35] Lin Z H, Two-phase flow measurements with sharp-edged orifices. International Journal of Multiphase Flow, (1982)
[4.36] Lin Z H, Gas_liquid two-phase flow and boiling heat transfer. Xi'an: Xi'an Jiaotong University Press, (2003)
[4.37] Jitschin W , Gas flow measurement by the thin orifice and the classical Venturi tube, Vacuum 76, (2004)
[4.38] Steven R, Horizontally installed differential pressure meter wet gas flow performance review. In: North sea flow measurement workshop, (2006)
[4.39] Oliveira, Passos, Verschaeren, van der Geld, Mass flow rate measurements in gas–liquid flows by means of a venturi or orifice plate coupled to a void fraction sensor, Experime. Them. And Fluid Science, (2009)
[4.40] OMEGA, Complete Flow and Level Measurement Handbook and Encyclopedia®, OMEGA Press, (2005)
[4.41] Whalley P B, Boiling, Condensation, and Gas–Liquid Flow, Oxford University Press, New York, 1987.
[4.42] Zhang, Yue, Huang, Investigation of oil–air two-phase mass flowrate measurement using venturi and void fraction sensor, Journal of Zhejiang University Science 6A (6) (2005)
[4.43] www.engineeringToolBox.com
[4.44] Emerson dos Reis and Leonardo Goldstein Jr, A procedure for correcting for the effect of fluid flow temperature variation on the response of capacitive void fraction meters, Flow Measurement and Instrumentation, (2005),
[4.45] Hardy and Hylton, Double-layer impedance string probe for two-phase void and velocity measurements, ORNL, Int. J. Multiphase Flow, (1983)
[4.46] Olsen (1967), Theoretical and Experimental Investigation of Impedance Void Meter, Kjeller Research Establishment, Norway.
[4.47] Maxwell J C, A Treatise on Electricity and Magnetism. Oxford: Clarendon Press, 1882.
[4.48] Bernier R J N, Unsteady two-phase flow instrumentation and measurement, PhD Thesis, California Institute of technology, (1982)
[4.49] Stott, Green, Seraji, Comparison of the use of internal and external electrodes for the measurement of the capacitance and conductance of fluids in pipes, J. Phys. E: Sci. Instrum. 18 (1985)
[4.50] Abouelwafa, Kendall, The use of capacitance sensor s for phase percentage determination in multiphase pipelines, IEEE Trans. Instrum. Meas. 29 (1) (1980).
[4.51] Huang, Fielden, Green, Beck, A new capacitance transducer for industrial applications, J. Phys. E: Sci. Instrum. 21 (1988)
[4.52] Merilo M, Dechene L, Cichowlas M, Void fraction measurements with a rotating electric field conductance gauge. J. Heat Transfer 1977
[4.53] Ahmed and Ismail, Innovative Techniques for two-phase flow Measurements, recent Patents on Electrical Engineering, (2007)

[4.54] Fossa M, Design and performance of a conductance probe for measuring the liquid fraction in two-phase gas-liquid flows, Flow Measurement and Instrumentation, (1998)
[4.55] Coney M W E, The theory and application of conductance probes for the measurement of liquid film thickness in two-phase flow. J. Phys. E: Scient. Instrum. 1973
[4.56] Tsochatzidis N A, Karapantios T D, Kostoglou M V, Karabelas A J, A conductance method for measuring liquid fraction in pipes and packed beds. Int. J. Multiphase Flow 1992
[4.57] Yang, Stott, Beck, High frequency and high resolution capacitance measuring circuit for process tomography, IEE Proceedings Circuits Devices Systems 141, (1994)
[4.58] Halliday, Resnick, Walker, Fundamentals of Physics, 5th edition, J. Wiley & Sons, 1997.
[4.59] Jaworek, A, Krupa A and Trela M, Capacitance sensor for void fraction measurement in water/steam flows, Flow Measurement and Instrumentation, (2004)
[4.60] Rouhani S Z, Sohal M S, Two-phase flow patterns: a review of research results, Prog. nucl. Energy, 1983 11 219–259
[4.61] Reinecke N, Petritsch G, Boddem M, Mewes D, Tomographic imaging of the phase distribution in two-phase slug flow. International Journal of Multiphase Flow, 1998 24 617–34.
[4.62] Prasser H M, Böttger A, Zschau J, A new electrode-mesh tomograph for gas–liquid flows. Flow Measurement and Instrumentation 1998 9 111–9.
[4.63] Prasser H M, Krepper E, Lucas D, Evolution of the two-phase flow in a vertical tube-decomposition of gas fraction profiles according to bubble size classes using wire-mesh sensors, Int. J. Therm. Sci., 2002 41 17–28
[4.64] Da Silva M J, Schleicher E, and Hampel U, Capacitance wire-mesh sensor for fast measurement of phase fraction distributions. Measurement Science and Technology, 2007 18 2245-2251.
[4.65] https://www.hzdr.de/db/Cms?pOid=25191&pNid=3018
[4.66] Pietruske H, Prasser H M, Wire-mesh sensors for high-resolving two-phase flow studies at high pressures and temperatures. Flow Measurement and Instrumentation, 2007 18 87-94.
[4.67] Prasser H M, Misawa M and Tiseanu I, Comparison between WMS and ultra-fast X-ray tomography for an air-water flow in vertical pipe Flow Meas. Instrum. 16 73-83, 2005

Chapter 5

[5.1] Rouhani S Z, Sohal M S, Two-phase flow patterns: a review of research results, Prog. nucl. Energy, 1983 11 219–259
[5.2] Dukler A E, Hubbard M G, A model for gas–liquid slug flow in horizontal and near horizontal tubes Industrial & Engineering Chemistry Fundamentals, 1975 14 337–34
[5.3] Andreussi P, Bendiksen K, Investigation of void fraction in liquid slugs for horizontal and inclined gas-liquid pipe flow, Int. J. Multiphase Flow, 1989 15 (6) 937-946
[5.4] Canière H, T'Joen C, Willockx A, De Paepe M, Capacitance signal analysis of horizontal two-phase flow in a small diameter tube, Experimental Thermal and Fluid Science, 2008 32 892–904

[5.5] Hardy J E, Jallouk P A, Leavell W H, Advanced Instrumentation for Reflood Studies Program Quarterly Progress Report, October 1-December 31, 1977 NUREG/CR-0213 (OR NL/NUREG/TM-202);
[5.6] Reinecke N, Petritsch G, Boddem M, Mewes D, Tomographic imaging of the phase distribution in two-phase slug flow. International Journal of Multiphase Flow, 1998 24 617–34.
[5.7] Prasser H M, Böttger A, Zschau J, A new electrode-mesh tomograph for gas–liquid flows. Flow Measurement and Instrumentation 1998 9 111–9.
[5.8] Prasser H M, Krepper E, Lucas D, Evolution of the two-phase flow in a vertical tube-decomposition of gas fraction profiles according to bubble size classes using wire-mesh sensors, Int. J. Therm. Sci., 2002 41 17–28
[5.9] Pietruske H, Prasser H M, Wire-mesh sensors for high-resolving two-phase flow studies at high pressures and temperatures. Flow Measurement *and Instrumentation,* 2007 18 87-94.
[5.10] Teletronic Rossendorf GmbH, Wire Mesh Sensor System, WMS200 Manual, Version 1.2, December 9, 2010
[5.11] Kendal M C, Stuart A, The Advanced Theory of Statistics. Vol. 2. Griffin London (1961).
[5.12] Dobson M K, Heat transfer and flow regimes during condensation in horizontal tubes, Ph.D. Thesis, University of Illinois, Urbana, IL, 1994.
[5.13] J. Thome, Engineering Data Book III, Wolverine Tube INC., 2004.
[5.14] Baker O (1954), Simultaneous Flow of Oil and Gas, Oil and Gas Journal, 53 185-190.
[5.15] Mandhane J M, Gregory G A, Aziz K, A flow pattern map for gas-liquid flow in horizontal pipes, Int. J. Multiphase Flow, Vol. 1 537-553, (1974)
[5.16] De Salve M, Monni G, Panella B, Horizontal Air-Water Flow Analysis with Wire Mesh Sensor. J. Physics. Conf. series, vol. 395, 012179 - ISSN 1742-6588 (2012)
[5.17] De Salve M, Monni G, Panella B, Horizontal Two-Phase Flow Pattern Recognition, presented at 8th World Conf. on Exp. Heat Transfer, Fluid Mech., and Thermodyn., Lisbon, Portugal, June 16-20 (2013)
[5.18] De Salve M, Monni G, Panella B, Horizontal Air-Water Flow Pattern Recognition, WIT Transactions on Engineering Sciences, Vol 79, WIT Press 2013, doi:10.2495/MPF130381

Chapter 6

[6.1] Murdock J W,Two-Phase Flow Measurement with Orifices, Trans. ASME, J. Basic Eng. 84, 419-33 (1962).
[6.2] Collins D B and Gacesa M, Measurement of Steam Quality in Two-Phase Upflow with Venturimeters and Orifice Plates, Trans. ASME, J. Basic Eng. 3, 11-21 (1971).
[6.3] Rouhani S Z, Application of the Turbine Type Flowmeters in the Measurements of Steam Quality and Void, Symposiwn on In-Core Instrumentation, OSLO, June 1974.
[6.4] Aya I, A model to calculate mass flow rate and other quantities of two-phase flow in a pipe with densitometer , a drag disk and a turbine meter, ORNL-TM-4759, 1975
[6.5] Hardy, Mass flow measurements under PWR reflood conditions in downcomer and at a core barrel vente valve location, NUREG/CR-2710, (1982)
[6.6] Whalley P B, Boiling, Condensation, and Gas-Liquid Flow.
[6.7] Thom J R S, Prediction of Pressure Drop During Forced Circulation Boiling of Water,

Int. J. Heat Mass Transfer 2, 709-24 , (1964)
[6.8] De Salve M, Monni G, Panella B. Analisi delle prestazioni di uno *Spool Piece* in deflusso orizzontale bifase aria-acqua . SPOOL PIECE costituto da TURBINA e DRAG DISK. Report ENEA Luglio 2011
[6.9] Bertani C, De Salve M, Malandrone M, Monni G, Panella B, State-of-Art and selection of techniques in multiphase flow measurement, Report RdS/2010/67 ENEA

Chapter 7

[7.1] Prasser H M, Bottger A and Zschau J, A new electrode-mesh tomography for gas – liquid flows Flow Meas. Instrum. 9 111-9, 1998
[7.2] Prasser H M, Misawa M and Tiseanu I, Comparison between WMS and ultra-fast X-ray tomography for an air-water flow in vertical pipe Flow Meas. Instrum. 16 73-83, 2005
[7.3] ISO 5167-1:4 :2003 (E)
[7.4] Baker C R, Flow Measurement Handbook (Cambridge University Press) , 2000
[7.5] Lockhart R W and Martinelli R C, Proposed correlation of data for isothermal two-phase two-component flow in pipe Chem. Eng. Prog. 45 39-48, 1949
[7.6] Murdock J W, Two-phase flow measurement with orifices J Basic Eng. 84 419-33
[7.7] Chisholm D and Rooney D H 1974 Research note: Two-phase flow through sharp-edged orifices J Mech. Eng. Sci. 16 353-55, 1962
[7.8] De Leeuw R , Liquid correction of venturi meter readings in wet gas flow In: North sea workshop paper 21, 1997
[7.9] Xu L, Xu J, Dong F and Zhang T, On fluctuation of the dynamic differential pressure signal of Venturi meter for wet gas metering Flow Meas. Instrum. 14 211-17, 2003
[7.10] Baroczy C J, A systematic correlation for two-phase pressure drop, AIChE reprint 37 presented at 8th National Heat Transfer Conference, Los Angeles

Chapter 8

[8.1] De Salve M, Monni G, Panella B, Experimental Study of Horizontal air-water Two-Phase Flow with a Spool Piece, Report ENEA Settembre 2011
[8.2] De Salve M, Monni G, Panella B, Turbine Flow Meter and Drag-Disk in Horizontal Air Water Flow. In: UIT2011, Torino (Italia), 20-22 June 2011. pp. 107-112
[8.3] De Salve M, Monni G, Panella B, A Model for a Spool Piece made up of Venturi and Void fraction Flow Meter in Horizontal Flow, Trans. ANS, Vol. 108 1013-1016, Atlanta, Georgia, June 16–20 (2013)
[8.4] Achilli A, Greco M, Progettazione di una sonda capacitiva per misurazione del grado di vuoto medio di sezione di miscele bifase acqua-vapore. Report RdS/2010/x ENEA
[8.5] De Salve M, Monni G, Panella B, Caratterizzazione di una Sonda capacitiva in deflusso verticale ascendente aria-acqua Report RdS/2011/121
[8.6] Monni G, De Salve M, Panella B, Randaccio C, Electrical Capacitance Probe Characterization for Vertical Annular air-water Flow, in 9th International Conference on Heat Transfer, Fluid Mechanics and Thermodynamics, July 2012 Malta
[8.7] Ishii M, Mishima K, Two-fluid model and hydrodynamic constitutive relations, Nuclear Engineering and Design, 82, 107-126 (1984)

[8.8] Baker J L L, Flow regime transitions at elevated pressures in vertical two-phase flow, Argonne National Laboratory Report, No. 7093, (1965),
[8.9] Bennett A W, Hewitt G F, Kearsey H A, Keeys R K F, and Lacey M P C, Flow visualization studies of boiling at high pressure, Proc. Inst. Mech. Eng., 180 (Part 3C), 1–11, (1965),
[8.10] Bertani C, De Salve M, Malandrone M, Monni G, Panella B, Mosetto A, SPES-3 Facility analysis, reference data for postulated accident simulation; criteria for general and special instrumentation selection, Report RdS/2010/68 ENEA, (2010),
[8.11] Carelli M, Conway L, Dzodzo M, et al., The SPES3 experimental facility design for the IRIS Reactor simulation, Science and Technology of Nuclear Installations, Vol. 2009
[8.12] Costigan G, Whalley PB, Slug flow regime identification from dynamic void fraction measurement in vertical air-water flows, Int. J. Multiphase Flow, Vol. 23, No. 2, pp. 263-282, (1997)
[8.13] De Salve M, Monni G, Panella B, State of art and Selection of techniques in Multiphase Flow Measurement, Report RdS/2010/67, ENEA, (2010)
[8.14] Elkow K J, Rezkallah K, Void fraction measurements in gas–liquid flows using capacitance sensors, Meas. Science and Technology, Vol. 7, No 8, pp. 1153-1163, (1996)
[8.15] Ferri R, Congiu C, SPES3-IRIS facility RELAP5 base case transient analyses for design support, SIET document 01 489 RT 09 Rev.0 (2009)
[8.16] Ferri R, Achilli A, Congiu C, et al., SPES3 facility and IRIS reactor numerical simulations for the SPES3 final design, in Procs. of the European Nuclear Conference (ENC '10), Barcelona, Spain, May- June 2010
[8.17] Hazuku T, Takasama T, Hibiki T, Ishii M, Interfacial area concentration in annular two-phase flow, Int. J. of Heat and Mass Transfer, (2007), Vol. 50, pp. 2986-2995
[8.18] Hewitt GF, Roberts DN, Studies of two-phase flow patterns by simultaneous X-ray and flash photography, UKAEA Report AERE-M 2159, (1969)
[8.19] Ishii M, Mishima K,Two-fluid model and Hydrodynamic constitutive relations, Nuclear Engineering and Design Vol. 82, pp. 107-126, (1984)
[8.20] Okawa T, Kotani A, Shimada N, Kataoda I, Effects of a Flow Obstacle on the Deposition Rate of Droplets in Annular Two-Phase Flow, J. of Nuclear Science and Technology, Vol. 41, No. 9, pp. 871-879, (2004)
[8.21] Randaccio C, Prove a caldo di una sonda capacitiva per la misura del grado di vuoto in miscela bifase SIET document 01 876 RP 12 (2012)
[8.22] Rochal M S, Cabral E L L and Simões-Moreira JR, Capacitance Sensor for Void Fraction Measurement in a Natural Circulation Refrigeration Circuit, International Nuclear Atlantic Conference - INAC 2009

Chapter 9

[9.1] De Salve M, Monni G, Panella B, A Model for a Spool Piece made up of Venturi and Void fraction Flow Meter in Horizontal Flow, Trans. ANS, Vol. 108 1013-1016, Atlanta, Georgia, June 16–20 (2013).
[9.2] Monni G, De Salve M, Panella B, Two-phase flow measurements at high void fraction by a Venturi meter, submitted to Progress of Nuclear Energy, February 2014.

[9.3] Monni G, De Salve M, Panella B, and Randaccio C, Electrical Capacitance Probe Characterization in Vertical Annular Two-Phase Flow, Science and Technology of Nuclear Installations, Vol. 2013, Article ID 568287, 12 pages, ISSN: 1687-6075 (2013).

[9.4] Chisholm D, Two-phase flow through sharp edged orifices. J. Mech. Eng. Sci., 19(3), 128–30 (1977).

[9.5] Murdock J W, Two-phase Flow Measurement with Orifices, ASME J. Basic Eng., December, 419-433 (1962).

[9.6] Zhang H J, Yue W T, Huang Z Y, Investigation of oil–air two-phase mass flow rate measurement using venturi and void fraction sensor, J. Zhejiang University Science 6A (6) (2005).

[9.7] Meng Z Z, Huang Z Y, Ji H F, Li H Q., Yan Y, Air-water two-phase flow measurement using a Venturi meter and an electrical resistance tomography sensor, Flow Meas. and Instr., 21, 268-276 (2010).